# INELASTIC NEUTRON SCATTERING SPECTROSCOPY OF POLYPEPTIDES AND MOLECULAR CRYSTALS.

Richard Laurence Hayward.

Submitted in satisfaction of the requirements for the degree of Doctor of Philosophy.
The University of Edinburgh.
1995.

**ABSTRACT.** A predictive and practical theory for a fundamental biological problem - the relation between a protein's three dimensional folded form and its function - will rest on an accurate description of the potential energy surface as a function of the protein configuration, and, thereby, on an accurate description of dynamic and thermodynamic properties. A successful theory of this sort will provide the means for rational design of proteins and ligands with desirable properties. Modern computational chemistry techniques have been applied, with qualitative success, to the calculation of protein potential energy functions, and resulting dynamics and ligand binding properties. These calculations have led to suggestions for new drug design. Improvement in the accuracy of predictions from such calculations will require a consistent programme of refinement of parameterisation and approximation schemes, by comparison with experimental data. This thesis describes the application to this task of inelastic neutron scattering experiments on samples of polypeptides (collagen, $(prolylprolylglycine)_{10}$ and polyproline II) and molecular crystals of biological relevance (acetanilide and two isotopomers). The experimental data were analysed for each of the samples in the context of models for their dynamics on the picosecond time scale. Improvements of the form and parameters of the dynamical models are suggested by comparison of the experimental data with the results of numerical calculations. An appendix describes an idea I have had for the model independent exploitation of neutron scattering data, and a second appendix records inelastic neutron scattering data collected for two further molecular crystals of biological relevance, l-alanine and acetyl-alanyl-methylamide.

This thesis is dedicated to the memory of my granny, Mary Kathleen Hay Byrne, who had a great sense of humour, and who saw me start this thesis, but died before I could finish it. She's pushing up roses, as she did all her life!

**DECLARATION.**

I declare that this thesis has been composed by myself and that the work described herein is my own except where stated.

12/6/95

**ACKNOWLEDGEMENTS.**

I thank my supervisors, Jeremy Bradshaw, Richard Ashley, and Andrew Miller who consistently (and patiently!) supported me during my sometimes erratic journey towards completing this thesis. Thanks to the boys in Edinburgh who kept me going in thin times with a diet of pristine jokes - Kevin Duff, Pete Gilchrist, Andy Cudmore, Ray Gilmour and Dermot McGinnity. Thanks to the secretaries in Edinburgh too - Norah Farquharson for mediating with the higher powers, Anne Stirling-White, Susanne Sellar and Elaine Chalmers for mediating with the fax machine and the photocopyer, and Frances Fettes for keeping an eye on me.

Thanks especially to Dieter Middendorf, who had many of the ideas in this thesis and the generosity to put me to work on them. I benefited a lot from his experience, and his knowledge of the literature and personalities of neutron scattering. Without him I would be thinner, having missed a lot of delicious midnight *piqniques* at RAL, and also the (scientifically critical) hospitality of Dieter, and Helen Saibil, at Berkhamstead.

I'm also grateful to Jeremy Smith for taking Dieter up on a challenge, and showing an ignorant medic how to do molecular dynamics. The four months spent at Saclay in Jeremy's lab were happy and productive. There were also quite a gang at Saclay conspiring to get me this thesis. I have to thank especially Emanuele Paci for his cultured Roman hospitality, though his conspiracies were more to do with finding me an Italian wife, and also Mafalda Nina for all the looking after, the feeding and the encouragement. Alex Micu, Marc Souaille, Cathy Tennette, Nicolas Folloppe all helped too, not least by nurturing my parasitic appearance on the computers at Saclay. Boris Velikson I have to thank for hospitality and a futile effort to improve my French. Thanks too to Massimo Marchi for pleasant times mushroom hunting, and a persistent effort to improve my physics.

I'm indebted to George Sims and to Drs. Celia Goodhew, Stewart Parker, John Tomkinson, Colin Carlile, Ulderico Wanderlingh, Colin Pulham and Graham Pettigrew for technical help and advice.

Last but not least I want to thank my mother, Mary, who fed me every day, and still applied her brains to my problems, Jenny and Owen for musical inspiration and outdoor inspiration and for taking me with a large pinch of salt, and my father, Richard, for having the strength and courage to make a come back.

I was financially supported throughout this thesis by a Wellcome Research Fellowship, and, for the visit to Saclay, by a short term European Molecular Biology Organisation grant.

CONTENTS.

LIST OF FIGURES AND TABLES.

Figures.

**Chapter III.**



**Chapter IV.**

Figure 6.5. As for Fig. 6.4 on an expanded energy scale.
Figure 6.6. INS spectrum calculated using the parameters of Table 5.1, Chapter V, in the three phonon approximation compared with experimental INS spectrum for ACN-D5.
Figure 6.7. As for Fig. 6.6 on an expanded energy scale.
Figure 6.8. INS spectrum for ACN-D8 calculated using the parameters of Table 5.1, Chapter V, in the one-phonon approximation at the Brillouin zone centre for ACN-D8.
Figure 6.9. INS spectrum calculated using the parameters of Table 6.1 in the three phonon approximation compared with experimental INS spectrum for ACN. The effect of the reduced crystal field splitting of the methyl peak produces a tall narrow peak, though the integrated intensity agrees with experiment [Fig. 6.12].
Figure 6.10. INS spectrum calculated using the parameters of Table 6.1 in the three phonon approximation compared with experimental INS spectrum for ACN-D5. The effect of the reduced crystal field splitting of the methyl peak produces a tall narrow peak, though the integrated intensity agrees with experiment [Fig. 6.14].
Figure 6.11. INS spectrum for ACN-D5 calculated using the parameters of Table 6.1 in the three phonon approximation compared with experimental INS spectrum for ACN.
Figure 6.12. As for Fig. 6.11, expanded energy scale.
Figure 6.13. INS spectrum for ACN-D5 calculated using the parameters of Table 6.1 in the three phonon approximation compared with experimental INS spectrum for ACN-D5.
Figure 6.14. As for Fig. 6.11, expanded energy scale.
Figure 6.15. INS spectrum for ACN-D8 calculated using the parameters of Table 6.1 in the one-phonon approximation at the Brillouin zone centre, compared with experimental INS spectrum for ACN-D8.

**Appendix B.**

Figure B.1. Experimental INS spectrum for L-alanine, 25 K.
Figure B.2. Experimental INS spectrum for acetyl-alanyl-methylamide at 25 K.

**Tables.**

**Chapter V.**



**Chapter VI.**

Table 6.6. The assignment of the ACN-D5 crystal phonon bands above 160 $cm^{-1}$ in terms of intra-molecular modes of the isolated molecule.

Table 6.7. The assignment of the ACN-D5 crystal phonon modes below 210 $cm^{-1}$ in terms of rigid body motions or intra-molecular modes of the isolated molecule.

Table 6.8. The assignment of the ACN-D8 crystal phonon bands above 160 $cm^{-1}$ in terms of intra-molecular modes of the isolated molecule.

Table 6.9. The assignment of the ACN-D8 crystal phonon modes below 210 $cm^{-1}$ in terms of rigid body motions or intra-molecular modes of the isolated molecule.

**LIST OF ABREVIATIONS USED.**

| | |
|---|---|
| ACN | fully hydrogenous acetanilide |
| ACN-D5 | acetanilide with phenyl hydrogens exchanged for deuterium |
| ACN-D8 | acetanilide with methyl and phenyl hydrogens exchanged for deuterium |
| ACN-D9 | fully deuterated acetanilide |
| a.m.u. | atomic mass units |
| $cm^{-1}$ | optical wavenumbers (1 $cm^{-1}$ = 8.07 meV) |
| C | carbon |
| $C_{me}$ | methyl carbon |
| $C_{ph}$ | phenyl carbon |
| D | deuterium |
| FWHM | full width half maximum |
| fs | femtoseconds |
| H | hydrogen |
| He | helium |
| ILL | Insitut Laue Langevin, Grenoble, France |
| INS | inelastic neutron scattering |
| IR | infra red |
| MD | molecular dynamics |
| $\mu$eV | microelectron Volts |
| meV | millielectron Volts |
| MeV | megaelectron Volts |
| ms | milliseconds |
| $\mu$s | microseconds |
| N | nitrogen |
| NMR | nuclear magentic resonance |
| NMA | N-methyl-acetamide |
| ns | nanoseconds |
| PEF | potential energy function |
| PPII | polyproline II |
| $(PPG)_{10}$ | $(ProlylProlylGlycine)_{10}$ |
| $(PPG)_{10}$-d | $(ProlylProlylGlycine)_{10}$ with amide hydrogen exchanged for deuterium |
| ps | pseconds |

| | |
|---|---|
| RAL | Rutherford Appleton Laboratory, Didcot, Oxfordshire |
| RMS | root mean square deviation |
| TFXA | Time Focusing Crystal Spectrometer |

## CHAPTER I - INTRODUCTION.

I will begin this thesis by discussing a fundamental biological problem - the relation between protein structure, dynamics, and function. I will briefly review some relevant experimental data and efforts to understand these in quantitative terms by the use of theoretical methods. I will illustrate why these theoretical efforts have been encouraging, why they might be useful in practical terms, and therefore why it is worthwhile attempting to improve the quantitative accuracy of the methods. The only way to achieve this is to test the theoretical results by comparison with relevant experimental data. This is the context for the central part of the thesis, which contributes inelastic neutron scattering (INS) data for several systems of biological interest, and an analysis of these data in terms of theoretical methods for the description of molecular dynamics. I hope that the thesis will be part of a wider program of testing and improving the theoretical methods used, and thereby will ultimately contribute to a quantitative understanding of protein dynamics and function.

The structure of the thesis is as follows. This introduction is Chapter I, Chapter II will review the theory of INS which is essential for the understanding of the subsequent Chapters. The short Chapter III will describe two tools used in common in all the subsequent Chapters. They are brought together for ease of reference. The first is the Time Focusing Crystal Analyser Spectrometer (TFXA) at Rutherford Appleton Laboratory, on which all the INS data in this thesis were collected. The second is the central tool of the computational approach to analysis of the experimental data - the CHARMM molecular mechanics program and potential energy function (PEF) [Brooks *et al.*, 1983a]. Chapter IV describes the

collection of INS data for the natural protein collagen, and two synthetic polypeptide models of collagen, (ProlylProlylGlycine)$_{10}$ and Polyproline II. The data are analysed in terms of an analytical mixed harmonic model, and in terms of numerical calculations using the CHARMM program. Chapter V describes the collection of INS data for the peptide bond model compound acetanilide in the crystalline state, and the refinement of the parameters of the CHARMM PEF to fit the INS data. The refined PEF is used to study the anharmonic temperature dependent dynamics of the acetanilide crystal. Chapter VI describes the collection of INS data for two further isotopomers of acetanilide, and further refinement of the CHARMM PEF to fit the INS data for all three isotopomers. Chapter VII gives conclusions. Appendix A will discuss an idea I have had for the model independent exploitation of INS data. Appendix B records INS data I collected for two further molecular crystals, for which computational analyses by collaborators are in an early stage only.

### 1.1. A BASIC QUESTION FOR BIOLOGY.

The fundamental dogma of biology since the 1950's declares that genetic information is stored as the sequence of a nucleic acid polymer, and is expressed by translation into one dimensional protein sequences and folding of these sequences into functional proteins of well defined three dimensional form. During the last forty years a great deal of structural data for proteins have been amassed. Structural information at atomic resolution derives largely from the increasingly sophisticated science of x-ray crystallography. Recent advances in nuclear magnetic resonance (NMR) techniques have allowed determination of small protein structures at atomic resolution in solution [Smith *et al.*, 1993; Berndt *et al.*, 1992]. The wealth of structural data provides a major

challenge for biophysicists and biochemists concerned with the relation of protein structure to function. There remain several major questions, with practical implications for the design of new proteins or ligands with useful properties.

A basic question, then, is - what is the dependence of a protein's function on it's folded three dimensional structure? Subsidiary to this question are many others - what ligands will bind to a given protein, where, and what will be the functional consequences of the binding? How does the structure of an enzyme determine its catalytic properties? What is the role of protein dynamics in function? Is the functional state of a protein best described as a stable or a meta-stable state? What is the role of non-equilibrium kinetic phenomena and energy transport, as opposed to equilibrium thermodynamics, in enzymatic reaction mechanisms? From a technological viewpoint, given the three dimensional structure of a protein, is it possible to understand and predict its functional properties?

I will now briefly discuss some of the experimental studies of the role of protein structure and dynamics in protein function, and the theoretical efforts to understand these experiments. I will describe a central tool used in these theoretical efforts - the potential energy function (PEF). I will then discuss the relevance of INS experiments to these questions.

### 1.1.1. Protein dynamics, ligand binding, and reaction mechanisms - experiment.

The advance in knowledge of crystal and solution structures of proteins has exposed the inadequacy of structural data, alone, to explain the kinetics and mechanisms of protein action. Indeed an early x-ray structure of myoglobin showed no open pathway for access

of ligands to the haem group, providing proof that protein function requires flexibility [Perutz and Matthews, 1966]. Very recently an x-ray crystal structure for the photolysed state of carbonmonoxy-myoglobin has been obtained at low temperature (20 K). This remarkable experiment demonstrates the photolysed carbonmonoxide ligand trapped in the heme binding site, unable to escape the pocket because conformational fluctuations freeze at low temperature [Schlichting *et al.*, 1994].

**1.1.1.1. Direct experimental evidence of protein dynamics.** A range of experimental evidence demonstrates dynamic phenomena in proteins directly. NMR and fluorescence depolarisation measurements indicate protein motions contributing to relaxations on the nanosecond (ns) to picosecond (ps) time scale [Hochstrasser and Negus, 1984; Wagner and Wutrich, 1986; Brooks *et al.*, 1988, Dobson and Karplus, 1986]. Low temperature x-ray diffraction [Hartmann *et al.*, 1982; Parak *et al.*, 1987] and Mössbauer spectroscopy experiments [Parak *et al.*, 1982; Bauminger *et al.*, 1983] reveal a transition in the dynamics of myoglobin near 220 K, with a sudden increase in the temperature dependence of atomic mean square displacements at higher temperatures, attributed to the onset of fluctuations between conformational substates. Quasi-elastic neutron scattering experiments have detected the same dynamical transition in myoglobin [Doster *et al.*, 1989; Section 1.3.2.1, below], and inelastic neutron scattering experiments suggest that the dynamics at low temperature can be seperated into vibrational dynamics within local potential energy minima, combined with intermittent transitions between different local minima [Cusack and Doster, 1990]. Remarkable low temperature x-ray experiments demonstrating the dynamical transition near 220 K in crystalline ribonuclease A, have proved the

functional significance of flexibility for this protein. Substrate access into and out of the active site becomes frozen below the dynamical transition [Rasmussen *et al.*, 1992; Tilton *et al.*, 1992]. Electron transfer reaction rates in cytochrome complexes are also dependent on conformational substates, and fluctuations between them [Nocek *et al.*, 1991; Wallin *et al.*, 1991].

**1.1.1.2. Spectroscopic evidence for fluctuations between conformational substates.**

Optical spectroscopic methods measuring the rebinding of photolysed carbon monoxide [CO] to haem in myoglobin display non-exponential time dependence. This phenomenon has been attributed to a distribution of enthalpic barriers to rebinding, resulting from multiple frozen conformational substates at temperatures below 160 K [Ormos *et al.*, 1990]. At physiological temperatures rebinding of CO to haem in myoglobin becomes exponential, and this is attributed to fluctuations of the protein, amongst its substates, occurring on a time scale rapid relative to ligand rebinding, so that the effective enthalpic barrier is an average over the substates. An alternative mechanism generating non-exponential kinetics at high temperature has been suggested to explain the rebinding kinetics of nitrous oxide. This ligand rebinds more rapidly than CO after photolysis. The relaxation of the protein, triggered by the perturbation of ligand dissociation, results in the enthalpic barrier to rebinding changing on the same time scale as rebinding itself occurs. The changing enthalpic barrier during rebinding produces non-exponential rebinding behaviour [Petrich *et al.*, 1991].

The functional significance of multiple conformational substates and the dynamic transitions between them have also been inferred from spectral and kinetic hole burning

experiments in haem proteins. Three major conformational substates of myoglobin, with bound CO, have been distinguished spectroscopically on the basis of the CO stretch frequencies of the bound ligand. Each major substate has a distinct characteristic angle between the CO dipole and the haem plane [Ansari *et al.*, 1987; Hong *et al.*, 1990]. Selective photolysis of bound CO from individual major substates of myoglobin is achieved using monochromatic exciting light and different rebinding rates for each major substate have been detected. The effect of spectral hole burning on rebinding kinetics proves that the rates of rebinding are correlated with the major conformational substates defined spectroscopically. Each major substate independently demonstrates non-exponential rebinding [Ormos *et al.*, 1990]. This non-exponential rebinding has been attributed, in turn, to a distribution of enthalpic barriers correlated with a further tier of minor substates distinguished on a lower energy scale [Berendzen *et al.*, 1990; Ansari *et al.*, 1987]. Further spectroscopic evidence for relaxations between substates comes from time and temperature dependent measurements of spectral line intensities and positions after photolysis [Steinbach *et al.*, 1991; Niehaus *et al.*, 1992].

**1.1.1.3. Experimental evidence for the function role of coherent vibrational motion in proteins.**

Recently, multicolour near-infrared femtosecond (fs) spectroscopy experiments have demonstrated a functional significance for low frequency intra-molecular vibrational modes in the reaction centre of a purple bacterium. This is an important demonstration of a role for coherent vibrational dynamics, as opposed to the relaxational dynamics represented by transitions between substates. In purple bacterium reaction centre during photoexcitation, the protein vibrates coherently on the time scale of the

lifetime of the excited electronic state, modulating the energy gap between the excited and ground electronic states [Vos *et al.*, 1993]. Theory suggests that coherent nuclear motion can mediate efficient rates of electron transfer [Skourtis *et al.*, 1992]. Similar experiments have been performed for rhodopsin, indicating that coherent nuclear motion contributes to the high quantum yield in the primary step of vision [Wang *et al.*, 1994].

### 1.1.2. Protein dynamics, ligand binding, and reaction mechanisms - theory.

Given these experimental results, MD simulations have been extensively applied to the detailed interpretation of dynamical phenomena in proteins. The starting point is generally the crystal structure derived from x-ray diffraction, and the time scale accessible to full, all atom calculations is currently limited by computational requirements to a few ns at the very most. Nevertheless significant insights have been achieved into the nature of ligand binding, enzymatic mechanisms and, recently, electron transfer reactions, with at least qualitative agreement with experiments [Karplus and Petsko, 1990].

#### 1.1.2.1. Calculations for myoglobin.

The early observation of the need for flexibility in myoglobin has been investigated in this manner. MD results demonstrate conformational substates in the neighbourhood of the native structure, thermally accessible at room temperature, but predictive of glass-like behaviour at low temperature, in accord with the conclusions of experiments [Elber and Karplus, 1987; Frauenfelder *et al.*, 1991]. Further simulations under non-equilibrium conditions demonstrate that there are probably multiple pathways for release of ligand from the haem site, related to the contribution from multiple conformational substates of the

protein [Karplus and Petsko, 1990]. The temperature dependence of calculated mean atomic fluctuations for myoglobin at equilibrium are in agreement with x-ray diffraction and inelastic neutron scattering results [Kuczera *et al.*, 1990; Smith *et al.*, 1990b], including the distribution of mean square displacements amongst different regions of the protein [Levy *et al.*, 1985; Elber and Karplus, 1987]. MD simulations have also provided time correlation functions comparable with those of interest for experimental NMR or fluorescence depolarisation measurements [Brooks *et al.*, 1988; Levy *et al.*, 1985; Dobson and Karplus, 1986].

**1.1.2.2. Calculations for Ribonuclease.**

MD results for the enzyme ribonuclease have given qualitative agreement with experiment for changes in atomic mean square displacements, and in tryptophan fluorescence properties, when the free enzyme binds its substrate [MacKerell *et al.*, 1989]. Temperature dependent MD displays the dynamical transition observed in experiments around 220 K (Section 1.1.1.1), and indicates the importance of dynamical fluctuations for access of the substrate to the active site in agreement with experiment [Loncharich and Brooks, 1990]. Simulations of the ribonuclease active site, with and without bound substrate or transition state analog, provide good agreement with all three x-ray crystallographic structures, including the presence of stabilising interactions important for explaining the mechanism of catalysis. New insights into the role of water molecules in the active site have been obtained in this way [Brünger *et al.*, 1985].

**1.1.2.3. Further important examples.**

Further examples of calculations providing reasonable agreement with experiment include MD simulations of

thermal diffuse x-ray scattering experiments on lysozyme [Faure *et al.*, 1994], and calculations of NMR relaxation properties [Dobson and Karplus, 1986]. A theoretical explanation of the critical role of charge distribution in guiding substrate to the active site in the diffusion limited enzymatic mechanism of acetylcholinesterase has been obtained [Tan *et al.*, 1993; Ripoll *et al.*, 1993]. MD studies of the hydration shell of myoglobin and of an antibody/antigen complex have recently been performed, and correlated with experiment [Lounnas and Pettitt, 1994; Alary *et al.*, 1993].

The important observation of coherent protein vibrational modes coupled to the electron transfer reaction of purple bacterium [Vos *et al.*, 1993], has been successfully reproduced in MD simulations of the reaction centre, and helped to explain the non-exponential nature of the charge transfer kinetics [Gehlen *et al.*, 1994].

**1.1.2.4. Practical applications to drug design.**

Progress has already begun on the application of such computational techniques to problems of technological and medical significance. Recently an inhibitor of the influenza virus sialidase enzyme was designed *de novo*, based on the known structure of the enzyme. The designed ligand was synthesized, and found to act, as predicted, as a viral inhibitor in cell cultures and in animal models [Vonitzstein *et al.*, 1993]. This encouraging work provides a starting point for the development of clinically useful drugs. Utilising qualitative geometry dependent search algorithms, data bases of known small molecules and drugs have been successfully searched to predict compounds which will inhibit HIV protease [Desjarlais *et al.*, 1990]. Improvements of these search algorithms rely on more quantitative energy calculations [Meng *et al.*, 1992; Eisen *et al.*, 1994]. Radically new potential inhibitors of human

immuno-deficiency virus protease have been designed *de novo* by systematic energy calculations [Caflisch *et al.*, 1993; Sawyer *et al.*, 1992]. Calculations of this sort are already capable of correctly predicting qualitative trends for binding affinities of families of related ligands [Hendle *et al.*, 1993; Sansom *et al.*, 1992]. Finally, completing the circle from structure to dynamics and back again, MD calculations have been an important computational tool in the refinement of x-ray and NMR structures, allowing the exploration of the configurational space of the protein subject to a combination of experimental and theoretical constraints, expressed in a unified fashion by appropriate parameterisation of an empirical energy function [Brünger *et al.*, 1987].

Despite these successes, the full technological potential of understanding protein function and dynamics may only be realised when a **quantitative** understanding of these phenomena emerges. Ultimately a theoretical description must be capable of making precise predictions [Kuntz, 1994; Kollman, 1994]. Only then will it be possible to apply the powerful tools of molecular biology to the rational design and production of proteins, with improved or even novel functional properties, and of ligands capable of modifying protein functions in predictable fashion.

## 1.2. THE POTENTIAL ENERGY FUNCTION OF MOLECULAR DYNAMICS SIMULATIONS.

A fundamental concept in the theoretical treatment of many body systems is the PEF. This is constructed as a function of the instantaneous configuration of the system, and describes a surface in an N+1 dimensional space, where N is the number of degrees of freedom [Karplus and Petsko, 1990]. Hence the PEF for proteins can be visualised as an

energy landscape, dependent on the instantaneous configuration of the protein. This concept provides a useful unifying framework in which to discuss the experimental results on protein folding, as well as dynamic and kinetic phenomena. For proteins, solvent effects, ligand binding, or macromolecular interactions may be of interest. Then N is the number of degrees of freedom for the whole system, not just the isolated protein. Second derivatives of the PEF with respect to atomic coordinates provide the forces determining the dynamics of the system. Dynamics are studied by solving the classical equations of motion with or without quantum corrections. The classical equations of motion are appropriate for most applications to kinetic or dynamic problems, though where chemical reaction mechanisms or electron transfer reactions are studied quantum corrections are necessary [Karplus and Petsko, 1990, Gehlen *et al.*, 1994]. Solutions may be sought analytically by use of the harmonic approximation to the full PEF, which is particularly relevant at low temperatures [Brooks *et al.*, 1983b; Case, 1994]. Numerical integration over discrete time steps, given a set of initial conditions appropriate to the problem under study, extends the technique beyond the harmonic approximation. Relevant dynamical properties are then extracted from the calculated trajectories, for comparison with experiment. The real PEF for the system of interest provides, in principle, all the information necessary to calculate any dynamic properties [Karplus and Petsko, 1990]. Thermodynamic problems require calculations of entropic changes and these are achieved by algorithms which randomly sample the configurational space [Velikson *et al.*, 1992; McCammon and Harvey, 1987].

In practical applications, the potential energy calculated for a given configuration must be an

approximation to the real potential energy surface. It is generally represented by an empirical parameterisation, using the instantaneous value of internal coordinates corresponding, for example, to bond stretches, bond angle distortions, out-of-plane motions, and dihedral angle torsions, as well as pair wise potentials including Coulomb forces, van der Waals, and Urey Bradley terms [Karplus and Petsko, 1990].

The empirical parameters are derived from experimental data and *ab initio* quantum chemical calculations for small model compounds representing fragments of the macromolecular structure, relying on the assumption that these parameters can be reliably transfered to the macromolecule [Guo and Karplus, 1992; Reiher and Karplus, 1993].

As noted above, a range of time scales for protein dynamics have been identified experimentally. Folding phenomena have been resolved over a time scale ranging from the experimental dead time of a few milliseconds (ms) all the way up to many seconds. Allosteric transitions and complete enzymatic reactions occur in times ranging from microseconds ($\mu$s) to ms, global hinge bending motions and diffusional processes in ps to $\mu$s, and bond stretching and bending motions, as well as charge transfer and chemical bond breaking reactions, in fs to ps [McCammon and Harvey, 1987]. In fact proteins display dynamical phenomena on time scales ranging over at least twelve orders of magnitude [Frauenfelder, 1989]. The heirarchy of time scales has been associated with a heirarchy of scales on which structure occurs in the energy landscape of proteins [Frauenfelder *et al.*, 1991]. Molecular dynamics calculations have demonstrated that the potential energy surface of myoglobin is characterised by a large number of thermally accessible local minima in the neighbourhood of the native structure [Elber and Karplus, 1987].

If an empirical parameterisation of a protein PEF is to allow quantitative predictions, it must accurately reflect the real potential surface on the energy scale corresponding to the time scale of the phenomenon under study, and yet allow calculations in a reasonable amount of time. The heirarchy of time scales identified experimentally suggest that a heirarchy of approximations might be suitable for different applications. Examples introduced to reduce computational requirements include the extended atom approximation, wherein carbon atoms and the non-polar hydrogens bound to them are lumped together in an extended atom, with appropriate mass, geometry and energy parameters [Brooks *et al.*, 1983a]. This reduces the number of degrees of freedom for computation. A similar approximation fixes all bond lengths at their equilibrium values, treating only bond angle and dihedral angle degrees of freedom. Recent developments along these lines have involved MD calculations on *several* different time scales. For calculations in solution, continuum approximations for the solvent may be used. All these approximations extend the time scale accessible to simulation, but the limits of their validity are not yet well defined [Karplus and Petsko, 1990].

The critical questions are, then:

**(i)** for any given level of the heirarchy, what is the accuracy of the parametrisation in reproducing the real PEF?

**(ii)** which approximations are appropriate for a given application, and which are necessary to allow solution of the equations of motion?

**(iii)** which are the appropriate equations of motion, quantum or classical?

**(iv)** what degree of dynamical coupling between different levels of the heirarchy is functionally relevant?

The qualititative and quantitative predictions derived

from simulations can be improved by a programme of refinement of the parameterisations and approximations by comparison with relevant experimental data. Neutron scattering experiments provide such data.

### 1.3. THE RELEVANCE OF NEUTRON SCATTERING EXPERIMENTS.

Neutrons are generated for scattering experiments by two types of sources: spallation sources, which produce pulsed neutron beams, like the ISIS facility at Rutherford Appleton Laboratory (RAL) in Oxford, and reactor sources, producing continuous neutron beams, like the Institute Laue Langevin (ILL) in Grenoble. Neither source is cheap, and the availability of neutron beam time is restricted by competing demands from many branches of science. Neutron fluxes from either source are many orders of magnitude weaker than photon fluxes from conventional optical spectroscopic machines, or from x-ray generators, let alone from modern synchrotron light or x-ray sources. This low flux severely restricts the types of experiment which can be performed. Sample sizes need to be of the order of 2 grams, and data collection runs of the order of many hours, to accumulate good counting statistics.

Despite these drawbacks, neutrons are uniquely suited to the study of dynamical phenomena at the atomic scale in condensed matter, by virtue of their basic properties (for a more complete discussion of basic properties and theory see Chapter II). There are several essential features which distinguish neutron scattering from optical and x-ray techniques. In particular, theory establishes an analytical relationship directly to space and time dependent correlation functions of atomic positions, the scattering is very sensitive to isotopic modification, and there are no symmetry selection rules. These constitute the major advantages of neutron scattering over optical techniques, and provide the motivation for overcoming the

difficulties of low neutron flux [Middendorf, 1984; Middendorf and Randall, 1985, Smith, 1991, Middendorf, 1992].

### 1.3.1. Basic features of neutron scattering.

Neutron scattering, then, is governed by two basic quantities, the momentum transfer $\hbar\mathbf{Q}$ and energy transfer $\hbar\omega$ [Lovesey, 1984]. The appropriate conservation equations for momentum and energy, respectively, are:

$$\hbar\mathbf{Q} = \hbar\mathbf{k}_f - \hbar\mathbf{k}_i \qquad (1.4.1)$$

$$\hbar\omega = E_f - E_i = \tfrac{1}{2}m(v_f^2 - v_i^2) = \tfrac{1}{2}(\hbar^2/m)(k_f^2 - k_i^2) \qquad (1.4.2)$$

here k,v and E denote the wavenumber, velocity and energy of scattered neutrons, and subscripts i,f refer to incident and final beam properties, respectively. Planck's constant is $2\pi\hbar$ and m is the neutron rest mass. For $E_f=E_i$ or $|\mathbf{k}_f|=|\mathbf{k}_i|$, the scattering is elastic. Otherwise the scattering is inelastic.

In neutron scattering from organic materials in general, the measured spectra contain contributions from both incoherent and coherent scattering. The coherent component is more informative in principle, because all atomic pair correlations contribute to the scattering. Coherent *elastic* scattering gives rise to neutron diffraction, analogous to x-ray diffraction. Neutron diffraction has been successfully applied to a range of biological problems. The structure of aqueous solvent in protein crystals can be determined, and exchangeable protons of the protein identified [Wlodawer and Sjolin, 1983; Lounnas and Pettitt, 1994; Gallagher *et al.*, 1992; Finermoore *et al.*, 1992; Cheng and Schoenborn, 1991; Parak *et al.*, 1992, Zhang and Matthews, 1994]. Large macromolecular complexes, have been studied by small angle

scattering and contrast variation techniques [Berkovitchyellin *et al.*, 1992]. The low resolution structure of proteins and peptides in phospholipid membranes have been successfully determined [Duff *et al.*, 1994; Samatey *et al.*, 1994]. All of these experiments exploit the isotope dependence of neutron scattering by selective deuteration of components of the structures, or by comparison of scattering in $H_2O$, and in $D_2O$ solvents.

In biological applications the energy-dependent properties giving rise to coherent *inelastic* scattering are more difficult to measure and to interpret [Jones, 1985; Belissent-Funel *et al.*, 1989]. This is a consequence of the large background contribution of incoherent inelastic scattering relative to coherent inelastic scattering in organic materials, and the need for large samples. Very detailed dynamical information for large crystals of small fully deuterated organic molecules can be obtained however, by determination of the phonon dispersion curves, which describe the dependence of harmonic excitation frequencies on the spatial periodicity of the excitation. This kind of experimental information, unique to coherent inelastic *neutron* scattering, has been obtained for fully deuterated crystals of L-alanine [Durand *et al.*, 1993], and of acetanilide [Barthes *et al.*, 1988], a peptide bond model molecule. Such data provides, in principle, a stringent test of any dynamical model [Durand *et al.*, 1993; Micu *et al.*, in press].

Incoherent scattering arises as a consequence of the dependence of atomic neutron scattering lengths on random nuclear spin and isotope distributions. The randomness gives rise to the incoherent component of scattering, for which interference effects of scattering from different atoms are abolished. Incoherent scattering therefore probes *self* correlations of atomic motion only. The scattering of cold or thermal neutrons from any natural

(i.e. not covalently deuterated) biopolymer or organic material is predominantly incoherent because of the high content of hydrogen and the large hydrogen incoherent cross-section of 80 barn vs. an average of 5-6 barn for the total cross section of heavier nuclei (1barn=$10^{-28}$ $m^2$). For this reason, most INS experiments on samples of biological interest have concentrated on interpreting the dominant incoherent component.

### 1.3.2. Neutron scattering experiments with energy resolution in practice.

In practice, neutron scattering experiments with energy resolution fall into three different regimes, depending on the practical requirements of the experimental arrangement:

#### 1.3.2.1. Quasielastic and incoherent elastic neutron scattering experiments.

Incoherent *elastic* scattering reflects the average self correlation function for atoms of the sample in the long time limit. Generally speaking the more confined an atom is, the more intense will be its elastic incoherent scattering, and for a liquid or gas, where the atoms are not confined in a microscopic volume, it is zero. Quasi-elastic scattering measure the broadening of the elastic line, in energy space, as a function of momentum transfer. High energy resolution is required of the experimental arrangement (micro-electron Volts, $\mu$eV), and the information obtained generally relates to barrier-crossing transitions, relaxational motion, or diffusional dynamics in the sample. Measurements of the incoherent elastic and quasi-elastic scattering, as a function of momentum transfer, have given information on the average mean square displacement of hydrogens in myoglobin and lysozyme, as a function of temperature [Doster *et al.*,

1989; Doster *et al.*, 1990; Cusack and Doster, 1990]. An abrupt change, near 200 K, in the temperature dependence of mean square displacements has been associated with the onset of dynamical transitions between conformational substates. Below 180 K the INS results were consistent with typical normal mode dynamics of an harmonic solid. Equivalent conclusions were drawn from a molecular dynamics simulation of myoglobin, from which mean square atomic displacements in good agreement with the neutron results were derived, [Smith *et al.*, 1990b]. Quasi-elastic experiments have also given important insight into the dynamical behaviour of nucleic acids, and of gels of biological significance [Middendorf, 1992].

**1.3.2.2. Vibrational INS experiments.**

These measure intensity at finite values of energy transfer, in the meV range, and reflect the under-damped oscillatory dynamics of the sample. Early biological applications of vibrational neutron spectroscopy have concentrated on the low frequency features of protein dynamics [Cusack *et al.*, 1988; Cusack and Doster, 1990; Smith *et al.*, 1990a; Smith *et al.*, 1990b; Smith, 1991]. Vibrational INS data for molecular crystals of biological significance has also been compared with MD calculations [Kneller *et al.*, 1992; Micu *et al.*, in press].

The results of early INS experiments on proteins were consistent with harmonic dynamics at low temperature, and with a combination of harmonic dynamics in local potential energy minima with intermittent rapid transitions between wells at high temperature, in support of theoretical methods involving separations of time scale [Doster *et al.*, 1989; Doster *et al.*, 1990; Cusack and Doster, 1990]. Harmonic normal mode models of small proteins have been developed [Brooks *et al.*, 1983b; Levitt *et al.*, 1985; Go, 1990; Case, 1994], and vibrational neutron scattering

properties calculated from them [Cusack *et al.*, 1988; Smith *et al.*, 1990a]. The comparison of calculated INS spectra for bovine pancreatic trypsin inhibitor with INS experiments was used to test the extended atom approximation, and several truncation schemes for electrostatic interactions used in the normal mode calculations [Smith, 1985; Smith, 1991]. A large fraction of the total atomic mean square displacements at room temperature were attributed to low frequency normal modes involving approximately rigid body collective motions of helical secondary structural elements. However the dynamical transition, discussed above, observed near 200 K for several different proteins by many different experimental and simulation techniques demonstrates the limited validity of harmonic normal mode dynamics at physiological temperatures. Temperature dependent simulated INS spectra have also been calculated from anharmonic MD simulations on the full potential energy surface, and compared with experiment [Loncharich and Brooks, 1990; Smith *et al.*, 1990b; Kuczera *et al.*, 1990]. For both harmonic calculations and full MD simulations, more structure was observed in the simulated than in the experimental INS spectra. This was interpreted as evidence for incompletely sampled multiple conformational substates in MD simulations [Smith *et al.*, 1990b] or for frictional damping of normal modes in harmonic analyses [Smith *et al.*, 1990a].

In the early INS experiments difficulties with resolution, and limitations on the accessible range of energy transfer, restricted the useful data to the region below 25 meV [Smith, 1991]. Recent improvements in the instrumentation of time-of-flight spectrometers, especially at the RAL pulsed neutron source, have extended the accessible range of energy transfer up to 500 meV. The main part of this thesis describes vibrational INS

experiments exploiting this extended energy transfer range to study molecular systems of biological relevance. The data is interpreted in the light of modern computational techniques of chemical physics, with the aim of improving the precision of these techniques in describing biological phenomena on the ps to ns time scale.

**1.3.2.3. Compton INS experiments.**

These exploit the epithermal content of neutron beams produced by spallation sources, and are a recent innovation in neutron scattering. Energy transfers in the eV range can be measured. The impulse approximation relates the scattered intensity directly to the momentum distribution of the scattering nuclei. Information is gained on the local potential experienced by the scattering atoms. Successful experiments on large crystals of simple molecules have exploited selective deuteration and crystal anisotropy to demonstrate double well character in hydrogen bonding potentials [Postorino *et al.*, 1991]. The useful information available for natural biopolymers is restricted by the heterogeneity of the samples. Future experiments would require simple model systems with selective deuteration of all but one uniform population of hydrogens of interest.

## CHAPTER II - THE THEORY OF INELASTIC NEUTRON SCATTERING.

The theory of neutron scattering essential for the understanding of the analysis in subsequent Chapters will be reviewed briefly here. The treatment is adapted from that given in Lovesey, 1984, and Squires, 1978.

### 2.1. BASIC PROPERTIES OF NEUTRONS.

A quantum mechanical treatment is essential for the understanding of neutron scattering from condensed matter. The wave properties of neutrons must be considered. The de Broglie wave length of a neutron with velocity v is:

$$\lambda = h/mv \qquad (2.1.1)$$

where h is Planck's constant, m the neutron mass. The neutron wave vector, **k**, is defined to have the magnitude:

$$k = 2\pi/\lambda \qquad (2.1.2)$$

and points in the direction of propagation of the neutron. The neutron momentum, **p**, and energy E, are defined as:

$$\mathbf{p} = \hbar\mathbf{k} \qquad (2.1.3)$$

$$E = \hbar^2k^2/2m \qquad (2.1.4)$$

where here and throughout the following $\hbar = h/2\pi$.

Neutrons propagating in a beam, for example in an incident wave packet during a scattering experiment, can be considered as a superposition of plane waves, and the amplitude of the beam at the point **r** written:

$$|\psi_i(\mathbf{r})\rangle = \int A_k \exp(i\mathbf{k}.\mathbf{r})\, d\mathbf{k} \qquad (2.1.5)$$

Here the complex constants $A_k$ give the amplitudes of the

plane wave component with wave vector **k**. For a monochromatised beam, with well defined energy, the integral over **k** will run over the narrow band defined by the energy resolution of the beam. The integration adds together complex components and the value of the wavefunction $|\psi_i(\mathbf{r})>$ is therefore complex, and displays interference effects typical of wave motion. A useful interpretation of the wave properties of neutrons, expressed by this wavefunction, is to associate the square of the amplitude of the wavefunction at a point **r**, a real number, with the probability, P(**r**), of finding the neutron there:

$$P(\mathbf{r}) = \left| \int \delta(\mathbf{r}'-\mathbf{r})\psi_i(\mathbf{r}')d\mathbf{r}' \right|^2 \qquad (2.1.6)$$

Here the three dimensional Dirac delta function centred on **r**, $\delta(\mathbf{r}'-\mathbf{r})$ is used, which can be defined as an integral:

$$\delta(\mathbf{r}'-\mathbf{r}) = 1/(2\pi)^3 \int \exp(i\mathbf{k}.(\mathbf{r}'-\mathbf{r}))d\mathbf{k} \qquad (2.1.7)$$

and has the properties:

$$\delta(\mathbf{r}'-\mathbf{r}) = 0 \text{ if } \mathbf{r}' \neq \mathbf{r} \qquad (2.1.8)$$

$$\delta(\mathbf{r}'-\mathbf{r}) = \infty \text{ if } \mathbf{r}' = \mathbf{r}$$

and:

$$\int \delta(\mathbf{r}'-\mathbf{r})d\mathbf{r}' = 1 \qquad (2.1.9)$$

$$\int \delta(\mathbf{r}'-\mathbf{r})f(\mathbf{r}')d\mathbf{r}' = f(\mathbf{r})$$

for $f(\mathbf{r}')$ any arbitrary function.

From the quantum mechanical view point Eq. 2.1.7 can be thought of as representing the wavefunction of a particle

situated at a fixed point in space. Then the integral in Eq. 2.1.7 expresses Heisenberg's uncertainty principle, which states that, if the position of a particle is known precisely, its momentum, associated with the vector **k** in Eq. 2.1.7, cannot be specified.

Generally, in accordance with Eq. 2.1.6, given the initial state $|\psi_i(\mathbf{r})\rangle$ of Eq. 2.1.5, the probability of finding a neutron in the state $|\psi_{k'}(\mathbf{r})\rangle$ is given by:

$$\begin{aligned} P_{k'} &= |\langle\psi_{k'}(\mathbf{r})||\psi_i(\mathbf{r})\rangle|^2 \\ &= |\int\exp(-i\mathbf{k}'.\mathbf{r})\int A_k \exp(i\mathbf{k}.\mathbf{r})\, d\mathbf{k}\, d\mathbf{r}|^2 \\ &= |A_{k'}|^2 \end{aligned} \qquad (2.1.10)$$

where the notation for $\langle\psi_{k'}(\mathbf{r})||\psi_i(\mathbf{r})\rangle$ is defined.

Because neutrons are uncharged, they can approach closely to the nucleus of atoms, and are scattered by nuclear forces. The energy of thermal neutrons is too small to change the internal energy of an atomic nucleus, and so neutrons can only impart kinetic energy and momentum to the nucleus. The neutron-nucleus interaction is of very short range ($\sim 10^{-5}$Å). Because the de Broglie wavelength of thermal neutrons is ~1Å, very much longer than the range of nuclear forces, the nucleus appears to scatter neutrons as if it were a point particle, so that the scattering from a single fixed nucleus is spherically symmetrical. Hence for this circumstance the scattered neutron wavefunction at the point **r** can be written:

$$\psi_{sc} = -b/|\mathbf{r}|\ \exp(i|\mathbf{k}_f||\mathbf{r}|) \qquad (2.1.11)$$

Here $\mathbf{k}_f$ is the wavevector of the scattered neutron. For elastic scattering, with no change in energy of the neutron, $|\mathbf{k}_f| = |\mathbf{k}_i|$, where $\mathbf{k}_i$ is the wave vector of the

incident neutron. This equation serves to define the scattering length b for a given nucleus. The strength of scattering from a given nucleus is proportional to its scattering cross section, $b^2$. Neutrons have an intrinsic spin ½. Every nucleus with non-zero spin, I, can form a neutron-nucleus system with combined spin I+½, or I-½. Each of these spin states has its own value of scattering length, determined empirically. Their values vary erratically from one nuclear isotope to another, and also vary from one spin state to another, but fall in a range approximately $10^{-6}$-$10^{-3}$Å, always small relative to the mean separation of atoms. Hence the total scattering cross section for a sample is equal to the sum of those for its individual atoms, and the amplitude of a wave scattered from one atom is small at the position of neighbouring atoms. This implies that the scattering of neutrons by condensed matter can be considered a weak process, despite the fact that the neutron-nucleus interaction involves strong nuclear forces. It is this which allows perturbation theory in the first Born approximation, to give a good description of the neutron scattering process [Merzbacher, 1970].

## 2.2. NEUTRON CROSS SECTION.

The neutron cross section for a target is defined as:

$$\sigma = N/F \qquad (2.2.1)$$

where N is the total number of neutrons scattered by the target per unit time, and F is the flux of incident neutrons, defined as the number of incident neutrons per unit area per unit time. The differential cross section, $d\sigma/d\Omega$, is defined as the number of neutrons scattered into the solid angle $d\Omega = \sin\theta\, d\theta\, d\phi$, in the direction $\theta$, $\phi$. Hence both the cross section and the differential cross

section have units of area. The double differential cross section is defined as the number of neutrons scattered into the solid angle $d\Omega = \sin\theta\, d\theta\, d\phi$, in the direction $\theta$, $\phi$, and with final energy between $E_f$ and $E_f + dE$.

The double differential cross section is related, in the first Born approximation, to a fundamental quantum mechanical result known as Fermi's Golden rule. This rule gives the rate of transition of a quantum system from an initial state to a final state when subjected to a perturbation. Thus:

$$d^2\sigma/d\Omega dE = k_f/k_i\ (m/2\pi\hbar^2)^2 \sum_{tf,ti} p_{ti} \qquad (2.2.2)$$

$$\times\ \ |\langle\psi_{ki}|\langle\psi_{tf}|V|\psi_{ti}\rangle|\psi_{ki}\rangle|^2\ \delta[E_{ti}-E_{tf}+E_{ki}-E_{kf}]$$

$$= k_f/k_i\ (m/2\pi\hbar^2)^2 \sum_{tf,ti} p_{ti}$$

$$\times\ \ \left|\int \exp(i(\mathbf{Q}.\mathbf{r}))\langle\psi_{tf}|V|\psi_{ti}\rangle d\mathbf{r}\right|^2\ \delta[E_{ti}-E_{tf}+E_{ki}-E_{kf}]$$

In the first line of this expression (Eq. 2.2.2) the initial state of the combined neutron/target system is represented as the product, $|\psi_{ki}\rangle|\psi_{ti}\rangle$, of the initial neutron plane wave state, $|\psi_{ki}\rangle$ with wavevector $k_i$ and energy $E_{ki}$, and target state, $|\psi_{ti}\rangle$ with energy $E_{ti}$, a long time before their interaction. The final state of the combined neutron/target system is represented as the product, $|\psi_{kf}\rangle|\psi_{tf}\rangle$, of a final neutron state, $|\psi_{kf}\rangle$, with wavevector $k_f$ and energy $E_{kf}$, and final target state, $|\psi_{tf}\rangle$ with energy $E_{tf}$, a long time after their interaction, and the transient interaction between neutron and target is represented by a perturbation V. The delta function ensures conservation of energy and fixes the final neutron energy, $E_{kf}$. In the second line of Eq. 2.2.2, the initial and final plane wave neutron states have been written explicitly to reveal the central role of the spatial

Fourier transform, $\int \exp(i(\mathbf{Q}.\mathbf{r}))\langle\psi_{tf}|V|\psi_{ti}\rangle d\mathbf{r}$, in determining the scattering. The scattering vector $\mathbf{Q} = \mathbf{k}_i - \mathbf{k}_f$. The sum runs over initial and final target states, weighted by the statistical probability, $p_{ti}$, of finding the target in the initial state labelled ti. This is the essential expression on which the theory of thermal neutron scattering in the first Born approximation rests. To evaluate the expression a form for the interaction potential V is required. The factor $k_f/k_i$ arises from the normalisation of the neutron wavefunctions [Squires, 1978].

## 2.3. FERMI INTERACTION PSEUDO-POTENTIAL, COHERENT AND INCOHERENT SCATTERING.

The thermal neutron scattering from a single nucleus is expected to be isotropic, since the range of the neutron-nucleus interaction is very short relative to the de Broglie wavelength of the neutron. The only form of the interaction potential V which gives isotropic scattering in the Born approximation (Eq. 2.2.2), is a delta function. If a single nucleus is at the position **R**, the Fermi pseudo potential is defined as:

$$V(\mathbf{r}) = 2\pi\hbar^2/m \; b \; \delta(\mathbf{r}-\mathbf{R}) \qquad (2.3.1)$$

where b is the scattering length of the nucleus, positive for a repulsive potential, which as noted above depends on the isotope and the nuclear spin. Inserting this expression in Eq. 2.2.2, for a target consisting of a single nucleus at the origin, gives the required isotropic scattering.

For a rigid array of nuclei:

$$V(\mathbf{r}) = 2\pi\hbar^2/m \; \Sigma_l \; b_l \; \delta(\mathbf{r}-\mathbf{R}_l) \qquad (2.3.2)$$

Since the nuclei are rigidly fixed the scattering must be elastic. The scattering length $b_l$ depends on the isotope and its nuclear spin at site $\mathbf{R}_l$. Since nuclear spin and isotope are uncorrelated for different sites, from Eq. 2.2.2:

$$d\sigma/d\Omega = \Sigma_{ll'} \exp(i\mathbf{Q}.(\mathbf{R}_l-\mathbf{R}_{l'}))\langle b_l b_{l'}\rangle \qquad (2.3.3)$$

where <..> denotes a thermal average over nuclear spin and isotope distributions. In general:

$$\langle b_l b_{l'}\rangle = \langle b\rangle^2 + \delta_{l,l'}(\langle b^2\rangle-\langle b\rangle^2) \qquad (2.3.4)$$

Here the delta function has the value 1 if $l = l'$, otherwise zero. Hence the cross section can be written as the sum of two parts:

$$d\sigma/d\Omega = [d\sigma/d\Omega]_{coh} + [d\sigma/d\Omega]_{inc} \qquad (2.3.5)$$

where from (2.3.3) and (2.3.4):

$$[d\sigma/d\Omega]_{coh} = \langle b\rangle^2 \left| \Sigma_l \exp(i\mathbf{Q}.\mathbf{R}_l) \right|^2 \qquad (2.3.6)$$

and:

$$[d\sigma/d\Omega]_{inc} = N(\langle b^2\rangle-\langle b\rangle^2) \qquad (2.3.7)$$

Here N is the number of atoms. These formulae illustrate, in the case of elastic scattering from a rigid monatomic array of nuclei, the profound difference between *incoherent* and *coherent* scattering. Coherent elastic scattering displays interference effects, giving rise to diffraction from the rigid array for example, and is therefore markedly dependent on **Q**. Incoherent elastic scattering displays no interference and is independent of

Q. The results of the same separation of the total cross section, applied to inelastic scattering, are most clearly seen in the correlation function formalism of van Hove.

## 2.4. INTEGRAL REPRESENTATION OF THE ENERGY DELTA FUNCTION, AND VAN HOVE TIME DEPENDENT CORRELATION FUNCTIONS.

The energy delta function in Eq. 2.2.2 can be represented as an integral with respect to time [van Hove, 1954; Merzbacher, 1970; Lovesey, 1984]:

$$2\pi\hbar\,\delta[E_{ti}-E_{tf}+E_{ki}-E_{kf}] = \int \exp[i/\hbar(E_{tf}-E_{ti})t]\,\exp(-i\omega t)\,dt \qquad (2.4.1)$$

where:

$$\hbar\omega = E_{ki}-E_{kf} \qquad (2.4.2)$$

If $H_t$ is the unperturbed Hamiltonian of the target, then:

$$\exp(i/\hbar\ H_t)|\psi_{ti}\rangle = \exp(i/\hbar\ E_{ti})|\psi_{ti}\rangle \qquad (2.4.5)$$

$$\exp(i/\hbar\ H_t)|\psi_{tf}\rangle = \exp(i/\hbar\ E_{tf})|\psi_{tf}\rangle \qquad (2.4.6)$$

From Eq. 2.2.2, and using the convolution theorem:

$$d^2\sigma/d\Omega dE \qquad (2.4.7)$$

$$= k_f m^2/k_i(2\pi/\hbar^2)^2\ \Sigma_{tf,ti}\ p_{ti}$$

$$\times\ |\int \exp(i(\mathbf{Q}.\mathbf{r}))\langle\psi_{tf}|V|\psi_{ti}\rangle d\mathbf{r}\ |^2\ \delta[E_{ti}-E_{tf}+E_{ki}-E_{kf}]$$

$$= k_f m^2/k_i(2\pi/\hbar^2)^2\ \Sigma_{ti}\ p_{ti}\ \int\int d\mathbf{r}'dt\ \exp(i(\mathbf{Q}.\mathbf{r}'-\omega t))$$

$$\times\ [\int\langle\psi_{ti}|V^*(\mathbf{r}+\mathbf{r}')\exp(i/h\ H_t t)\ V(\mathbf{r})\ \exp(-i/h\ H_t t)|\psi_{ti}\rangle d\mathbf{r}]$$

$$= k_f/k_i \int\int \mathbf{dr'}dt \exp(i(\mathbf{Q}.\mathbf{r'}-\omega t))$$

$$\times [\int <\Sigma_l b_l^* \delta(\mathbf{r'}-\mathbf{r}+\hat{\mathbf{R}}_l)(\Sigma_{l'} b_{l'} \delta(\mathbf{r}-\hat{\mathbf{R}}_{l'}(t))>\mathbf{dr}]$$

Here the Fermi pseudo-potential Eq. 2.3.2 is used. The notation <..> again signifies the thermal average over initial target states. The position operator for the target nucleus labelled l is $\hat{\mathbf{R}}_l$, and $\hat{\mathbf{R}}_l(t)$, in the Heisenberg representation, at time 0, and t, respectively. The sum over final target states has been eliminated by use of the closure relation, expressing the orthonormality of the unperturbed energy eigenfunctions of the target:

$$\Sigma \; |\psi_{tf}><\psi_{tf}| \; = 1 \qquad (2.4.8)$$

Seperating the total cross section into its coherent and incoherent parts in accordance with Eq. 2.3.5 gives, for a monatomic target sample:

$$[d^2\sigma/d\Omega dE]_{coh} \qquad (2.4.9)$$

$$= k_f/k_i \; <b>^2 \int\int \mathbf{dr'}dt \exp(i(\mathbf{Q}.\mathbf{r'}-\omega t))$$

$$\times [\Sigma_{l,l'} \int <\delta(\mathbf{r'}-\mathbf{r}+\hat{\mathbf{R}}_l)\delta(\mathbf{r}-\hat{\mathbf{R}}_{l'}(t))>\mathbf{dr}]$$

$$[d^2\sigma/d\Omega dE]_{inc} \qquad (2.4.10)$$

$$= k_f/k_i \; <b^2>-<b>^2 \int\int \mathbf{dr'}dt \exp(i(\mathbf{Q}.\mathbf{r'}-\omega t))$$

$$\times [\Sigma_l \int <\delta(\mathbf{r'}-\mathbf{r}+\hat{\mathbf{R}}_l)\delta(\mathbf{r}-\hat{\mathbf{R}}_l(t))>\mathbf{dr}]$$

The van Hove pair correlation and self correlation functions are defined, respectively, as:

$$G(\mathbf{r}',t) \qquad (2.4.11)$$

$$= 1/N \; [\Sigma_{1,1'}\int<\delta(\mathbf{r}'-\mathbf{r}+\mathbf{R}\hat{}_1)\delta(\mathbf{r}-\mathbf{R}\hat{}_{1'}(t))>d\mathbf{r}]$$

$$G_s(\mathbf{r}',t) \qquad (2.4.12)$$

$$= 1/N \; [\Sigma_1\int<\delta(\mathbf{r}'-\mathbf{r}+\mathbf{R}\hat{}_1)\delta(\mathbf{r}-\mathbf{R}\hat{}_1(t))>d\mathbf{r}]$$

so that:

$$[d^2\sigma/d\Omega dE]_{coh} = k_f/k_i \; N \; <b>^2 \; S_{coh}(\mathbf{Q},w) \qquad (2.4.13)$$

$$[d^2\sigma/d\Omega dE]_{inc} = k_f/k_i \; N \; <b^2>-<b>^2 \; S_{inc}(\mathbf{Q},w) \qquad (2.4.14)$$

Here $S_{coh}(\mathbf{Q},w)$ and $S_{inc}(\mathbf{Q},w)$ are four dimensional Fourier transforms, with respect to space and time, of the pair correlation function Eq. 2.4.11, and the self correlation function Eq. 2.4.12, respectively:

$$S_{coh}(\mathbf{Q},\omega) = \int\int d\mathbf{r}'dt \; \exp(i(\mathbf{Q}.\mathbf{r}'-\omega t)) \; G(\mathbf{r}',t) \qquad (2.4.15)$$

$$S_{inc}(\mathbf{Q},\omega) = \int\int d\mathbf{r}'dt \; \exp(i(\mathbf{Q}.\mathbf{r}'-\omega t)) \; G_s(\mathbf{r}',t) \qquad (2.4.16)$$

Generally $S_{coh}(\mathbf{Q},\omega)$ is called the coherent dynamic structure factor, $S_{inc}(\mathbf{Q},\omega)$ is called the incoherent dynamic structure factor, and the sum of these is called the total dynamic structure factor.

For a monatomic sample the pair correlation function can be viewed as the correlation function of the nuclear density. For polyatomic samples, the mean scattering length of one type of atom will differ from those of another. In this case the scattering lengths cannot be averaged and taken outside the correlation functions, as in Eq. 2.4.9. The correlation function formalism is still

useful however, though the pair correlation function now describes the correlation of neutron scattering length density, instead of directly describing the correlation of nuclear density. Similarly the incoherent scattering will now reflect a weighted sum over the various atomic species, labelled for example by d:

$$[d^2\sigma/d\Omega dE]_{inc} = k_f/k_i \int\int \mathbf{dr'}dt \exp(i(\mathbf{Q}.\mathbf{r'}-\omega t)) \qquad (2.4.17)$$

$$\times \quad [\Sigma_{1,d} <b_d^2>-<b_d>^2 \int <\delta(\mathbf{r'}-\mathbf{r}+\mathbf{R}\hat{}_{1d})\delta(\mathbf{r}-\mathbf{R}\hat{}_{1d}(t))>d\mathbf{r}]$$

So the self correlation function can be viewed as a weighted sum over the self correlation functions of the individual atomic species. $<b_d^2>-<b_d>^2$ the incoherent cross section for atom d will be denoted by $b_{dinc}^2$.

## 2.5. SUMMARY OF THEORY.

The theory of thermal neutron scattering from condensed matter requires a quantum mechanical treatment of the wave properties of the neutrons. Thermal neutrons, being uncharged, penetrate deeply into condensed matter and scatter from the nuclei of the sample. Thermal neutrons have energies in the milli-electron Volt range (meV), and de Broglie wavelengths comparable to interatomic distances. They exchange an appreciable fraction of their momentum and energy with the target. The double differential scattering cross section can be measured experimentally as a function of energy and momentum transfer. The interaction of a neutron with a nucleus is governed by strong nuclear forces, but the range of these forces is very short relative to the neutron de Broglie wavelength. The atomic scattering lengths are very short relative to inter-atomic distances. Together these features allow the description of neutron scattering by perturbation theory in the first Born approximation,

through the use of the Fermi pseudo-potential. Because first order perturbation theory provides a good description, measured neutron scattering spectra reflect the unperturbed structure and dynamics of the target sample. Because the atomic scattering length depends sensitively on randomly distributed nuclear isotope and spin, neutron scattering spectra contain a *coherent* and an *incoherent* component. The physical theory establishes a remarkable reciprocal analytical relationship, through Fourier transformation, between the coherent and incoherent dynamic structure factors, and the van Hove pair and self correlation functions of the unperturbed target system, respectively. The correlation function formalism allows the explicit calculation of neutron scattering properties from models of the dynamics of a target sample, and direct comparison with the experimental spectra. This will be a theme in each of the experimental chapters of this thesis, and the necessary theoretical developments and details of these calculations will be described there.

The properties of neutrons and the resulting highly developed theory make neutron scattering uniquely suited to the study of the structure and dynamics of condensed matter. The main disadvantages lie in the practical difficulties of obtaining an intense incident beam of neutrons, whilst achieving good energy and momentum resolution of the incident and scattered neutrons, over a wide range of energy and momentum transfer. In the next chapter I will discuss the TFXA spectrometer, the machine on which the bulk of the experiments described in this thesis were performed.

## CHAPTER III - THE TOOLS OF THE TRADE.

In this short Chapter I will describe the Time Focusing Crystal Analyser Neutron Spectrometer (TFXA) and also the CHARMM molecular mechanics program and PEF. These are brought together here for reference because they are common elements in the experiments and calculations described in subsequent Chapters.

### 3.1. THE TIME FOCUSING CRYSTAL ANALYSER SPECTROMETER AT RUTHERFORD APPLETON LABORATORY.

The vibrational INS experiments described in the main part of this thesis were conducted on the Time Focusing Crystal Analyser (TFXA) spectrometer at ISIS pulsed neutron source, RAL. Neutrons are generated at ISIS by a process known as spallation. Hydride ions ($H^-$) are accelerated in a linear accelerator to an energy of 80 MeV, and passed through a thin metal foil into a synchrotron. Passage through the foil removes the electrons from the hydride ions, and the resulting protons are accelerated round the synchrotron in two bunches, to an energy of 800 MeV. Bunches are extracted from the synchrotron ring at a frequency of 50 Hz, and passed down a beam line to collide with a Tantalum target. The time for the two bunches to collide with the target is 250 ns. The incoming protons are absorbed by the nuclei of the target, producing an unstable state which decays by generating a cascade of neutrons. For every proton absorbed approximately 12 neutrons are generated. These are emitted isotropically, and those travelling in the direction of the TFXA beam line pass through a poisoned water moderator, designed to modify the raw energy spectrum of the emitted neutrons. TFXA thus receives pulses of neutrons at 50 Hz, with a Maxwellian thermal spectrum (~10 - 200 meV), along with an epithermal spectrum of exponential form [S.F. Parker, personal

communication].

TFXA is an indirect geometry time of flight spectrometer [Penfold *et al.*, 1986]. It uses a time focussed pyrrolytic graphite analyser to give good count rates, and good energy resolution over a wide range of energy transfer (2-500 meV ≡ 16-4000 $cm^{-1}$). Time focussing is achieved by having the sample and detector arrays in the same plane, and the analysing crystal set parallel to this plane (Fig. 3.1).

The collimated beam impinging on the sample has vertical dimension of 50 mm, and horizontal dimension of 25 mm. The analyser graphite crystal has dimensions 80 mm × 80 mm, with a depth of 2 mm. The neutrons scattered from the sample impinge on the analyser crystal over a range of solid angles, $\theta$, centred on 135° to the <002> Bragg plane. Bragg reflection occurs, and the scattered neutrons reach elements of the detector array. Bragg reflection ensures that for each angle, $\theta$, a single value of the final neutron wavevector is selected, according to the Bragg equation:

$$2\pi/|\mathbf{k}_f| = \lambda_f = 2d\sin\theta \qquad (3.1.1)$$

where d is the separation of the <002> Bragg planes. This equation applies to the first order of Bragg scattering, and higher orders are suppressed by a cooled Beryllium filter placed between the analyser crystal and the detectors. The angle $\theta$ also determines which element of the one dimensional array of detectors is the final destination of the scattered neutron. Each detector element always receives neutrons of a fixed final wavevector, and energy. Within the limit of resolution generated by the mechanisms to be discussed below, the final neutron energy for all detectors is thus 3.95 meV. Furthermore, as can be seen from the spectrometer geometry

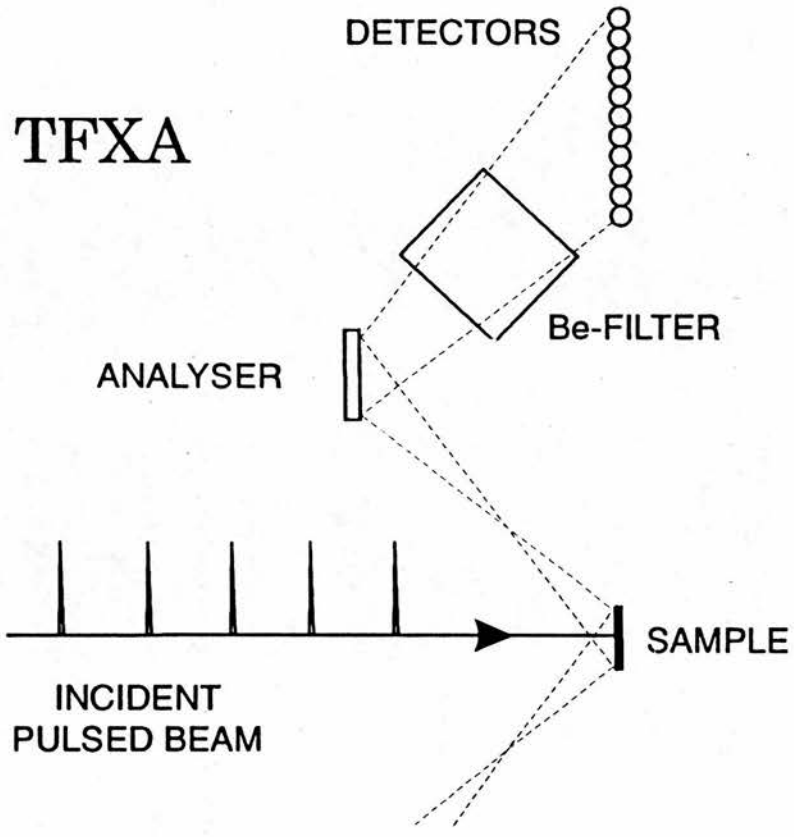


Figure 3.1. Schematic of the TFXA Spectrometer

(Fig. 3.1), the length of the secondary flight path (sample to detector) is inversely proportional to $\sin\theta$, and so is the neutron velocity $|\mathbf{v}_f| = \hbar|\mathbf{k}_f|/m$. Hence, for an ideal analyser crystal in this arrangement, the time of flight of the neutrons over the secondary flight path is a constant for all the detector elements. This time focussing effect contributes significantly to the energy resolution of the machine (see below), and is the origin of the name TFXA. A symmetrical arrangement of two analyser/detector systems either side of the sample, and a design effort to minimise the final flight path, and the distance between sample and analyser planes, maximises the effective solid angle of scattering in which neutrons are detected.

The initial detectors in each array are 16 $He_3$ gas tubes, with a depth of 6mm. The incoming neutrons interact with the helium atoms generating a charged particle, and these are detected as a current in a wire passing down the centre of the tube. The incoming counts are sorted by their time of arrival, synchronised to each pulse of the spallation source. Hence for every pulse a time sorted spectrum is accumulated in each of the detector elements. Since the time of flight on the secondary flight path is constant, the total time of flight depends only on the length of the primary flight path (from source to sample), and on the initial energy of the incident neutrons. Thus the total time of flight allows the calculation of the initial energy and the transferred energy from the known geometry of the spectrometer.

An approximate calculation for the energy resolution of the spectrometer, in terms of measured parameters, yields a Gaussian distribution of energy transfers of width $\Delta\hbar\omega$ [Penfold *et al.*, 1986]. The individual contributions to the resolution are also Gaussian functions. Convolution of these contributions yields an expression for $\Delta\hbar\omega$:

$$[\Delta\hbar\omega]^2 = [(\partial\hbar\omega/\partial E_f)\Delta E_f]^2 + [(\partial\hbar\omega/\partial L_2)\Delta L_2]^2 \qquad (3.1.2)$$

$$+ [(\partial\hbar\omega/\partial L_1)\Delta L_1]^2 + [(\partial\hbar\omega/\partial t)\Delta t]^2$$

where $L_1$, $L_2$ are primary and secondary flight paths, respectively. $E_f$ is the final energy, and t the total time of flight.

The energy resolution of TFXA is improved by the time focussing arrangement because this removes uncertainty due to finite collimation of the incident and scattered beams. The uncertainty in the secondary flight path therefore arises only from the finite size of sample, analyser crystal, and detector. Experimental samples are contained in aluminium cells, the scattering from which, though structured, is very weak. The temperature of the sample chamber is controlled by a helium cryostat, and monitored continuously by a thermocouple strapped to the sample can. The depth of the samples along the axis of the incident wavevector is approximately 1 mm. The final energy resolution achieved is between 1.4 and 4.5 % of energy transfer, as shown in Fig. 3.2. The detected neutron counts are binned in energy to give discrete experimental points on the energy axis. The density of these experimental points on the energy axis is 0.5 % of the energy transfer (the width of the bins on the energy axis is 0.5 % of energy transfer, always much less than the energy resolution). To allow for this variation in the density of experimental points, the neutron counts are expressed in this thesis in terms of counts per millielectron Volt. This means that the statistics at the lowest energy transfers tend to deteriorate as a consequence of the very high density of measured points on the energy axis, with many narrow energy bins, each with a small number of counts and hence poor statistics.

The detected neutrons are backscattered from the sample.

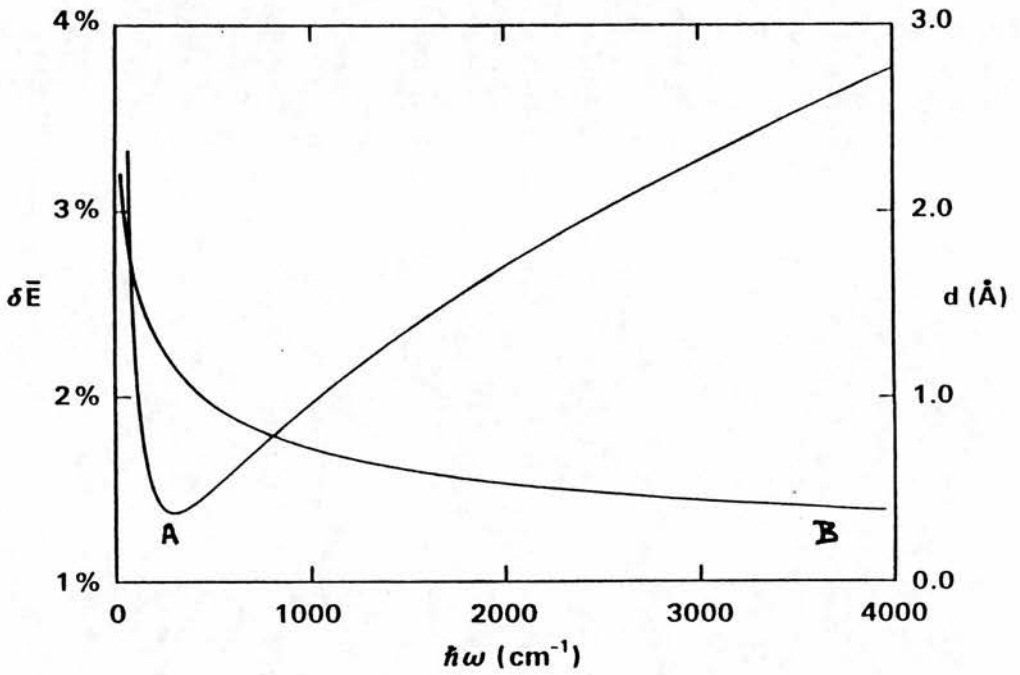


Figure 3.2. TFXA resolution function (curve A), and relation between d (= $2\pi/|\mathbf{Q}|$) and $\omega$ (curve B).

The final energy is small relative to the initial energy for all the detectors. From the momentum conservation Eq. 1.4.1 (Chapter I) it is apparent, therefore, that the scattering vector **Q** is essentially parallel with the incident wavevector for all values of energy transfer. This means that **Q** cannot be varied significantly for any value of the energy transfer. Since the final neutron energy for each detector is fixed, the conservation Eqs. 1.4.1 and 1.4.2 (Chapter I) impose a relation between energy and momentum transfer:

$$|\mathbf{Q}|^2 = \mathbf{Q}.\mathbf{Q} \qquad (3.1.3)$$

$$= \mathbf{k}_i.\mathbf{k}_i - 2\mathbf{k}_i.\mathbf{k}_f + \mathbf{k}_f.\mathbf{k}_f$$

$$= 3.813 + (0.2287\omega+7.27)^{\frac{1}{2}} + 0.06\omega$$

where $\hbar\omega$ is the energy transfer, $|\mathbf{Q}|^2$, is the square of the scattering vector. The numerical relations hold for $\omega$ in units of wavenumbers ($cm^{-1}$) and $|\mathbf{Q}|^2$, in units of $Å^2$, and is displayed in Fig. 3.2. Here and throughout the following, optical wavenumbers ($cm^{-1}$) are used as convenient energy units ( 1 $cm^{-1}$ = 124 $\mu$eV), since this facilitates comparison with optical spectroscopic papers. For reference 1 meV ≡ 8.07 $cm^{-1}$ ≡ 0.24 THz, and 1 THz ≡ 33.35 $cm^{-1}$. The relation (3.1.3) render the TFXA spectrometer unsuitable for the study of the **Q** dependence of the energy transfer spectrum. In particular coherent scattering cannot be usefully exploited, and the relation (Eq. 3.1.3) merely complicates the interpretation of coherent scattering spectra. It is not possible to make scans of constant **Q** for example. On the other hand the low final energy offers advantages for the interpretation of spectra which are isotropic in **Q**, in particular INS spectra dominated by incoherent scattering, and powder samples.

The low final neutron energy, and the sample thickness of only ≈1 mm, ensure that multiple scattering processes are negligible for organic samples [Goyal *et al.*, 1986], like those described in this thesis. As noted above the scattering vector is almost parallel to the incident beam for all directions of the final wavevector after a first inelastic scattering event. Second scattering events must be predominantly elastic, because the final energy after the first event is so low. Since these secondary elastic scattering events will be isotropic in powder samples, they will not change the observed double differential cross section. In this thesis the effect of multiple scattering is therefore neglected. (Note: multiple scattering is to be distinguished from multiphonon scattering in the harmonic approximation, which results from a single scattering event creating or destroying multiple phonons. Where the harmonic approximation is applied to calculating INS spectra, the calculation of multi-phonon scattering will be discussed.)

The dependence of the resolution on energy transfer (Fig. 3.2), and the relation between energy and momentum transfer (Eq. 3.1.3; Fig. 3.2) have important consequences for the intensity observed at different energy transfers. A fuller discussion of the application of the theory of thermal neutron scattering to each of the experimental problems discussed in this thesis will be given in the relevant chapters. There the practical implications of the characteristics of TFXA will become apparent.

## 3.2. THE CHARMM PROGRAM AND POTENTIAL ENERGY FUNCTION.

The theoretical description of the dynamics of many body systems by analytical means has had limited success. Indeed a complete analytical solution of the three body problem is still awaited. As a result of these analytical difficulties, numerical approximations have been applied

extensively to the simulation of many body dynamics, in the hope that qualitatively and perhaps quantitatively accurate results can be derived. In the last decade computational power sufficient for large many body systems has become available. As noted in Chapter I, this technique has been extensively applied to the numerical simulation of macromolecular dynamics. The CHARMM program is one of a number of software packages which have been developed for this purpose, and particularly for the simulation of protein dynamics. The version of the CHARMM program used for all the calculations discussed in this thesis was implemented on Hewlett/Packard 9000/735 networked computers at the Section des Biophysique des Proteines et des Membranes, Centre d'Etudes Atomique, Saclay, France, with the permission of, and lots of help from, the chief of the section, Dr. Jeremy Smith.

The CHARMM program allows the calculation of an empirical potential energy for molecular systems as a function of atomic coordinates. The configurational space of the system can be searched to find a local or global energy minimum, and the structure at this minimum can be compared with the structure derived from experimental studies. Forces acting on the atoms of the system are calculated as the second derivatives of the PEF by numerical differentiation with respect to the atomic degrees of freedom. The matrix of second derivatives can be used directly in the calculation of harmonic dynamics, or the calculated forces can be used in Newton's classical equations of motion. Numerical integration techniques based on discrete time steps can then be used to yield a discrete approximation to the full classical molecular dynamics of the system studied.

The central tool of simulation methods is thus the empirical PEF, which for all the calculations in this thesis has the following form (Eq. 3.2.1):

$$V = \sum_{bonds} k_b(b-b_o)^2 + \sum_{angles} k_\theta(\theta-\theta_o)^2 + \sum_{1:3} k_u(u-u_o)^2$$

$$+ \sum_{dihedrals} k_\phi(1+\cos[n\phi-\delta]) + \sum_{impropers} k_\omega(\omega-\omega_o)^2$$

$$+ \sum_{i,j} 4\epsilon_{ij}\left[(\sigma_{ij}/r_{ij})^{12} - (\sigma_{ij}/r_{ij})^{6}\right] + \sum_{i,j}(q_iq_j/4\pi\xi r_{i,j})$$

The model used treats all atoms in the system explicitly. However for the purpose of defining the potential energy parameters, the atoms are classified into atom types, and the parameters given in terms of these atom types. This technique aims to derive parameters which are transferable amongst the same atom types in different structures. The approach can be viewed as an application of local symmetry. Thus for example the three hydrogen atoms of a methyl group are equivalent by local symmetry and are assigned to a single atom type, although it might be expected that the local environment of each atom could affect fine details of its interaction with neighbours. Such induced effects, like for example induced polarisation, are neglected in the present CHARMM model. The PEF includes bonded interactions, comprising bond stretches, bond angle bends, and dihedral angle contributions, and non-bonded interactions between pairs (i,j) of atoms. In Eq.3.2.1 b, u, $\theta$ and $\omega$ are the bond lengths, Urey-Bradley 1:3 distances, angles, and improper torsional angles at any given configuration and $b_o$, $u_o$, $\theta_o$, $\omega_o$ are the reference values for these properties; the associated force constants are $k_b$, $k_u$, $k_\theta$ and $k_\omega$. The improper dihedral contributions are used to represent out-of-plane deformations of planar groups. For the intrinsic dihedrals $\phi$ is the torsional angle, n is the symmetry number of the rotor (e.g., 3 for methyl group) and $\delta$ is the phase angle. Pairs of atoms on the same molecule separated by two bonds may interact via a Urey-Bradley term harmonic in displacements from the reference distance

between atoms i, j. The non-bonded interactions between pairs i, j of atoms on different molecules and pairs i, j of atoms on the same molecule separated by three or more bonds, consist of a Lennard-Jones term, with parameter $\epsilon_{ij}$ and van der Waals radius $r_{min} = 2\sigma_{ij}$ and an electrostatic interaction between partial charges $q_i$, $q_j$. The dielectric constant $\xi$ was set to 1.0. Hydrogen bonds are described by the non-bonded terms in the energy function. In all the calculations long-range electrostatic interactions were brought to zero at a cut-off of between 12 and 15 Å by a cubic switching function [Brooks *et al.*, 1983a].

Clearly the only source for anharmonic terms in this PEF are the dihedral terms with a cosine dependency, and the non-bonded electrostatic and van der Waals terms. The PEF notably fails to explicitly include interaction terms for the influence of displacement in one internal coordinate of the molecule on the effective force constant for another internal coordinate, although these terms are second order in small displacements of the atoms. Explicit interaction terms are avoided because of the undesirable proliferation of refinable parameters produced by their inclusion, from order N to order $N^2$ where N is the number of atoms, with consequent penalties in computational time. Such interaction terms are included only implicitly through non-bonded terms of the potential. Interaction terms are usually included in harmonic models of molecular vibrations by off-diagonal terms in the force constant matrix, making easier the adjustment of harmonic frequencies to fit experimental data. As noted a further effect missing from the CHARMM PEF is the inclusion of induced polarisation effects. Again these effects are neglected to save computational time.

The parameters of the PEF are generally derived from *ab initio* quantum chemical calculations for small models of fragments of the macromolecule, or from dynamical models

fitted to spectroscopic data. An example of such *ab initio* calculations is furnished by the case of N-methyl acetamide (NMA), in which the effects of hydrogen bonding have been investigated [Guo and Karplus, 1992; Reiher and Karplus, 1993]. Parameterisation of the *ab initio* energy calculations by empirical force constants then lead to a model for the CHARMM PEF for NMA [Baudry and Smith, 1993]. Sufficient uncertainty in the results of quantum chemical calculations, and particularly in the question of transferability of small molecule parameters to macromolecules justifies a continuing effort to refine the empirical parameters by comparison with relevant spectroscopic data. The next three Chapters describe the collection of INS data for several systems of biological interest. The analysis of the data included comparison with CHARMM calculations.

## CHAPTER IV - VIBRATIONAL NEUTRON SPECTROSCOPY OF COLLAGEN AND MODEL POLYPEPTIDES.

A pulsed-source neutron spectrometer was used to measure vibrational INS spectra ( 20 to 3600 $cm^{-1}$ ) of dry and hydrated type I collagen fibres, and dry powders of the model polypeptides of collagen, polyproline II and $(ProlylProlylGlycine)_{10}$, at temperatures between 30 and 35K. The spectra obtained provide the first high-resolution neutron views of the proton-dominated modes of a natural biopolymer and its model polypeptides over a wide energy range from the low-frequency phonon region to the rich spectrum of localised high-frequency modes. The low-frequency features of the INS spectra were analysed in terms of the density of vibrational states and the principal high-frequency features are discussed in the context of relevant optical spectroscopic work. Dynamical properties of the water associated with collagen were extracted from the data. A molecular dynamics simulation of $(ProlylProlylGlycine)_{10}$ is described and INS spectral properties calculated from the simulation are compared with experiment. Numerical harmonic analyses of the dynamics of Polyproline II were also performed. INS intensities calculated from the harmonic analyses were compared with experiment.

### 4.1. INTRODUCTION.

#### 4.1.1. Why study collagen?

Collagen is the principal protein constituent of a wide variety of connective tissues in animals [Miller, 1984]. Its structure has been investigated extensively by electron microscopy [Hulmes *et al.*, 1981] and by diffraction techniques using x-rays [Fraser *et al.*, 1987] and neutrons [Wess *et al.*, 1990]. A consensus has emerged about the molecular structure and packing of Type I collagen, the most common form [Fraser *et al.*, 1983,

Miller, 1984, Fraser *et al.*, 1987]. Type I collagen makes up 98 % of the protein content of tendons, and is readily available from the tail tendons of adult laboratory rats. Collagen retains its structural integrity over a wide range of hydration [Fraser *et al.*, 1979; Fraser and McRae, 1979], and the structure and dynamics of water associated with tendon collagen have been studied by NMR, dielectric measurements and sorption techniques [Grigera and Berendsen, 1979, Hoeve and Tata, 1978; Peto *et al.*, 1990]. At least three distinct populations of water have been identified, associated with fully hydrated tendon collagen. Several simpler synthetic polypeptides are available which provide structural models of Type I collagen. Polyproline II (PPII), polyglycine II (PGII) and polyprolylprolylglycine $(PPG)_n$ are examples. Infrared (IR) and Raman spectroscopic studies of collagen and its model polypeptides have been published [Isemura *et al.*, 1968; Smith *et al.*, 1969; Gupta *et al.*, 1973; Fanconi and Finegold, 1975; Frushour and Koenig, 1975; Brodsky-Doyle *et al.*, 1975; Dwivedi and Krimm, 1982; Diem *et al.*, 1984; Krimm and Bandekar, 1986].

The biological role of type I collagen in tendon is essentially mechanical, transmitting muscular contractile force to bone, and the time scale of this motion is many orders of magnitude greater than the ps to fs time scale of INS. Therefore INS experiments cannot yield dynamical information of direct relevance to the biological function of collagen. However, as noted in Chapter I, INS provides experimental data for testing and refining models of the PEF and dynamics of proteins in general. Collagen is constructed from the same constituent amino acids as any other protein. Recently, short stretches of left handed helix, typical of the polyproline II and collagen structure, have been identified as a new structural motif in many globular proteins [Adzhubei and Sternberg, 1993].

Furthermore, proline cis/trans isomerisation appears to be a rate limiting step in the folding of many globular proteins, and the folding rate depends on the potential energy barrier to isomerisation [Miranker *et al.*, 1993]. The extensive structural data for type I collagen and its associated water, the new found relevance of the characteristic structural motif to globular proteins in general, the availability of collagen in gram quantities from tendon, and the availability of well characterised model polypeptides combine to make type I collagen an attractive protein for study by INS.

### 4.1.2. Early INS experiments for collagen.

The Q-dependent coherent component [Chapter II] of INS is more informative, in principle, than the incoherent component, and an early experiment measured the Q-dependence of INS from collagen non-covalently deuterated by soaking in $D_2O$ [Jones, 1985]. The residual content of non-exchangeable hydrogens produced a large incoherent scattering background, making the identification of phonon bands difficult. Count rates obtained were at the limit of significance. Nevertheless inelastic peaks corresponding to longitudinal phonons were tentatively identified, and yielded sound velocities in good agreement with those obtained from Brillouin scattering experiments.

Another early INS experiment attempted to determine the vibrational density of states in collagen by measuring the dominant incoherent scattering from dry powders of native collagen. This experiment suffered from difficulties in energy resolution, but identified structure in the INS spectrum below 200 $cm^{-1}$ [Berney *et al.*, 1987].

### 4.1.3. Why use newer INS spectrometers?

New INS spectrometers offer improved energy resolution and access to a wider energy transfer range. In

collaboration with Dr. J. Bradshaw, Professor A. Miller and Dr. H.D. Middendorf, who originated the project, I have used TFXA, the Time Focused Crystal Analyser spectrometer at the ISIS Pulsed Neutron Facility (Rutherford Appleton Laboratory, Chilton, UK) [Penfold and Tomkinson, 1986; Windsor, 1981; Chapter III], to measure neutron spectra in the frequency range 20-3600 $cm^{-1}$ from dry and hydrated collagen fibres, and dry powders of polyproline II and $(PPG)_{10}$. The latter was examined in either the hydrogenous form, or with the amide hydrogen exchanged for deuterium. The scattering arrangement on TFXA does not allow determination of the Q-dependence of the INS spectrum [Chapter III], but because of the high content of hydrogen, the spectra from the samples discussed in this chapter were dominated by incoherent scattering, for which the Q-dependent properties, being an average over a large variety of different hydrogens, are anyway not especially informative. On the other hand the TFXA spectrometer is unique in that it allows both the low-frequency region (with its intrinsically collective excitations) and the whole of the intermediate and higher $\hbar\omega$ region (non-dispersive optical phonons, localised excitations) to be covered.

### 4.1.4. Structure of this chapter.

In this chapter the molecular properties of collagen and its model polypeptides are reviewed. The preparation of the hydrated collagen samples, the method of hydrogen/deuterium exchange and the characterisation of the model polypeptide samples by powder x-ray diffraction and IR spectroscopy are described. The INS experimental methods are explained. The quality of the resulting spectra is considered. The low-frequency parts of the spectra ($< 400$ $cm^{-1}$) are compared for the different samples, and analysed in terms of the hydrogen weighted

vibrational density of states. The necessary developments of the theory of inelastic neutron scattering are discussed. Tentative assignments for higher frequency features are made by comparison with optical spectroscopic results. A difference INS spectrum for the water of hydration of collagen is extracted. Finally a molecular dynamics simulation of the $(PPG)_{10}$ molecule and an harmonic analysis of PPII, using the CHARMM program and PEF [Chapter III] are described. Experimental properties extracted from the INS data are compared with calculations of INS spectra from the MD simulation of $(PPG)_{10}$ and the harmonic analysis of PPII.

## 4.2. MOLECULAR PROPERTIES OF TYPE I COLLAGEN AND ITS MODEL POLYPEPTIDES.

### 4.2.1. Polyproline II.

The helical structure of PPII was determined in the 1950's and 1960's by x-ray diffraction [Cowan and McGavin, 1955; Sasisekharan, 1959; Arnott and Dover, 1968]. The helix is left handed, of $3_1$ symmetry, with an axial translation per residue of 3.12 Å and a pitch of 9.36 Å. PGII adopts a similar structure [Crick and Rich, 1955].

### 4.2.2. Collagen.

In adult rat tail tendon, type I collagen molecules are packed together in quasi-hexagonal fashion forming fibrils [Hulmes and Miller, 1979] which stretch over several micrometres and reach 5000 Å in diameter [Miller, 1984]. The packing is sufficiently crystalline to allow molecular structure determination by x-ray diffraction and model building [Fraser *et al.*, 1983]. Type I collagen consists almost entirely of the characteristic triple stranded helix, seen in some portion of all collagens. The individual collagen molecule is cylindrical, approximately 3000 Å long and 12.5 Å in diameter, with the long axis

approximately parallel with the tendon axis [angular half-width 5° - Jones, 1985]. In very dry preparations of tendon collagen the orientational disorder around the fibril axis increases, though other features of the structure are preserved [Fraser *et al.*, 1979; Fraser and McRae, 1979]. The molecule consists of two identical α1(I) chains and one homologous but distinct α2(I) chain [Miller, 1984]. Each chain is 1055 amino acid residues long and the complete amino acid sequences of α1(I) and α2(I) chains are known [Miller, 1984]. The three polypeptide chains each have a central region of 1014 residues with a repeating Gly-X-Y sequence where Gly is the amino acid glycine, and X and Y are any other amino acid, but are often the imino acids proline (largely in site X) and hydroxyproline (almost exclusively in site Y). X-ray diffraction studies of tendon indicate that the backbone of the central section of each chain adopts a PPII type left handed $3_1$ helical structure, the local structure of which is slightly distorted by supercoiling and by the precise nature of the residues X and Y in the local tripeptide unit [Fraser *et al.*, 1983]. Thus the left handed PPII helix is supercoiled to form a right handed $10_1$ superhelix of 86.8 Å pitch. Each turn of the supercoil requires ten tripeptide repeating units. The three chains of each molecule are supercoiled around a common axis, and asssociated together to form a three stranded rope-like structure. This supercoiled triple helical arrangement is favoured by the presence of glycine at every third residue, reducing steric hindrance, and providing one interchain hydrogen bond per tripeptide unit. A left handed $10_3$ helix of pitch 9.65 Å, axial rise per tripeptide of 2.89 Å, and azimuthal rotation per tripeptide unit of -108° dominates the x-ray crystallographic pattern [Fraser *et al.*, 1983]. This left handed crystallographic helix does not connect covalently bonded residues, but rather

can be drawn through tripeptide units located sequentially on each of the three different strands of the molecule in turn. Each turn of this crystallographic helix requires 10/3 tripeptide units. The short amino- and carboxy-terminal sequences which do not contain the regular repeating motif appear to adopt a more globular structure, though irregular packing of these terminal regions prevents determination of their structure at atomic resolution [Hulmes *et al.*, 1980].

### 4.2.3. (ProlylProlylGlycine)$_{10}$.

Synthetic polypeptides with the sequence $(PPG)_n$ also adopt a left handed PPII type helical structure, each chain supercoiling in a right handed $7_1$ helix of 60.2 Å pitch, similar to, though more tightly coiled than, the $10_1$ helix in collagen. Furthermore, three strands of $(PPG)_n$ are supercoiled round a common axis and associated to form a triple helical arrangement with one interchain hydrogen bond per tripeptide unit [Yonath and Traub, 1969; Okuyama *et al.*, 1981]. The left handed crystallographic helix drawn connecting tripeptides on each strand, in turn, of the triple helix of $(PPG)_{10}$, has axial rise of 2.87 Å per tripeptide unit and azimuthal rotation per tripeptide unit of -102.9°, each turn of the helix requiring approximately 3.5 tripeptide units. The packing of the residues is therefore close to that in collagen. A recent x-ray diffraction study of a single crystal of the polypeptide $(ProHypGly)_4ProHypAla(ProHypGly)_5$ (Gly -> Ala peptide) [Bella *et al.*, 1994], has shown the triple helical structure distorted at the Gly -> Ala substitution site. Circular dichroism and NMR studies of $(GlyProHyp)_n$ and the Gly -> Ala peptide in solution have also indicated the triple helical arrangement, and allowed characterisation of the kinetics of folding and the thermal stability of the helix [Li *et al.*, 1993]. These studies have confirmed



the role of glycine in the structural integrity of the triple helix. IR and Raman experiments for collagen in various states of hydration have been performed, particularly in the frequency range >400 $cm^{-1}$, and assignments for collagen spectra have been made on the basis of normal mode analyses and optical spectroscopy of PGII, PPII and $(PPG)_{10}$ [Isemura *et al.*, 1968; Smith *et al.*, 1969; Gupta *et al.*, 1973; Fanconi and Finegold, 1975; Frushour and Koenig, 1975; Brodsky-Doyle *et al.*, 1975; Dwivedi and Krimm, 1982; Diem *et al.*, 1984; Krimm and Bandekar, 1986]. Thus the structural properties of PGII, PPII, and $(PPG)_{10}$ make these useful spectroscopic model systems for collagen.

**4.2.4. Water in triple helical polypeptides.**

Three populations of bound water have been identified in tendon by NMR, dielectric, and sorption experiments [Grigera and Berendsen, 1979; Peto *et al.*, 1990]. The most tightly bound fraction consists of two water molecules for every three amino acid residues, and provides water bridges between the three strands of the collagen molecule, linking backbone carbonyl groups [Ramachandran and Chandrasekharan, 1968]. This represents a water content of 12.5% by weight (12.5g water per 100g dry collagen). These water molecules behave anisotropically in NMR experiments [Peto *et al.*, 1990]. At 25% hydration, these tight binding sites are occupied approximately 90% [Grigera and Berendsen, 1979]. A second, less tightly bound fraction is localised in the interstices of the quasi-hexagonal packing arrangement of collagen. At least a further 35g per 100 g dry collagen can be absorbed exclusively in this site, in hydrogen bonded chains of water molecules [Hoeve and Tata, 1978]. Recently x-ray diffraction of single crystals of the collagen model triple helical peptide $(ProHypGly)_4ProHypAla(ProHypGly)_5$

[Bella *et al.*, 1994] have directly demonstrated an inter-helical network of bound water between the close packed cylindrical triple helices. X-ray diffraction results for $(PPG)_{10}$ single crystals have also demonstrated a network of hydrogen-bonded water molecules, though the full interhelical network was not resolved [Okuyama *et al.*, 1981]. A third population of more loosely bound water can be absorbed in the ground substance of tendon, in which collagen fibrils are embedded. The ground substance also contains mucopolysaccharides and totals ~2g per 100g dry collagen.

## 4.3. METHODS AND MATERIALS.

### 4.3.1. Sample Properties and Preparation.

#### 4.3.1.1. Collagen.

Samples of Type I collagen used in the INS experiments were from the tail tendons of adult laboratory rats. Completely dessicated collagen was prepared, for reference, by drying over $P_2O_5$ for 72 hours followed by further drying in vacuo at 120 °C for 7 hours. Heating to this temperature is known to result in the loss of tight bound water [Renugopalakrishnan *et al.*, 1989]. 'Dry' collagen samples were prepared by drying over $P_2O_5$ in dry atmosphere for 72 hours. They have a residual water content of 6%, representing the most tightly bound fraction of water, and similar to the residual water present in $(PPG)_{10}$ after drying. The dry samples were handled in dry nitrogen gas atmosphere. $D_2O$ exchanged samples dried in this way were previously examined on the D17 neutron diffractometer at the Institute Laue Langevin by Dr. H.D. Middendorf and Dr. J. Bradshaw, and showed good crystalline order (Fig. 4.1). X-ray fibre diffraction of the dry collagen samples also demonstrated good helical order, though the expected increase in orientational disorder around the fibre axis was evident (Fig. 4.2). For

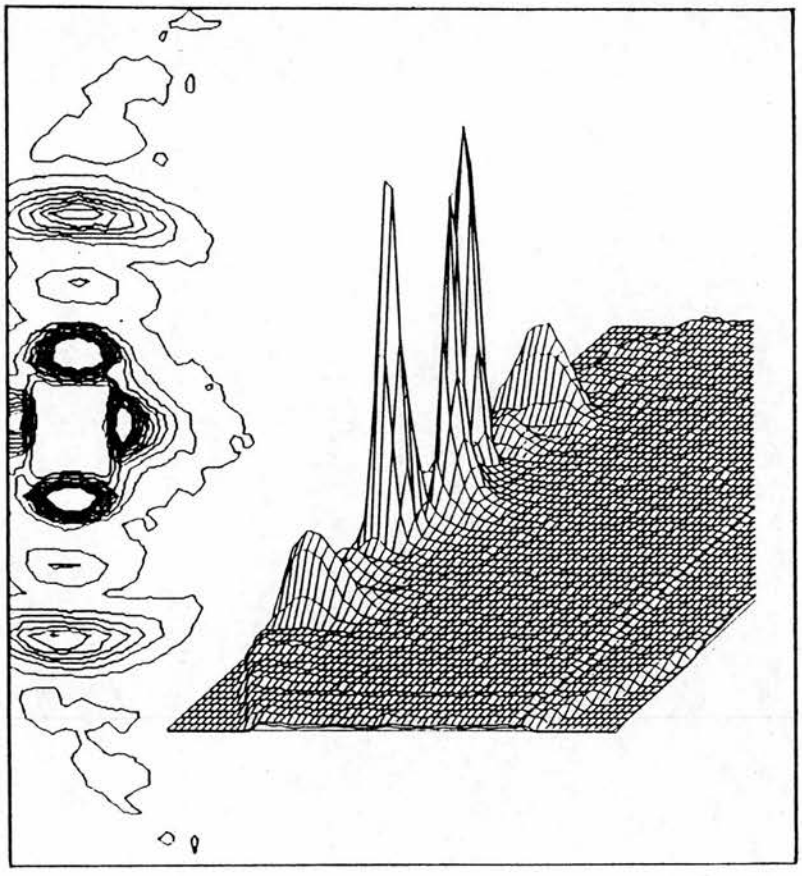

Figure 4.1. Neutron diffraction pattern obtained from $D_2O$-exchanged collagen dried over $P_2O_5$, measured using diffractometer D17 at ILL, Grenoble, by H.D. Middendorf and J. Bradshaw (personal communication). Four to five meridional orders are seen (vertical sequence of maxima), the first at **Q** = 0.0094 $Å^{-1}$ corresponding to 670 Å.

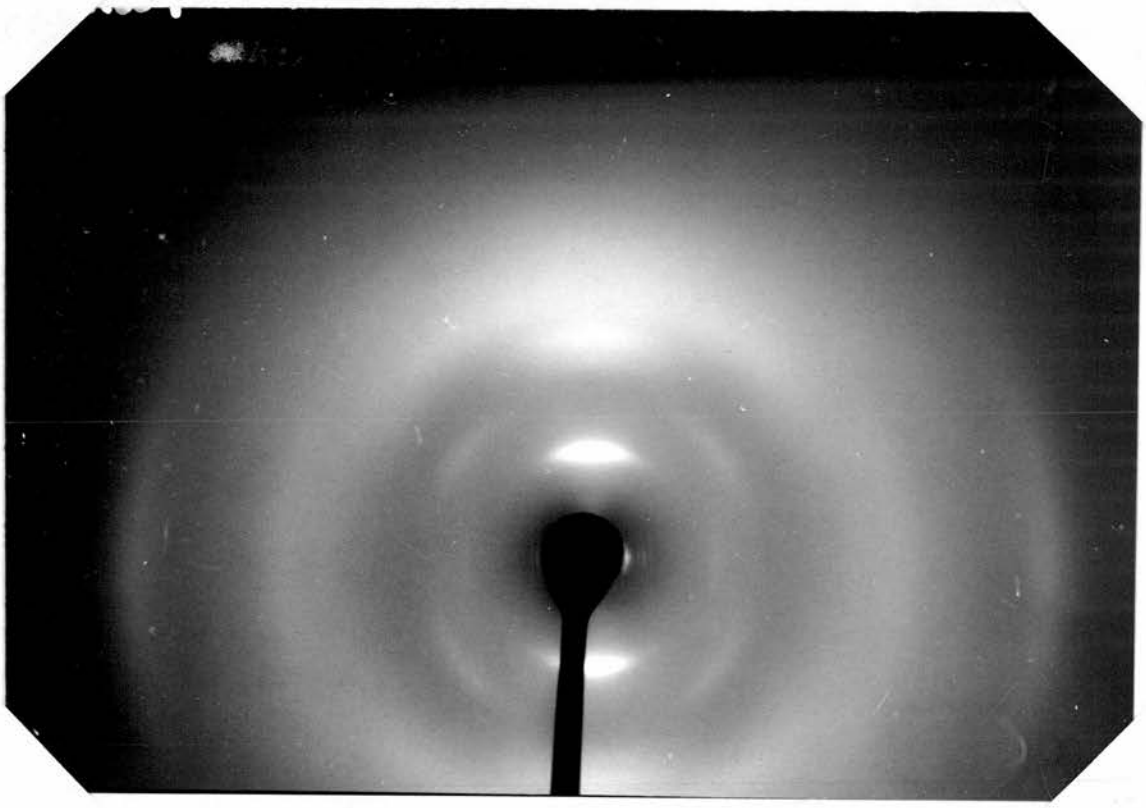

Figure 4.2. X-ray fibre diffraction pattern obtained from collagen dried over $P_2O_5$, measured using GX-13 xray generator at Edinburgh (6% hydration). Good helical order observed, though with increased angular disorder round fibre axis (arcing of the equatorial reflections). No accurate calibration attempted since the aim was simply to demonstrate that drying did not destroy the triple helical structure.

these experiments a dried fibre was mounted in a capillary tube sealed with wax. The capillary tube was mounted in the beam of the rotating copper anode x-ray generator GX-13 in the Biochemistry Department, Edinburgh University, and the x-ray pattern collected over a period of 24 hours on photographic film. No attempt at accurate calibration of the patterns was made, as the purpose was merely to check the retention of helical order after drying. $H_2O$ hydrated collagen fibres were prepared by exposure of fibres, soaked in $H_2O$, to atmosphere in equilibrium with saturated solution of sodium chromate salt, at room temperature for 70 hours. This provides an hydration of ~25% [Grigera and Berendsen, 1979]. The hydration of these samples was checked after the INS experiments by drying to the completely dessicated state and was found to be 23%. As noted above, at this hydration essentially all of the water is located in tight bound water bridge sites or in the interstices of the quasi-hexagonal packing arrangement.

#### 4.3.1.2. (ProlylProlylGlycine)$_{10}$.

$(PPG)_{10}$ was purchased from Peptide Institute Ltd., Osaka, Japan. The manufacturers analysis indicated carbon, nitrogen and hydrogen contents within 1% of that predicted for $(PPG)_{10}$:11 $H_2O$. The material was therefore used without further purification, because of the cost and quantity of material required. Deuterated samples were prepared in which the labile amide hydrogens were exchanged for deuterium by solvation in 1% (v/v) acetic acid in $D_2O$ (99 % purity) for one week, freeze drying the sample and repeating the exchange in an excess volume of 1% acetic acid in $D_2O$ for a further week. The deuterated sample will be referred to as $(PPG)_{10}$-d. Native samples, with no deuteration, were prepared by a similar procedure using $H_2O$ instead of $D_2O$ solutions, to ensure comparability of the

deuterated and native samples.

After the first week of H/D exchange in the preparation of the deuterated samples IR spectra were collected for lyophilised $(PPG)_{10}$ and $(PPG)_{10}$-d samples at room temperature (Figs. 4.3 + 4.4). Potassium Bromide (KBr) disc samples were prepared from the dry powders finely ground together with KBr, and compressed in a die press. The mixing was performed in dry nitrogen atmosphere, though the final stage of disc preparation required exposure of the mixed powder to air, and the discs themselves were exposed to air during collection of the spectra. The spectra were collected on a Nicolet 7000 series Fourier Transform Infra Red spectrometer in the department of Chemistry, Edinburgh University at 4 $cm^{-1}$ resolution, under the guidance of Dr. Colin Pulham.

In fact the $(PPG)_{10}$-d spectra showed only ~ 50 % replacement of the amide hydrogens by deuterium after the first period of exchange, demonstrating the need for a second period of H/D exchange, as described above. This second period provided H/D exchange of the amide hydrogen of > 90%. This was shown by the loss of intensity in the NH stretch (3344 $cm^{-1}$) and particularly the NH in-plane bending regions (Amide II 1550 $cm^{-1}$) in IR spectra collected for me after the INS experiment (Fig. 4.5), over a wider range of energy transfer (400 $cm^{-1}$ - 4000 $cm^{-1}$), by Dr. S. F. Parker of Rutherford Appleton Lab. These spectra were used in the preparation of the publication [Middendorf *et al.*, submitted].

Dried samples of $(PPG)_{10}$ and $(PPG)_{10}$-d were prepared by freeze drying *in vacuo* for 72 hours over silica gel. After drying all samples were handled in dry nitrogen atmosphere over silica gel. $(PPG)_{10}$ dried *in vacuo* contains approximately one water molecule per ProlylProlylGlycine triplet [Sakakibara *et al.*, 1972]. X-ray diffraction studies of single crystals of $(PPG)_{10}$ have demonstrated

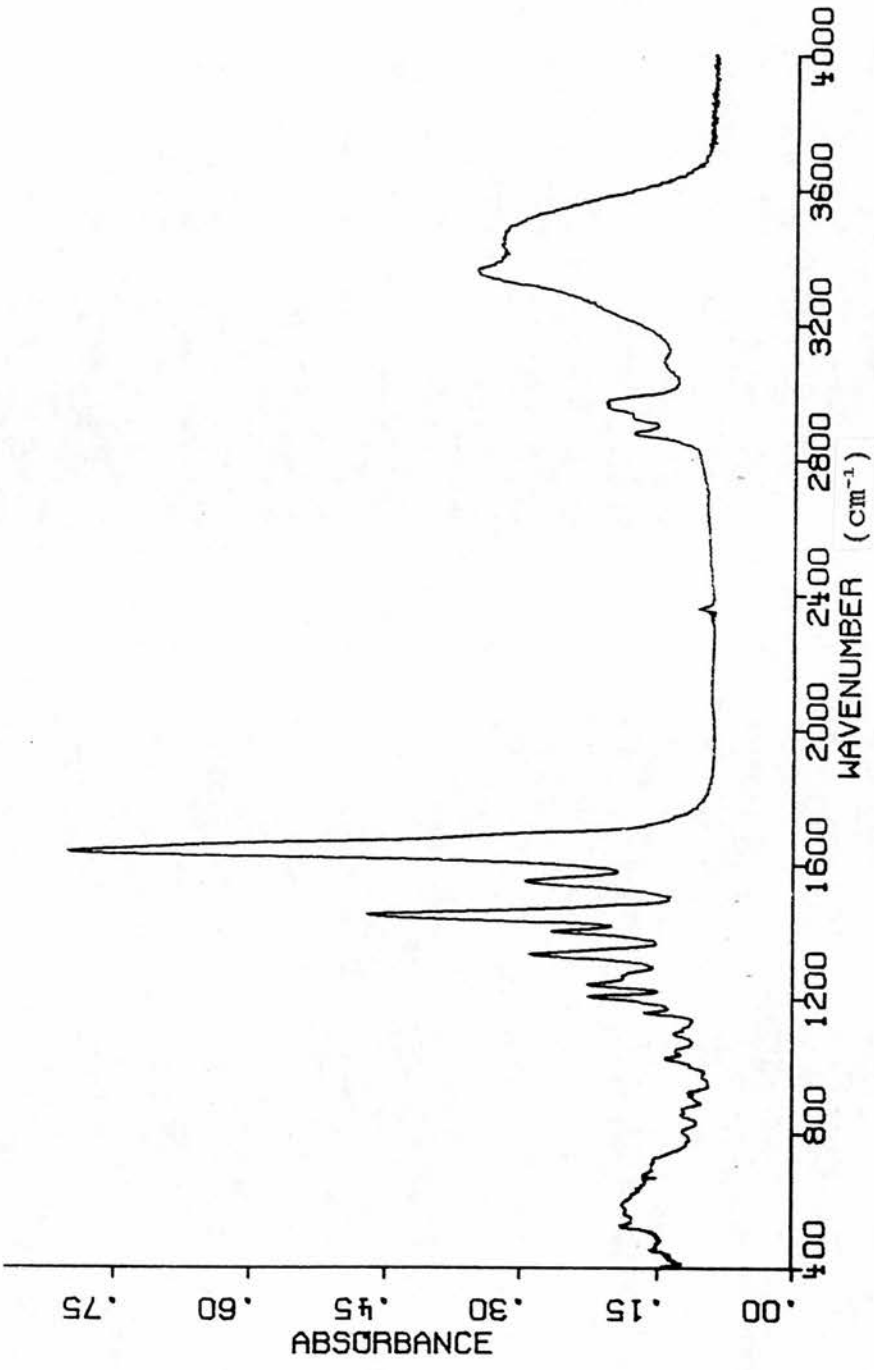


Figure 4.3. IR absorbtion spectrum for dry lyophilised powder of $(PPG)_{10}$ in KBr discs, collected after the first period of H/D exchange, with the help of Dr. C. Pulham, using a Nicolet 7000 series Fourier transform infrared spectrometer, Chemistry Department Edinburgh. Energy resolution 4 $cm^{-1}$. Powder sample was handled in dry nitrogen atmosphere until the final stages of preparation of KBr discs in die press and collection of IR spectra in atmosphere.

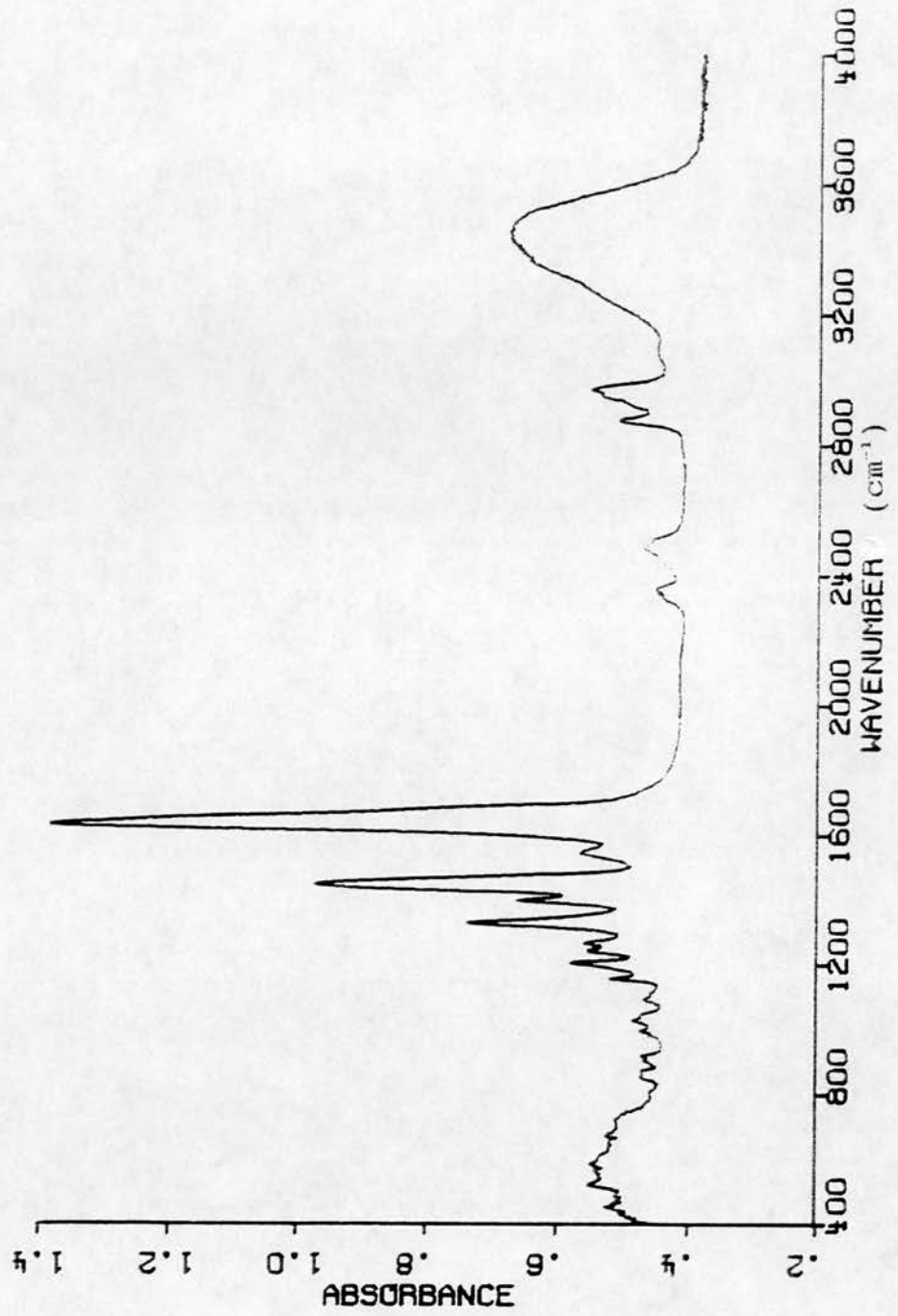


Figure 4.4. IR absorbtion spectrum for dry lyophilised powder of $(PPG)_{10}$-d in KBr discs, collected after the first period of H/D exchange, with the help of Dr. C. Pulham, using a Nicolet 7000 series Fourier transform infrared spectrometer, Chemistry Department Edinburgh. Energy resolution 4 $cm^{-1}$. Powder sample was handled in dry nitrogen atmosphere until the final stages of preparation of KBr discs in die press and collection of IR spectra in atmosphere.

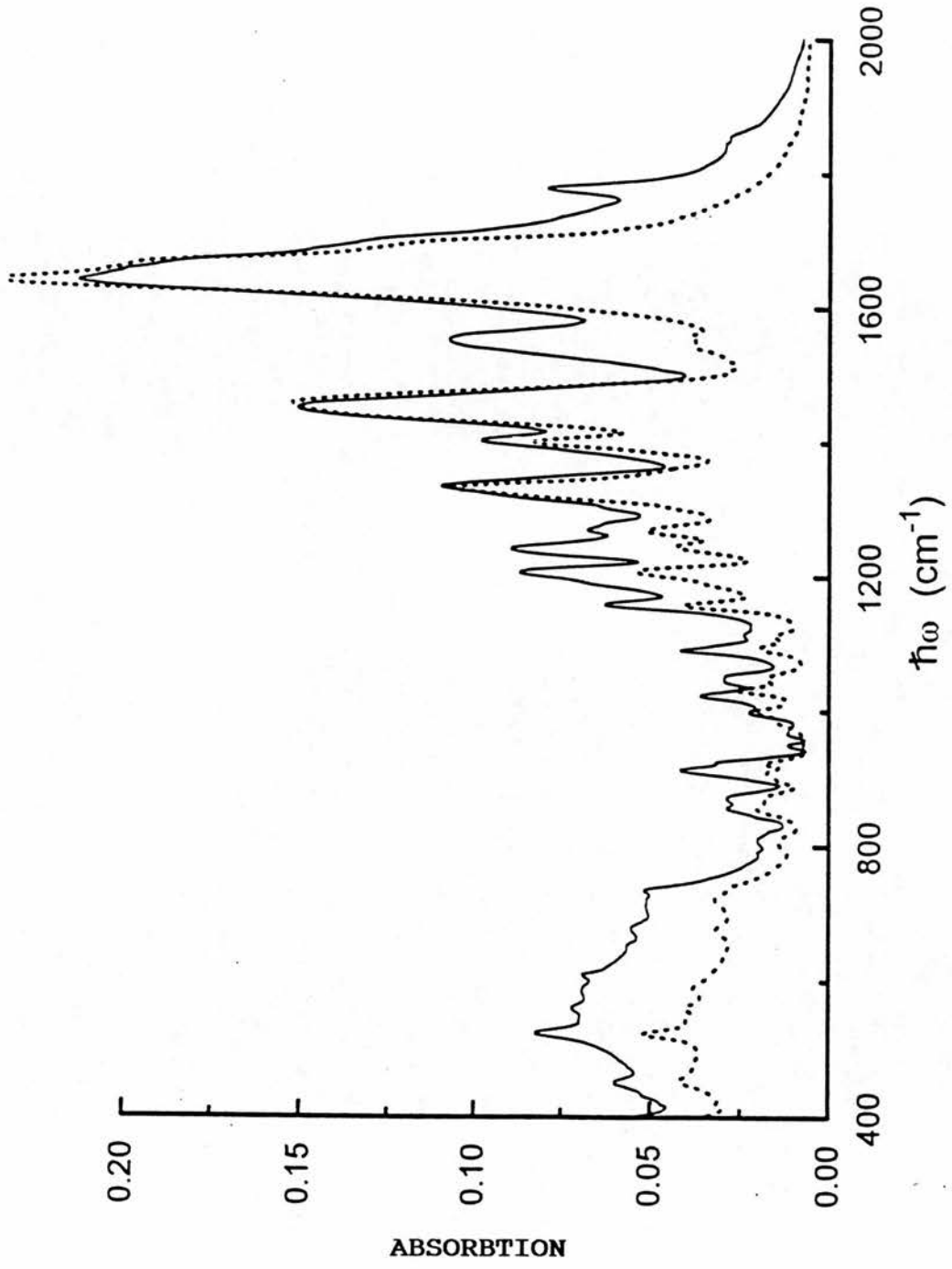


Figure 4.5. IR absorbtion spectra for dry lyophilised powders of $(PPG)_{10}$ and $(PPG)_{10}$-d in KBr discs, collected for me after the second period of H/D exchange and after the INS experiments, by Dr. S.F. Parker, Rutherford Appleton laboratory. Energy resolution 4 $cm^{-1}$.

three separate water bridge sites in an extended hydrogen-bonded network of water molecules [Okuyama *et al.*, 1981]. One water molecule forms the primary intra-chain hydrogen-bonded bridge between the glycine oxygen and the oxygen of the second proline in the same (ProProGly) triplet. Two further water molecules form a network from this first water molecule. The water content of single crystals of $(PPG)_{10}$ is approximately 46 % by weight [Okuyama *et al.*, 1981]. At lower hydration, near the stoichiometric ratio of one water molecule per tripeptide, I have assumed that the remaining most tightly bound water molecule was that molecule forming the primary intrachain water bridge, in agreement with the conclusions of Okuyama *et al.* In the $(PPG)_{10}$-d samples this water was exchanged for $D_2O$.

All the IR spectra for the lyophilised $(PPG)_{10}$ and $(PPG)_{10}$-d samples, both before and after the second period of H/D exchange, showed equal intensity in the -OH stretch region centred on 3400 $cm^{-1}$ (Fig. 4.3, 4.4 and 4.5), demonstrating the presence of $H_2O$ in the KBr discs during the IR experiments. As noted below, PPII IR spectra also demonstrated significant -OH stretch intensity (Fig. 4.10), indicating that the water was non-specifically absorbed in the KBr discs. The powders for the IR experiments were handled in dry nitrogen atmosphere until the final stages of preparation of KBr discs in a die press, and collection of IR spectra in atmosphere. This water was not intrinsic to the lyophilised $(PPG)_{10}$-d samples, since these were lyophilised from $D_2O$ solution, and this was confirmed because subsequent storage did not result in reversal of NH -> ND exchange (Fig. 4.5). Evidence for the presence of tight bound $D_2O$ after lyophilisation was provided by the OD stretch band at 2485 $cm^{-1}$ (see below). Together this suggested that the brief exposure to atmosphere during disc preparation and data aquisition was the origin of the absorbed $H_2O$. Guided by

this observation, the samples for INS experiments were strictly handled throughout in dry atmosphere, until sealed in the TFXA sample cans. The INS spectra of the lyophilised powders provided no evidence of an OH stretching band for $(PPG)_{10}$-d, though an OH stretch band at 3400 $cm^{-1}$ was evident for $(PPG)_{10}$ from the presence of tight bound $H_2O$ after lyophilisation (Fig. 4.21), as expected [Sakakibara, *et al.*, 1972].

The IR spectra confirmed this - the NH stretch band at 3344 $cm^{-1}$ in $(PPG)_{10}$ was at the value identified as typical of $(PPG)_{10}$ in the presence of tight bound water (Fig. 4.5). This NH stretch frequency shifts to 3355 $cm^{-1}$ when $(PPG)_{10}$ is completely dried [Brodsky-Doyle *et al.*, 1975]. For $(PPG)_{10}$-d samples the ND stretch band and the OD stretch band of the tight bound water contributed to a complex doublet in the room temperature IR spectrum at 2511 and 2485 $cm^{-1}$, with a shoulder at 2440 $cm^{-1}$ (Fig. 4.5). $D_2O$ closely associated with myoglobin at low hydration and room temperature has an OD stretch band at 2470 $cm^{-1}$ with a shoulder at 2415 $cm^{-1}$ suggesting that the 2485 $cm^{-1}$ maximum and the 2440 $cm^{-1}$ shoulder in $(PPG)_{10}$-d sample were due to tight bound $D_2O$ in water bridge sites [Doster *et al.*, 1986]. The IR spectra also demonstrated features characteristic of the triple helical state. The high NH stretch frequency (3344 $cm^{-1}$) in $(PPG)_{10}$, (Fig. 4.5), is typical of triple helical polypeptides, compared with maximal values of 3305 $cm^{-1}$ for NH stretch bands in non-triple helical peptides [Dwivedi and Krimm, 1982; Krimm and Bandekar, 1986]. Collagen itself has an NH stretch band at 3322-3329 $cm^{-1}$, which shifts down to 3300 $cm^{-1}$ on denaturation [Brodsky-Doyle *et al.*, 1975]. The ND stretch band can be expected to be up-shifted by a similar degree, from typical values of 2470 $cm^{-1}$ [Dwivedi and Krimm, 1982; Krimm and Bandekar, 1986]. Therefore the band at 2511 $cm^{-1}$ was identified with ND stretch in $(PPG)_{10}$-d samples (Fig.

4.5). Dr. S. F. Parker also collected $(PPG)_{10}$ Raman spectra for me, after the INS experiment, and these spectra demonstrated a triplet structure between 760 and 930 $cm^{-1}$, (Fig. 4.6), which is characteristic of the triple helical state for $(PPG)_{10}$ when compared with the tripeptide ProlylProlylGlycine [Diem *et al.*, 1984].

Powder X-ray diffraction experiments were performed to check the triple helical structure of the samples, using the freeze dried powders, handled in a dry nitrogen atmosphere over silica gel in a glove box, and sealed in 0.5 mm diameter capillary tubes. The capillary tube was mounted in the beam of the rotating copper anode x-ray generator GX-13 in the Biochemistry Department, Edinburgh University, and the powder x-ray pattern collected over a period of 24 hours on photographic film located 9.53 cm from the sample. The sample to film distance was calibrated by inclusion of powdered calcium carbonate mixed with one sample. The patterns for samples as supplied by the manufacturer, and for both isotopomers freeze dried from aqueous 1% acetic acid solution (in $D_2O$ or $H_2O$) were indistinguishable, showing the rings characteristic of the triple helical structure (Figs. 4.7 and 4.8). The observed spacings were 2.85, 3.94, 4.34, 5.41, 7.20, and 10.75 Å in agreement with the main features of an x-ray study of $PPG_{10}$ in the dry state and at 56 % hydration [Yonath and Traub, 1969]. In that study at both hydrations spacings of 2.85, 3.85, 4.4, 5.45, 7.21, and 10.85 Å were observed and indexed for triple helical molecules with a radius of approximately 12.5 Å close packed on a hexagonal lattice. Heating of the $(PPG)_{10}$ samples to 360 K in acetic acid solution resulted in an irreversible change in the diffraction pattern, indicating partial denaturation of the triple helical arrangement, though a background of the native pattern persisted.

The x-ray diffraction, IR and Raman results together

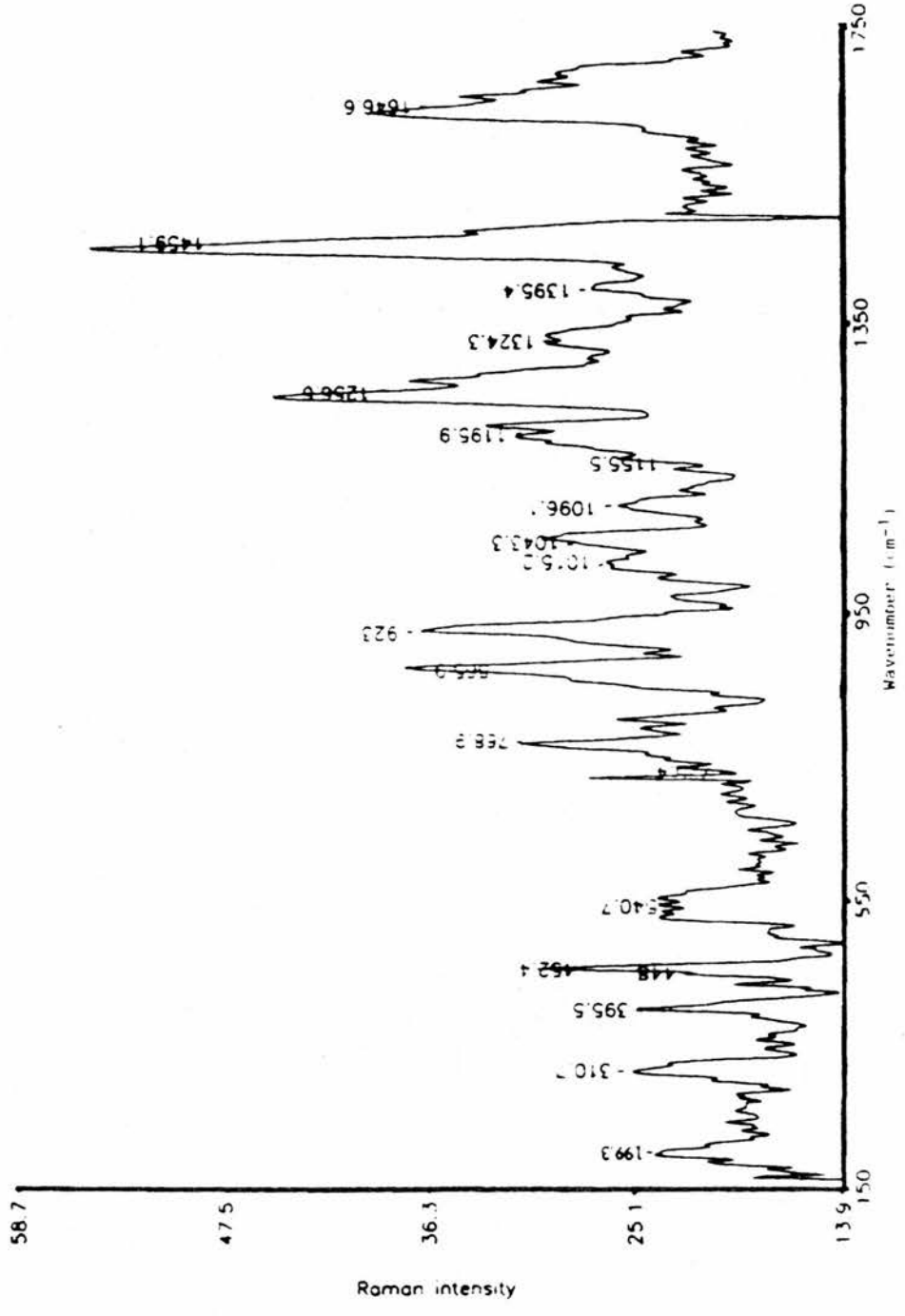


Figure 4.6. Raman spectrum for dry lyophilised powders of $(PPG)_{10}$, collected for me after the second period of H/D exchange and after the INS experiments, by Dr. S.F. Parker, Rutherford Appleton laboratory. The triplet structure between 760 and 930 $cm^{-1}$ is characteristic of the triple helical state of $(PPG)_{10}$.

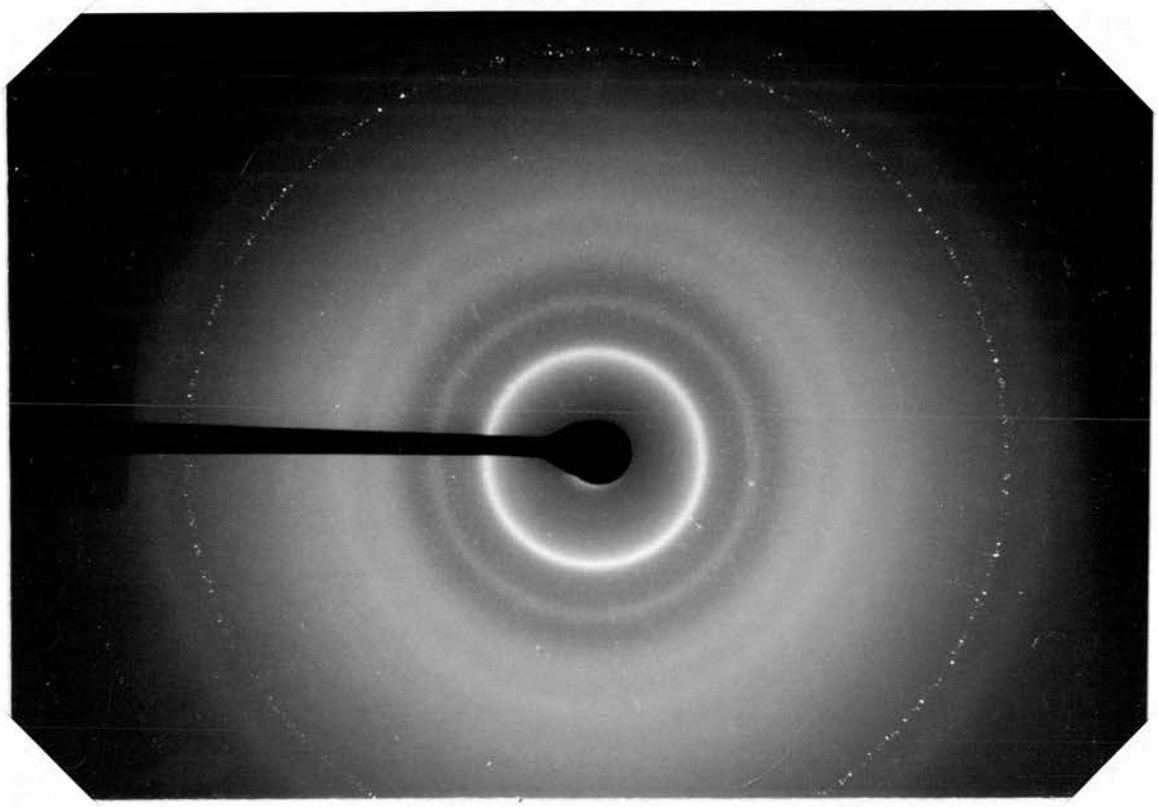

Figure 4.7. X-ray powder diffraction pattern collected on GX-13 x-ray generator for lyophilised $(PPG)_{10}$ powder as supplied by manufacturer, calibrated by inclusion of powdered calcium carbonate in the sample. The powder patterns for the $(PPG)_{10}$ and $(PPG)_{10}$-d samples used for INS experiments were unchanged (e.g. Fig. 4.8)

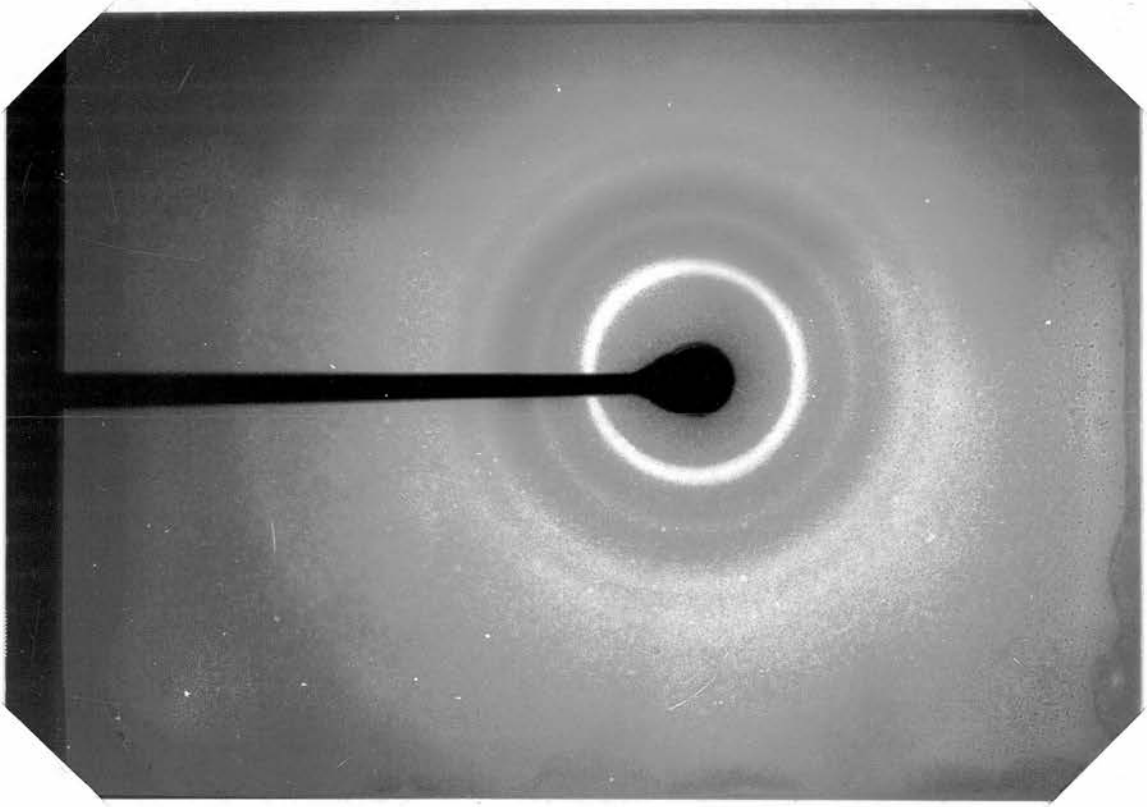

Figure 4.8. X-ray powder diffraction pattern collected on GX-13 x-ray generator for lyophilised $(PPG)_{10}$-d powder after H/D exchange by dissolution in 1% acetic acid in $D_2O$ for two weeks. Powder sample was handled in dry nitrogen atmosphere.

showed that the $(PPG)_{10}$ and $(PPG)_{10}$-d samples used for the INS experiments had the expected triple helical arrangement with one $H_2O$ or $D_2O$ molecule per tripeptide bound tightly in intra-chain water bridge sites.

**4.3.1.3. Polyproline II.**

Synthetic polyproline of mean molecular weight 6000 Daltons was purchased from Sigma Chemicals. The material had a broad range of molecular weights, between 1000 and 10000 Daltons, representing a range of polymerisations from 12 to 120 residues. Again, because of the cost and quantity of material required no attempt was made to obtain a narrower molecular weight distribution. Further INS experiments with high molecular weight fractions of PPII, which are available commercially also, might be performed in future to check the dependence of the INS spectrum on the degree of polymerisation, but time on the TFXA spectrometer for these experiments has not yet been obtained. The material as supplied was dialysed against pure water before lyophilisation [Sigma technical information], and is therefore expected in the type II left handed *trans* form [Sasisekharan, 1960; Traub and Shmueli, 1963]. Other investigators have found this material to be in the type II *trans* rather than the type I *cis* form, and with a wide range of molecular weights [Lin and Brandts, 1979]. As expected for type II, but not for type I [Sasisekharan, 1960], the material was readily soluble in water. X-ray powder diffraction gave a pattern consistent with that of the PPII form with the rings appearing at d-spacings of 5.76 (strong), 4.91 (strong), 4.35 (weak), 3.65 (moderate), 3.26 (weak and broad), 3.0 (weak and broad), 2.72 (weak and broad) Å (Fig. 4.9), in comparison with 5.76 (strong), 4.90 (strong), 3.65 (moderate), 3.35 (weak), 3.13 (weak), 2.88 (weak), 2.75 (weak), 2.71 (weak) Å for the rings shown in the powder

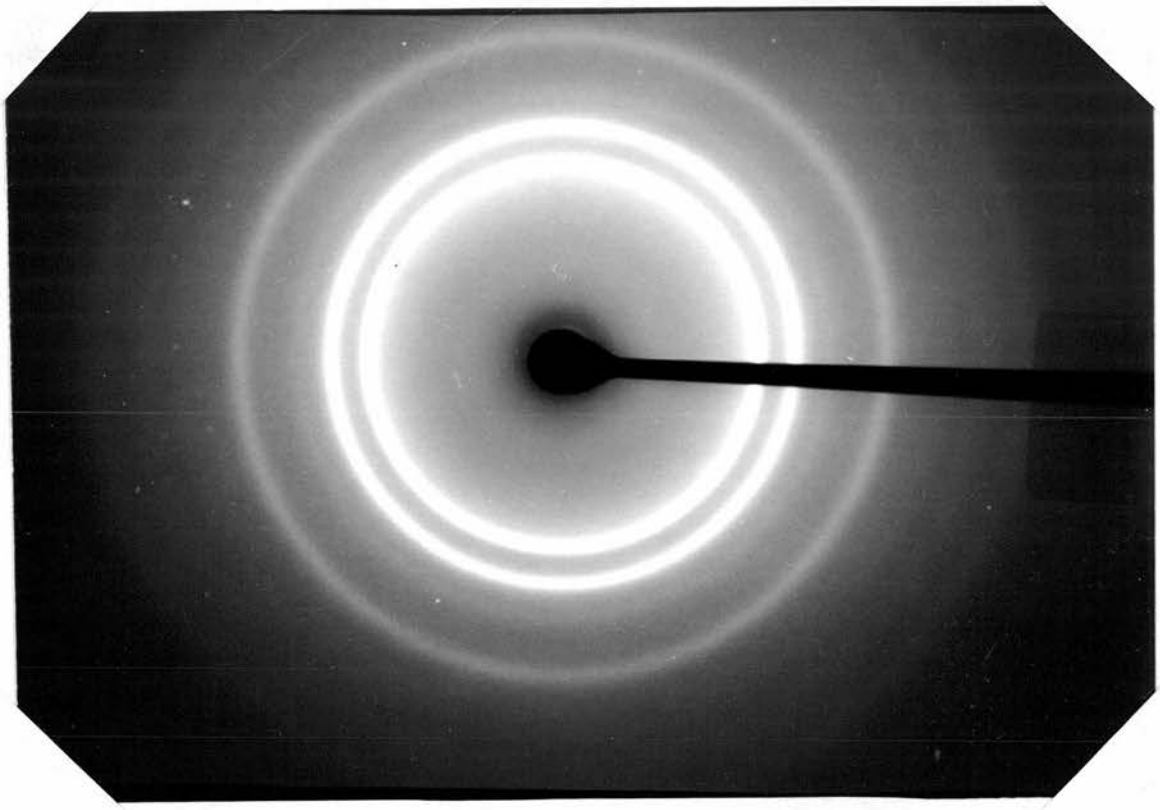

Figure 4.9. X-ray powder diffraction pattern collected on GX-13 x-ray generator for lyophilised PPII powder as supplied. Sample to film distance was 9.3 cm. The first strong ring is at d = 5.76 Å.

pattern of PPII [Sasisekharan, 1959], and 5.76, 4.90, 3.65, and 2.72 Å for the features in the partially oriented pattern for PPII [Cowan and McGavin, 1955]. The single additional weak feature at 4.35 Å observed here, which was not noted in the early diffraction experiments, was also present for high molecular weight fractions of PPII (molecular weight 10000-30000) and given its isolated appearance without other additional features is unlikely to be due to low molecular weight species in a different structural form. Although it is close to an observed d-spacing of 4.42 Å for PPI, the absence of all the other features of PPI, which gives up to 20 observable powder diffraction rings, including very strong features at d-spacings of 7.84, 4.96, moderate features at 4.42, 4.10, and 2.94 Å, and a weak feature at 3.90 Å [Sasisekheran, 1960; Traub and Shmueli, 1963], excludes its assignment to contaminating PPI. Furthermore, IR spectra confirmed the presence of the band at 675 $cm^{-1}$ characteristic of the left handed PPII form, and the absence of the bands at 1355 and 960 $cm^{-1}$ characteristic of the right handed helical polyproline I form [Isemura *et al.*, 1968], (Fig. 4.10). The IR spectra for the dry PPII samples in KBr discs reveal the infrared -OH stretching band at 3400 $cm^{-1}$, as in the $(PPG)_{10}$ samples, indicating the non-specific absorption of water by the KBr/powder peptide samples during production of the discs (Fig. 4.10).

**4.3.2. INS experiments and quality of spectra.**

Each collagen sample for the INS experiments consisted of three layers assembled from several hundred fibres, giving a final weight of about 1-2 grams protein. These and the powder samples (also 1-2 grams) of synthetic polypeptides were contained in aluminium foil sachets, and mounted in aluminium canisters in slab geometry on the TFXA spectrometer. The sample depth was 1 mm along the incident

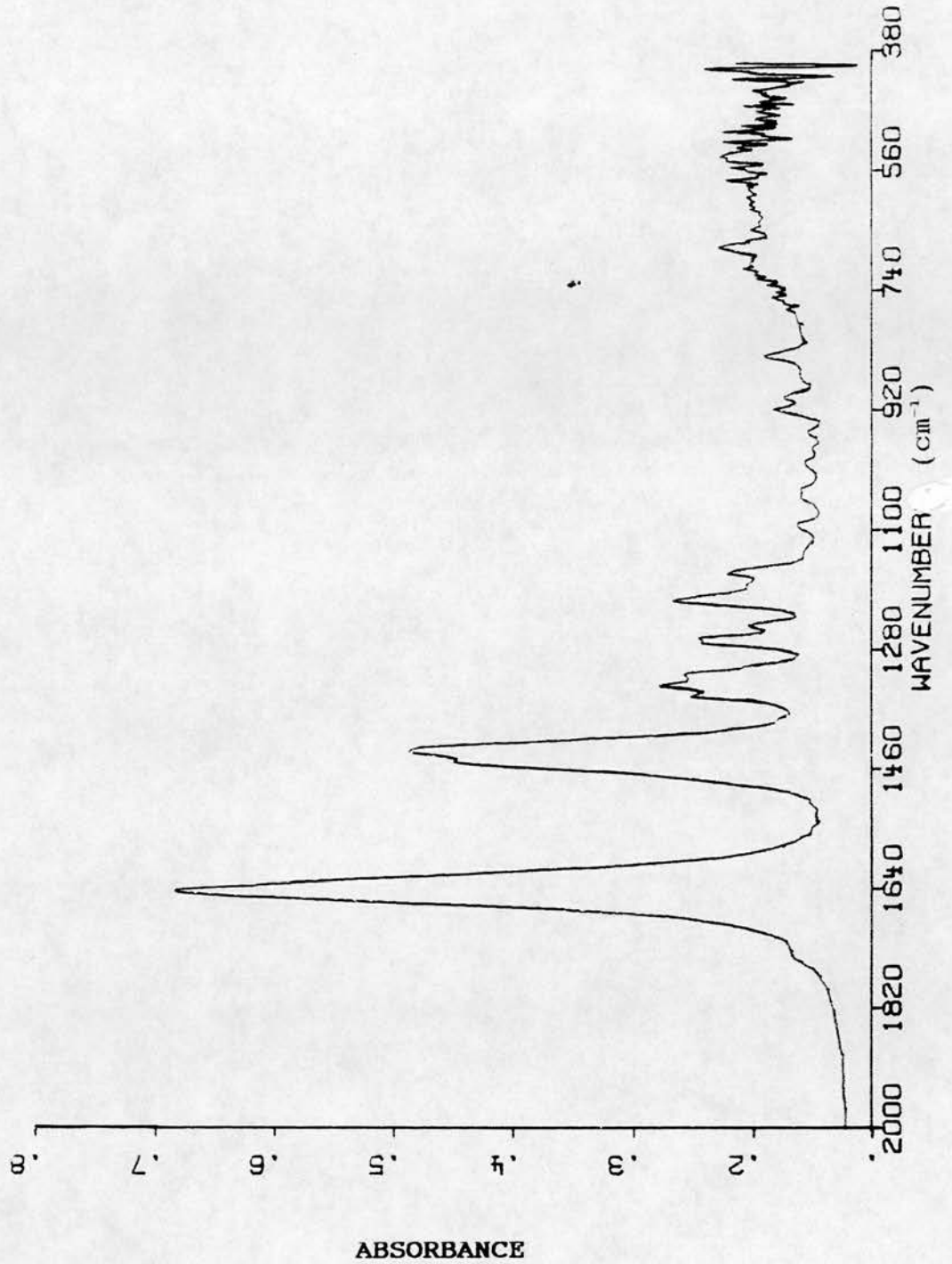


Figure 4.10. IR absorbtion spectrum for dry lyophilised powder of PPII in KBr discs, collected with the help of Dr. C. Pulham, using a Nicolet 7000 series Fourier transform infrared spectrometer, Chemistry Department Edinburgh. Energy resolution 4 $cm^{-1}$.

beam direction. All parts of the sample canister not immediately overlying the sample were covered with cadmium shielding to reduce background scattering. The background scattering from an empty aluminium canister shielded in this way, though structured, was less than 0.5% of total scattering for each of the samples, and was neglected in the analysis. Spectra were obtained at 30K for 'dry' collagen (6% hydration) (Fig. 4.11), 35K for 'hydrated' collagen (23% hydration) (Fig. 4.12), and 30K for the synthetic polypeptides (Fig. 4.13 - 4.15). The spectra shown in Figs. 4.11 - 4.15 have been smoothed by a 7 point Pascal smoothing function. The smoothing function eliminates marked variation from one energy bin to the next at low energy transfers, which is a consequence of the high density of experimental points at low energy transfer. The statistical counting errors are diplayed on the figures and the relatively large errors below 100 $cm^{-1}$ are evident. These arise because of the low number of counts per energy bin at low energy transfers, as a consequence of the high density of points on the energy axis [Chapter III]. Spectra were accumulated until the statistical counting error, proportional to the inverse of the square root of the number of counts, was small enough to allow unequivocal identification of the major spectral features and differences between samples. A typical exposure time to achieve the counting statistics evident in Figs. 4.11 - 4.15 for a single sample of 1-2 grams of a peptide was 12-16 hours. The turn around time for changing a sample and re-establishing a low stable temperature in the sample chamber was ~3 hours (greatly improved recently at RAL by introduction of a sample holder carrying four samples at once). During most allocations there was some loss of time due to intermittent problems with neutron production at RAL. A typical 2 day allocation of beamtime at RAL therefore

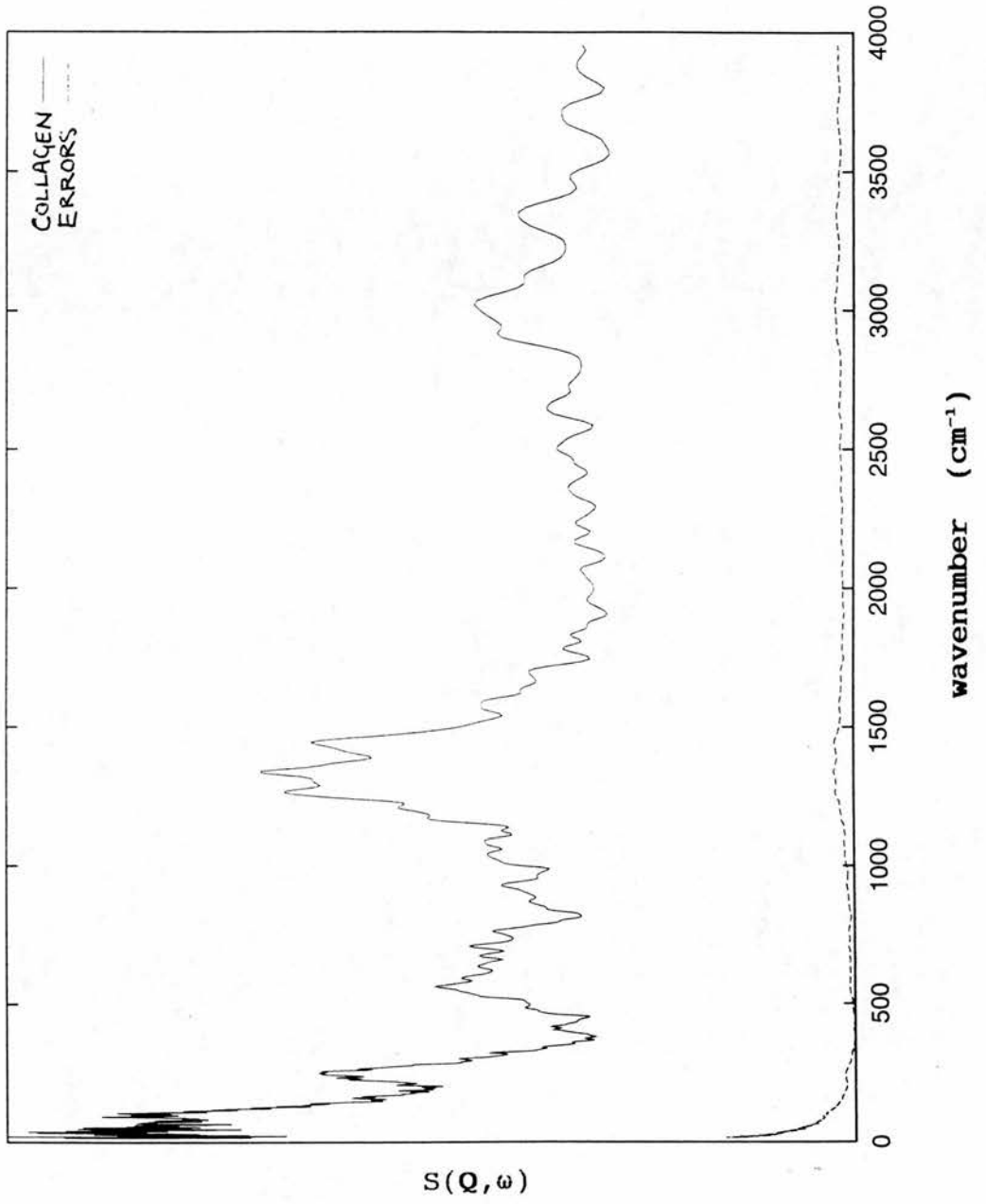


Figure 4.11. Inelastic neutron scattering spectrum for collagen at 6% hydration at 30 K, collected on the TFXA spectrometer, RAL. Seven point Pascal smoothing procedure applied. The statistical counting error, proportional to $(1/N)^{0.5}$ where N is the number of detected counts, is displayed on the figure.

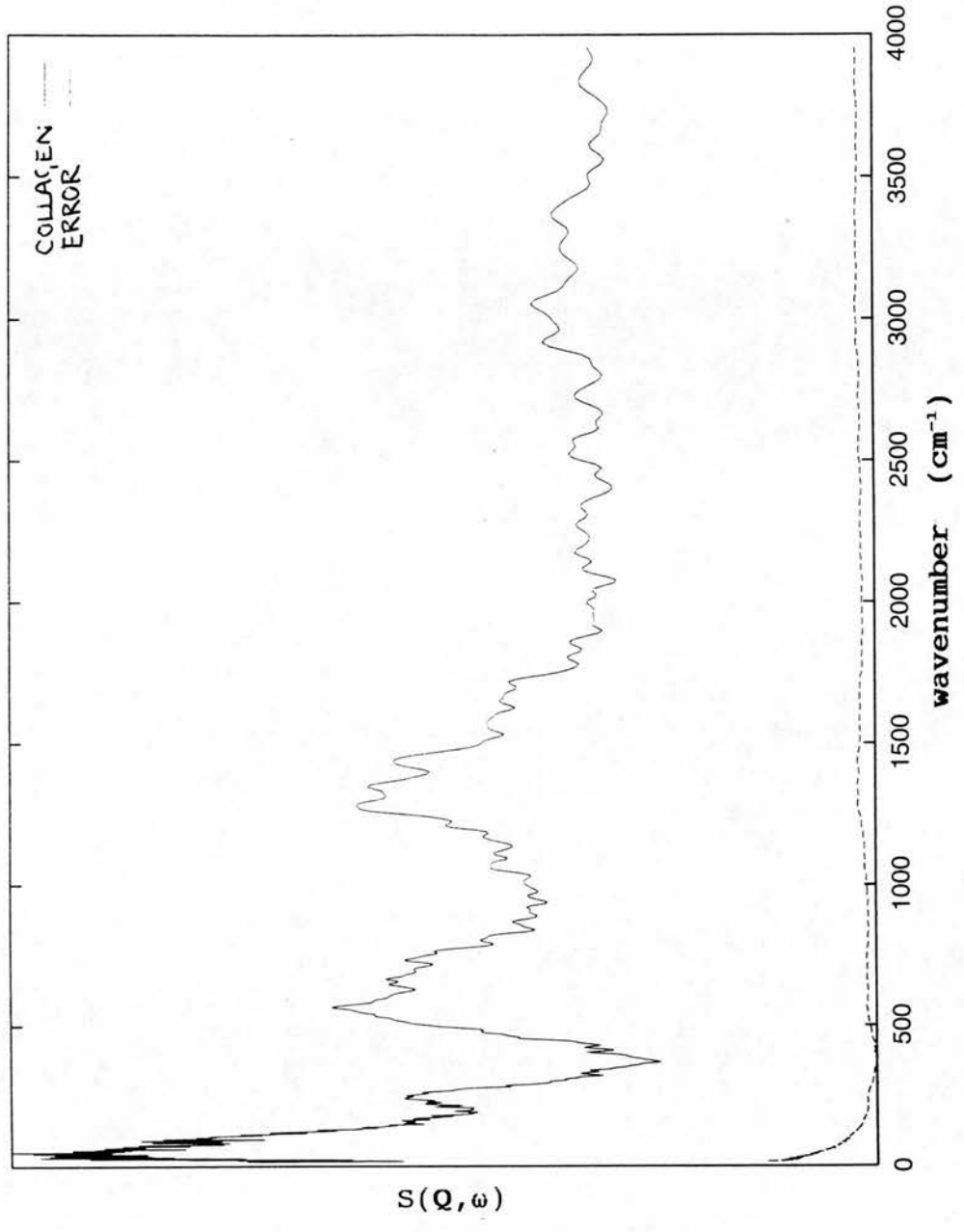


Figure 4.12. Inelastic neutron scattering spectrum for collagen at 23% hydration at 30 K, collected on the TFXA spectrometer, RAL. Seven point Pascal smoothing procedure applied. The statistical counting error, proportional to $(1/N)^{0.5}$ where N is the number of detected counts, is displayed on the figure.

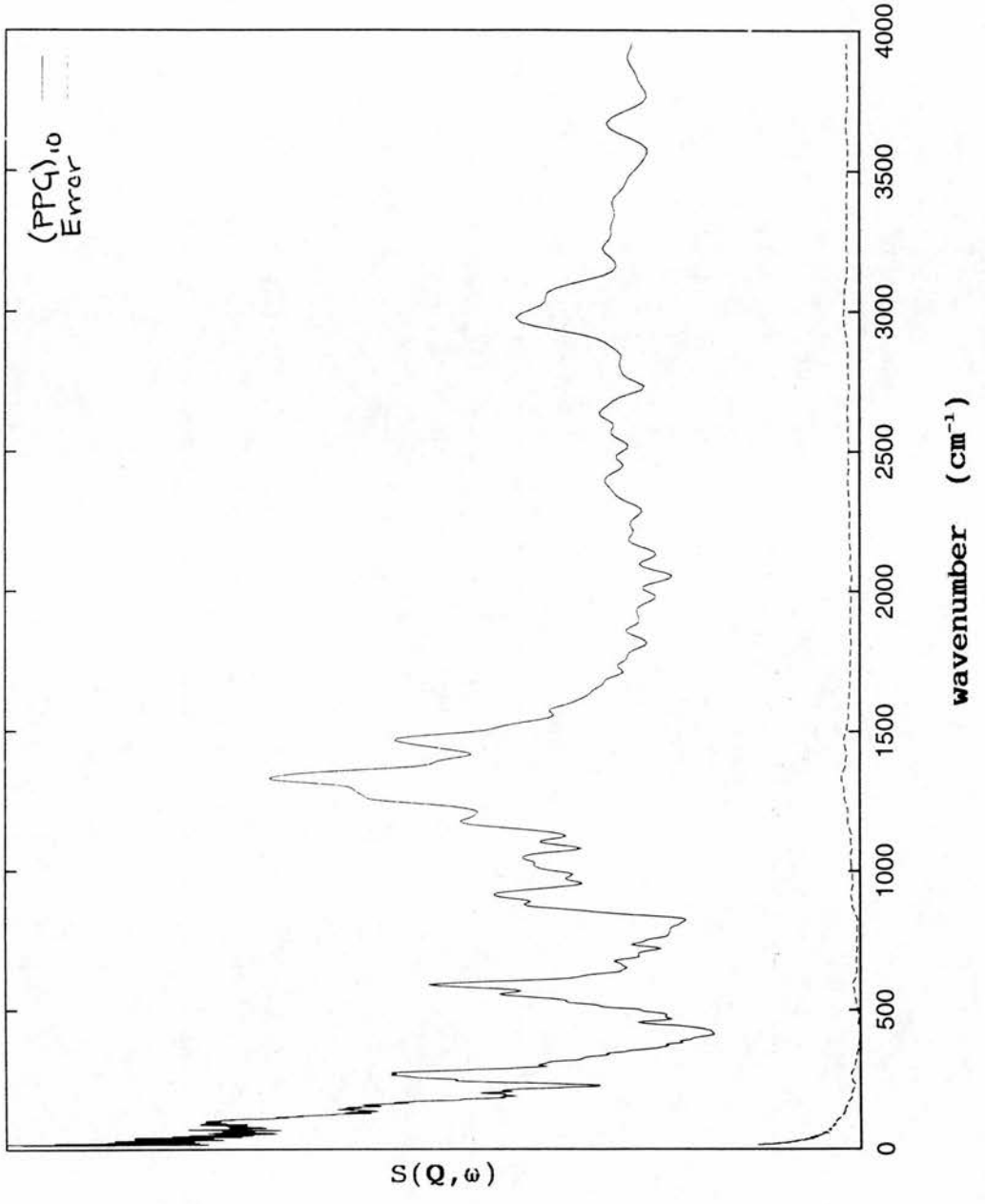


Figure 4.13. Inelastic neutron scattering spectrum for $(PPG)_{10}$ at 35 K, collected on the TFXA spectrometer, RAL. Seven point Pascal smoothing procedure applied. The statistical counting error, proportional to $(1/N)^{0.5}$ where N is the number of detected counts, is displayed on the figure.

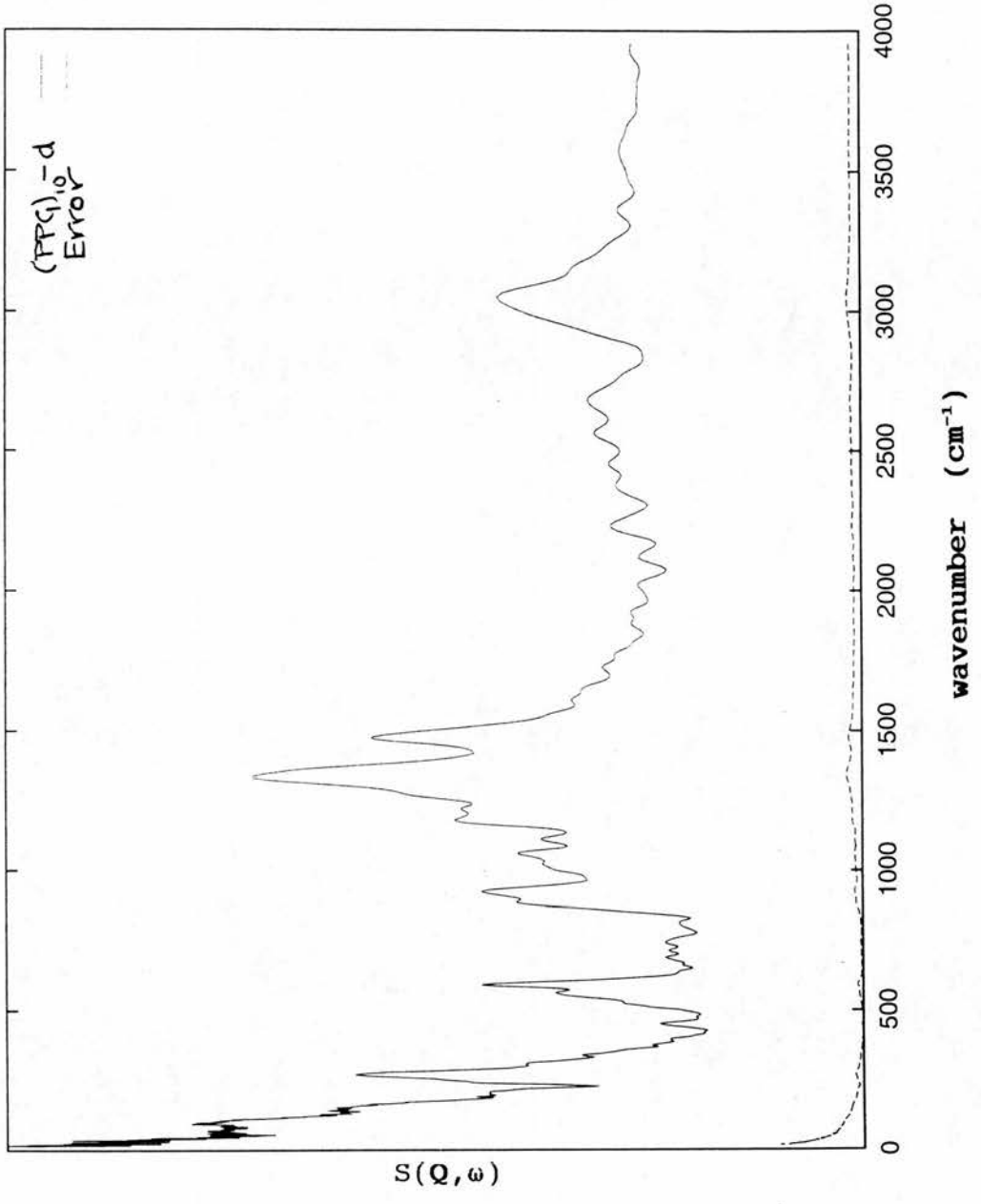


Figure 4.14. Inelastic neutron scattering spectrum for $(PPG)_{10}$-d at 35 K, collected on the TFXA spectrometer, RAL. Seven point Pascal smoothing procedure applied. The statistical counting error, proportional to $(1/N)^{0.5}$ where N is the number of detected counts, is displayed on the figure.

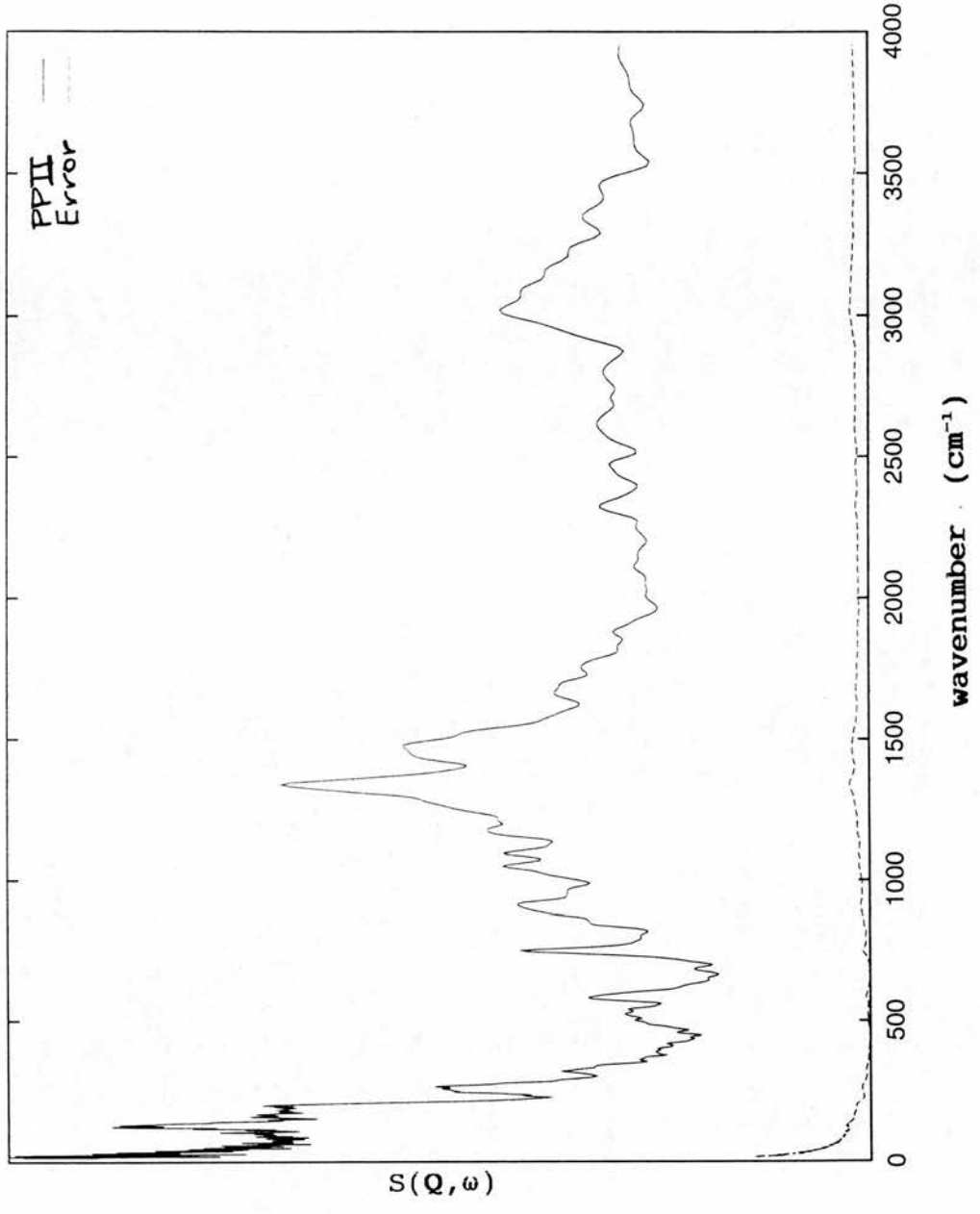


Figure 4.15. Inelastic neutron scattering spectrum for PPII at 35 K, collected on the TFXA spectrometer, RAL. Seven point Pascal smoothing procedure applied. The statistical counting error, proportional to $(1/N)^{0.5}$ where N is the number of detected counts, is displayed on the figure.

yielded two or three spectra of the quality described in this thesis. As the counting errors are proportional to the square root of the number of counts, a further improvement of statistics by a factor of only 1.44 requires a counting time twice as long, or more than one day. The main restriction on the statistical quality of the spectra, and the need to apply a smoothing procedure to the data, thus arose from a compromise, dictated by the limited beam time allocations available, between the collection of very few spectra with good counting statisitics, and the collection of spectra for several different samples with only adequate counting statistics. The TFXA spectrometer had an oversubscription rate of approximately five during the time of this thesis, partly as a consequence of the temporary closure of the Institut Laue Langevin, greatly reducing the availability of beam time. Further details of the TFXA spectrometer have been given in Chapter III.

Fig. 4.16 compares the spectra for dry and hydrated collagen, Fig. 4.17 for $(PPG)_{10}$ and $(PPG)_{10}$-d, Fig. 4.18 for dry collagen and $(PPG)_{10}$, and Fig. 4.19 for $(PPG)_{10}$ and PPII. The spectra in Fig. 4.16 - 4.19 have been corrected for the effect of temperature through the Bose-Einstein factor, $[\exp\{\hbar\omega/kT\}-1]^{-1}$ (Section 4.4.2 below), and smoothed by the seven point Pascal method.

## 4.4. INS RESULTS FOR COLLAGEN, $(PPG)_{10}$ AND PPII, AND ANALYSIS BY MIXED HARMONIC MODEL.

### 4.4.1. Overall properties of neutron spectra and relevant development of the basic neutron scattering theory.

Interpretation of the collagen and model polypeptide INS spectra reported in this chapter was based on the well-established theory of neutron scattering from polymers and molecular crystals [Lovesey, 1984; Windsor, 1981]. In this Section I discuss the theoretical framework used for the

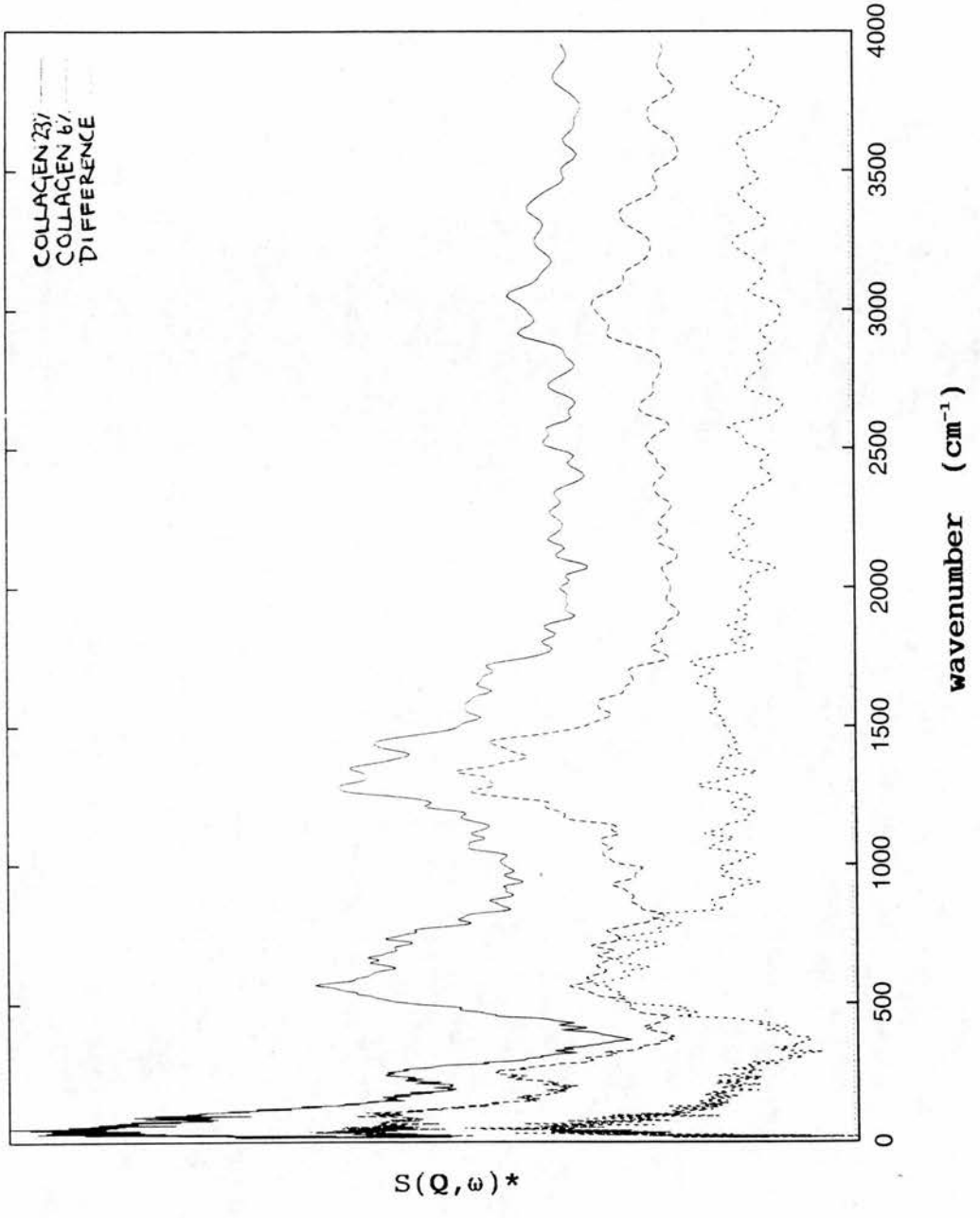


Figure 4.16. Inelastic neutron scattering spectra corrected for Bose Einstein thermal factor, for collagen at 6% hydration, and collagen at 23% hydration collected on the TFXA spectrometer, RAL. Seven point Pascal smoothing procedure applied. Difference spectrum (Collagen 23% - collagen 6%) due to water of hydration.

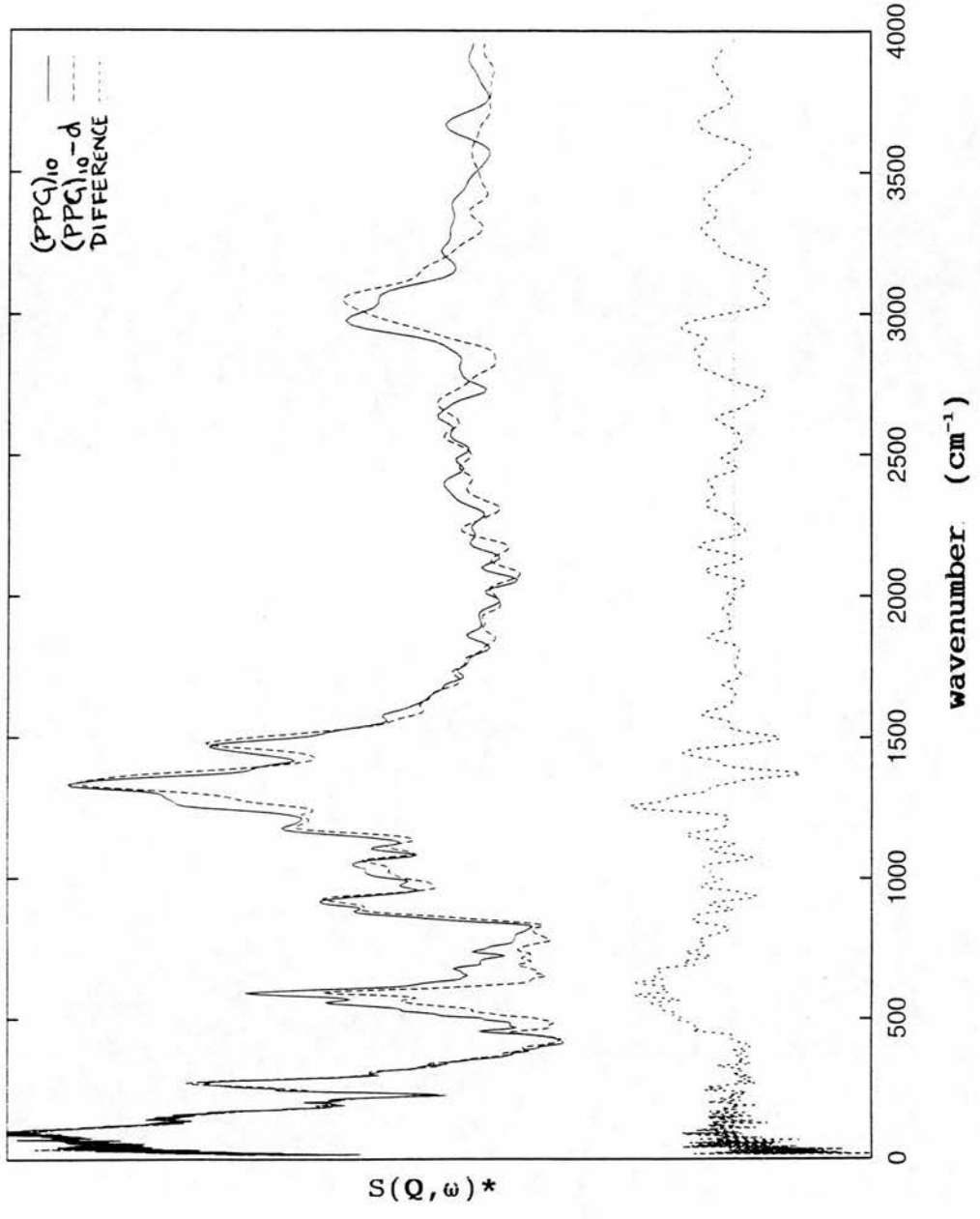


Figure 4.17. Inelastic neutron scattering spectra corrected for Bose Einstein thermal factor, for $(PPG)_{10}$, and $(PPG)_{10}$-d collected on the TFXA spectrometer, RAL. Seven point Pascal smoothing procedure applied. Difference [$(PPG)_{10}$ - $(PPG)_{10}$-d] attributed to deuteration of the amide hydrogen and the tight bound water.

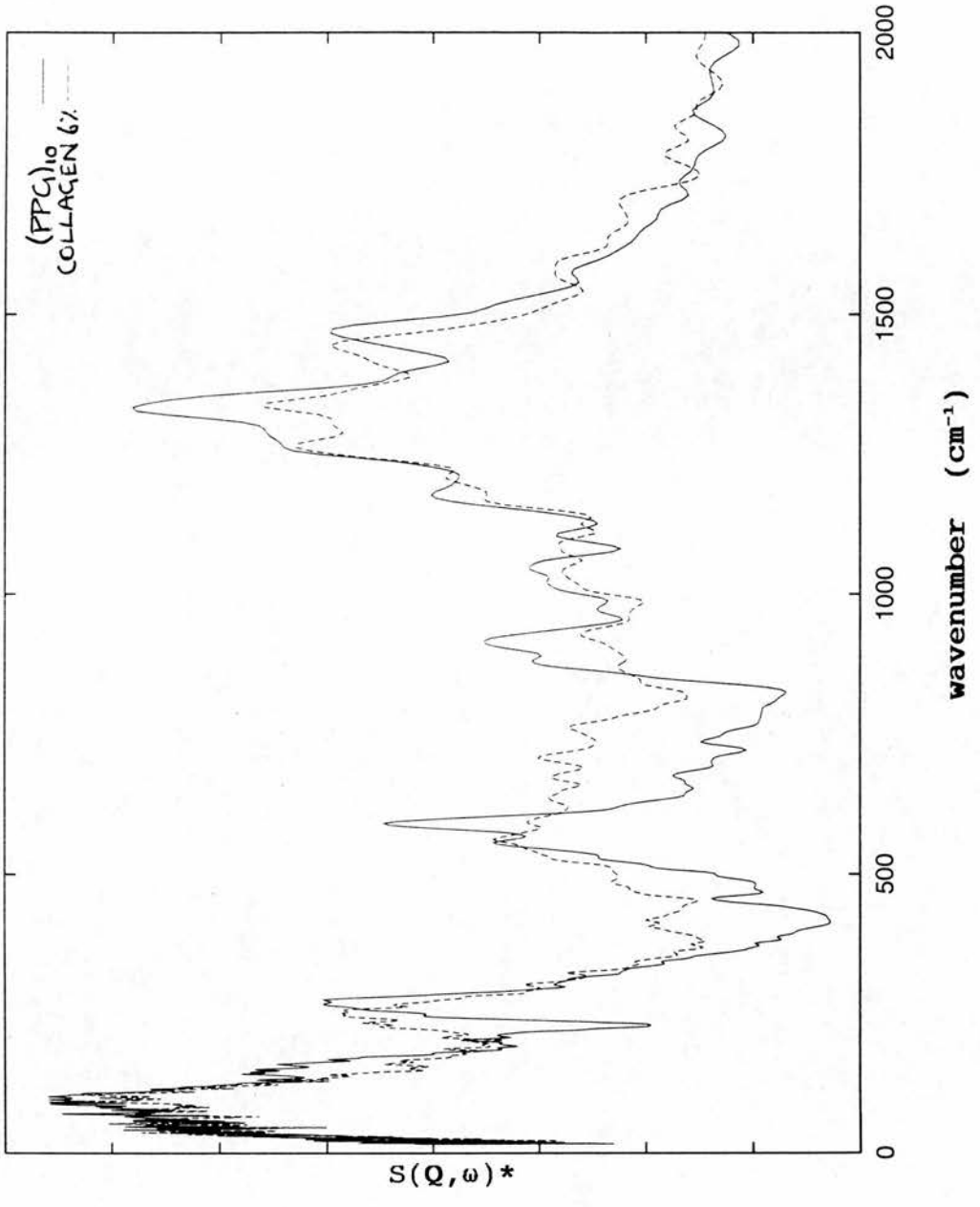


Figure 4.18. Inelastic neutron scattering spectra corrected for Bose Einstein thermal factor, for collagen at 6% hydration, and $(PPG)_{10}$ collected on the TFXA spectrometer, RAL. Seven point Pascal smoothing procedure applied.

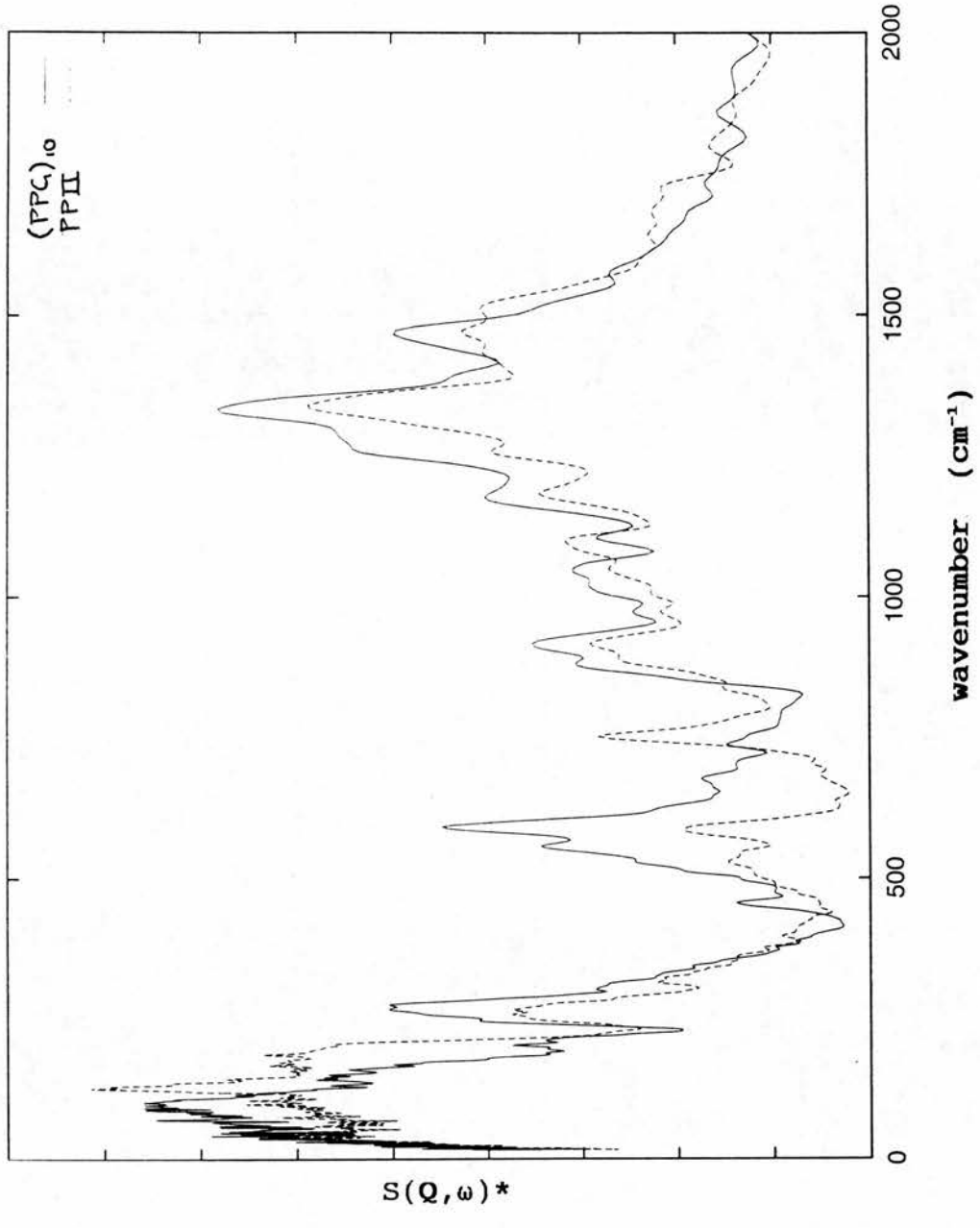


Figure 4.19. Inelastic neutron scattering spectra corrected for Bose Einstein thermal factor, for $(PPG)_{10}$, and PPII collected on the TFXA spectrometer, RAL. Seven point Pascal smoothing procedure applied.

analysis in terms of two basic processes: scattering from low-frequency collective phonons and from localized high-frequency oscillators. This approach arises from a simplified mixed harmonic model of the dynamics of the polypeptides. The polypeptide is considered as a chain of heavy elements (identified with extended atom groups - Section 4.4.2 below), undergoing low-frequency dispersive harmonic dynamics. To each heavy element are attached light atoms, protons, undergoing independent high-frequency harmonic oscillations in a coordinate frame attached to the heavy elements. Spectral details and assignments to particular modes will be examined in subsequent sections.

The dynamic structure factors $S_{inc/coh}(\mathbf{Q},\omega)$ and the nuclear trajectories are directly related through $t \rightarrow \omega$ Fourier transforms of $\mathbf{Q}$-dependent time correlation functions, the so-called 'intermediate' scattering functions [Lovesey 1984; Windsor, 1981; Chapeter II]. These are given by

$$F_{coh}(\mathbf{Q},t) \qquad (4.4.1)$$

$$= \int S_{coh}(\mathbf{Q},\omega) \exp\{i\omega t\}\, d\omega$$

$$= \sum_{i,j} \langle \exp(-i\mathbf{Q}\cdot\mathbf{R}_i(0)) \exp(i\mathbf{Q}\cdot\mathbf{R}_j(t)) \rangle_{thermal}$$

together with a similar function $F_{inc}(\mathbf{Q},t)$ for which only the diagonal terms i=j are summed:

$$F_{inc}(\mathbf{Q},t) \qquad (4.4.2)$$

$$= \int S_{inc}(\mathbf{Q},\omega) \exp\{i\omega t\}\, d\omega$$

$$= \sum_{i} \langle \exp(-i\mathbf{Q}\cdot\mathbf{R}_i(0)) \exp(i\mathbf{Q}\cdot\mathbf{R}_i(t)) \rangle_{thermal}$$

The limits of the integration are +/- $\infty$. The brackets <..>

refer to a thermal average over the unperturbed states of the sample. Eq. 4.2.1 relates to coherent scattering since it covers all pair correlations including the 'self' terms i=j; for $F_{inc}(\mathbf{Q},t)$ in Eq. 4.2.2 the single-particle correlations described by i=j are sufficient. A further Fourier transformation, with respect to the conjugate variables $\mathbf{Q} \leftrightarrow \mathbf{r}$ instead of $\omega \leftrightarrow t$, leads from $F_{inc}(\mathbf{Q},t)$ and $F_{coh}(\mathbf{Q},t)$ to the van Hove space-time correlation functions $G_s(\mathbf{r},t)$ and $G(\mathbf{r},t)$, respectively [Lovesey, 1984; Windsor, 1981; van Hove, 1954; Chapter II].

For a hierarchically organised macromolecular structure, a useful approximation is to split $\mathbf{R}_i(t)$, the position operator for atom i, into components due to restricted diffusive motions, low-frequency dispersive phonon modes (including acoustic modes), and localized (nondispersive) high-frequency oscillators. For the temperatures of interest in the present context, and at frequencies $>10^{12}$ Hz or 33 $cm^{-1}$, the spectral contribution from restricted diffusive motions is zero or negligibly small. Diffusion is neglected hereafter, so that the instantaneous position of each atom i can be written as the sum of a time independent equilibrium position $\mathbf{R}_i^\circ$ and a time dependent deviation from equilibrium, $\delta\mathbf{R}_i(t)$:

$$\mathbf{R}_i(t) = \mathbf{R}_i^\circ + \delta\mathbf{R}_i(t) \qquad (4.4.3)$$

$$\delta\mathbf{R}_i(t) = \mathbf{u}_i(t) + \mathbf{v}_i(t)$$

$$\langle(\delta\mathbf{R}_i(t))^2\rangle = \langle\mathbf{u}_i^2\rangle + \langle\mathbf{v}_i^2\rangle$$

$\mathbf{u}_i(t)$ is the time dependent operator giving the displacement from equilibrium for the atom i due to phonons, $\mathbf{v}_i(t)$ is the time dependent operator giving the displacement from equilibrium for atom i due to localised oscillators. These two operators are assumed to commute, which is equivalent to assuming that the high-frequency localised oscillators are independent of the phonon modes. This independence allows a factorization of the

intermediate scattering function [Warner *et al.*, 1983].

For dominant incoherent scattering from the protons only $F_{inc}(\mathbf{Q},t)$ need be considered:

$$F_{inc}(\mathbf{Q},t) \qquad (4.4.4)$$

$$= \sum_i \langle \exp(-i\mathbf{Q}.\mathbf{u}_i(0)) \exp(i\mathbf{Q}.\mathbf{u}_i(t)) \rangle$$

$$\times \langle \exp(-i\mathbf{Q}.\mathbf{v}_i(0)) \exp(i\mathbf{Q}.\mathbf{v}_i(t)) \rangle$$

where the sum runs over atoms labelled i.

At low temperature where the harmonic approximation to the dynamics is useful, the factorisation of $F(\mathbf{Q},t)$ allows $S(\mathbf{Q},\omega)$ to be written in terms of a phonon expansion for the low-frequency phonon modes of a chain of heavy beads, and a set of independent high-frequency oscillators for the light particles bound harmonically to the heavy beads [Warner *et al.*, 1983] (Eq. 4.4.5). This is the mixed harmonic model discussed above. Then for n quanta exchanged with a high-frequency oscillator of frequency $\omega_o$, with $\hbar\omega \gg kT$, we have the expression [Warner *et al.*, 1983], dropping the subscript 'inc':

$$S_n(\mathbf{Q},\omega) \qquad (4.4.5)$$

$$= \sum_i S_L^i(\mathbf{Q},\omega-n\omega_o) \exp\{-2W_o^i(\mathbf{Q})\}$$

$$\times (\hbar | \mathbf{Q}.\mathbf{e}_o^i |^2/2m_i\omega_o)^n$$

Here n is the number of quanta exchanged with the high frequency oscillator. $S_L^i(\mathbf{Q},\omega-n\omega_o)$ is the dynamic structure factor for atom i due to lattice phonon modes:

$$S_L^i(\mathbf{Q},\omega) \qquad (4.4.6)$$

$$= \exp\{-2W_L^i(\mathbf{Q})\} \prod_\lambda \Big[ \sum_n \exp\{-n_\lambda\hbar\omega_\lambda/2kT\}$$

$$\times I_n (\hbar | \mathbf{Q}.\mathbf{e}_\lambda^i |^2/2M_i\omega_\lambda \sinh\{\hbar\omega_\lambda/2kT\}) \Big] \delta(\omega - \sum_\lambda n_\lambda\omega)$$

In these expressions i labels atoms with masses $M_i$ and eigenvector $e_{\lambda/o}^{i}$ in the phonon mode $\lambda$, or the high-frequency oscillator o, respectively. $I_n$ (x) is the $n_\lambda^{th}$ order modified Bessel function with argument x, and $n_\lambda$ the number of quanta exchanged with mode $\lambda$ whose fundamental frequency is $\omega_\lambda$. In Eqs. 4.4.5 and 4.4.6, $W_{L/o}^{i}(Q)$ are Debye Waller factors for atoms labelled i due to phonon modes (L) and high-frequency oscillators (o), respectively.

$$W_{L/o}^{i}(Q) \qquad (4.4.7)$$

$$= \sum \cosh\{\hbar\omega_{\lambda/o}/2kT\}\ \hbar\ |\ Q.e_{\lambda/o}^{i}\ |^2/2M_i\omega_{\lambda/o}$$

At low kT, the zero-phonon and one-phonon terms are sufficient to describe the scattering response and the intermediate scattering function corresponding to one-phonon terms can be formulated in terms of the frequency distribution $Z(\omega)$ of phonon modes. Thus:

$$F_L^{i}(Q,t) \qquad (4.4.8)$$

$$= \exp\{-2W_L^{i}(Q)\}$$

$$\times \int (b_i^2\ |\ Q.e_{i\zeta}\ |^2/\omega M_i)\ \coth\{\hbar\omega/2kT\}\ Z(\omega)\ e^{-i\omega t}\ d\omega$$

$Z(\omega) = \sum_\lambda \delta(\omega - \omega_\lambda)$, where the sum runs over phonons labelled $\lambda$. The limits of the integral are +/- $\infty$.

In practice I chose to consider a separation of the spectra at the intensity minimum evident between 360 and 400 $cm^{-1}$ (Figs. 4.11 - 4.15). This choice was indicated by the general results of normal mode analyses of peptide-bond model molecules [Fillaux *et al.*, 1993; Hayward *et al.*, in press; Chapter V] and polypeptides [Krimm and Bandekar, 1986; Noguti and Go, 1982], as well as molecular dynamics simulations [Levy *et al.*, 1985; Karplus and

Petsko, 1990]. These suggest that at frequencies below 400 $cm^{-1}$ the extended atom approximation may be a useful simplification. This approximation reduces the number of degrees of freedom by grouping the light hydrogen atoms together with the heavy groups to which they are attached, and assigning an appropriate mass to the group. At frequencies below 400 $cm^{-1}$ peptide backbone torsions and deformations result in relative motion of extended atom groups (e.g CH, $CH_2$, NH, O), and these modes are of a collective nature. At higher frequencies modes involve stretches or bends of individual X-H bonds where X is a heavy atom. Examples of these high-frequency oscillators, discussed below, are the Amide modes II to V lying between 500 and 1550 $cm^{-1}$, the in-plane and out-of-plane bending modes of aromatic ring hydrogens between 600 and 1600 $cm^{-1}$, and the methylene and methyl deformation modes between 950 and 1450 $cm^{-1}$. At low temperatures where harmonic dynamics are expected the extended atom approximation becomes equivalent to the mixed harmonic model.

**4.4.2. Extraction of density of states and estimate of an average effective mass for the heavy elements of the mixed harmonic model.**

One of the basic dynamical quantities characterising a vibrating chain molecule is $Z(\omega)$, the distribution of vibrational frequencies known as the density of states. Eqs. 4.4.5 and 4.4.6 show that one phonon processes dominate the incoherent inelastic scattering spectrum at low temperature and low **Q** (and hence low energy transfer on TFXA), and Eq. 4.4.8 demonstrates the formulation of $F(\mathbf{Q},t)$ in terms of the density of phonon vibrational states under these conditions. $S(\mathbf{Q},\omega)$ can also be expressed in terms of the hydrogen weighted phonon density of states, $G(\omega)$, when one phonon processes dominate [Smith, 1991].

$$G(\omega) = \Sigma\, b_i^2\, |e_{i\lambda}|^2/M_i\, \delta(\omega - \omega_\lambda) \qquad (4.4.9)$$

The summation runs over the index i labelling atoms, and the index $\lambda$ labelling phonons. $b_i$ is the incoherent scattering length for atom i. $e_{i\lambda}$ is the eigenvector for atom i in mode $\lambda$, and $M_i$ is the mass of atom i. $\omega_\lambda$ is the frequency of phonon $\lambda$. $G(\omega)$ is dominated by the contribution from hydrogen because of the large scattering length $b_i$ for hydrogen relative to other atoms. The summation over i can therefore be restricted to the hydrogen atoms, the contribution from heavy atoms being neglected. $G(\omega)$ is thus approximately equal to $Z(\omega)$ weighted by the atomic eigenvectors, masses and scattering cross sections for the hydrogen atoms participating in each mode. Since the intensity observed at each frequency contains contributions from all phonon modes of that frequency, and since many hydrogen atoms are involved in each low-frequency phonon mode, the further approximation is made in the low-frequency region of a uniform average weighting of $G(\omega)$ by these terms. Normalisation of $G(\omega)$ then yields an approximation to $Z(\omega)$.

Following earlier authors [Smith, 1991; Lovesey, 1984; Warner, 1983; Cusack and Doster, 1990] from Eq. 4.4.8:

$$S_L(\mathbf{Q},\omega) = \exp[-2W_L(\mathbf{Q})]\ [q^2/2\omega]\ G(\omega)\ [n_{BE}(\omega)+1] \qquad (4.4.10)$$

Here the exponential term is the Debye-Waller factor characterising the atomic mean square displacement along **Q**. Consistent with the use of an average weighting for the atomic polarisation vectors, this Debye-Waller factor also represents an average over the hydrogen atoms of the sample. The factor $n_{BE}(\omega)$ is the Bose-Einstein thermal population factor, $[\exp\{\hbar\omega/kT\}-1]^{-1}$.

To extract the frequency distributions from the measured spectra at low energy transfer, it was thus necessary to

correct for the effect of the Debye-Waller factor and the factor $Q^2/\omega$ as well as the thermal population factor, and then normalise the resulting $G(\omega)$. Given the relation between **Q** and $\omega$ imposed by the conservation equations and the scattering parameters of TFXA, the factor $Q^2/\omega$ in Eq. 4.4.10 was easy to evaluate. The exponent of the Debye Waller factor is:

$$2W(\mathbf{Q}) = Q^2\langle u^2\rangle \qquad (4.4.11)$$

and the average atomic mean square displacement $\langle u^2\rangle$ for the hydrogen atoms of the sample was therefore needed. Dr. H. D. Middendorf has determined this quantity and its temperature dependence from a series of high-resolution quasi-elastic spectra (FWHM=15 $\mu$eV) for collagen, using the backscattering spectrometer IRIS at ISIS [Middendorf, personal communication]. The $\langle u^2\rangle$ displacements measured for collagen should be close to the corresponding values for PPII and $(PPG)_{10}$ samples. From these quasi-elastic experiments $\langle u^2\rangle$ was 0.021 Å$^2$ at 70 K, and 0.026 Å$^2$ at 120 K [Middendorf, personal communication]. Extrapolation yielded an estimate for the average hydrogen mean square displacement at 30 K of 0.018 +/- 0.005 Å$^2$. (Quantum ground state vibrations ensure that the mean square displacement has a finite, temperature independent contribution at low temperature). The temperature dependence of low-temperature values obtained in this way were in good agreement with experimental results for globular proteins. The absolute values were larger by approximately 0.01 Å$^2$ than those obtained for hydrated myoglobin powders [38% hydration], 0.01 +/- 0.005 Å$^2$ at 80 K, [Doster *et al.*, 1989; Cusack and Doster 1990] but smaller than those obtained for dry myoglobin powders, 0.03 +/- 0.002 Å$^2$ [Martel, 1992]. Similar errors [+/- 0.005 Å$^2$] for the quasi-elastic experimental determinations for collagen can

be expected [Middendorf, personal communication]. Higher absolute values than for dry powders of globular proteins may be a consequence of the degree of hydration of the collagen [Martel, 1992]. On the other hand the higher absolute values for collagen were in better agreement with the average values obtained from analysis of x-ray diffraction data for globular proteins, which give values over a range from less than 0.01 to 0.025 $Å^2$ at 80 K for the heavy atoms, and these should significantly underestimate the hydrogen parameters by virtue of the lighter hydrogen mass [Frauenfelder *et al.*, 1979; Hartmann *et al.*, 1982]. For example, the calculated isotropic mean square displacments for the heavy atoms of acetanilide at 30 K are approximately one half of the calculated isotropic mean square displacements of the hydrogens [Chapter V, Section 5.3.4]. It should be noted that the calculated mean square displacements for the hydrogens of acetanilide at 15 K were in excellent agreement with those derived from neutron diffraction data for acetanilide at 15 K [Chapter V below, Table 5.4; Johnson, Eckert, and Barthes, personal communication]. Similarly the calculated mean square displacements for the heavy atoms of acetanilide at 113 K were in good agreement with x-ray diffraction data at 113 K. The accuracy of the calculated mean square displacements is further supported by the agreement of the calculated and experimental acetanilide spectra over a broad range of energy transfer [Chapter V, Section 5.3.4].

The assumptions of the mixed harmonic model include the idea that low frequency dynamics dominate the motions of the heavy elements, with the light hydrogens rigidly attached. The low frequency excitations below 400 $cm^{-1}$ accounted for 90 % of the total mean square displacements for the heavy atoms of acetanilide, but only 60 % for hydrogens, in keeping with the assumptions of a mixed

harmonic model. It was assumed therefore that the low frequency dynamics below 400 $cm^{-1}$ dominated the total mean square displacements for heavy atoms but provided only 60% of the total mean square displacments for hydrogens. The experimental density of states was therefore normalised up to the natural cut off provided by the minimum at 400 $cm^{-1}$. The choice of this cut-off has been discussed above, Section 4.4.1, and was also indicated by the divergence of $G(\omega)$ extracted from the data at values above 400 $cm^{-1}$. This behaviour indicated that at higher energy transfer (and hence higher momentum transfer), the multiphonon contribution to the experimental INS spectra was sufficient to preclude the approximations required for extraction of $G(\omega)$.

The isotropic mean square displacement for a normalised frequency distribution $Z(\omega)$ of quantum harmonic oscillators at temperature T is:

$$\langle u^2 \rangle = \int Z(\omega) \langle e^2(\omega) \rangle \, d\omega \qquad (4.4.12)$$

where:

$$\langle e^2(\omega) \rangle = (\hbar/6\omega M(\omega)) \coth(\hbar\omega/2KT)$$

Here $M(\omega)$ is an effective mass for the harmonic oscillators, and depends on $\omega$. Consistent with the other approximations made, M is assumed to be constant for all $\omega$. This is not exact for a real complex hetero-polymer, particularly where librational as well as translational motions contribute to the density of states, but the resulting average effective mass gives an indication of the mass of the heavy beads in the idealised chain model underlying this analysis. Using Eq. 4.4.12 along with the approximation described above for $Z(\omega)$, the average effective mass M was adjusted to yield self consistent

agreement with the temperature dependence and the absolute values of the average mean square displacements provided by the quasi-elastic experiments [Middendorf, personal communication] and similar results in the literature [Doster *et al.*, 1989; Martel *et al.*, 1992], and from the calculations for acetanilide described below.

From this approximate analysis an average effective mass of 9 atomic mass units (a.m.u.) was obtained for the heavy elements of the chain. This value provided good agreement with the temperature dependence, for which there is greater consensus in the literature, but indicated that the absolute values of the atomic mean square displacements should lie in the upper part of the range indicated by the quasi-elastic experiments. Thus the analysis described above yielded values for the isotropic mean square displacements of 0.019 $Å^2$ at 30 K, 0.021 $Å^2$ at 70 K and 0.026 $Å^2$ at 120 K. The value of 9 a.m.u. indicated that, on the one hand the hydrogen atoms do behave as though rigidly attached to a heavier element (effective mass definitely larger than one), but on the other hand the mass of this heavier element is not so large as to be identifiable with an amino acid residue, or larger structural subunit of a polypeptide. The value is therefore consistent with an underlying idealised chain model where extended atom groups are the heavy beads of the chain, lending experimental support to the use of the extended atom approximation for the study of low-frequency motions in proteins. Despite the continuing developments in speed and memory of computers, such approximations remain necessary for extending the length of molecular dynamics simulations into the biologically important ns to $\mu$s domain [Karplus and Petsko, 1990].

### 4.4.3. Assignments for experimental S(Q,ω) and Z(ω) below 400 $cm^{-1}$.

In order to compare collagen and PPII spectra collected at 30 K with $(PPG)_{10}$ spectra collected at 35 K the experimental spectra were corrected for the Bose-Einstein thermal population factor. The resulting corrected spectra are shown up to 2000 $cm^{-1}$ in Fig. 4.16 for dry and hydrated collagen, and their difference spectrum, Fig. 4.17 for $(PPG)_{10}$-d and $(PPG)_{10}$ and their difference spectrum. Fig. 4.18 compares the corrected spectra for dry collagen and $(PPG)_{10}$, and Fig. 4.19 for PPII and $(PPG)_{10}$. The hydrogen weighted density of states G(ω) extracted for collagen, $(PPG)_{10}$ and PPII all displayed a similar overall structure in the region below 400 $cm^{-1}$, though the details differed significantly (Fig. 4.20). Fig. 4.21 compares the high frequency INS spectra in the region of the CH, NH, and OH stretch bands for collagen at 6% hydration, $(PPG)_{10}$ and $(PPG)_{10}$-d. The general form of the low-frequency G(ω) for collagen and $(PPG)_{10}$ (Fig. 4.20) was similar to that calculated for polyglycine II (PGII) [Fanconi and Finegold, 1975]. The structure of the first band in $(PPG)_{10}$ and in dry collagen was essentially identical (Fig. 4.20). Two submaxima were evident in both samples, at 45 and 110 $cm^{-1}$. The maximum at 45 $cm^{-1}$ was better seen in Fig. 4.18, uncorrected for the Debye-Waller factor and the term $Q^2/\omega$, as both these corrections tend to suppress the low-frequency region below 100 $cm^{-1}$. Peaks at 40 and 110$cm^{-1}$ have been previously observed in collagen by inelastic neutron scattering at higher temperature [Berney *et al.*, 1987]. In calculations for PGII, the maximum due to longitudinal modes has been estimated at 13$cm^{-1}$ in the isolated molecule, but was displaced upward to 40 $cm^{-1}$ when hydrogen bonding to neighbouring chains was taken into account [Fanconi *et al.*, 1971]. The 45$cm^{-1}$ peak in collagen and $(PPG)_{10}$ spectra was therefore identified with a maximum

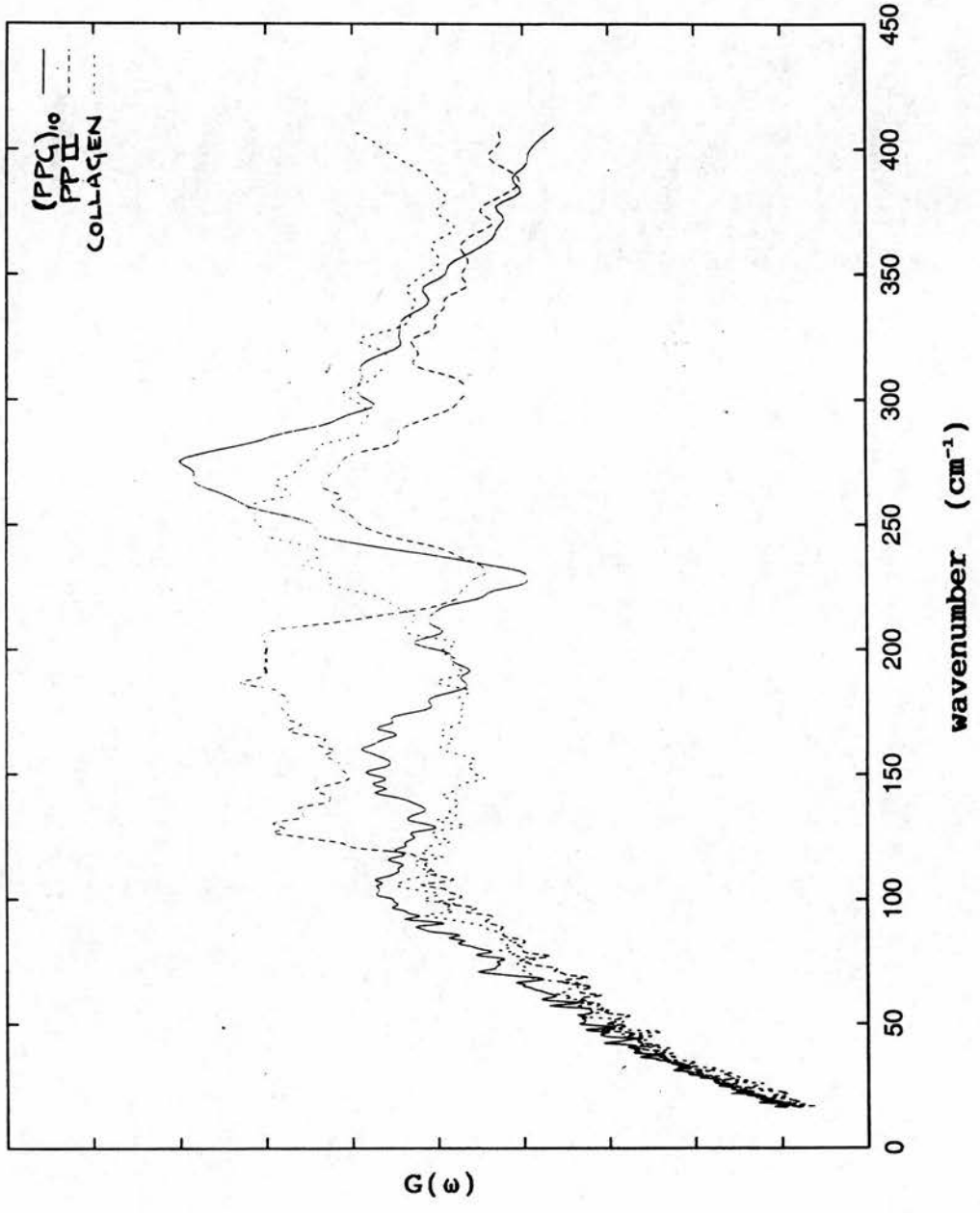


Figure 4.20. G(ω) collagen 6% hydrated, $(PPG)_{10}$, PPII, extracted from the INS data.

for longitudinal acoustic modes, since collagen and $(PPG)_{10}$ consist of PGII like chains hydrogen bonded and supercoiled to form the triple helix. Between 50 and 120 $cm^{-1}$, calculations for PGII have revealed modes involving torsions of the peptide backbone [Dwivedi and Krimm, 1982], and a maximum in $Z(\omega)$ found at 110 $cm^{-1}$ [Fanconi and Finegold, 1975]. The 110 $cm^{-1}$ maximum in collagen and $(PPG)_{10}$ spectra was assigned, therefore, to peptide backbone torsional modes.

Remarkable features of the PPII spectra were the high and sharp torsional phonon band edge at 200 $cm^{-1}$, and an intense peak at 130$cm^{-1}$ (Figs. 4.19 + 4.20). The origin of the 130 $cm^{-1}$ maximum was unclear, but may reflect the presence of modes with a particularly high contribution from hydrogens, or a particularly low effective mass, rather than a peak in the density of states. The high value for the torsional phonon band edge was in agreement with calculations of the phonon dispersion curves of PPII [Gupta *et al.*, 1973], and indicated a much stiffer effective force constant for torsional modes in PPII than in PGII. These spectral features presumably reflect the close packing arrangement of neighbouring pyrrolidine rings in PPII, and the contribution of the ring to the peptide backbone stiffness. Stiffening of the peptide backbone as a consequence of pyrrolidine ring closure, as well as close packing of neighbouring rings, have been invoked to explain the structural stability of PPII in solid state and solution, despite the absence of hydrogen bonds [Hopfinger, 1971]. Similar proline/proline packing has been suggested to contribute to the stability of the triple helical structure of $(PPG)_{10}$ [Bhatnagar *et al.*, 1988]. In $(PPG)_{10}$ and collagen this packing arrangement is relieved at every third amino acid residue by the prescence of glycine. Nevertheless both dry collagen and $(PPG)_{10}$ INS spectra showed additional features on the

downward slope of the 110 $cm^{-1}$ band edge, attributable to the effects of imino residues (Fig. 4.18). The calculated band gap at 200 $cm^{-1}$ for PGII remained apparent, though not complete, in the spectra of the regular helices $(PPG)_{10}$ and PPII (Figs. 4.19 and 4.20). For imino acid residues, the high band edge for torsional modes explains the incomplete nature of the 200 $cm^{-1}$ band gap, despite the regularity of these helices. The band observed around 250 $cm^{-1}$ was also in agreement with the qualitative features of calculations for PGII [Fanconi and Finegold, 1975; Dwivedi and Krimm, 1982] and was assigned to deformations and torsions in the peptide backbone and amino acid side chains by analogy with these calculations. In dry collagen spectra the maximum of the skeletal deformation band appeared at lower frequency (Figs. 4.19 and 4.20), possibly because methyl torsional modes, absent from $(PPG)_{10}$, contribute intensity near 240 $cm^{-1}$. Also the band gap was more nearly filled. Calculations of the frequencies of polypeptide skeletal torsion and deformation modes have revealed a significant variation with side chain type [Krimm and Bandekar, 1986]. The more complete filling of the band gap in collagen, at low temperature, was therefore attributed to its complex amino acid sequence. As a first approximation, the sequence variation can be viewed as disorder in bead mass and force constants of a mixed harmonic model of the perfectly regular $(PPG)_{10}$ type helix. Such disorder is expected to produce modes where there are band gaps for the regular helix.

Deuteration of the $(PPG)_{10}$ amide hydrogen and the tight bound water had little effect on the shape of the spectrum below about 400 $cm^{-1}$ (Fig. 4.17). The eigenvectors of the corresponding harmonic excitations must therefore involve the motion of many different hydrogen atoms, so that deuteration of the lone amide hydrogen and the single water molecule per tripeptide did not result in

appreciable intensity change. This observation represents further experimental support for the collective nature of the modes below 400 $cm^{-1}$.

### 4.4.4. Multi-quanta scattering

Because of the relation between momentum transfer **Q** and the energy transfer $\hbar\omega$, imposed by the geometry of the TFXA spectrometer, at higher energy transfers the harmonic nature of low temperature dynamics can be expected to produce intensity at energy transfers corresponding to combinations of low-frequency dispersive phonons with high-frequency group vibrations [Warner *et al.*, 1983; Jobic and Lauter, 1988]. Such intensity should appear as phonon wings above each high-frequency fundamental. At intermediate energy transfers **Q** is large enough to produce significant multi-phonon scattering, but not so large as to reduce the scattering strongly through the Debye Waller factor. In the spectrum of polyproline II, the intermediate energy transfer region showed strong peaks due to group vibrations. These were not clearly separated by regions of zero intensity, but instead showed asymmetric broadening, maximal on the high-frequency side. The mode at 745 $cm^{-1}$ in the PPII spectrum displayed this best (Fig. 4.19). The next highest fundamental mode observed in IR [Isemura *et al.*, 1968] or Raman [Smith *et al.*, 1969] spectra of PPII is expected at 836 $cm^{-1}$, well above the region of asymmetric broadening of the 745 $cm^{-1}$ mode. This asymmetric broadening was therefore attributed to phonon wings. It was not possible to clearly identify the effect in $(PPG)_{10}$ or collagen (Fig. 4.18), where many more fundamental modes are expected. At higher energy transfers, above 1000 $cm^{-1}$, increasing multiquanta scattering can be expected to contribute to a broad background, on which the peaks due to the harmonic fundamentals are superimposed. This is a consequence of

the relation between $\omega$ and $Q^2$ for TFXA spectra [Chapter III], which ensures that multi-phonon terms, which are proportional to higher orders of $Q^2$, become more important at high energy transfers.

**4.4.5. Hydration effects.**

The effect of hydration was explored for collagen and for $(PPG)_{10}$. Two broad hydration dependent bands were seen for collagen. A difference spectrum of dry collagen (6% hydration) and hydrated collagen (23% hydration) is shown in Fig. 4.16. Additional intensity was present in the hydrated sample in the acoustic phonon region at 50 $cm^{-1}$. An acoustic band has been observed in pure $H_2O$ ice at this frequency [Li and Ross, 1992]. At 23% hydration however, all the water in the collagen sample is associated with protein, and there is no pure ice. Nevertheless, in the interstices between collagen helices packed in quasi-hexagonal arrangement there are water molecules participating in extended, hydrogen bonded water chains and clusters [Hoeve and Tata, 1978]. Such extended networks are capable of sustaining collective phonon excitations [White, 1976]. The 50 $cm^{-1}$ peak in the difference spectrum was therefore assigned to phonon excitations propagating through this inter-helical water fraction. This assignment was supported by the absence of a similar 50 $cm^{-1}$ peak in the difference spectrum between deuterated and hydrogenous $(PPG)_{10}$ (Fig. 4.17). The 6% of water present in the $(PPG)_{10}$ samples can be expected to be all tightly bound in water bridge sites on the peptide backbone [Okuyama *et al.*, 1981]. At this hydration level, water does not form an extended hydrogen-bonded network, and so cannot sustain collective ice-like phonon excitations. Hence, as observed, no intensity difference in the acoustic region is expected when $H_2O$ is replaced by $D_2O$ at 6% hydration.

The coincidence of longitudinal acoustic phonon frequency in collagen (45 $cm^{-1}$) and in its associated interhelical water (~ 50 $cm^{-1}$) raises the possibility of coupling between solvent and polypeptide modes [White, 1976]. Indeed the longitudinal acoustic mode velocity in collagen has been shown to vary with water content at room temperature by Brillouin light scattering [Cusack and Lees, 1984].

$D_2O$ exchange of the tight bound water fraction in $(PPG)_{10}$ produced a marked loss of intensity in a broad band between 450 and 800 $cm^{-1}$, evident in the difference spectrum in Fig. 4.17. This corresponded with a similar band in the difference spectrum between dry and hydrated collagen in Fig. 4.16, though the details of the two difference spectra were not identical. The collagen difference spectrum showed intensity reaching 1100 $cm^{-1}$, with further broad differences above 1500 $cm^{-1}$. Together these features suggested that both tight bound water, and interhelical water, contributed to the 450 to 800 $cm^{-1}$ band, whilst only interhelical water contributed to the acoustic phonon band at 50 $cm^{-1}$. Pure $H_2O$ ice INS spectra display a similar broad band of intensity between 540 $cm^{-1}$ and 900 $cm^{-1}$ which has been assigned to non-dipersive librational excitations of $H_2O$ molecules [Li and Ross, 1992]. The broader librational band observed here in the INS difference spectrum of dry and hydrated collagen perhaps reflects the variation in detailed environment for water molecules participating in a hydrogen bonded network with amino acid side chain groups. Water molecules tightly bound in water bridge sites in $(PPG)_{10}$ at 6% hydration appear to have a narrower range of environments, with a librational band of width similar to pure ice but displaced toward lower frequencies. This down field shift may reflect coupling to librational dynamics of heavy protein groups.

4.4.6. Localised group vibrations: Amide and high-frequency modes.

All spectra were very complex in the high-frequency region (Figs. 4.16-4.19). The present assignments were based on comparison with the simpler neutron spectra of the model polypeptides PPII and $(PPG)_{10}$, and with published IR and Raman data for collagen and its models, along with normal coordinate analyses of polypeptide vibrational spectroscopy. As noted new IR data were collected for dry powders of $(PPG)_{10}$ and $(PPG)_{10}$-d, the amide-deuterated isotopomer (Figs. 4.3 - 4.5).

For the purpose of comparing spectra from different polypeptides containing a large molar fraction of proline, it is natural to use the spectral signature of proline as a reference intensity. All three types of sample (collagen, $(PPG)_{10}$ and PPII) showed a strong peak at 1320 $cm^{-1}$, and another at 3000 $cm^{-1}$ in INS spectra (Figs. 4.16 - 4.21). A moderately strong peak has been observed at 1320 $cm^{-1}$ in the IR [Isemura *et al.*, 1968] and Raman [Smith *et al.*, 1969] spectra of polypeptides containing proline, and assigned to $CH_2$ twist motion in proline. The peak centred on 3000 $cm^{-1}$ has been assigned to the CH stretch band. These features were therefore used to quantitatively relate the various spectra.

**4.4.6.1. Amide I, II, and III.**

Apart from the water libration band discussed above, there were several features in the difference spectrum between $(PPG)_{10}$ and $(PPG)_{10}$-d which corresponded to changes in the IR spectra on deuteration of the amide hydrogen (Figs. 4.5 and 4.17). The most conspicuous change was a loss of intensity at 1250 $cm^{-1}$, with lesser changes at 1500 and 1550 $cm^{-1}$, and around 930 and 1020 $cm^{-1}$ in the $(PPG)_{10}$-d spectra (Fig. 4.17). In the IR spectra a peak at 1550 $cm^{-1}$ and another at 1250 $cm^{-1}$ were markedly reduced by

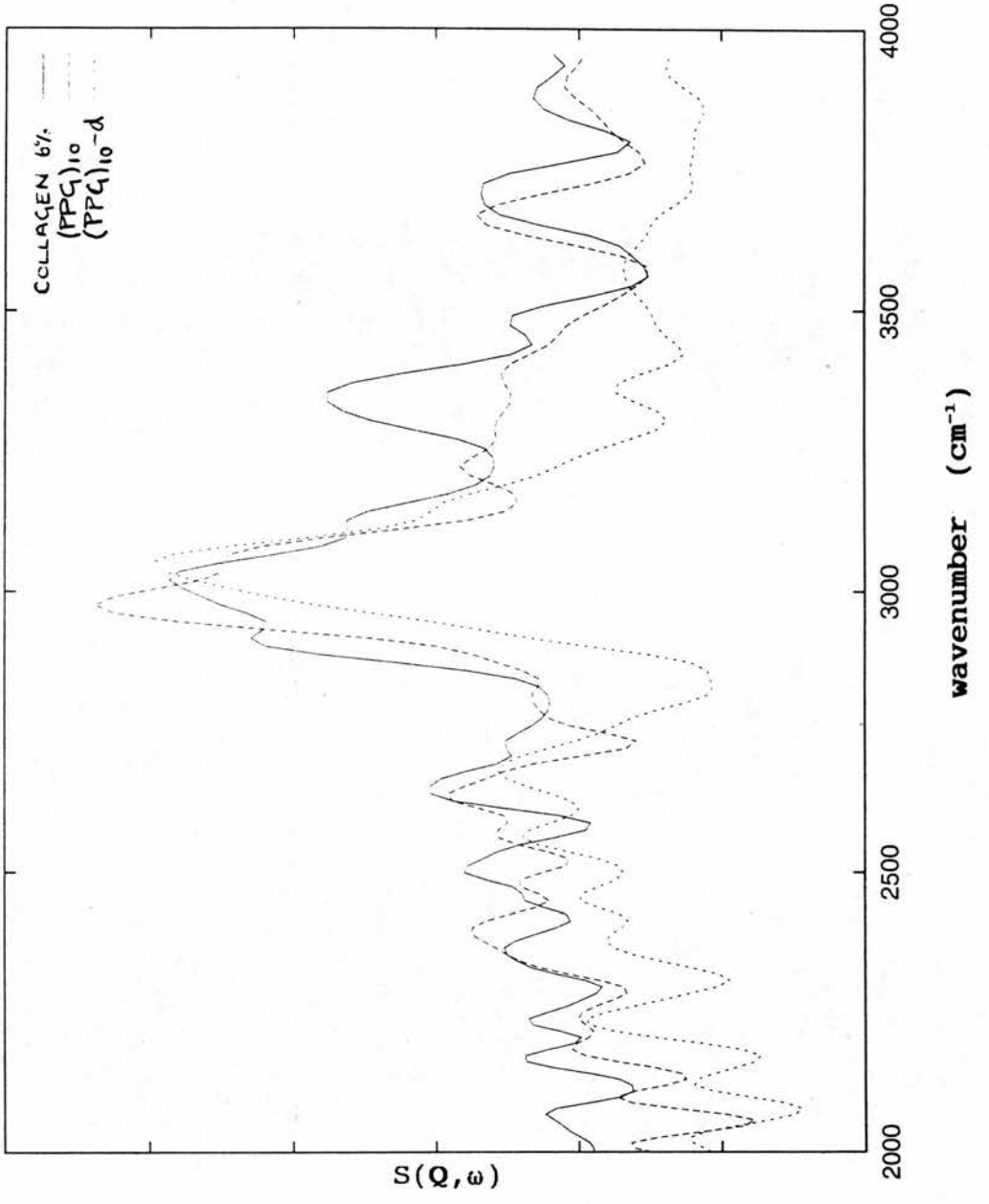


Figure 4.21. Inelastic neutron scattering spectra in the region of the CH, NH, and OH stretch bands, for collagen at 6% hydration, $(PPG)_{10}$ and $(PPG)_{10}$-d.

deuteration (Fig. 4.5), as were two lesser peaks at 920 and 1029 $cm^{-1}$. The peaks at 1550 $cm^{-1}$ and 1250 $cm^{-1}$ have been identified, in normal coordinate analyses of PGII [Dwivedi and Krimm, 1982], polyalanine [Fanconi *et al.*, 1971], and the peptide bond model compound N-methylacetamide [Fillaux *et al.*, 1993; Krimm and Bandekar, 1986], with in-plane bending of the amide hydrogen, coupled with stretching of the CN bond (Amide II and III). These assignments thus agree with the effects of deuteration on the $(PPG)_{10}$ INS spectra (Fig. 4.17). Clearly the formation of the peptide bond with an imino acid, rather than an amino acid, and the results of helix supercoiling, do not greatly perturb these vibrational frequencies. As expected the peaks at 1250 and 1550 $cm^{-1}$ were absent from the PPII IR and INS spectra (Figs. 4.10 and 4.19), because no amide hydrogens are present in PPII. Relative to the peak at 1320 $cm^{-1}$, both Amide II and Amide III were stronger in dry collagen spectra than in $(PPG)_{10}$ (Fig. 4.18), as expected from the higher ratio of amino to imino acids in collagen. The origin of the spectral changes with deuteration in $(PPG)_{10}$ near 925 and 1025 $cm^{-1}$ was unclear, as there were no amide modes expected in this region. It may be that these changes were related to excitations involving the tight bound water molecules.

Amide I is expected to be weak in INS spectra if it involves little H-atom motion. No significant intensity was observed at 1650 $cm^{-1}$ (Fig. 4.18), where Raman and IR spectroscopy have revealed the Amide I peak in collagen [Brodsky-Doyle *et al.*, 1975; Frushour and Koenig, 1975] and $(PPG)_{10}$ [Diem *et al.*, 1984]. This supported the assignment of Amide I to C=O stretch, with little H-atom motion.

**4.4.6.2. Amide V, skeletal modes and effects of higher-order molecular structure.**

In PGII [Dwivedi and Krimm, 1982], polyalanine [Fanconi *et al.*, 1971], and the hydrogen bonded crystals of the peptide bond model compounds N-methyl acetamide [Fillaux *et al.*, 1993; Krimm and Bandekar, 1986] and acetanilide, [Barthes *et al.*, 1991; Hayward *et al.*, in press; Chapter V], the NH out-of-plane bending mode, Amide V, mixed with C=O in-plane bending, appears at 750 $cm^{-1}$. This is typical for a hydrogen-bonded amide hydrogen. A mode involving C=O in-plane bending mixed with skeletal deformation has also been calculated to occur at 707 $cm^{-1}$ in PGII [Dwivedi and Krimm, 1982]. In PGII INS spectra a strong peak has been observed in this region [Fillaux, personal communication]. In PPII there was a strong peak in INS spectra at 745 $cm^{-1}$ (Fig. 4.19), corresponding to a very weak peak in the IR spectrum [Isemura *et al.*, 1968], and a moderate peak in the Raman spectrum [Smith *et al.*, 1969]. Normal coordinate analysis has assigned this feature to C=O in-plane bending along with in-plane bending of the backbone skeleton, and deformation of the proline ring [Gupta *et al.*, 1973]. A remarkable feature of the triple-helical $(PPG)_{10}$ and $(PPG)_{10}$-d INS spectra was the absence of any corresponding strong peak in the region between 650 and 820 $cm^{-1}$ (Fig. 4.17). Neither an Amide V mode, nor a C=O in-plane bending mode was observed in this region. On the other hand, when compared with PPII, excess intensity in the spectra of $(PPG)_{10}$ was apparent in the strong doublet peak at 555 and 590 $cm^{-1}$ and also near 630 $cm^{-1}$ (Fig. 4.19). The shape of the doublet peak did not change in $(PPG)_{10}$-d, though the overall intensity in this region changed as a result of intensity arising from the underlying water librational band (Fig. 4.17). An effect of triple helix formation on high-frequency modes of the peptide linkage has been previously observed in Raman studies comparing the

tripeptide ProlylProlylGlycine with $(PPG)_{10}$, and ascribed to secondary structure formation [Diem *et al.*, 1984]. The effect of helix-sheet transitions or peptide *cis/trans* isomerisation on skeletal modes is well recognised [Krimm and Bandekar, 1986]. The dramatic change observed in the Amide V region on passing from the left handed helical arrangement of PPII and PGII, to the supercoiled triple helical $(PPG)_{10}$ structure, must be attributed instead to the tertiary structure. The change is forcefully demonstrated by the superposition of the $(PPG)_{10}$ INS spectrum with an artificial spectrum constructed by summation of the PPII INS spectrum with a PGII TFXA INS spectrum kindly provided by F. Fillaux [Fillaux, personal communication] in a ratio reflecting the content of two prolines to each glycine residue in $(PPG)_{10}$ (Fig. 4.22). Thus the effect of triple-helical supercoiling is to shift the Amide V mode due to the Gly-Pro linkage, and the skeletal deformation and C=O in-plane bending modes of the Pro-Pro linkages of $(PPG)_{10}$, away from the region between 700 and 800 $cm^{-1}$. The shift may be downward to the region of 590 $cm^{-1}$, though the NH out-of-plane bending mode was not clearly identified in this region by H/D exchange in the triple-helical peptides, because of the background due to water libration. The effect may be mediated by supercoiling distortion of the intra-triple-strand hydrogen bond and the backbone dihedral angles in $(PPG)_{10}$. In the crystal structure of $(PPG)_{10}$, the local distortion from standard values of the backbone dihedral angles, bond angles, and endocyclic ring conformation angles are only 7, 2, and 5 degrees respectively, and vary with the detail of the molecular model [Okuyama *et al.*, 1981]. The intra-triple-strand hydrogen bond, between Glycine NH on one chain and Proline CO on a neighbouring supercoiled chain also varies in length, and in N-H..O angle with the molecular conformation [Yonath and Traub, 1969; Okuyama *et*

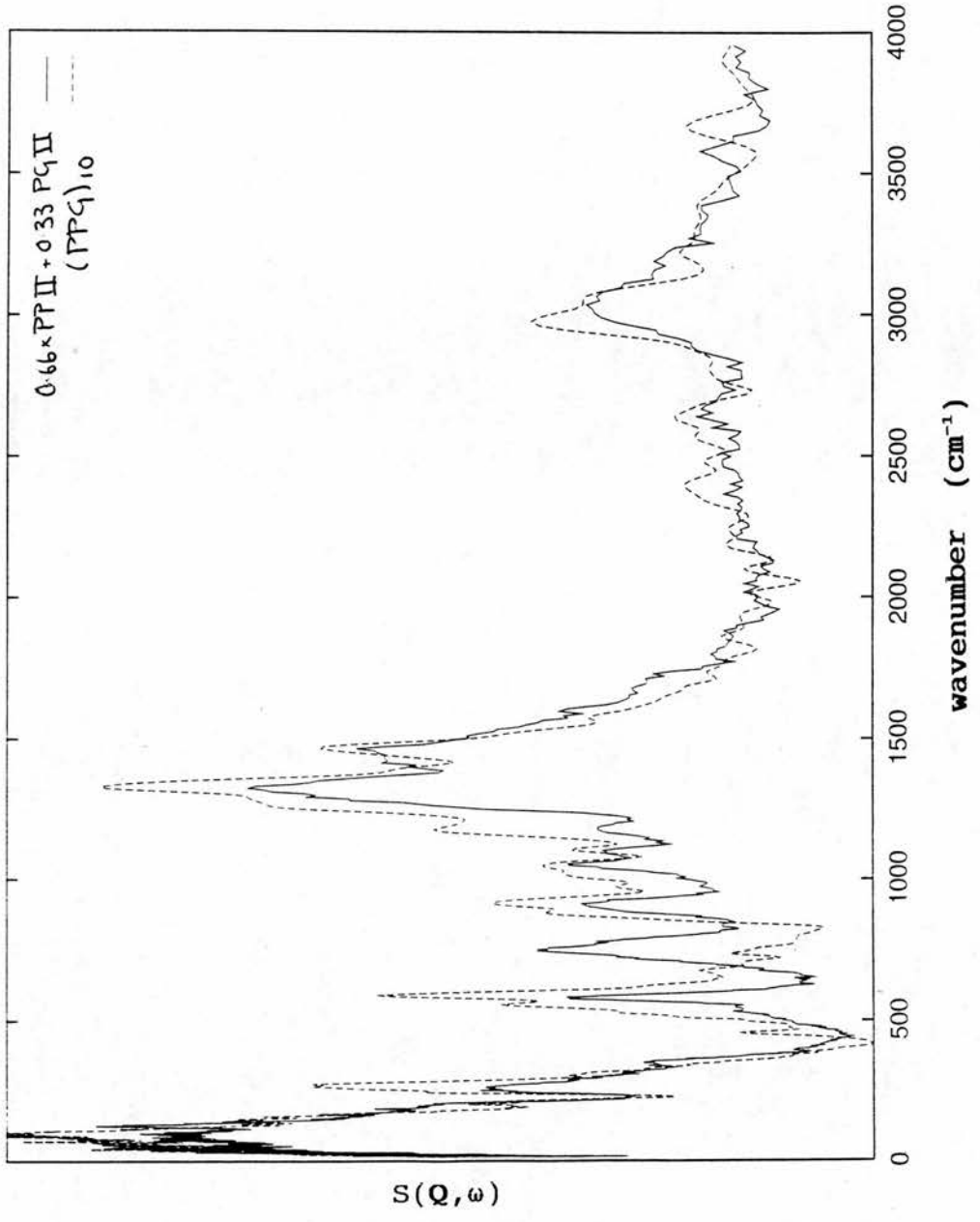


Figure 4.22. Inelastic neutron scattering spectra corrected for Bose Einstein thermal factor, for $(PPG)_{10}$, and for an artificial spectrum constructed from the sum of a PGII spectrum (F. Fillaux, personal communication) and a PPII spectrum, in the ratio of 1:2, both collected on the TFXA spectrometer, RAL. Seven point Pascal smoothing procedure applied. The dramatic reduction of intensity in the region of 750 $cm^{-1}$ and the increased intensity in the region of 600 $cm^{-1}$ is evident.

*al.*, 1981; Bhatnagar *et al.*, 1988]. The equivalent hydrogen bond and backbone geometries in models of collagen also vary with the details of the molecular structure [Fraser *et al.*, 1983]. Theoretical normal mode analyses have predicted significant effects of minor angle variation, and hydrogen bonding, on Amide V modes [Krimm and Bandekar, 1986]. The observation of a dramatic spectral effect of the subtle supercoiling distortion raises the possibility of coupling between low-frequency modes and high-frequency peptide backbone modes. Low-frequency dispersive modes can significantly alter local supercoiling and hydrogen-bond length. Such anharmonic coupling may be an important mechanism of energy transport in biological systems [Scott, 1992], and Amide V has been recently identified as a markedly anharmonic mode, and a candidate for such coupling, in acetanilide [Barthes *et al.*, 1993; Hayward *et al.*, in press; Chapter V]. In polyproline, a moderate infrared band at 675 $cm^{-1}$ is characteristic of the left handed PPII arrangement and has been assigned by normal mode calculation to a mixture of skeletal stretch with pyrrolidine ring in-plane deformation [Gupta *et al.*, 1973]. This mode was weak only in the PPII INS spectra, indicating little hydrogen atom motion in the mode (Fig. 4.19).

**4.4.6.3. Collagen spectra compared with PPII and $(PPG)_{10}$ spectra.**

The dry collagen INS spectrum revealed significantly more intensity than the $(PPG)_{10}$ spectrum in the 600 to 750 $cm^{-1}$ region (Fig. 4.18). Phenylalanine and tyrosine ring torsional modes can be expected in this region, along with phenyl ring hydrogen out of plane bending modes [Krimm and Bandekar, 1986]. These were all strong features in INS spectra calculated for the model compound acetanilide, because of the large component of H-atom motion [Hayward

*et al.*, in press; Chapter V]. The series of bands in this region can be attributed to phenyl ring modes of phenylalanine or tyrosine, on an underlying background due to the water libration band (Fig. 4.16 + 4.18). The relative weakness of these bands, compared to $CH_2$ twist and wag modes of the imino acid pyrrolidine ring at 1320 $cm^{-1}$ and 1450 $cm^{-1}$, can be attributed due to the high abundance of these imino acids in collagen. The imide II band at 1445-1485 $cm^{-1}$ has been of recent interest in resonance Raman studies of X-Pro or Pro-Pro cis/trans isomerisation (X = any amino acid) and imino hydrogen bonding [Tageuchi and Harada, 1990]. This band is another example of a high-frequency mode affected by a major change in backbone conformation. The band was not seen in the INS spectra, as it was obscured by the very strong pyrrolidine ring $CH_2$ deformation band at 1450 $cm^{-1}$ (Fig. 4.16 - 4.19). This illustrates a difficulty in interpreting neutron spectra, where modes of particular interest may involve little H-atom motion. Selective deuteration of the pyrrolidine ring methylene groups might allow observation of the imide II band in future. In the collagen spectra (Fig. 4.16 + 4.18), additional intensity not present in the $(PPG)_{10}$ spectra around 1435 $cm^{-1}$ was attributed to methyl group deformations, by comparison with the calculations of Chapter V for the model molecule acetanilide [Hayward *et al.*, in press; Chapter V]. Based on those calculations, intensity in the collagen spectra between 1050 and 1070 $cm^{-1}$ was also attributed to methyl modes. These assignments have also been made by calculation and INS experiment for the model compound N-methylacetamide [Fillaux *et al.*, 1993].

Several features common to PPII and $(PPG)_{10}$, notably at 920, 1040, 1100 and 1170 $cm^{-1}$, were also apparent in the collagen spectra, again reflecting the high content of imino acids (Figs. 4.18 and 4.19). Calculations have

attributed the modes at 920 and 1040 $cm^{-1}$ to pyrrolidine ring stretch modes, and those at 1100 and 1170 $cm^{-1}$ to mixed ring stretch and ring methylene modes [Gupta *et al.*, 1973; Lagant *et al.*, 1983]. The ring stretching modes at 1250 to 1260 $cm^{-1}$, seen in the PPII and $(PPG)_{10}$-d spectra, were obscured by the Amide III mode in $(PPG)_{10}$ and collagen spectra (Fig. 4.16 - 4.19).

Centred on 3000 $cm^{-1}$, a strong CH-stretch band was seen in all samples (Fig. 4.21). The resolution of the TFXA spectrometer at the highest energy transfers is only about 100 $cm^{-1}$ [Penfold *et al.*, 1986]. This prevented the direct observation of splitting of the NH stretching modes, Amide A and B, though a band attributable to NH stretch centred at 3300 $cm^{-1}$ was apparent in collagen spectra (Fig. 4.21). The same band was not well distinguished in $(PPG)_{10}$, because of the much lower molar content of NH groups. Again, selective deuteration of CH groups would be likely to reveal these modes. The $(PPG)_{10}$ and dry collagen sample displayed a similar OH stretch band at 3400 $cm^{-1}$, which was absent from $(PPG)_{10}$-d, as expected from the exchange of tight bound water for $D_2O$ (Fig. 4.21).

## 4.5. DISCUSSION OF THE MIXED HARMONIC ANALYSIS.

So far I have presented high resolution neutron spectra from collagen, the most ubiquitous fibrous protein, and interpreted the data with reference to analytical theories of scattering from complex polymers, and with the help of parallel neutron and optical spectroscopy experiments for two closely related synthetic polypeptides.

From an experimental point of view, the neutron spectra are the first from any natural protein extending from the low-frequency phonon region up to the highest bond stretching modes. Earlier neutron work on fibrous and globular biomolecules was more restricted with respect to both frequency range and energy resolution [Smith, 1991;

Berney *et al.*, 1987]. Developments in pulsed neutron techniques have now allowed a much wider frequency range (up to 4000 $cm^{-1}$) to be examined, with a resolution that is still inferior to IR and Raman spectroscopy, but sufficiently fine to reveal much spectral detail. This new spectral information relates primarily to the dynamics of hydrogens, protonated groups and closely associated water. In combination with quasi-elastic neutron scattering techniques [Middendorf, 1992], it is feasible to probe hydration processes and biopolymer-water coupling over length scales from 0.1 to 100 Å, with the capability, not easily accomplished by optical techniques, of varying the scattering contrast between constituents of a heterogenous system.

There are, broadly, two avenues for exploiting this type of inelastic neutron scattering data from complex biopolymers: the first, as has been demonstrated so far in this Chapter, is to focus on those features which complement information derived from optical techniques, and to extract density of states functions relating to basic thermodynamic properties. Notable conclusions from this approach include:

(i) there is an apparent dramatic shift of the Amide V mode in triple-helical polymers, indicating a marked effect of supercoiling on the dynamics of the hydrogen bond,

(ii) density of states information provides an estimate of the effective mass of 9 a.m.u. for the low-frequency oscillators of a mixed harmonic model of the polypeptide dynamics, which suggests that the extended-atom approximation will be a useful simplification for calculations of protein dynamics over times prolonged beyond the ns scale,

(iii) exploiting the technique of contrast variation, at least two populations of water bound to the triple helical

polypeptides can be distinguished dynamically, tight bound water which does not sustain collective excitations, and loosely bound inter-helical water, which can sustain collective low-frequency phonon excitations.

Secondly however, the analytical relationship between neutron $S(Q,\omega)$ data and fundamental space and time dependent correlations at the atomic level, opens up the possibility of direct comparison with results from molecular dynamics (MD) simulations. The potential of INS to provide experimental constraints on calculations of the low-frequency dynamics of proteins has been demonstrated [Smith, 1991]. While much interest relates to the functional significance of these low-frequency collective excitations and their relaxational and anharmonic behaviour, recent work on vibrational energy transport mechanisms has focused on the coupling of low- and high-frequency modes [Scott, 1992]. Such mode coupling mechanisms are potentially significant for the function of enzymes which need to transport localised 'packets' of energy, with minimal losses, between active sites which may be seperated by appreciable distances [Scott, 1992]. The utility of simulations for studying mode coupling mechanisms will rest on the accurate description of high- as well as low-frequency vibrational modes. MD simulations allow the calculation of space and time dependent atomic correlation functions over the time domain from a few *f*s up to a few *n*s, producing spectral information from a few $10^3$ $cm^{-1}$ down to values below 1 $cm^{-1}$ [Karplus and Petsko, 1990]. The present neutron experimental work opens up the vibrational spectral region from 20 - 3600 $cm^{-1}$, with improved resolution, providing new stringent tests for the parameters and assumptions entering into simulations of biomolecular dynamics. However, the data were collected at low temperatures where the suppression of intensity, due to the Debye-Waller factors, was minimal, and where the

intrinsic resolution of the spectra was not obscured by multi-phonon scattering. Low temperature restricts the dynamics probed to the harmonic region of the potential energy surface, and the data will be useful primarily in this region for improving the parameterisation of MD PEFs. On the other hand, high-frequency modes in proteins and model molecules remain largely harmonic at higher temperatures. Furthermore, as noted, the data lend support to the utility of the extended-atom approximation, which treats the high-frequency localised oscillators as harmonic oscillators, essentially independent of the low-frequency and markedly more anharmonic collective modes.

As noted, it has been possible to extract difference spectra related to the dynamics of two different populations of protein-associated water. Such spectra can similarly provide an important test of calculations of, especially, the high-frequency harmonic modes of tightly bound water molecules. These high-frequency modes reflect the hydrogen bonding parameters of water molecules occupying water bridge sites, information of interest for understanding the functional role of the primary hydration shell of proteins.

Given these points, I have performed numerical calculations of the dynamics of $(PPG)_{10}$ and PPII, using the CHARMM program and PEF (Chapter III). The results demonstrate the potential of INS data to test the accuracy of the parameterisation and approximations used. Clearly improvement of the parameterisations will be required for accurate quantitative models of the dynamics. The next section describes these calculations.

## 4.6. NUMERICAL CALCULATIONS OF INS SPECTRA FOR $(PPG)_{10}$.

All the dynamical calculations in this section used a version of the CHARMM program [Brooks *et al.*, 1983a] implemented on the Hewlett/Packard 9000/735 computers in

the laboratory of Dr. Jeremy C. Smith, Section de Biophysique des Proteines et des Membranes, Centre d'Etudes Atomique, Saclay, France. All other calculations of this Chapter were also carried out using the computers in Dr. Smith's Laboratory.

### 4.6.1 Calculations for $(PPG)_{10}$.

#### 4.6.1.1. Energy Minimisation.

The starting set of coordinates for $(PPG)_{10}$ were taken from the published 2.2 Å resolution single crystal x-ray diffraction structure [Okuyama *et al.*, 1981]. This x-ray structure was refined assuming a quasi-infinite stacking of identical perfect helices, so that the refined structure does not describe effects associated with the terminal regions of the individual $(PPG)_{10}$ helices. Therefore the structure refers predominantly to the average structure of the central triple helical region of each $(PPG)_{10}$ helix [Okuyama *et al.*, 1981]. It is notable that the authors of this study were unable to distinguish amongst the four different possibilities for the proline ring pucker arrangement in each tripeptide unit, on the basis of the x-ray data. All four possible arrangements gave an equally good fit to the data. The model with Proline ring 1 puckered down, and Proline ring 2 puckered up was arbitrarily chosen by the authors for detailed discussion, and the coordinates given were the set used here. Only the positions of the heavy atoms were taken from the x-ray structure. The positions of the hydrogens, which are poorly defined by x-ray diffraction, were added using a facility of the CHARMM program. This facility adds hydrogens using standard bond length and angle parameters, before energy minimising the resulting structure.

The water content of the single crystals of $(PPG)_{10}$ in the x-ray study was approximately 46 % [Okuyama *et al.*, 1981], and it is to be expected therefore that the structure in

the dry powder form may be slightly different. As noted above the dry powder form contains one tightly bound water molecule per tripeptide, forming an intrachain water bridge [Sakakibara *et al.*, 1972; Okuyama *et al.*, 1981]. This water molecule was included in the calculations, using the coordinates provided by the single crystal x-ray study. The carboxy- and amino- termini of each polypeptide chain were modelled as charged groups.

With the starting structure for the isolated molecule constructed in this way the potential energy was calculated by use of the current set of CHARMM parameters for proteins, using the PEF described in Chapter III. The complete set of protein parameters currently used with CHARMM were kindly provided by Dr. A. D. Mackerell. The parameters for the proline residues were derived from *ab initio* quantum chemical calculations for Acetyl Proline Methylamide [Dunbrack *et al.*, 1992]. The non-bonded interactions were brought to zero by a cubic switching between 10 and 12 Å. The dielectric constant was set at 1.0 for all coulomb interactions except those between atoms seperated by two bonds. For these 1:4 interactions the dielectric constant was reduced to 0.5. The CHARMM potential energy was then minimised by applying the Adopted Basis Set Newton Raphson algorithm. The energy-minimised model of the isolated molecule with tightly bound water molecules was stable, with a CHARMM potential energy of -757 kcal/mol. The energy-minimised structure was compared with that of the x-ray structure. The minimum root mean square deviation of the atomic cartesian coordinates (RMS) was calculated, after rigid body reorientations of the whole triple helix were performed to superimpose the two structures as far as possible. The RMS deviation for all heavy atoms of the structure, including water, was 1.09 Å. Hydrogens were excluded because they are not well defined in x-ray diffraction structures.

Excluding the terminal 3 residues at each end of each polypeptide chain, which are likely to be affected most markedly by the end effects neglected in the x-ray structure refinement, the RMS deviation for the heavy atoms alone was only 0.63 Å. Restricting the comparison to only the central tripeptide unit yielded an RMS deviation of only 0.44 Å. These results show that the energy-minimised structure of the central region of the triple helix, where terminal effects are minimum, retains the major features of the x-ray structure, to within an RMS error less than one third of the resolution of the x-ray structure determination. The RMS deviation between the average structure during the MD simulation at 30 K, and the x-ray structure, excluding water, hydrogens and the terminal three residues of each chain, was 1.22 Å. Such agreement is comparable to that obtained between molecular dynamics simulations and x-ray diffraction experiments for globular proteins [Levy *et al.*, 1985].

Low frequency large amplitude motions of an extended helical macromolecule like $(PPG)_{10}$ may be significantly affected by the environment of the molecule, and these motions can contribute intensity below 100 $cm^{-1}$ in INS spectra. To provide a more realistic representation of the structure of the powder samples used for the INS experiments, the close packed environment of the helices was modelled by the generation of images of the primary $(PPG)_{10}$ molecule on a hexagonal lattice with radial distance between the centre of neighbouring helices of 12.5 Å, in agreement with the results of powder diffraction studies of $(PPG)_{10}$ [Yonath and Traub, 1969]. The length of the hexagonal cell was fixed at 92 Å, sufficient to accommodate the undistorted $(PPG)_{10}$ helix, though no direct experimental data was available for this dimension. The energy-minimised structure for this model including the powder environment, was more stable with a

final CHARMM potential energy of -1263 kcals/mol. The RMS deviation for comparison of x-ray and energy minimised cartesian coordinates for all heavy atoms of the structure, including water atoms, was 1.44 Å. Excluding the terminal three residues at each end of each polypeptide chain, the RMS deviation for the heavy atoms was 0.93 Å. Restricting the comparison to the central tripeptide unit yielded an RMS deviation of only 0.59 Å. Thus, though the final structure in the powder model was more stable, and the RMS deviation remained approximately one quarter of the resolution of the diffraction experiment, the agreement with the x-ray structure was marginally less good. Some of this disparity may have resulted from the significant differences in packing between the crystal structure and the powder.

A further source for the disparity were errors in main chain dihedral angles, which produce a cumulative error in cartesian coordinates when propagated over several helical repeats. In fact as noted above, when a single tripeptide unit from the central region of the energy minimised models was compared with the x-ray diffraction structure, the RMS deviation for the heavy atoms was significantly less than for the entire structure, demonstrating that propagation of errors in dihedral angles was indeed an important source of RMS differences in the cartesian coordinates.

Despite the global agreement with the x-ray structure as measured by the RMS deviation, a more detailed comparison in terms of the values of internal coordinates (especially dihedral angles) revealed several marked local deviations of the energy minimised structure from the x-ray structure. These were most marked in the terminal regions, and the anisotropic environment of the helix arising from end effects and especially packing in the hexagonal lattice ensured that the regular helical structure was not

perfectly maintained in the powder model. Local differences in internal coordinates compensated each other sufficiently to maintain the global fit to the x-ray structure. Bond angles were generally within 3 % of the x-ray structure, and bond lengths within 0.03 Å, but some dihedral angles varied by as much as 90°. These variations were concentrated particularly in the proline rings. The origin for this discrepancy, and for the disparity between the individual tripeptide units and the x-ray structure, was the proline ring pucker arrangement. In the energy minimised structure both prolines of each tripeptide unit pucker down. As noted above, this form gave no less reasonable a fit to the x-ray data than the down-up form reported in detail by the authors of the x-ray paper [Okuyama *et al.*, 1981]. It is possible therefore that the puckering arrangement in the energy-minimised structure is the preferred arrangement in the real powder.

**4.6.1.2. Molecular Dynamics Calculations.**

Both the isolated molecule of $(PPG)_{10}$ and the model of the powder system were too large to allow normal mode calculations with CHARMM. The investigation of the dynamics proceeded directly therefore to a molecular dynamics simulation of the $(PPG)_{10}$ molecule in the powder environment with discrete time steps of 0.5 fs, using periodic boundary conditions. The periodic boundary conditions imposed the condition that the motion of an atom in the primary molecule was followed exactly in the image molecules used to model the powder environment. Interactions of the primary molecule with its neighbouring images arose through non-bonded terms of the PEF. The non-bonded interactions were brought to zero at 12 Å, preventing interaction of any atom directly with its images. The temperature of the simulation was 30 K corresponding with the experimental conditions.

The system was heated in increments of 5 K every 100 fs to a final temperature of 30 K, by reassignment of atomic velocities selected at random from a thermal distribution. A prolonged equilibration period of 20 ps followed, allowing the kinetic energy to be distributed amongst the degrees of freedom of the system, and allowing fluctuations of temperature and energy associated with the incremental heating steps to settle down. The actual molecular dynamics production run proceeded from the equilibrated system for a further 40 ps. During the production run the total energy was stable, with a value of -1087 kcal/mol, and an RMS flucutation of 0.011 kcal/mol. The ratio of the RMS fluctuation of total energy to that of kinetic energy was less than 0.005. The average temperature was 30.36 K, and the RMS fluctuation 0.67 K. The atomic coordinates and velocities at every step of the production run were saved. This dense sampling on the time axis (every 0.5 fs) was necessary to follow the behaviour of high frequency excitations in the system.

**4.6.1.3. Incoherent INS intensities from molecular dynamics trajectories.**

Calculations of INS intensities from the molecular dynamics (MD) simulations were made using the program package nMOLDYN [Kneller, in press]. Calculations of INS intensities from classical MD simulations yield a classical approximation to the dynamics structure factor, denoted here by $S_{cl}(\mathbf{Q},\omega)$, because classical MD trajectories yield classical atomic correlation functions and intermediate scattering functions.

To save CPU time $S_{cl}(\mathbf{Q},\omega)$ was calculated from the MD simulations in the Gaussian approximation. The Gaussian approximation is exact for harmonic models of molecular dynamics. In the present case the system is studied at 30 K by molecular dynamics simulations, but at this low

temperature it can be expected that the full dynamics will closely approximate to those expected in a harmonic treatment. It is expected therefore that the Gaussian approximation will give a good estimate of the INS intensity. Using the cumulant expansion [Boon and Yip, 1980]:

$$\langle \exp[i\mathbf{q}.(\mathbf{R}_\alpha(t)-\mathbf{R}_\alpha(0))] \rangle \qquad (4.6.3)$$

$$= \exp[-0.5\langle \{\mathbf{q}.(\mathbf{R}_\alpha(t)-\mathbf{R}_\alpha(0))\}^2 \rangle \pm \ldots]$$

and truncating the series after the first term, the intermediate incoherent scattering function can be written as:

$$F_{cl}(\mathbf{Q},t) \sim 1/N \sum_\alpha \exp[-0.5\langle \{\mathbf{q}.(\mathbf{R}_\alpha(t)-\mathbf{R}_\alpha(0))\}^2 \rangle] \qquad (4.6.4)$$

Since the experiments were performed on an isotropically scattering polycrystalline powder sample the exponent was averaged over all directions of **Q**:

$$F_{cl}(\mathbf{Q},t) \sim 1/N \sum_\alpha \exp[-q^2\langle \{\mathbf{R}_\alpha(t)-\mathbf{R}_\alpha(0)\}^2 \rangle/6] \qquad (4.6.5)$$

The calculation of the neutron spectra in the Gaussian approximation thus involved computation of the time-dependent mean square displacements, $\{\mathbf{R}_\alpha(t) - \mathbf{R}_\alpha(0)\}^2$. These were calculated from the molecular dynamics configurations as follows:

$$\langle \{\mathbf{R}_\alpha(m)-\mathbf{R}_\alpha(0)\}^2 \rangle \qquad (4.6.6)$$

$$\approx 1/N-m \sum_{k=0}^{N-m-1} \{\mathbf{R}_\alpha(k) - \mathbf{R}_\alpha(k+m)\}^2$$

where the steps in the trajectory are denoted by $\mathbf{k} = 0,..,N_t - 1$. Eq. 4.6.6 was evaluated using an efficient

FFT-based algorithm [Kneller, 1988]. $S_{cl}(\mathbf{Q},\omega)$ in the Gaussian approximation was obtained by numerical Fourier transformation of $F_{cl}(\mathbf{Q},t)$ as defined by Eq. 4.6.5 for several values of $\mathbf{Q}$. The resulting calculated spectra represent $S_{cl}(\mathbf{Q},\omega)$ for constant $\mathbf{Q}$ in the Gaussian approximation. Because of the relation between $\mathbf{Q}$ and $\omega$ for TFXA these cannot be compared directly with TFXA data (Chapter III).

As noted above, classical MD simulations allow the calculation of classical atomic correlation functions or intermediate scattering functions only and exact quantum expressions for calculating INS spectra have not been derived. This is because, in the classical limit the atomic position operators $\mathbf{R}_\alpha(t)$ involved in the definition of the correlation functions commute at all times t, for all atoms $\alpha$. This yields a symmetry of the classical correlation functions under time inversion. The quantum mechanical detailed balance condition:

$$S(\mathbf{Q},\omega) = \exp(\beta\hbar\omega)S(-\mathbf{Q},-\omega) \qquad (4.6.1)$$

which holds for inelastic neutron scattering therefore does not hold for calculations made in the classical limit. To try to take account of this a semiclassical correction can be used [Lovesey, 1984]. A semi-classical correction for isotropic systems such as the polypeptide powder under consideration is [Kneller *et al.*, 1992]:

$$S(\mathbf{Q},\omega) \sim \beta\hbar\omega/[1-\exp(-\beta\hbar\omega)]\ S_{cl}(\mathbf{Q},\omega) \qquad (4.6.2)$$

where $S_{cl}(\mathbf{Q},\omega)$ is the classical dynamic structure factor. However this semi-classical correction is strictly valid only in the linear response regime ($h\omega < K_BT$) [Kneller, *et al.*, 1992]. Because the experimental data extended over a very wide energy range, and the temperature was so low,

it was not possible to find a single correction scheme valid throughout. This lead to serious discrepancies between the calculated classical $S_{cl}(\mathbf{Q},\omega)$ and the measured $S(\mathbf{Q},\omega)$ (Fig. 4.23). It is possible to circumvent this problem by proceeding directly to calculation of the hydrogen-weighted density-of-states $G(\omega)$ from the classical dynamical structure factor $S_{cl}(\mathbf{Q},\omega)$. The resulting $G(\omega)$ is correct formally in the quantum case [Kneller, *et al.*, 1992], and can be compared with $G(\omega)$ extracted from the experimental data as described in Section 4.4.2 above. This method eliminates problems with the relation between $\mathbf{Q}$ and $\omega$ for TFXA because $G(\omega)$ is independent of $|\mathbf{Q}|$.

**4.6.1.4. Hydrogen weighted density-of-states calculations.**
The calculation of the hydrogen-weighted density-of-states, $G(\omega)$, from the molecular dynamics simulations was made using the program package nMOLDYN [Kneller, in press] according to:

$$G(\omega) = \lim_{|\mathbf{Q}|\to 0} \omega^2/Q^2 \; S_{cl}(\mathbf{Q},\omega) \qquad (4.6.7)$$

First the classical dynamical structure factor, $S_{cl}(\mathbf{Q},\omega)$, was calculated as described above, for constant $|\mathbf{Q}|$. $|\mathbf{Q}|$ was chosen as 2.0 $Å^{-1}$ so that $Q^2 \langle u_\alpha^2 \rangle < 0.1$, ensuring that the Debye-Waller factor approached 1, and could be neglected. Thus $G(\omega)$ was extracted according to :

$$G(\omega) = \omega^2/Q^2 \; S_{cl}(\mathbf{Q},\omega) \qquad (4.6.8)$$

where the limiting process in Eq. 4.6.7 has been approximated by taking $\mathbf{Q}$ such that $Q^2/\langle u_\alpha^2 \rangle < 1$ for all atoms $\alpha$. Eq. 4.6.7 holds formally also in the quantum case [Kneller *et al.*, 1992].

In Fig 4.24 the results of this calculation are compared

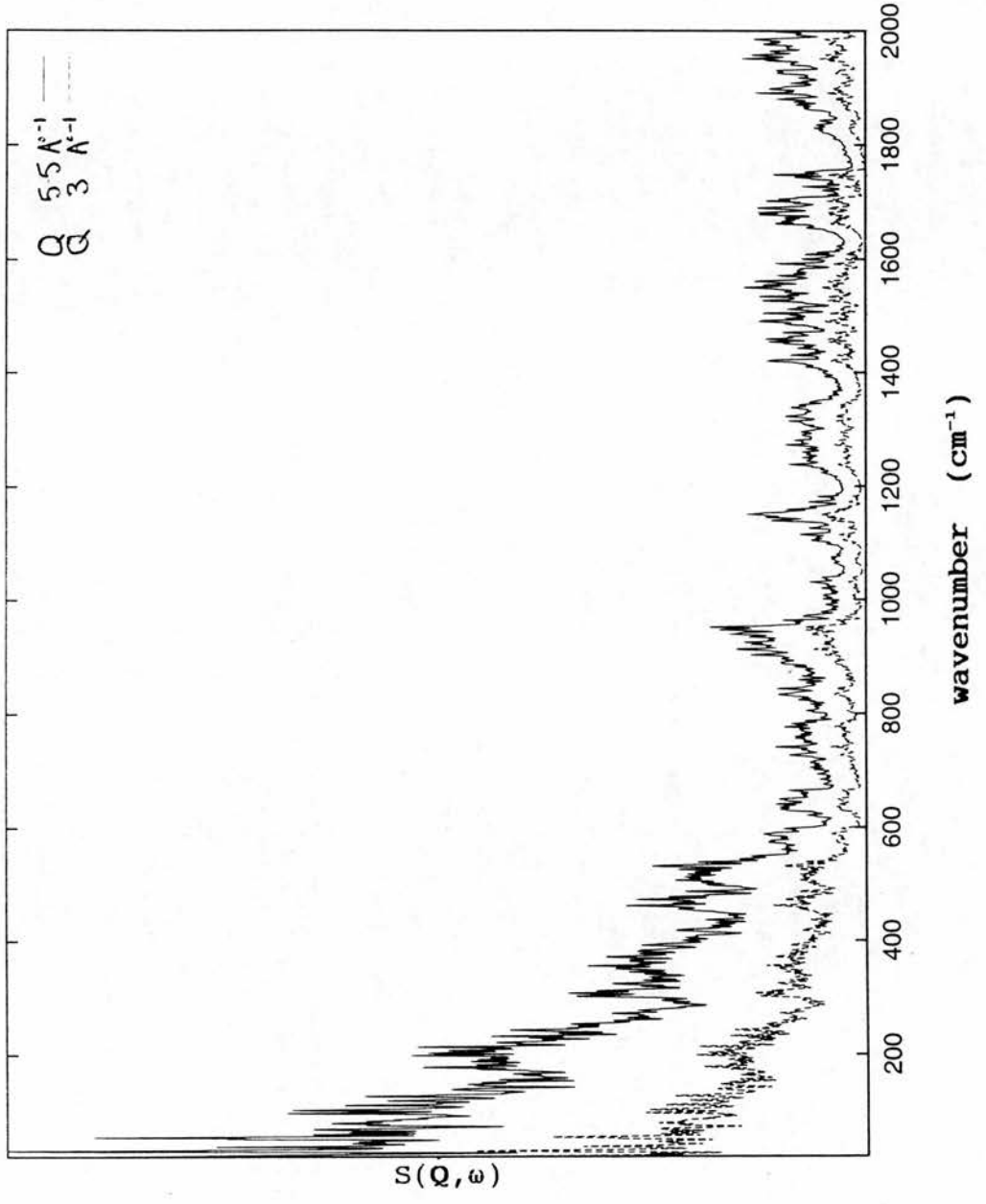


Figure 4.23. Numerical calculation of $S(\mathbf{Q},\omega)$ for $(PPG)_{10}$, with semi-classical correction applied, at two values of $|\mathbf{Q}|$ 3 Å$^{-1}$ (lower) and 5.5 Å$^{-1}$ (upper).

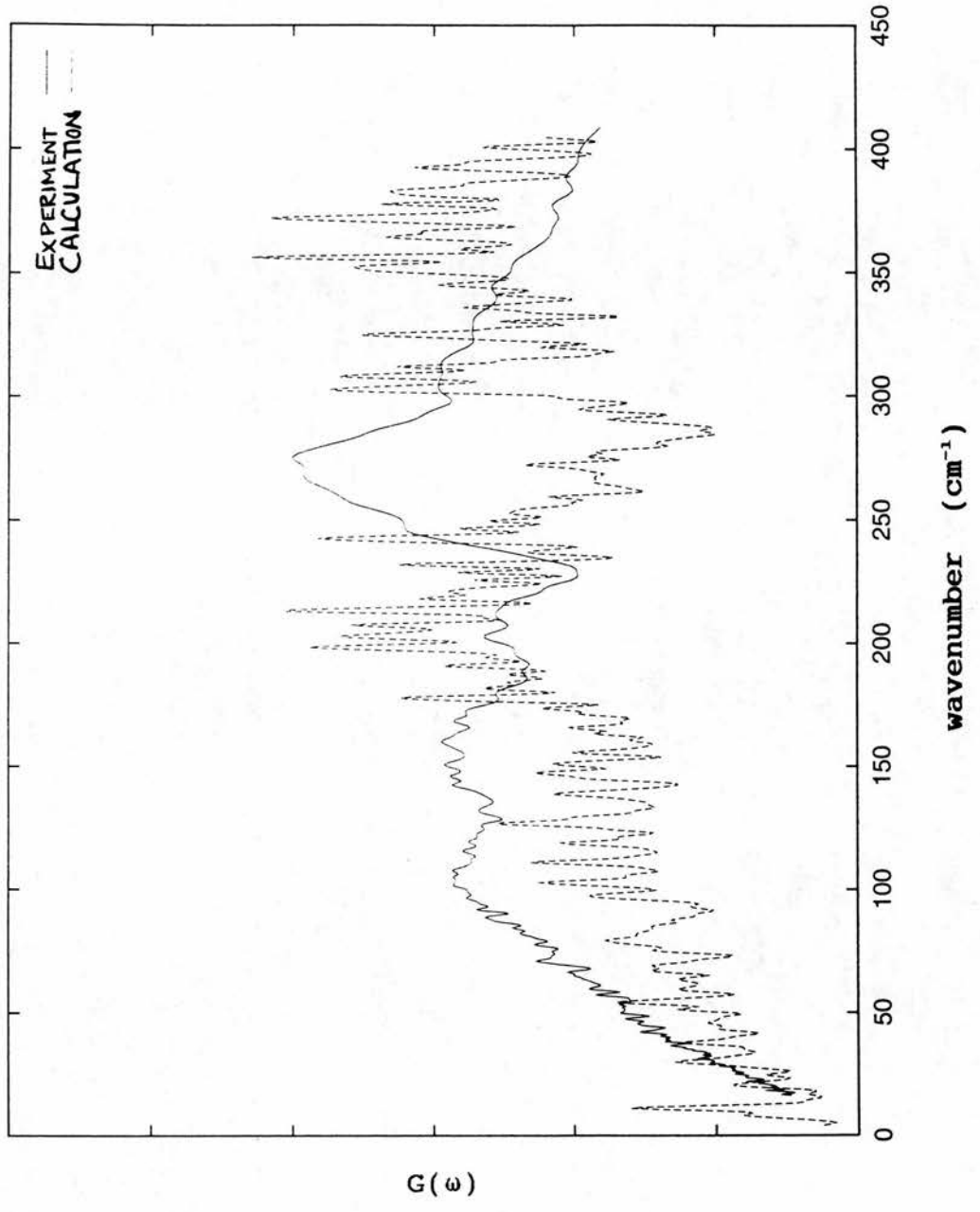


Figure 4.24. Numerical calculation of G(ω) for $(PPG)_{10}$ from molecular dynamics simulation, compared with G(ω) extracted from INS spectrum..

with the experimental density of states extracted for $(PPG)_{10}$ from the INS data as described in Section 4.4.2. Clearly the major problems associated with comparison of the classical dynamic structure factor with the experimental spectra have been circumvented. It is now possible to compare the calculated and experimental density-of-states, in the restricted spectral region up to 400 $cm^{-1}$ where the experimental density of states has been obtained. Although the experimental and calculated spectra really were very different in their details, the demonstration of structure in the calculated density of states of comparable detail to that in the experimental spectra raises the prospect of refining the parameters of the CHARMM PEF to fit the experimental data. Several difficulties for such a project are apparent however. First, though detail is available in the calculated spectra, the features cannot be readily assigned to particular degrees of freedom of the $(PPG)_{10}$ structure. Hence it is impossible to know, *a priori*, which terms of the PEF to improve. A simple trial and error approach is precluded by the complexity of the structure, and the number of different parameters involved, and especially by the prolonged nature of the MD calculations. For each adjustment of the parameters, a new energy minimisation of the structure must be performed, and the MD simulations started from the heating phase. This is simply prohibitively expensive of computational time. One means of achieving assignments of spectral features to particular degrees of molecular freedom is provided by the technique of harmonic vibrational analysis. At the low temperature of 30 K the atoms in the MD simulation have low kinetic energies and make only small excursions from their equilibrium positions. Therefore low temperature MD simulation explores primarily the harmonic region of the potential energy surface round the local minimum

representing the equilibrium structure. Such an MD simulation could be analysed usefully by comparison with an harmonic analysis. Harmonic analyses of molecular vibrational dynamics potentially provide explicit assignments of particular vibrational excitations to particular combinations of molecular degrees of freedom. Unfortunately the $(PPG)_{10}$ system, either in the powder structure or isolated *in vacuo* is too large for harmonic analyses using the current version of CHARMM implemented at Saclay. Therefore, with the aim of gaining insight into the role of proline parameters, an harmonic analysis of PPII was attempted instead. This analysis (and its problems!) are presented next, along with the relevant theory of harmonic vibrational analyses for isolated molecules.

### 4.6.3. Harmonic analysis of PPII.

#### 4.6.3.1. Energy minimisations.

The starting coordinates for PPII were taken from the published x-ray fibre diffraction structure [Cowan and McGavin, 1955]. The x-ray structure of PPII shows a left handed $3_1$ helix of pitch 9.36 Å, and an axial translation per residue of 3.12 Å. A helix of 30 imino acid residues was used in the model, representing 10 turns of this $3_1$ helix. The x-ray structure was refined assuming a quasi-infinite perfect helix, so that the refined structure does not describe effects associated with the terminal regions of individual PPII helices [Cowan and McGavin, 1955]. Therefore the structure refers predominantly to the average structure of the central helical region of the PPII helix. As for $(PPG)_{10}$, only the positions of the heavy atoms were taken from the x-ray structure. The positions of the hydrogens were added using the same facility of the CHARMM program.

With the starting structure for the isolated PPII helix

constructed in this way the potential energy was calculated by use of the current set of CHARMM parameters for proteins, using the PEF described in Chapter III, as for $(PPG)_{10}$. The CHARMM potential energy was then minimised by applying the Adopted Basis Set Newton Raphson algorithm. The energy-minimised model of the isolated molecule was unstable, with a CHARMM potential energy of +422 kcal/mol. The energetic instability arose largely from the existence of marked deviations of bond angles and dihedral angles from the minimum specified by the CHARMM parameters. In particular the dihedral angles of the pyrrolidine ring and the main chain dihedral angles all deviated significantly from their energetic minima. The dihedral angles of the x-ray structure differed even more from the energretic minima, and the x-ray structure was much more energetically unstable than the minimised structure. As noted above the parameters for proline were derived by *ab initio* quantum chemical calculations for acetyl-proline-methylamide. It is possible that these parameters do not describe the energetics of the polymeric form of proline well.

Despite this unsatisfactory energetic instability, the energy-minimised structure was compared with that of the x-ray structure. The minimum root mean square deviation of the atomic Cartesian coordinates (RMS) was calculated, after rigid body reorientations of the whole helix were performed to superimpose the two structures and minimise the RMS. The RMS deviation for all heavy atoms of the structure was 0.984 Å. Hydrogens were excluded because they are not well defined in x-ray diffraction structures. Excluding the terminal 3 residues at each end of the chain, which are likely to be affected most markedly by the end effects neglected in the x-ray structure refinement, the RMS deviation for the heavy atoms alone was 0.820 Å.

As for $(PPG)_{10}$, a major source for the disparity were errors in main chain dihedral angles, which produce a cumulative error in Cartesian coordinates when propagated over several helical repeats. In fact, when a single helix turn from the central region of the energy-minimised was compared with the x-ray diffraction structure, the RMS deviation for the heavy atoms was only 0.392 Å, demonstrating that propagation of errors in dihedral angles was indeed an important source of RMS differences in the cartesian coordinates. A more detailed comparison in terms of the values of internal coordinates (especially bond and dihedral angles) revealed several marked local deviations of the energy minimised structure from the x-ray structure. These were most marked in the terminal regions, as expected given the influence of end effects. Elsewhere however main chain dihedral angles, and pyrrolidine ring dihedrals differed by up to 20° from the x-ray values. From one residue to the next in the central region of the helix, however, the equivalent dihedral and bond angles differed by less than 2°, indicating the regular structure of the helix was well preserved in the energy-minimised structure.

A check was made to determine whether the stability of the PPII helix in powder form was significantly affected by the environment of the molecule. To provide a more realistic representation of the structure of the powder samples used for the INS experiments, the close packed environment of the powder was modelled by the generation of images of the primary PPII molecule on a hexagonal lattice with radial distance between the centre of neighbouring helices of 6.7 Å, in close agreement with the results of powder diffraction studies. The length of the hexagonal cell was fixed at 96 Å, sufficient to accommodate the undistorted PPII helix, though no direct experimental data was available for this dimension. The

energy-minimised structure for this model including the powder environment, was still unstable with a final CHARMM potential energy of + 60 kcal/mol. Furthermore the anisotropic environment of the helix arising from end effects and packing in the hexagonal lattice ensured that the regular helical structure was not perfectly maintained. The RMS deviations from the x-ray structure were larger than for the isolated model. For these reasons, and because the model including the powder environment was too big for conducting harmonic dynamics calculations, the dynamical calculations were restricted to the isolated PPII molecule.

**4.6.3.2. Harmonic analyses.**

The energetic instability of the PPII model precluded investigation of the dynamics by MD simulations because the energy-minimised structure presumably lies in a local minimum of the PEF near the x-ray structure. Thermal energy introduced in MD simulations would allow the structure to escape this local minimum, and drift further away from the x-ray structure, making the calculated trajectory largely irrelevant to the conditions of the INS experiment. Therefore the harmonic approximation was used for the dynamical calculations. For the harmonic approximation the absolute value of the energy at the minimum is irrelevant, though the fact that the structure appeared to be unstable in the CHARMM model remains an unsatisfactory result. Harmonic dynamics depend only on the second derivatives of the potential energy surface in the immediate vicinity of the local minimum. The harmonic approximation is most relevant at low temperatures. This approach is therefore relevant to the circumstances of the INS experiment, since the experiments were conducted at 30 K.

Harmonic analyses were performed on the energy-minimised

isolated molecule. Inclusion of the powder environment presented too large a computational task. The unsatisfactory device of simply ignoring the powder environment, which can be expected to have a significant effect especially on the lowest frequency modes of the molecule, can only be justified if it is assumed that higher frequency features are little affected by the environment of the molecule, but instead depend on internal properties of the molecule. This however is an assumption underlying any study of the dynamics of a molecule *in vacuo* [Smith, 1991].

The theory of molecular vibrations in the harmonic approximation has been given by Wilson *et al.*, 1980, and will be reviewed briefly here. The theory applies to any collection of atoms, whether bonded or not, for which a potential energy can be calculated as function of the atomic coordinates.

The position of the $\alpha^{th}$ atom in the structure, containing a total of N atoms, is denoted by:

$$\mathbf{R}_\alpha = \mathbf{l}_\alpha + \mathbf{u}_\alpha \qquad (4.6.9)$$

where $\mathbf{l}_\alpha$ is the equilibrium position, and $\mathbf{u}_\alpha$ is the displacment of atom $\alpha$ from the equilibrium position, with Cartesian components $u_{\alpha i}$, i = 1,2,3. The potential energy of the atoms U is assumed to be lowest when all the **u**'s are zero, so that the $\mathbf{l}_\alpha$ corresponds to the position of the $\alpha^{th}$ atom in the energy-minimised structure. Expanding U in a Taylor series around the minimum equilibrium value $U_o$, the first non-zero term of the expansion must therefore be quadratic in the **u**'s. Neglecting all higher order terms in the Taylor series expansion yields the harmonic approximation to the potential energy.

$$U-U_o = \tfrac{1}{2} \sum_\alpha \sum_i \sum_\beta \sum_j u_{\alpha i} A_{\alpha i \beta j} u_{\beta j} + \ldots\ldots \qquad (4.6.10)$$

By the equality of mixed partial derivatives, the $A_{\alpha i \beta j}$, the second-order derivatives of the PEF with respect to atomic displacements, satisfy:

$$A_{\alpha i \beta j} = A_{\beta j \alpha i} \qquad (4.6.11)$$

This force constant matrix can be constructed by numerical differentiation of the CHARMM PEF with respect to atomic coordinates.

The classical Hamiltonian in the harmonic approximation is:

$$H_{cl} \qquad (4.6.12)$$

$$= \sum_{\alpha} \sum_{i} 1/2M \; p_{\alpha i}^{2} + \tfrac{1}{2} \sum_{\alpha} \sum_{i} \sum_{\beta} \sum_{j} u_{\alpha i} \; A_{\alpha i \beta j} \; u_{\beta j}$$

where M is the mass of the nucleus and $\mathbf{p}_{\alpha}$ the momentum conjugate to $\mathbf{u}_{\alpha}$, with Cartesian components $p_{\alpha i}$.

The equation of motion for the atom $\alpha$ is:

$$M\ddot{u}_{\alpha i} = -\sum_{\beta} \sum_{j} A_{\alpha i \beta j} \; u_{\beta j}. \qquad (4.6.13)$$

There are three such equations for each atom $\alpha$, corresponding to each Cartesian direction i. This set of 3N linear equations can be reduced to a set of 3N independent harmonic oscillators by introduction of normal coordinates. First letting the displacements have a time dependence $\cos(\omega t)$:

$$-M\omega^{2}u_{\alpha i} = -\sum_{\beta} \sum_{j} A_{\alpha i \beta j} \; u_{\beta j} \qquad (4.6.14)$$

The above set of 3N equations has 3N linearly independent solutions labelled for convenience by the index l, each characterised by a 3N dimensional eigenvector $\mathbf{e}_{l}$, and an eigenvalue $\omega_{l}$, which gives the time dependence of the

atomic motion along the eigenvector $e_l$. Because there are three rigid body translational and three rigid body rotational degrees of freedom for an isolated molecule, six solutions have zero frequency. Any solution of the classical equations of motion for the 3N-6 internal degrees of freedom of the molecule in the harmonic approximation can then be represented by a superposition of 3N-6 harmonic motions.

$$u_{\alpha i}(t) = \sum_{l=1}^{3N-6} A_l \, e_{\alpha il}/(M_\alpha)^{\frac{1}{2}} \cos(\omega t + \phi_l) \qquad (4.6.15)$$

where $A_l$ is an amplitude and $\phi_l$ a phase of the oscillator l. According to the equipartition theorem of classical mechanics, in thermal equilibrium at a temperature T the amplitude $A_l$ obeys:

$$(A_l)^2 = k_B T/(\omega_l)^2 \qquad (4.6.16)$$

where $K_B$ is Boltzmanns constant.

A quantized treatment of the harmonic approximation reveals that for a given PEF, the eigenvectors and eigenvalues of the classical Hamiltonian are the same as those of the quantised Hamiltonian. The main difference from the classical treatment arises from the quantisation of excitations of the harmonic oscillators, and the consequent Bose statistics for occupancy of the quantized energy levels [Lovesey, 1984]. The amplitude $A_l$ takes discrete quantized values, and obeys:

$$(A_l)^2 = \hbar/2\omega_l \coth(\hbar\omega_l/2K_B T) \qquad (4.6.17)$$

Thus, changing notation, the eigenvectors for each atom, $e_{\alpha l}$, and the eigenfrequencies $\omega_l$ were calculated for PPII using the VIBRATION facility of the CHARMM program.

**4.6.3.3. INS intensities from harmonic analyses.**

All of the calculations described in this section used a program package I wrote in Fortran during an EMBO short term fellowship spent in Dr Jeremy Smith's laboratory.

Under the assumption of harmonic dynamics the transforms in Eq. 4.2.2 may be performed analytically, and the result expanded in a power series over the normal modes of the molecule, labelled l [Zemach and Glauber, 1956]. The following expression is obtained:

$$S(\mathbf{Q},\omega) \qquad (4.6.18)$$

$$= \sum_{\alpha} \exp[-2W_{\alpha}(\mathbf{Q})]$$

$$\times \prod_{l} [\sum_{n} \exp[n_l \hbar\omega_l \beta/2] \, In \, [\hbar(\mathbf{Q}.\mathbf{e}_{l\alpha})^2/2M\omega_l \sinh(\hbar\omega_l\beta/2)]]$$

$$\times \delta[\omega - \sum_{l} n_l\omega_l]$$

$W_{\alpha}(\mathbf{Q})$ is the exponent of the Debye-Waller factor, $\exp[-2W_{\alpha}(\mathbf{Q})]$ for hydrogen atom $\alpha$ which may also be expressed in terms of a sum over the normal modes:

$$2W_{\alpha}(\mathbf{Q}) \qquad (4.6.19)$$

$$= Q^2 \langle u_{\alpha}^2 \rangle$$

In the above equations N is the number of normal modes, M the hydrogen mass, l labels the normal mode, $n_l$ is the number of quanta exchanged with the normal mode labeled l, $n(\omega_l)$ is the Bose occupancy, $\mathbf{e}_{l\alpha}$ is the atomic eigenvector for hydrogen $\alpha$ in the normal mode l, and $\omega_l$ the mode angular frequency. $\beta = 1/k_B T$ where $k_B$ is Boltzmann's constant and T the temperature. $I_n(x)$ is the $n_l$th order modified Bessel function. $\langle u_{\alpha}^2 \rangle$ is the atomic mean square displacement.

Eq. 4.6.18 is an exact quantum mechanical expression. It can be interpreted as follows. The Bose occupancies determine the energy distribution amongst the modes, ensuring that processes involving neutron energy gain are weaker than those involving neutron energy loss, in compliance with the quantum principle of detailed balance. In the present case the experimental data were neutron energy loss spectra and the calculations were restricted to this part of the spectrum. The case where all of the $n_\lambda$ equal zero corresponds to elastic scattering. The case where $\sum_\lambda n_\lambda = 1$ corresponds to single quanta processes. The case where $\sum_\lambda n_\lambda = 2$ corresponds to two quanta processes. Higher terms represent multiquanta scattering. Inserting the calculated eigenvectors and eigenvalues from the harmonic analyses into Eqs. 4.6.18 and 4.6.19, allows a calculation of the incoherent INS in the harmonic approximation to any degree of multiquanta scattering. In the present work a one-quantum calculation was made.

The label $\lambda$ runs over the 3N-6 = 1269 normal modes calculated for the 30 residue model of PPII. To take account of the isotropic nature of the powder sample, whilst retaining a computational task of reasonable size, the incoherent INS spectra were calculated for the three principal directions of the neutron scattering vector relative to the molecular structure and the resulting spectra summed.

The experimental values for the average atomic Debye Waller factor was estimated from quasi-elastic experiments to be 0.018 +/- 0.005 Å$^2$. This estimate was tested in the calculation of the INS intensity by using the experimental values for the average mean square displacement $\langle u^2 \rangle$ discussed in Section 4.4.2 to replace $\langle u_\alpha^2 \rangle$ in Eq. 4.6.19. The relation between $Q^2$ and $\alpha$ for TFXA spectra (Chapter III) produces rapid variation at high energy transfer, of the factor $\exp\{-2W_\alpha(\mathbf{Q})\}$ in Eq. 4.6.18. As a result relative

peak intensities in the high frequency region are highly sensitive to $\langle u_\alpha^2 \rangle$. The comparison of experimental and calculated INS intensities over a wide range in energy transfer, from 20 to 3600 $cm^{-1}$ therefore provides a sensitive test of the values used for the atomic mean square displacements. Proceeding on this basis INS intensities were calculated for the harmonic model. A value for the mean square displacement of 0.023 $Å^2$ (i.e. at the upper limit of the experimental estimate) gave the best agreement with the experimental distribution of INS intensity between low (< 400 $cm^{-1}$), intermediate (400 - 2000 $cm^{-1}$) and high (> 3000 $cm^{-1}$) frequency regions, although the detailed agreement with the experimental intensities was very poor. This higher value for the average mean square displacment was in better agreement with the values calculated for acetanilide at 25 K (Chapter V, Table 5.4).

Again extensive refinements of the parameters would be required to produce a spectrum sufficiently comparable with the experimental spectrum to provide useful assignments of the spectral features. Given the difficulties associated with the energetic instability of the PPII helix, and the problems of an harmonic analysis *in vacuo* for such an extended molecule, such a refinement was not attempted. It was first decided to establish the general feasibility of refining the parameters of the CHARMM PEF for a smaller, simpler, and better characterised system.

### 4.6.4. Summary and conclusions from the numerical calculations.

The numerical calculations of this Chapter dealt with INS data for a natural protein and two polypeptide models. The CHARMM PEF and program were used to examine the structure of the model polypeptide (ProlylProlylGlycine)$_{10}$ (PPG)$_{10}$.

Calculations were performed for the isolated molecule, and for a model simulating the powder environment. The commonly used parameters of the PEF for proteins yielded a stable energy-minimised structure for $(PPG)_{10}$ showing significant deviations from the x-ray structures. These deviations were largely explicable in terms of understandable effects, including uncertainty in the x-ray structure itself. A molecular dynamics simulation was performed for $(PPG)_{10}$ in the powder environment and the program n-MOLDYN used to calculate a hydrogen-weighted vibrational density-of-states below 400 $cm^{-1}$ from the trajectory. This was compared with the hydrogen-weighted density-of-states extracted from the INS experimental data. The agreement was poor. The complexity of the $(PPG)_{10}$ structure and the computational size of the calculations precluded direct improvement of the potential energy parameters for $(PPG)_{10}$. The parameters for proline and proline-proline bonds were further tested by calculations for the simpler homopolypeptide PPII. The energy minimised structure again deviated significantly from the x-ray structure, and was energeticlly unstable both *in vacuo* and in a model simulating the powder environment. This instability precluded an MD simulation of the dynamics for PPII. A harmonic analysis of the dynamics of PPII *in vacuo* was made. Incoherent neutron scattering spectra were calculated in the harmonic approximation for the isolated molecule. The calculated spectra were compared with experiment. Again the agreement was poor. The computational difficulties for even this simple homopolypeptide system together with uncertainty in the structural data, and the complexity of the INS spectra, prevented direct improvement of the parameters. This experience with macromolecular systems suggested the need to study simpler molecular systems, for which more detailed structural and spectroscopic data was available.

## CHAPTER V - DYNAMICS OF CRYSTALLINE ACETANILIDE: ANALYSIS USING INELASTIC NEUTRON SCATTERING AND COMPUTER SIMULATION.

Problems with a numerical model for the dynamics of two polypeptides were demonstrated in Chapter IV, and the difficulties of directly improving the model for macromolecules discussed. The need to study simpler systems was indicated. Crystalline acetanilide ($C_6H_5CONHCH_3$) has been considered a useful model for α-helical polypeptides because of its structure. (This molecule is therefore not of relevance to the parameters for proline or imide bonds or directly to collagen, polyproline or polyprolylprolylglycine.) Acetanilide contains a planar -NHCO- group with geometry close to that for the peptide bond of proteins. The molecules of acetanilide are hydrogen bonded in parallel chains in the crystal, and the geometry of the hydrogen bond is close to those in α-helices of proteins. The dynamics of crystalline acetanilide have been the subject of recent interest due to the anomalous temperature dependence of several vibrational optical spectroscopic bands. The Amide I anomaly has been attributed to solitonic or polaronic dynamical behaviour, and similar non-linear dynamics may provide a mechanism for efficient vibrational energy localisation and transport in proteins. In the work described in this Chapter the vibrational dynamics of crystalline acetanilide were examined over a spectral range of 20 - 4000 $cm^{-1}$ using inelastic neutron scattering (INS) experiments, phonon normal mode analyses and molecular dynamics (MD) simulations, and calculations of INS spectra. The experimental INS spectra provide detailed information on the vibrations of the hydrogen atoms in the crystal. A molecular mechanics energy function was used to perform normal mode calculations in the full configurational space of the crystal. The resulting

normal modes provide a description of the dynamics in the harmonic approximation, including intra-molecular modes and inter-molecular lattice modes. The force field was parameterized to reproduce the optical frequencies, and the neutron intensities at 25 K in the incoherent approximation. A complete assignment of the fundamental modes was achieved. Incoherent INS intensities in the one-, two- and three-phonon approximation were calculated. Anharmonic effects were examined using the full potential function for MD simulations of the crystal between 80 and 300 K. Several of the calculated spectral features exhibit temperature-dependent behaviour in qualitative agreement with experiment, including the amide hydrogen out-of-plane mode, the methyl torsional libration and the lattice vibrations. The temperature dependence of the Amide I mode was not reproduced. The significance of these results for the interpretation of the anomalous spectroscopic behaviour is discussed.

## 5.1. INTRODUCTION

### 5.1.1 Why study molecular crystals?

The previous chapter dealt with INS data for a natural protein, including numerical simulations of the dynamics of two simpler polypeptide models. These simulations were used to calculate quantities comparable with data extracted from experimental INS spectra, and the agreement was poor. The computational difficulties for even the simple homopolypeptide system, Polyproline II, together with uncertainty in the structural data and in spectroscopic assignments, prevented direct improvement of the dynamical simulations. This experience with macromolecular systems suggested the need to study simpler molecular systems, for which more detailed structural and spectroscopic data is available in the hope that improvements in the parameters for these simpler systems

will be readily transfered to macromolecules. A similar strategy has been adopted by others in the development of parameters for macromolecules on the basis of *ab initio* quantum chemical calculations, which are currently possible only for small model systems [Guo and Karplus, 1992; Reiher and Karplus, 1993; Micu *et al.*, in press]. Molecular crystals provide simple, structurally well-characterized systems for the determination of environmental effects on molecular vibrations.

### 5.1.2. Why choose acetanilide?

Acetanilide ($CH_3CONHC_6H_5$, or N-phenyl acetamide) forms molecular crystals of particular biological interest [Careri *et al.*, 1984], and was chosen for the work described in this Chapter for three main reasons:

**i)** Acetanilide contains a peptide group that links the molecules of the crystal together via hydrogen bonds in parallel chains [Wasserman *et al.*, 1985; Brown and Corbridge, 1954]. The geometry of the peptide group and the hydrogen bonds are close to those in $\alpha$-helices of proteins [Careri *et al.*, 1984]. These similarities prompt the hope that accurate parameters for the PEF of acetanilide might be transferable to proteins. Similar reasoning has been applied to the peptide bond model molecule N-methyl acetamide (NMA). Indeed extensive optical spectroscopic investigations and harmonic models of the dynamics of NMA underly much of the current interpretation of polypeptide infra-red (IR) and Raman spectra in terms of peptide group dynamics [Krimm and Bandekar, 1986]. The harmonic calculations have been predominantly based on models of the isolated NMA molecule, and this restricts the information available on the hydrogen bond dynamics. Modern computational power makes it possible to perform calculations which explicitly

include the influence of the crystal environment on molecular vibrations. These calculations rely on empirical parameterisation of a PEF for the molecular system. Parameter development for hydrogen bonded peptide groups has been based on *ab initio* quantum chemical calculations for NMA [Guo and Karplus, 1992; Reiher and Karplus, 1993]. Important information on the hydrogen bond dynamics of peptide groups and improvement in parameterisation should emerge from experimental and theoretical calculations for acetanilide in the crystalline state.

**ii)** Recently, INS spectroscopy of crystalline NMA has suggested a radical new interpretation of peptide group dynamics [Kearley *et al.*, 1994]. One aspect of these INS studies was the parameterisation of an harmonic model for an isolated molecule of NMA and the calculation of incoherent INS spectra from the resulting harmonic dynamics [Fillaux *et al.*, 1993]. Difficulties in achieving an adequate fit to the experimental data were solved by separating the dynamics of the amide hydrogen and the methyl group dynamics from those of the heavy atom skeleton. Furthermore the suggestion was made that the hydrogen bond between NMA molecules in the crystal is of partial ionic character with a near symmetric double minimum form for the potential energy for NH bond stretching. An extraordinarily low value of 1575 $cm^{-1}$ for the NH stretch frequency was derived [Fillaux *et al.*, 1993; Kearley *et al.*, 1994]. However, one general objection to the calculations leading to this model is the use of a parameterisation for the isolated molecule to derive conclusions for the dynamics of the crystal. The extensive division of the dynamical problem into independent sub-problems also raises questions about the generality of the model. The new interpretation requires confirmation therefore, and particularly its generality

tested for other peptide bond model compounds. If generally correct such an interpretation would have important implications for dynamical models of proteins, and for the practical interpretation of optical spectroscopy of proteins. One reason why an isolated molecule model was adapted to calculating INS data for crystalline NMA is the current lack of accurate knowledge of the crystal structure for NMA. In contrast the crystal structure of acetanilide has been determined at two temperatures, 300 K and 113 K [Brown and Corbridge, 1954; Wasserman *et al.*, 1985]. Acetanilide is therefore an appropriate test case for INS experiments and for calculations based on a full description of the crystal environment.

**iii)** IR and Raman spectroscopy have revealed intriguing anharmonic dynamics in the acetanilide crystal [Careri *et al.*, 1984]. An anomalous excitation at 1650 $cm^{-1}$ has an unusual temperature dependence and IR overtone spectrum [Scott *et al.*, 1985]. This has led to its assignment to absorption by a localized, self-trapped, CO vibrational excitation, modeled by soliton [Eilbeck *et al.*, 1984] or by polaron [Alexander and Krumhansl, 1986] theories. Analytical soliton and polaron theories are formulated in this context by extending an harmonic Hamiltonian for atomic displacements by inclusion of cubic or quartic anharmonic terms that lead to strong coupling of low-frequency modes with high frequency intra-molecular modes [Eilbeck *et al.*, 1984; Alexander and Krumhansl, 1986; Scott *et al.*, 1989]. The resulting non-linear equations have solutions, termed solitons or polarons, describing spatial localization of vibrational energy. Under certain conditions on the parameters of the models, solitons or polarons can be mobile and long lived, and hence capable of transporting vibrational energy with the remarkable

features of localisation of the wavepacket, and stability of the wavepacket to random geometric perturbations or dynamic thermal perturbations [Scott, 1992; Krumhansl, 1987; Förner, 1993]. From a teleological viewpoint such a mechanism is ideally suited for transport of vibrational energy in an enzyme across distances of many Angstroms, for example from a site of adenosine triphosphate hydrolysis to a distant active site. The soliton mechanism offers the distinct biological advantage, over harmonic wavepackets, of minimal energy dispersion or energy loss in the presence of a wide variety of perturbations. This has prompted a widespread search for evidence of soliton dynamics in natural biological molecular systems, but direct experimental evidence in molecular systems is lacking, despite examples of soliton wave behaviour in other natural phenomena [Scott, 1992; Förner, 1993]. This is the reason for intense interest in the soliton interpretation of the optical anomalies in the acetanilide crystal, viewed as a model for $\alpha$-helices in protein. To derive analytically tractable models for solitonic or polaronic energy transport in chains of hydrogen-bonded peptide groups it has been necessary to considerably simplify the description of the potential energy surface of the system. As a result, anharmonic terms are neglected that might play a role in determining the existence and lifetime of any self-trapped state, by coupling it to other excitations in the crystal [Förner, 1993]. Indeed, explanations of the temperature dependence of the anomalous amide I peak that do not involve self-trapped states have been proposed, including temperature tuning of Fermi resonance [Johnston and Swanson, 1985] or slight non-degeneracy of amide hydrogen atom positions in the crystal [Fann *et al.*, 1990]. Furthermore, recent experiments have identified several more anharmonic features in the optical spectra: the amide hydrogen out-

of-plane bending mode and low-frequency vibrations (<150 $cm^{-1}$) also manifest an unusual temperature dependence [Sauvajol *et al.*, 1989; Barthes *et al.*, 1992; Johnston *et al.*, 1991; Barthes *et al.*, 1988]. The above considerations indicate a limitation of simplified dynamical descriptions. While providing important insight into the specific phenomena which they model, they do not aim to provide a complete description of the dynamics. This can be obtained, in principle, by working in the full, 3N-dimensional configurational space of the crystal (where N is the number of atoms in the system) using computer simulation methods, with the aim of describing all structural and dynamical features of the crystal in a unified fashion. Numerical simulations of alkane polymers have detected soliton excitations, without the explicit inclusion of strong non-linear coupling terms, indicating that simple molecular mechanics PEFs are capable of producing non-linear soliton dynamics in a natural fashion [Doherty and Hopfinger, 1994].

### 5.1.3. Computational simulation of INS from molecular crystals.

The computer simulation of condensed phases using molecular mechanics energy functions is now commonplace [Allen and Tildesley, 1987]. The combination of MD simulation with INS provides a means of probing in detail the hydrogen atom dynamics in molecules, as the time and length scales accessible to INS and MD are the same, and the computation of INS intensities from atomic trajectories is relatively straightforward. In recent work this approach has been used to study the dynamics in pure and doped polyacetylene [Dianoux, *et al.*, 1993; Dianoux *et al.*, 1994], in the alanine dipeptide [Kneller, *et al.*, 1992], in L-alanine crystals [Micu *et al.*, in press] and in proteins [Smith *et al.*, 1990a; Smith *et al.*, 1990b;

Smith, 1991]. In the present Chapter I describe the application of the combined simulation/INS approach to examine the dynamics of crystalline acetanilide and to improve the dynamical model by refining the parameters of the PEF. The work proceeded in three stages, firstly refinement of the CHARMM parameters for ACN, secondly calculation of phonon dispersion relations and anharmonic dynamics, and thirdly further refinement of parameters for ACN, ACN-D5 and ACN-D8 together. This chapter describes the first two stages. Firstly, an improved parameterisation was obtained for fully hydrogenous acetanilide (ACN). Energy minimized structures and harmonic analyses of the ACN crystal were compared with low-temperature structural and spectroscopic data. The normal modes provide a description of the low-temperature intra-molecular and lattice vibrations. From the harmonic analysis results the incoherent INS intensities were calculated and compared with experimental data collected by Dr. H.D. Middendorf, Clarendon Laboratory, Oxford University. In a second stage the improved parameterisation was used to calculate phonon dispersion curves for fully deuterated acetanilide-D9, (ACN-D9), and the results compared with others' coherent INS experiments [Barthes *et al.*, 1988]. The full, anharmonic potential function was used in MD simulations of the ACN crystal at 80K, 140K and 300K. A number of the calculated spectral features exhibit temperature-dependence in agreement with experiment, including the amide hydrogen out-of-plane mode, the methyl torsional libration and the lattice vibrations. The results of this second stage can be viewed as independent tests of the parameterisation because no further adjustments of the parameters were made at this stage. I emphasise that all the structural and dynamic results presented in this Chapter are derived consistently from the final refined parameterisation given in Table

5.1, except where explicitly stated. All the calculations of this Chapter were carried out using the Hewlett Packard 9000/735 workstation computers in Dr. Smith's Laboratory.

Given the encouraging results described in this present Chapter, a third stage of work has been started. Further experiments were performed by myself and Dr. H.D. Middendorf, using the TFXA spectrometer to collect INS data for acetanilide-D8 (ACN-D8) and acetanilide-D5 (ACN-D5). ACN-D8 has all hydrogens except the amide hydrogen exchanged for deuterium, ACN-D5 has all phenyl hydrogens exchanged for deuterium. Comparison of the data with calculations based on the parameters derived in the present Chapter indicated several improvements which could be made. The next short Chapter (Chapter VI) describes these further refinements and discusses the comparison of harmonic calculations with the experimental INS data for all three isotopomers of acetanilide ACN, ACN-D5, and ACN-D8.

## 5.2. METHODS

### 5.2.1. The dynamic structure factor, S(Q,w), for molecular crystals.

For ACN, 9 of 19 atoms are hydrogen and the total hydrogen incoherent scattering cross section is 89% of the total cross section [Chapter II]. Neutron scattering from ACN is therefore dominated by incoherent scattering from the hydrogen atoms. The amplitude-weighting of scattered intensity leads to an even heavier predominance of incoherent scattering from the hydrogen atoms, which because of their small mass tend to make the largest excursions. In the present calculations only the contribution from the hydrogen atoms was included.

The inelastic scattering process probes time-dependent correlations of atomic positions [Chapter II; Lovesey, 1984; Middendorf, 1984]. For incoherent scattering the

Table 5.1. The refined set of parameters for the potential energy function. Units are $k_b$ kcal/mol/Å$^2$, $b_o$ Å, k kcal/mol/radian$^2$, $Y_o$ degrees, $k_u$ kcal/mol/Å$^2$, $u_o$ Å, k kcal/mol, $\delta$ degrees, $k_\omega$ kcal/mol/radian$^2$, $\omega_o$ degrees, $\epsilon$ kcal/mol, $r_{min}/2$ Å, $\epsilon_{1:4}$ kcal/mol, $r_{min}/2$ Å. The atomic partial charges, in units of the electron charge, for the phenyl group atoms, labelled relative to the carbon * at the N-substitution site are: a - carbons: * 0.0788, *ortho* -0.16845, *meta* -0.10275, *para* -0.1562. a - hydrogens: *ortho* 0.15075, *meta* 0.1339, *para* 0.1341.

| BONDS | $k_b$ | $b_0$ | | |
|---|---|---|---|---|
| $C_{ph}C_{ph}(ortho)$ | 380.0 | 1.375 | | |
| $C_{ph}C_{ph}(para)$ | 400.0 | 1.375 | | |
| $C_{ph}C_{ph}(meta)$ | 405.0 | 1.375 | | |
| $C_{me}C$ | 275.0 | 1.505 | | |
| $C_{me}H$ | 322.0 | 1.085 | | |
| $C_{ph}H$ | 340.0 | 1.080 | | |
| $C.N$ | 320.0 | 1.360 | | |
| $C_{ph}.N$ | 310.0 | 1.445 | | |
| $NH$ | 432.0 | 0.997 | | |
| $CO$ | 620.0 | 1.237 | | |
| ANGLES | $k_\theta$ | $\theta_0$ | $k_u$ | $u_0$ |
| $C_{ph}C_{ph}C_{ph}$ | 36.0 | 120.0 | 35.0 | 2.4162 |
| $C_{ph}.NC$ | 37.0 | 120.0 | | |
| $H.NC$ | 32.0 | 123.0 | | |
| $HNC_{ph}$ | 32.0 | 117.0 | | |
| $HC_{me}C$ | 30.0 | 109.5 | 30.0 | 2.163 |
| $HC_{me}H$ | 34.5 | 108.4 | 5.4 | 1.802 |
| $HC_{ph}C_{ph}(ortho)$ | 26.0 | 120.0 | 22.0 | 2.1525 |
| $HC_{ph}C_{ph}(meta)$ | 25.0 | 120.0 | 22.0 | 2.1525 |
| $HC_{ph}C_{ph}(para)$ | 25.0 | 120.0 | 22.0 | 2.1525 |
| $NC_{ph}C_{ph}$ | 32.0 | 120.0 | 22.0 | 2.1525 |
| $NCC_{me}$ | 70.0 | 116.5 | | |
| $OCC_{me}$ | 70.0 | 123.0 | | |
| $OCN$ | 70.0 | 121.5 | | |

Table 5.1 (continued)

| DIHEDRALS | $k_\phi$ | $n$ | $\delta$ | | |
|---|---|---|---|---|---|
| $C_{ph}C_{ph}C_{ph}C_{ph}(ortho/para)$ | 4.40 | 2 | 180.0 | | |
| $C_{ph}C_{ph}C_{ph}C_{ph}(meta)$ | 2.00 | 2 | 180.0 | | |
| $C_{me}C.NH.C_{me}C.NC_{ph}$ | 2.40 | 2 | 180.0 | | |
| $OC.NH.OC.NC_{ph}$ | 2.40 | 2 | 180.0 | | |
| $H.NC_{ph}C_{ph}$, $C.NC_{ph}C_{ph}$ | 0.69 | 2 | 180.0 | | |
| $HC_{ph}C_{ph}C_{ph}$ | 3.92 | 2 | 180.0 | | |
| $HC_{ph}C_{ph}H$ | 2.35 | 2 | 180.0 | | |
| $NC_{ph}C_{ph}C_{ph}$ | 3.00 | 2 | 180.0 | | |
| $NC_{ph}C_{ph}H$ | 2.35 | 2 | 180.0 | | |
| $NCC_{me}H$ | 0.87 | 3 | 0.0 | | |
| $OCC_{me}H$ | 0.87 | 3 | 0.0 | | |
| IMPROPER | $k_\omega$ | $\omega_0$ | | | |
| $CC_{me}.NO$ | 85.0 | 0.0 | | | |
| VAN DER WAALS AND PARTIAL CHARGES | $\epsilon$ | $r_{min}/2$ | $\epsilon_{1:4}$ | $r_{min\ 1:4}/2$ | partial charge |
| $C$ | -0.110 | 2.0000 | | | 0.50 |
| $C_{ph}$ | -0.070 | 1.9924 | | | [a] |
| $C_{me}$ | -0.080 | 2.0600 | -0.01 | 1.9000 | -0.247 |
| $H$ | -0.046 | 0.2245 | | | 0.28 |
| $H_{me}$ | -0.022 | 1.2000 | | | 0.1078 |
| $H_{ph}$ | -0.030 | 1.3582 | -0.030 | 1.3582 | [b] |
| $N$ | -0.200 | 1.8500 | -0.200 | 1.5500 | -0.49 |
| $O$ | -0.120 | 1.7000 | -0.120 | 1.4000 | -0.45 |

dynamic structure factor, $S_{inc}(\mathbf{Q},\omega)$, is a sum, over all the atoms of the system, of a dynamic structure factor $S_{\alpha inc}(\mathbf{Q},\omega)$ for each atom $\alpha$. As only hydrogen incoherent scattering was included in the calculations I drop the subscript 'inc' in the analysis, and sum over the hydrogens of the system. $S(\mathbf{Q},\omega)$ may be expressed as a time Fourier transform of an incoherent intermediate scattering function, which in turn is a spatial Fourier transform of the van Hove self correlation function [van Hove, 1954; Chapter II]. This formulation is useful for the analysis of harmonic dynamics, and of MD results described in this Chapter.

$$S(\mathbf{Q},\omega) = 1/2\pi \int dt \exp(-i\omega t)\, F(\mathbf{Q},t) \qquad (5.2.1)$$

$$F(\mathbf{Q},t) = \sum_{\alpha} b_{\alpha inc}^{2} \langle \exp(-i\mathbf{Q}.\mathbf{R}_{\alpha}(0))\, \exp(i\mathbf{Q}.\mathbf{R}_{\alpha}(t)) \rangle$$

The limits of the integral are +/- $\infty$. The position of atom $\alpha$ is specified by the time dependent operator $\mathbf{R}_{\alpha}(t)$ which acts on the state space of the target. $b_{\alpha inc}^{2}$ is the incoherent scattering cross section of atom $\alpha$. The brackets <..> denote an equilibrium thermal average over the unperturbed states of the target sample. It is tacitly assumed in Eq. (5.2.1) that multiple scattering is negligible, a good approximation for the experimental conditions used here [Chapter III and Goyal *et al.*, 1986].

For crystalline samples there are no symmetry restrictions on the observable excitations. INS intensity calculations are therefore much simpler than those of IR or Raman intensities, which require knowledge of transition dipole moments or the molecular polarizability tensor respectively, and are complicated by selection rules [Cheam and Krimm, 1985; Goodman *et al.*, 1991].

### 5.2.2. INS experiments.

The ACN was purchased from BDH chemicals Ltd., Poole, England, better than 99.5% pure, and used without further purification. IR spectra were collected for the polycrystalline powder in KBr discs on a Nicolet 7000 Series Fourier Transform Infrared Spectrometer in the Chemistry Department, Edinburgh University. These spectra were collected by me with the help of Dr. C. Pulham of the Chemistry Department, Edinburgh University (Fig. 5.1). The IR spectra confirmed the crystalline form of the sample, and were in agreement with those published for crystalline ACN, including demonstrations of the amide I anomaly [Careri *et al.*, 1984; Tariq *et al.*, 1984]. INS spectra were taken at 25 K on the Time Focusing Crystal Analyser (TFXA) at the ISIS spallation source, Rutherford Appleton Laboratory (Fig. 5.2). Dr. H.D. Middendorf collected the INS data for polycrystalline ACN, but he and I collected the data for the deuterated forms as described in the following Chapter, using the same experimental protocol. The samples were contained in aluminium cells, the scattering from which was < 0.5% of the total scattering. The depth of the sample along the axis of the incident neutron beam was 1 mm. A complete description of the experimental arrangement for TFXA can be found in Chapter III. As a consequence of the conservation equations for energy and momentum, the scattering geometry for TFXA imposes a relation between $Q^2$, the square of the scattering vector, and $\omega$, the energy transfer [Chapter III; Penfold and Tomkinson, 1986], and this is also of importance for the intensity of high frequency features of the spectra in particular, through the influence of the Debye Waller factor [Chapter II and Section 5.2.4 below]. The raw data from each detector were normalized to the incident neutron flux, to eliminate variations in detector response. In the backscattering geometry on TFXA, with the sample thickness

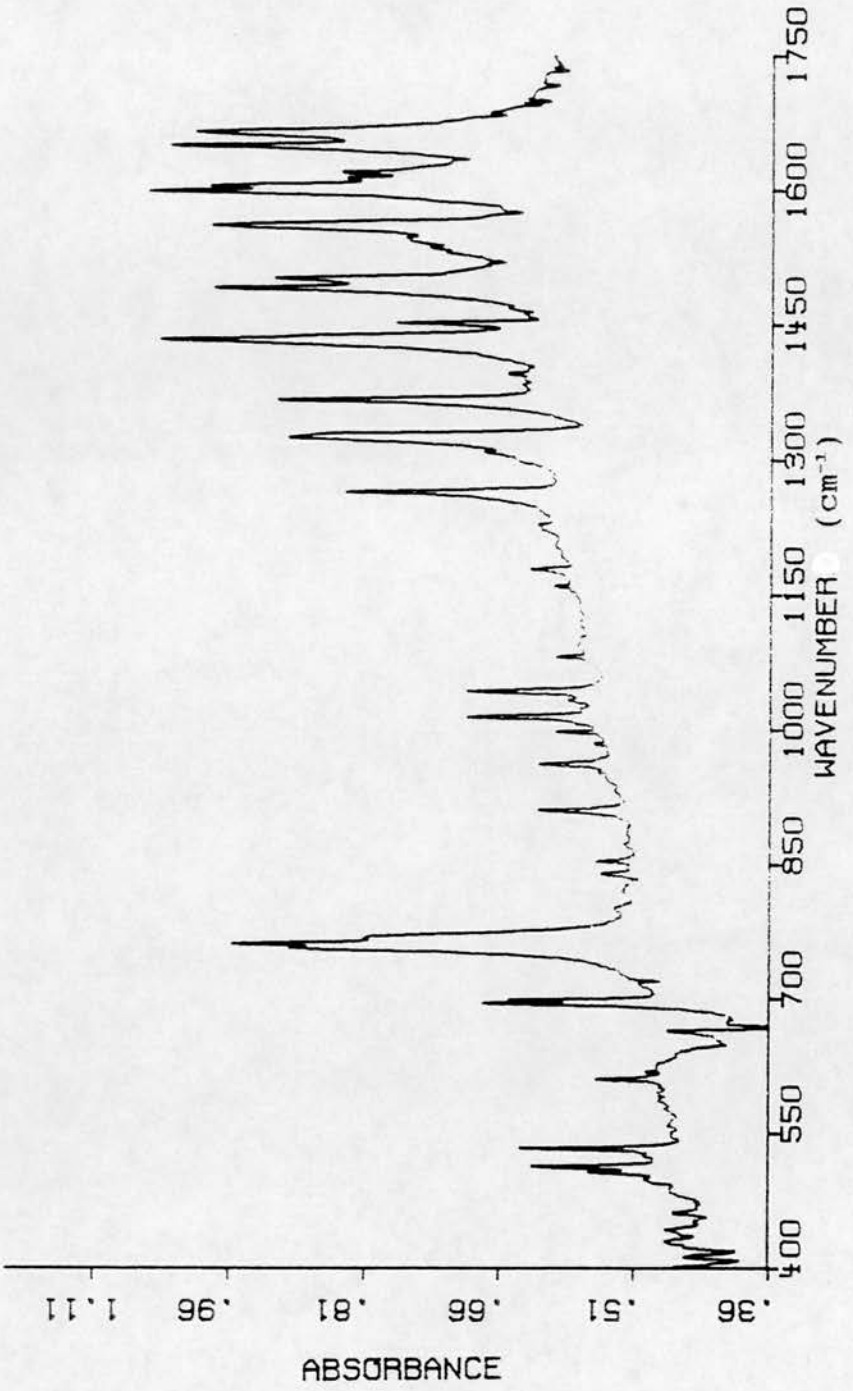


Figure 5.1. Infra-red spectrum at 77 K for ACN in KBr discs, collected with the help of Dr. C. Pulham, using a Nicolet 7000 series Fourier transform infrared spectrometer, Chemistry Department Edinburgh. Energy resolution 4 $cm^{-1}$.

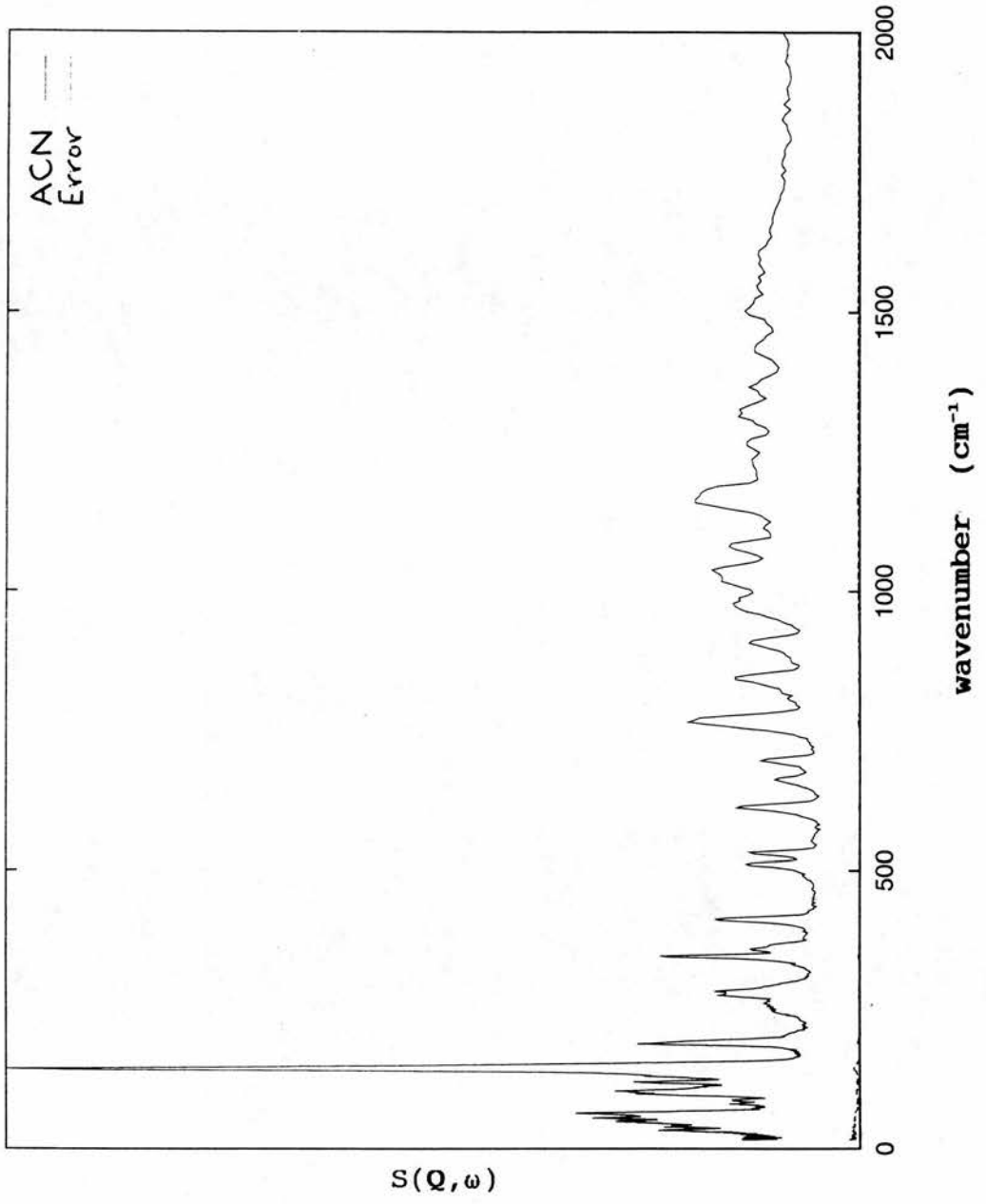


Figure 5.2. Inelastic neutron scattering spectrum for ACN at 25 K, collected on the TFXA spectrometer, RAL. The statistical counting error, proportional to $(1/N)^{0.5}$ where N is the number of detected counts, is displayed on the figure.

used, multiple scattering and absorption are negligible and were neglected [Goyal *et al.*, 1986].

Large plate like single crystals of ACN were grown by Dr. U. Wanderlingh, Department of Physics, Messina, Italy. Using these large composite single crystals (3 cm diameter, 1.5 mm thick) a test experiment was performed by myself and Dr. Middendorf, attempting to determine the orientation dependence of the INS for ACN. The plate like composite single crystals, arranged as grown in Messina, were mounted in aluminium foil sachets on the TFXA spectrometer, so that the scattering vector was perpendicular to the plane of the crystal plates. Unfortunately the spectra obtained were almost identical to those obtained for polycrystalline powder. This indicated that there was nearly spherical averaging of the crystallites in the composite single crystals, despite the macroscopic appearance of orientation. Further analysis of these spectra was not attempted, because the orientational averaging could not be known. Attempts to grow better oriented single crystals of ACN are underway at Messina.

### 5.2.3. Numerical calculations.

The CHARMM program and PEF [Brooks *et al.*, 1983a] were used for the molecular mechanics calculations, harmonic analyses and MD simulations. The CHARMM program has been extensively applied to examine the structure and dynamics of condensed phase molecular systems [Brooks *et al.*, 1988]. The form of the CHARMM PEF has been described in Chapter III. In all the calculations in this chapter long-range electrostatic interactions were brought to zero at a cut-off of 12 Å by applying a cubic switching function between 10 Å and 12 Å [Brooks, *et al.*, 1983a]. The parameters of the PEF were derived from calculations and experiments on model systems, and obtained from Dr. A. Mackerell, who is currently responsible for collating the

developmental parameters of the CHARMM program. The parameters were refined in the present work by repeated cycles of energy minimizations and harmonic analyses of the ACN crystal, with manual adjustment of the parameters to fit low-temperature structural and spectroscopic data for ACN. This was very time consuming. The parameterization was tested by calculation of phonon dispersion curves for fully deuterated acetanilide (ACN-D9). These were compared with results of coherent INS experiments by Barthes *et al.*, (1988). Anharmonic effects were examined using the full potential function for MD simulations of the ACN crystal at 80, 140 and 300 K.

**5.2.3.1. Crystal Calculations.**

Energy minimization and dynamical calculations were performed using the molecular mechanics PEF including the full crystal environment. The asymmetric unit of the 113 K X-ray crystallographic unit cell [Wasserman *et al.*, 1985] was built and the symmetry operations of the orthorhombic $P_{bca}$ space group applied. The resulting unit cell contains 8 acetanilide molecules. Its dimensions were $a$ = 19.509 Å, $b$ = 9.364 Å, $c$ = 7.778 Å, as for the x-ray structure. Crystal interactions were included using the non-bonded terms between atoms of the primary unit cell, and neighboring unit cells generated by application of the translation group symmetry operations for the crystal. The lattice parameters were fixed and the internal symmetry of the primary unit cell was maintained during all the calculations. Starting from the x-ray structure, the model structure was energy minimized using an adopted basis set Newton Raphson algorithm to a tolerance of $< 10^{-7}$kcals/mol [Brooks *et al.*, 1983a].

### 5.2.3.2. Harmonic Analyses.

Harmonic analyses were performed on the energy minimized crystal structure for ACN and ACN-D9. The method is based on the Born theory of lattice dynamics. For clarity this theory will be reviewed briefly for a monatomic Bravais lattice, *i.e.* where every unit cell contains only one atom situated on the lattice site. The resulting theory will be generalised readily to the more complex situation appropriate to the case of the acetanilide crystal. This review follows closely the treatment given in Lovesey, 1984.

The position of the $\alpha^{th}$ atom in the crystal is denoted by:

$$\mathbf{R}_\alpha = \mathbf{l}_\alpha + \mathbf{u}_\alpha \qquad (5.2.2)$$

where $\mathbf{l}_\alpha$ is the equilibrium position on a lattice site, and $\mathbf{u}_\alpha$ is the displacment of atom $\alpha$ from the lattice site, with Cartesian components $u_{\alpha i}$, i = 1,2,3. The potential energy of the atoms U is assumed to be lowest when all the **u**'s are zero. Expanding U in a Taylor series around this minimum equilibrium value $U_o$, the first non-zero term of the expansion must therefore be quadratic in the **u**'s. Neglecting all higher order terms in the Taylor series expansion yields the harmonic approximation to the potential energy.

$$U-U_o = \tfrac{1}{2} \sum_\alpha \sum_i \sum_\beta \sum_j u_{\alpha i} A_{\alpha i \beta j} u_{\beta j} + \ldots\ldots \qquad (5.2.3)$$

By the equality of mixed partial derivatives, the $A_{\alpha i \beta j}$, the second-order derivatives of the PEF with respect to atomic displacements, satisfy:

$$A_{\alpha i \beta j} = A_{\beta j \alpha i} \qquad (5.2.4)$$

and by the translational symmetry of the lattice the $A_{\alpha i \beta j}$

can depend
only on the relative positions of atoms $\alpha$, and $\beta$:

$$A_{\alpha i \beta j} = A_{ij}(\mathbf{l}_\alpha - \mathbf{l}_\beta) \qquad (5.2.5)$$

The classical Hamiltonian in the harmonic approximation is:

$$H_{cl} \qquad (5.2.6)$$

$$= \sum_\alpha \sum_i 1/2M\ p_{\alpha i}^2 + \tfrac{1}{2} \sum_\alpha \sum_i \sum_\beta \sum_j u_{\alpha i}\ A_{\alpha i \beta j}\ u_{\beta j}$$

where M is the mass of the nucleus and $\mathbf{p}_\alpha$ the momentum conjugate to $\mathbf{u}_\alpha$, with Cartesian components $p_{\alpha i}$.

The equation of motion for the atom $\alpha$ is:

$$M\ddot{u}_{\alpha i} = -\sum_\beta \sum_j A_{\alpha i \beta j}\ u_{\beta j}. \qquad (5.2.7)$$

This set of equations can be reduced to a set of independent harmonic oscillators by introduction of normal coordinates. First letting the displacements have a time dependence $\exp(-i\omega t)$:

$$M\omega^2 u_{\alpha i} = \sum_\beta \sum_j A_{\alpha i \beta j}\ u_{\beta j} \qquad (5.2.8)$$

Noting the translational symmetry of the lattice and assuming periodic boundary conditions, a Fourier transformation of the displacements can be made. Choosing to concentrate on a single term of the transformation for clarity, the substitution:

$$u_{\alpha i} = M^{-\frac{1}{2}} e_i \exp(i\mathbf{k}.\mathbf{l}_\alpha) \qquad (5.2.9)$$

is made to give:

$$M\omega^2 e_i \exp(i\mathbf{k}.\mathbf{l}_\alpha) = \sum_\beta \sum_j A_{\alpha i \beta j}\, e_j \exp(i\mathbf{k}.\mathbf{l}_\beta) \qquad (5.2.10)$$

and:

$$\omega^2 e_i \qquad (5.2.11)$$

$$= 1/M \sum_\beta \sum_j \exp(-i\mathbf{k}.\mathbf{l}_\alpha) A_{\alpha i \beta j}\, e_j \exp(i\mathbf{k}.\mathbf{l}_\beta)$$

$$= 1/M \sum_j \sum_l A_{ij}(\mathbf{l}) \exp(i\mathbf{k}.\mathbf{l})\, e_j$$

$$= \sum_j D_{ij}(\mathbf{k})\, e_j$$

where the $e_i$ are the Cartesian components for the atom $\alpha$ of the eigenvector $\mathbf{e}$, which is three dimensional because the lattice is a Bravais lattice. $\mathbf{k}$ is the wavevector of a spatially periodic wave of displacements in the lattice, and $D_{ij}(\mathbf{k})$ is the dynamical matrix:

$$D_{ij}(\mathbf{k}) = 1/M \sum_l A_{ij}(\mathbf{l}) \exp(i\mathbf{k}.\mathbf{l}) \qquad (5.2.12)$$

Here the sum runs over all the lattice vectors $\mathbf{l}$.

The linear equation Eq. (5.2.11) is of dimension three and so for each value of $\mathbf{k}$ there will be three values of $\omega$ satisfying the equation, and for each value of $\omega$, an eigenvector $\mathbf{e}$. The solutions $\omega$ and eigenvectors $\mathbf{e}$ will therefore be labelled by the wavevector $\mathbf{k}$, and by an index $m$, taking values 1,2,3. Then:

$$\omega_m(\mathbf{k})^2 e_{im}(\mathbf{k}) = \sum_j D_{ij}(\mathbf{k})\, e_{jm}(\mathbf{k}) \qquad (5.2.13)$$

The eigenvectors $\mathbf{e}_m(\mathbf{k})$ are orthonormalised. The number of vectors $\mathbf{k}$ is not unlimited. By the translational symmetry of the lattice the vectors $\mathbf{k}$, and $\mathbf{k}+\boldsymbol{\tau}$ will give the same displacements in Eq. (5.2.9) if $\mathbf{l}.\boldsymbol{\tau} = n2\pi$ where n is any integer. Thus it is only necessary to consider $\mathbf{k}$ vectors

in the first Brillouin zone, defined as the smallest region around the origin in reciprocal space formed by planes bisecting reciprocal lattice vectors. If the crystal has $N^3$ unit cells there will be $N^3$ wavevectors in the first Brillouin zone. The longest wavelength of any excitation propagating along a principal axis of the crystal and assuming periodic boundary conditions will be $N\lambda$, and hence the shortest $\mathbf{k}$ vector in that direction will be of length $1/(N\lambda)$. The $\mathbf{k}$ vectors form a lattice in reciprocal space with unit lattice vector in each principal crystallographic direction of length $1/(N\lambda)$ where $\lambda$ is the length of the crystal unit cell in that principal direction.

The analysis can be extended to non-Bravais lattices by introducing a position vector for each atom in the unit cell, and labelling the displacement coordinate accordingly:

$$\mathbf{R}_{\mathbf{l}} = \mathbf{l} + \mathbf{d} + \mathbf{u}_{\mathbf{l}\mathbf{d}} \qquad (5.2.14)$$

Here $\mathbf{d}$ is is the position vector of the $d^{th}$ atom in the $l^{th}$ unit cell. With r atoms per unit cell the label m on the solutions $\omega$, and eigenvectors $\mathbf{e}$ takes 3r values and the displacement of the atom at site $\mathbf{d}$ in unit cell $\mathbf{l}$ is now written, including contributions from all terms of the Fourier transformation:

$$u_{\mathbf{l}di} = (NM_d)^{-\frac{1}{2}} \sum_{\mathbf{k}'m} e_{idm}(\mathbf{k}') \exp(i\mathbf{k}'.\mathbf{l}) \qquad (5.2.15)$$

A similar derivation to that leading to Eq. (5.2.13) gives:

$$\omega_m(\mathbf{k})^2 e_{idm}(\mathbf{k}) = \sum_{jd'} D_{idjd'}(\mathbf{k})\, e_{jd'm}(\mathbf{k}) \qquad (5.2.16)$$

Eq. (5.2.16) is the system of linear equations, of

dimension 3r, which can be constructed and solved using the CRYSTAL facility of the CHARMM program, yielding 3r solutions for every value of **k**. These solutions form dispersion curves, or branches, in **k**, ω space, indexed by the label m. The dynamical matrix now takes the form:

$$D_{idjd'}(\mathbf{k}) = \sum_{\mathbf{l}} (1/M_d M_{d'})^{\frac{1}{2}} A_{idjd'}(\mathbf{l}) \exp(i\mathbf{k}.\mathbf{l}) \qquad (5.2.17)$$

Here $M_d$ is the mass of the atom at site **d**, i,j label cartesian coordinates, $A_{idjd'}(\mathbf{l})$ is the second derivative of the PEF with respect to displacement in direction i, of an atom in site **d** of the unit cell at the (arbitrary) origin, and with respect to simultaneous displacement in the direction j, of an atom at site **d'** of a unit cell at lattice site **l**. The second derivatives are calculated numerically by the CHARMM program. The sum over lattice sites continues up to the long range non-bonded cut off distance discussed in the section on the CHARMM potential function in Chapter III. The dependence on the wavevector **k** arises through the phase factor exp(i**k**.**l**) in this sum. The dynamical matrix is then diagonalised by standard numerical techniques and the eigenvectors $\mathbf{e}_m(\mathbf{k})$ and eigenvalues $\omega_m(\mathbf{k})$ found. These are then eigenvalues and eigenvectors of independent harmonic oscillators. The oscillators are characterised by a wavevector **k**, and belong to a branch labelled m, and are called, hereafter, phonons. A quantized treatment of the lattice dynamical equations reveals that for a given PEF, the eigenvectors and eigenvalues of the classical Hamiltonian are the same as those of the quantised Hamiltonian. The only significant difference arises from the quantisation of excitations of the harmonic oscillators, and the consequent Bose statistics for occupancy of the quantized energy levels [Lovesey, 1984].

Thus, changing notation, the eigenvectors for each atom,

$e_{\lambda\alpha}$, and the eigenfrequencies $\omega_\lambda$ (where $\lambda$ is a composite label for the phonons including the wavevector and branch index, and $\alpha$ labels the atom) were calculated for ACN as a function of the phonon wavevector, **k**, using the CRYSTAL facility of the CHARMM program.

For a crystal of N unit cells with r atoms per unit cell there are 3rN phonon solutions in the first Brillouin zone. Each of N **k**-points has 3r solutions, corresponding to 3r dispersion curves in the Brillouin zone. The present case of 8 molecules per unit cell and 19 atoms per molecule corresponds to 456 dispersion curves. Each calculation at a fixed **k**-point took approximately 30 minutes CPU time on a Hewlett Packard 9000/735 workstation. To provide a tractable computational problem and to allow for repeated cycles of refinement the symmetry of the ACN crystal was exploited, and 456 phonons calculated at each of 125 **k**-points uniformly distributed in one eighth of the Brillouin zone (the asymmetric unit), equivalent to treating a finite crystal of 512 unit cells. For ACN the symmetry of each branch of the dispersion curves was assigned according to the irreducible representations of the $P_{bca}$ point group at the Brillouin zone centre (**k** = 0) [Streitwolf, 1971], by examining the transformation properties of the eigenvector of the branch under the symmetry operations of the $P_{bca}$ point group [International Tables of X-ray Crystallography, 1983].

For comparison with coherent scattering experiments on fully deuterated acetanilide (ACN-D9) phonon calculations were made for ACN-D9 for each of the major crystallographic axes. The crystal structure was assumed to be the same as ACN. The dynamical effect of the isotopic substitution was modelled simply by assigning the mass of deuterium to every hydrogen of acetanilide. All other parameters were unchanged. These features of the model all rely on the validity of the Born-Oppenheimer

approximation [Merzbacher, 1970]. This approximation assumes that, because of the difference in time scale between nuclear and electronic motion, electronic states of a molecular system depend only on the instantaneous position of the nuclei of the system, and are independent of the nuclear kinetic energy, and hence independent of the mass of isotopic substituents in the molecule. Hence, in the Born-Oppenheimer approximation the potential energy surface, the equilibrium structure and therefore the crystal structure of deuterated forms of acetanilide will be identical to that of fully hydrogenous acetanilide. The only change in the dynamics arises from the mass effect of the isotopic substitution on the kinetic energies.

As for ACN, the symmetry of each branch of the dispersion curves was assigned according to the irreducible representations of the $P_{bca}$ point group at the Brillouin zone centre ($\mathbf{k} = 0$) by examining the transformation properties of the eigenvector of the branch under the symmetry operations of the $P_{bca}$ point group. Each continuous dispersion curve was traced, in each of the major crystallographic directions, through the finite series of **k**-points chosen for the calculations, by calculating the dot product of each eigenvector with the eigenvectors of all modes on neighboring **k**-points. Except at the Brillouin zone edge where degeneracies are expected, one neighboring eigenvector always gave a value for the dot product greater than 0.85, whereas all others were less than 0.3. The mode with the largest dot product was assigned as the continuation of the dispersion curve of interest.

It is instructive to compare the present molecular mechanics PEF approach with typical vibrational force fields that work directly with displacements in internal coordinates [Wilson *et al.*, 1980]. Molecular mechanics methods present the advantage of allowing a simultaneous description of the structure and dynamics of the molecule

that is not restricted to the harmonic approximation, and readily includes crystal effects. A comparison of the number of refinable parameters for the two approaches is of interest. For the isolated molecule of ACN a molecular vibrational force field would have a maximum of 2601 parameters, $(3N-6)^2$ where N is the number of atoms of the molecule and is 19 for ACN. In contrast, the CHARMM potential function used here can contain a maximum of 276 parameters. These include 51 internal coordinates equivalent to the force constants on the main diagonal of the dynamical matrix of a molecular vibrational force field. The present CHARMM potential function does not include parameters determining independently the force constants corresponding to the influence of the displacement of one internal coordinate on the force constant of any other. These off-diagonal terms only arise implicitly through non-bonded interactions of relevant atoms. A maximum of 87 parameters determine the non-bonded interactions, comprising two Lennard-Jones parameters for each atom and one atomic partial charge, and a maximum of 30 Urey Bradley 1:3 terms. As well as defining the off-diagonal terms in the dynamical matrix of the isolated molecule, the non-bonded parameters defined the inter-molecular interactions in the crystal. A maximum further 138 parameters define the reference values. Although both vibrational and molecular mechanics force fields can invoke local symmetry to reduce the number of independent parameters, this number is of order $N^2$ for each chemical group defined by local symmetry in a molecular vibrational force field, whilst it is of order N for the CHARMM PEF. In the present case, local symmetry restrictions were used to reduce the number of independent terms to 117: 52 force constants, 52 reference values, and 13 atomic partial charges. The complete final set of parameters is listed in Table 5.1.

**5.2.3.3. Molecular Dynamics Simulations.**

MD simulations were performed with periodic boundary conditions at temperatures of 80, 140 and 300 K. In the periodic boundary conditions method, the atoms in a primary box move according to the Newtonian equations of motion, unconstrained by any imposed symmetry. Around the primary box are constructed identical images, by application of the translation group symmetry operations. The atoms in the images interact with atoms in the primary box via the non-bonded terms in the PEF (Chapter III). It is preferable to work with a primary box as close to cubic as possible since this allows a maximal spherical cutoff for the electrostatic interactions. The primary box was chosen to be that of four unit cells, doubling the unit cell along the *b*-direction and *c*-direction. The resulting primary box dimensions are $a$ = 19.509 Å, $b$ = 18.728 Å, $c$ = 15.556 Å. The primary box consisted of 32 acetanilide molecules i.e., 608 atoms. All simulations were performed in the microcanonical ensemble.

The energy minimized crystal structure, obtained as described above, was used as the starting geometry for the simulations. Simulations were performed with an integration timestep of 0.5 fs. Each simulation consisted of three phases; an 8000 step heating phase, an equilibration run of 40000 steps with occasional velocity scaling to stabilize the temperature, and a production run of 66000 steps (33 ps), writing each alternate configuration to disk. The prolonged equilibration phase was necessary to ensure properly distributed population of the excitations of the system, which exchange energy slowly at the lower temperature simulated. The dense spacing of the dumped configurations on the time axis was necessary for the analysis of the high frequency region of the spectra. The production runs were long enough to fully

sample the lowest-frequency excitations expected in the simulations. The lowest frequency excitation expected in the MD simulation can be estimated from the calculated phonon dispersion curves. The periodic boundary conditions imposed on the MD simulations ensure that an excitation propagating in the $x$, $y$, or $z$ directions can have a maximum wavelength, $\lambda$, of $a$ = 19.509 Å, $b$ = 18.728 Å, $c$ = 15.556 Å respectively. This gives the minimum value of $\mathbf{k} = 2\pi/\lambda$ in each direction. Reading the frequency corresponding to this minimum $\mathbf{k}$ from the calculated dispersion curves gives an estimate for the lowest frequency expected in the MD simulations. The estimate is ~10 $cm^{-1}$ ≡ 0.3 THz. The period of such an excitation is ~3.3 ps and it will undergo ~10 cycles during the simulation.

### 5.2.4. Calculation of Incoherent INS Intensities

All of the calculations described in this section, along with density of states calculations from the harmonic model, as described below, used a program package I wrote in Fortran during an EMBO short term fellowship spent in the laboratory of Dr. Jeremy C. Smith, Section de Biophysique des Proteines et des Membranes, Centre d'Etudes Atomique, Saclay, France. These programs use, as input, the eigenvalues and eigenvectors calculated by the CRYSTAL facility of the CHARMM program.

#### 5.2.4.1. Calculations from the Harmonic Model.

Under the assumption of harmonic dynamics the transforms in Eq. (5.2.1) may be performed analytically, and the result expanded in a power series over the phonon normal modes for the crystal [Zemach and Glauber, 1956]. The

following expression is obtained:

$$S(\mathbf{Q},\omega) \tag{5.2.18}$$

$$= \sum_{\alpha} \exp[-2W_{\alpha}(\mathbf{Q})]$$

$$\times \prod_{\lambda} [\sum_{n} \exp[n_{\lambda}\hbar\omega_{\lambda}\beta/2] \; I_{n} \; [\hbar(\mathbf{Q}.\mathbf{e}_{\lambda\alpha})^{2}/2M\omega_{\lambda}\sinh(\hbar\omega_{\lambda}\beta/2)]]$$

$$\times \delta[\omega - \sum_{\lambda} n_{\lambda}\omega_{\lambda}]$$

$W_{\alpha}(\mathbf{Q})$ is the exponent of the Debye-Waller factor, $\exp[-2W_{\alpha}(\mathbf{Q})]$ for hydrogen atom $\alpha$ which may also be expressed in terms of a sum over the phonon modes:

$$2W_{\alpha}(\mathbf{Q}) \tag{5.2.19}$$

$$= 1/2NM \sum_{\lambda} \hbar(\mathbf{Q}.\mathbf{e}_{\lambda\alpha})^{2}/\omega_{\lambda} \; [2n(\omega_{\lambda})+1]$$

$$= Q^{2} \langle u_{\alpha}^{2} \rangle$$

In the above equations N is the number of phonon modes, M the hydrogen mass, $\lambda$ labels the phonon, $n_{\lambda}$ is the number of quanta exchanged with the phonon labelled $\lambda$, $n(\omega_{\lambda})$ is the Bose occupancy, $\mathbf{e}_{\lambda\alpha}$ is the atomic eigenvector for hydrogen $\alpha$ in the phonon $\lambda$, and $\omega_{\lambda}$ the phonon angular frequency. $\beta = 1/k_{B}T$ where $k_{B}$ is Boltzmann's constant and T the

temperature. $I_n$ (x) is the $n_\lambda$th order modified Bessel function. Eq. 5.2.19 serves also to define the atomic mean square displacement $\langle u_\alpha^2 \rangle$. Direct calculations indicated $x << 1$ throughout the Q and $\omega$ range of the experiments. Therefore, the small argument approximation:

$$I_n (x) = 1/n_\lambda! \ (x/2)^n \qquad (5.2.20)$$

was used throughout the calculations.

Eq. (5.2.18) is an exact quantum mechanical expression. It can be interpreted as follows. The Bose occupancies determine the energy distribution amongst the modes, ensuring that processes involving neutron energy gain are weaker than those involving neutron energy loss, in compliance with the quantum principle of detailed balance. In the present case the experimental data are neutron energy loss spectra and the calculations are restricted to this part of the spectrum. The case where all of the $n_\lambda$ equal zero corresponds to elastic scattering. The case where $\sum_\lambda n_\lambda = 1$ corresponds to single quanta processes termed one-phonon scattering. The case where $\sum_\lambda n_\lambda = 2$ corresponds to two quanta processes termed two-phonon scattering. Higher terms represent multi-phonon scattering. Inserting the calculated eigenvectors and eigenvalues from the harmonic analyses into Eqs. (5.2.18 and 19), allows a calculation of the incoherent INS in the harmonic approximation, to any degree in the phonon expansion. In the present work one-, two- and three-phonon calculations were made. The three-phonon approximation, for example, refers to the sum of one-, two-, and three-phonon scattering.

The label $\lambda$ runs over the 57000 phonon normal modes

calculated throughout the asymmetric unit of the Brillouin zone, weighted according to the positions of the **k**-points on symmetry elements of the Brillouin zone. This is equivalent to calculating 456000 phonon modes in the first Brillouin zone. This simplification was possible because all the symmetry elements of the point group for this crystal involve diagonal rotation matrices and all the irreducible representations are of dimension one. The intensity of each **k**-point in the asymmetric unit of the Brillouin zone is equal to the intensity at symmetry related **k**-points. Thus phonons at $\mathbf{k} = 0$ received a weight of one in the summation, at a **k**-point on one of the principal axes of symmetry a weight of two, at a **k**-point on a symmetry plane a weight of four, and at a general **k**-point a weight of eight.

To take account of the polycrystalline nature of the sample, whilst retaining a computational task of reasonable size, the incoherent INS spectra were calculated for the three principal directions of the neutron scattering vector relative to the crystallographic directions, and the resulting spectra summed.

#### 5.2.4.2. Incoherent INS intensities from MD trajectories.

INS intensities were calculated in the Gaussian approximation from the MD simulations for the isotropic polycrystalline powder of ACN, using the program package nMOLDYN [Kneller, in press]. A description of the methods have been given in Section 4.6.1.3. and will not be repeated here. The same semi-classical correction was used. The resulting calculated spectra represent $S_{cl}(\mathbf{Q},\omega)$ for constant **Q** in the Gaussian approximation. Because of the relation between **Q** and $\omega$ for TFXA these cannot be compared directly with TFXA data (Chapter III).

Nevertheless a Gauß-window in the time domain [Harris, 1978] was applied to the numerical Fourier transformations yielding smoothed spectra with a full-width half-maximum (FWHM) resolution depending on Q, in an attempt to mimic the energy dependence of the resolution function for TFXA (Chapter III). The inapplicability of the semi-classical correction over a wide range in energy transfer rendered the comparison with experimental data difficult. This problem was circumvented by calculation of the hydrogen weighted density of states from the MD simulations, and from the harmonic calculations.

### 5.2.5. Density-of-States.

The hydrogen-weighted density of states, $G(\omega)$, was calculated from the harmonic analyses as follows, using the programs I wrote for the purpose:

$$G(\omega) = \sum_{\lambda} \sum_{\alpha} (\mathbf{e}_{\lambda\alpha}.\mathbf{e}_{\lambda\alpha})/M \; \delta[\omega-\omega_{\lambda}] \qquad (5.2.27)$$

Here $\lambda$ labels the phonon with eigenfrequency $w_{\lambda}$, $\alpha$ labels the atom, M the mass of hydrogen, $e_{\lambda\alpha}$ is the displacement of atom $\alpha$ in phonon $\lambda$.

The hydrogen weighted density-of-states $G(\omega)$ was calculated from the MD simulation using the program package nMOLDYN [Kneller, in press] as the Fourier transform of the velocity autocorrelation function as follows:

$$G(\omega) = 1/N \sum_{\alpha} 1/2\pi \int dt \; \exp(-i\omega t) \; \langle \mathbf{v}_{\alpha}(0)\mathbf{v}_{\alpha}(t) \rangle \qquad (5.2.28)$$

where $\langle \mathbf{v}_\alpha(0)\mathbf{v}_\alpha(t)\rangle$ is the autocorrelation function of the velocities, $\mathbf{v}_\alpha(t)$, of atom $\alpha$, and $\langle..\rangle$ denotes a thermal average over the unperturbed states of the system. The limits of integration are $-/+\infty$. $G(\omega)$ can be interpreted as the kinetic energy of the hydrogen atoms in the system as a function of frequency [Boon and Yip, 1980]. Eq. 5.2.28 holds formally also in the quantum case [Clementi *et al.*, 1990]. The velocity autocorrelation function (VACF) was calculated from the MD simulations using a standard FFT-based algorithm for the efficient calculation of correlation functions [Brigham, 1974]:

$$\langle \mathbf{v}_\alpha(0)\mathbf{v}_\alpha(m)\rangle \sim 1/N-m \sum_{k=0,N-m-1} \mathbf{v}_\alpha(k)\mathbf{v}_\alpha(k+m) \qquad (5.2.29)$$

Here the indices k, m label the timesteps of the MD simulations, and N is the total number of time steps. $\mathbf{v}_\alpha(k)$ is the velocity of atom $\alpha$ at time step k. The approximate equality arises because the equilibrium thermal average $\langle..\rangle$ on the left hand side is approximated by an average over the MD trajectory on the right hand side, by invoking the ergodic postulate. The Fourier spectrum of the VACF was calculated by numerical Fourier transformation, applying a Gaussian-window in the time domain [Harris, 1978] yielding a smoothed spectrum with a full-width half-maximum (FWHM) resolution of 4 $cm^{-1}$. The analysis of the temperature dependence of the vibrational dynamics was made using $G(\omega)$ calculated with Eqs. 5.2.11-5.2.13.

## 5.3. RESULTS

The PEF was refined to give agreement with the crystal structure, optical spectra and the 25 K INS spectrum. The

dynamical calculations in this stage were performed in the harmonic approximation. For clarity, and to avoid laborious and irrelevant description of the multiple cycles of refinement which led to the model used, only the results of the final parameterization will be described.

An example of the refinement process is provided by the subsequent Chapter which describes further adjustments made to improve the fit to data for isotopomers of acetanilide. It should be borne in mind that the detailed results of this Chapter depend on the parameterisation, which was the best achieved at the time of the EMBO fellowship, but which is further improved in the subsequent Chapter. The results of this Chapter are described in detail, nonetheless, to illustrate the rich variety of quantities which may be calculated and compared with experiment.

### 5.3.1. Minimum energy geometry.

The energy minimised structure of two molecules in the ACN crystal is depicted in Fig. 5.3. The energy minimised structure, and the average structures during MD simulations can be compared with that obtained by x-ray diffraction at 113 K [Wasserman *et al.*, 1985]. For the comparison with the structure obtained from the energy minimization, or from the 140 and 300 K MD simulations, the RMS difference for the heavy atom positions (those well defined in the x-ray experiment) for an individual ACN molecule was 0.06 Å. The total RMS deviation for all molecules in the unit cell i.e. including differences in relative position and orientation of the eight ACN molecules in the unit cell, was 0.16 Å for the energy minimization, and 0.18 Å for the 140 K and 300 K MD simulations.

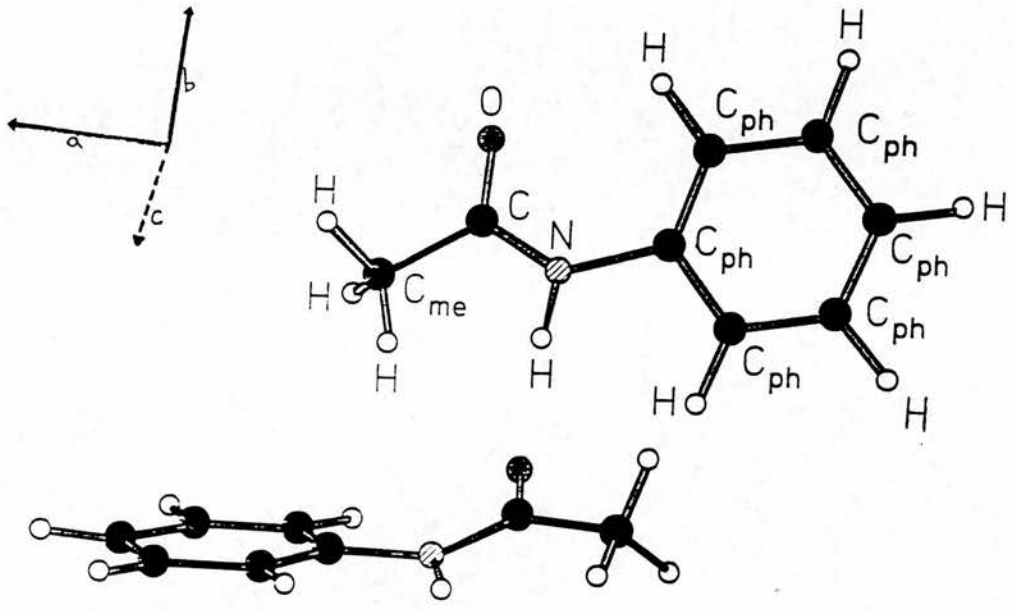


Figure 5.3. Two hydrogen-bonded molecules in the energy minimized crystal of ACN used for the calculations. The crystallographic axes are drawn as projections onto the plane of the figure of lines 2 Å long. The c-axis points away from the viewer.

5.3.1.1. Hydrogen-Bonding.

The temperature dependence of the hydrogen bond geometry gives information on the structural effects of anharmonicity in the hydrogen bonding potential. X-ray diffraction suggests that there is an increase in the N...O distance by ~ 0.03 Å from 2.915 Å at 113 K to 2.945 Å at 300 K, with the N-H...O angle 171° at both temperatures (the standard deviation of bond lengths determined in the x-ray studies was 0.002 Å and 0.003 Å respectively) [Wasserman *et al.*, 1985; Brown and Corbridge, 1954]. Lengthening of the N...O distance was also present, though to lesser extent, in the calculations, from 2.880 Å in the energy-minimized model crystal structure (equivalent to the structure at absolute zero temperature) to 2.885 Å for the average structure during the MD simulations at 140 K, and 2.895 Å at 300 Kelvin. As in the experiments the N-H...O angle was constant with temperature at 175°.

**5.3.1.2. Phenyl Ring.**

In the 113 K crystal x-ray structure the phenyl ring makes an angle of 15.5° relative to the peptide plane. This angle was 18.5° in the energy-minimized model, *i.e* within 3° of the x-ray value. An aromatic T structure is evident in the model, (Fig. 5.3), in agreement with the x-ray structure - the edge of each phenyl ring approached closely to the centre of the face of a neighboring phenyl ring, such that the two rings lie at a relative angle of 98° (100° in the X-ray structure). The interaction energy between the phenyl rings was -1.95 kcal/mol, -1.55 kcal/mol of which was van der Waals energy and -0.4 kcal/mol electrostatic. This is comparable with experimental values for the interaction energy of -2.4

kcal/mol for benzene dimers in the T-configuration in the gas phase [Grover *et al.*, 1987]. The adiabatic potential energy as a function of the phenyl ring rotation was calculated by constraining the N-$C_{ph}$ dihedral angle of one ACN molecule in the unit cell, whilst energy-minimizing all other conformational degrees of freedom for the crystal. The resulting potential energy barrier was 23 kcal/mol. Van der Waals interactions contribute 6 kcal/mol to this final barrier and electrostatic interactions contribute 9 kcal/mol. This is situated in the mid-range of a series of barriers to aromatic ring rotations in molecular crystals obtained from NMR measurements, these being 10-30 kcal/mol [Twyman and Dobson, 1988; Twyman and Dobson, 1990; Clayden, 1990].

#### 5.3.1.3. Methyl Group.

An important question concerns the value of the barrier to rotation of the methyl group. This barrier is related to the biologically important Ψ backbone torsion in proteins. *Ab initio HF/6 - 31G** quantum chemical calculations have suggested that the torsional barrier for the equivalent methyl group in the isolated N-methyl-acetamide molecule is < 0.2 kcal/mol. In the hydrogen bonded state, however, the *ab initio* calculations have suggested that a small barrier, of ~ 0.5 kcal/mol exists due possibly to polarization effects [Guo and Karplus, 1992]. The 113 K ACN x-ray structure for acetanilide defines the positions of the hydrogen atoms and thus the torsional angle of the methyl group around the $C_{co}C_{Me}$ axis [Wasserman *et al.*, 1989]. In the x-ray crystal structure a methyl group CH bond makes an angle of 5° with the plane of the peptide group. In a trial calculation of crystal structure energy-minimized with an intrinsic methyl

torsional force constant of zero, this angle was 40°. In the final refined parameter set an intrinsic 3-fold torsional force constant of 0.087 kcal/mol was introduced for each of the six torsional terms defined around the $C_{co}C_{Me}$ axis, with a minimum where a CH bond eclipses the NH bond. This led to an energy minimized structure in which a methyl CH bond made an angle of 3° with the plane of the peptide group, *i.e.* within 2° of the x-ray value. The methyl rotational dynamics is discussed later.

In the x-ray structure the methyl group is distorted from tetrahedral geometry. A lesser distortion of similar form was present in the model structure as a result of non-bonded interactions with the peptide group. In the present potential function local symmetry was imposed on the methyl group *i.e.*, equivalence of the three methyl hydrogens was imposed, so as to allow for a consistent description of the system when subjected to rotational transitions in MD simulations.

### 5.3.2. Harmonic dynamics at the Brillouin zone centre.

In this section a comparison is made of the frequencies and mode assignments obtained by others in optical spectroscopic analyses, with those obtained from harmonic analysis of the model ACN crystal structure at the Brillouin zone centre, where the phonon wavevector $\mathbf{k} = 0$, using the refined PEF. The mode assignments from optical spectra were made using isotopic substitution experiments or by comparison with spectra of related molecules. To examine the effects of crystal interactions on the vibrational dynamics of ACN, energy minimization and normal mode analyses of the isolated ACN molecule and of the ACN crystal were performed. As a consequence of crystal field splitting each mode in the isolated molecule

splits into a 'band' of eight components in the crystal spectrum. The eight components represent different phase combinations of the same molecular mode in the eight molecules of the unit cell, and each component has a different symmetry character. The calculated frequencies and assignments at $\mathbf{k} = 0$, are discussed in the text and listed in Tables 5.2 and 5.3. In Table 5.2 the crystal modes <210 $cm^{-1}$ are listed together with details of the crystal field splitting effects which were very marked for the low lying intra-molecular degrees of freedom. For those modes which were most accurately described by rigid-body motions of the ACN molecules in the crystal lattice, the librational or translational character of the modes is specified. The symmetry character of these lowest lying bands is also presented in Table 5.2. Above 200 $cm^{-1}$ there was relatively little splitting of the eight components of each band, and so for clarity only the frequency range of the components are listed in Table 5.3, and the mean frequencies discussed in the text. Hereafter I will use the term 'band' to refer collectively to the eight components of a crystal band, and the term 'mode' for describing vibrational excitations in isolated molecules, or for individual components of crystal bands. For each crystal band, the equivalent mode in the isolated molecule was defined as that mode for which the average value of the dot product formed with the eigenvectors of the modes in the crystal band was largest. The frequency shift for each mode on passing from the isolated molecule to the crystal gives a measure of the importance of the crystal interactions in determining the crystal band frequency. The value of the dot product, as defined above, gives a measure of the change in the form of each molecular mode on passing to the crystal, and is also displayed in Table 5.3. Apart from two vibrational bands discussed later all the fundamental frequencies were within 3% of their

Table 5.2. The assignment of the crystal phonon bands for ACN above 160 $cm^{-1}$ in terms of intra-molecular modes of the isolated molecule. Intra-molecular modes, in turn, assigned in terms of the potential energy distribution amongst internal coordinates used in construction of CHARMM potential energy function for the ACN molecule. Each phonon band carries eight modes, one each of the eight symmetry classes. Calculations use the parameters of Table 5.1.

| I | II | III |
|---|---|---|
| *[a] | 27[—] | $\tau(phenyl)(84)$ |
| *[a] | 85[—] | $\tau(CN)(52)\ \gamma(phenyl)(22)$ |
| *[a] | 115[—] | $\tau(methyl)(97)$ |
| 191-201 | 180[0.97] | $\tau(phenyl)(20)\ \tau(CN)(15)\ \delta(C_{me}CN)(8)\ \delta(NC_{ph}C_{ph})(7)\ \delta(CNC_{ph})(6)$ |
| 273-284 | 254[0.98] | $\gamma(phenyl)(43)\ \tau(CN)(30)\ \tau(phenyl)(7)$ |
| 310-324 | 300[0.96] | $\delta(NC_{ph}C_{ph})(29)\ s(CN)(17)\ \delta(CNC_{ph})(11)\ s(NC_{ph})(8)$ |
| 341-348 | 336[0.97] | $\delta(CC_{me})(44)\ \delta(CO)(12)\ \delta(NC_{ph}C_{ph})(16)\ s(NC_{ph})(9)$ |
| 418-433 | 405[0.99] | $\tau(C_{ph}C_{ph})(53)\ \gamma(C_{ph}H)(36)\ \gamma(phenyl)(9)$ |
| 497-511 | 489[0.98] | $\tau(C_{ph}C_{ph})(48)\ \gamma(C_{ph}H)(35)$ |
| 538-543 | 530[0.98] | $\delta(CO)(60)\ s(CC_{me})(10)\ s(NC_{ph})(6)\ \delta(CC_{me})(6)$ |
| 607-619 | 577[0.92] | $\gamma(CO)(69)\ \gamma(NH)(25)$ |
| 650-655 | 645[0.99] | $\delta(CO)(17)\ \delta(C_{ph}C_{ph}C_{ph})(14)\ s(CC_{me})(10)\ \delta(CNC_{ph})(10)\ \delta(CC_{me})(8)\ \delta(C_{ph}H)(8)$ |
| 681-686 | 672[0.90] | $\tau(C_{ph}C_{ph})(56)\ \gamma(C_{ph}H)(23)\ \gamma(NH)(11)$ |
| 688-691 | 683[0.94] | $\delta(C_{ph}C_{ph}C_{ph})(47)\ \delta(C_{ph}H)(16)\ s(C_{ph}C_{ph})(10)$ |
| 743-754 | 678[0.38][b] | $\gamma(NH)(45)\ \gamma(C_{ph}H)(21)\ \gamma(CO)(15)$ |
| 769-791 | 737[0.72] | $\gamma(C_{ph}H)(85)$ |
| 779-793 | 776[0.93] | $s(CN)(27)\ s(CO)(14)\ \delta(C_{ph}C_{ph}C_{ph})(9)\ \delta(CNC_{ph})(9)\ \delta(NCC_{me})(5)$ |
| 839-841 | 832[0.88] | $\gamma(C_{ph}H)(25)\ \delta(C_{ph}C_{ph}C_{ph})(20)\ s(CN)(14)\ s(CC_{me})(9)\ s(CO)(6)\ s(NC_{ph})(6)$ |
| 849-858 | 828[0.88] | $\gamma(C_{ph}H)(96)$ |
| 915-926 | 902[0.99] | $\gamma(C_{ph}H)(94)$ |
| 966-969 | 963[0.99] | $s(C_{ph}C_{ph})(24)\ \delta(C_{ph}C_{ph}C_{ph})(23)\ \gamma(C_{ph}H)(18)\ \delta(C_{ph}C_{ph}H)(16)\ s(NC_{ph})(6)$ |
| 980-984 | 978[0.88] | $methyl\ rock(61)\ s(CO)(7)\ s(C_{ph}C_{ph})(6)$ |
| 990-996 | 971[0.81] | $\gamma(C_{ph}H)(94)$ |
| 1014-1017 | 989[0.92] | $\gamma(C_{ph}H)(97)$ |
| 1035-1042 | 1023[0.95] | $methyl\ rock(76)\ \gamma(CO)(15)$ |

Table 5.2 (continued)
Column **I**: frequency range (wavenumbers) of **k** = 0 phonon bands with frequency > 160 $cm^{-1}$ ( Note a - for lower frequency bands see Table 6.9). Column **II**: frequency of corresponding isolated molecular mode (defined as mode with closest eigenvector **e** - numbers in square brackets give the dot product $\mathbf{e}_{isolated}.\mathbf{e}_{crystal}$). Note b - the bands at 752-765 $cm^{-1}$, 762-774, 775-788 $cm^{-1}$ in the crystal were mixed extensively with γNH - the dot products with the isolated molecular γNH mode at 634 $cm^{-1}$ were [0.45], [0.37], [0.3] respectively. Column **III**: assignments for isolated molecule modes (numbers in round brackets give percentage contribution to the potential energy of the mode, terms contributing > 5% are listed). s = bond stretch, $\delta$ = in-plane bend, $\gamma$ = out-of-plane bend, $\tau$ = torsion.

| **I***(cont.)* | **II***(cont.)* | **III***(cont.)* |
|---|---|---|
| 1040-1044 | 1030[0.93] | $s(C_{ph}C_{ph})(67)$ $\delta(C_{ph}C_{ph}H)(25)$ |
| 1067-1072 | 1067[0.99] | $s(C_{ph}C_{ph})(52)$ $\delta(C_{ph}C_{ph}H)(41)$ |
| 1173-1178 | 1165[0.95] | $\delta(C_{ph}C_{ph}H)(50)$ $s(C_{ph}C_{ph})(22)$ $\delta(NH)(19)$ $s(NC_{ph})(6)$ |
| 1184-1187 | 1184[0.82] | $\delta(C_{ph}C_{ph}H)(68)$ $s(C_{ph}C_{ph})(18)$ $\delta(NH)(9)$ |
| 1206-1215 | 1181[0.77] | $\delta(C_{ph}C_{ph}H)(35)$ $\delta(NH)(31)$ $s(C_{ph}C_{ph})(14)$ $s(C_{ph}N)(10)$ |
| 1252-1258 | 1245[0.97] | $s(CC_{me})(23)$ $\delta(NH)(14)$ $\delta(CO)(14)$ $s(NC_{ph})(14)$ $s(CN)(10)$ $\delta(C_{ph}C_{ph}H)(8)$ |
| 1323-1325 | 1323[0.99] | $\delta(C_{ph}C_{ph}H)(90)$ |
| 1384-1386 | 1376[0.99] | *methyl deformation*(88) |
| 1412-1414 | 1412[0.99] | $\delta(C_{ph}C_{ph}H)(47)$ $s(C_{ph}C_{ph})(41)$ |
| 1432-1433 | 1429[0.93] | *methyl deformation*(98) |
| 1436-1437 | 1434[0.88] | *methyl deformation*(79) $\delta(C_{ph}C_{ph}H)(7)$ |
| 1450-1452 | 1445[0.96] | $\delta(C_{ph}C_{ph}H)(54)$ $s(C_{ph}C_{ph})(22)$ *methyl deformation*(19) $\delta(NH)(8)$ |
| 1509-1525 | 1501[0.98] | $s(C_{ph}C_{ph})(26)$ $\delta(NH)(21)$ $s(CN)(16)$ $s(NC_{ph})(12)$ $\delta(C_{ph}C_{ph}H)(12)$ $s(CC_{me})(5)$ |
| 1555 | 1554[0.99] | $s(C_{ph}C_{ph})(79)$ $\delta(C_{ph}C_{ph}H)(14)$ |
| 1602-1603 | 1600[0.99] | $s(C_{ph}C_{ph})(84)$ $\delta(C_{ph}C_{ph}H)(7)$ |
| 1614-1619 | 1614[0.99] | $s(C_{ph}C_{ph})(61)$ $\delta(C_{ph}C_{ph}H)(18)$ |
| 1662-1667 | 1662[1.00] | $s(CO)(70)$ $s(CC_{me})(7)$ $s(CN)(6)$ $\delta(CC_{me})(6)$ |
| 2918 | 2914[1.00] | $s(C_{me}H)(99)$ |
| 2974 | 2971[1.00] | $s(C_{me}H)(99)$ |
| 2978-2979 | 2974[0.99] | $s(C_{me}H)(99)$ |
| 3061-3062 | 3111[1.00] | $s(C_{ph}H)(99)$ |
| 3064-3066 | 3112[1.00] | $s(C_{ph}H)(99)$ |
| 3066-3068 | 3113[1.00] | $s(C_{ph}H)(99)$ |
| 3069-3071 | 3115[1.00] | $s(C_{ph}H)(99)$ |
| 3077-3079 | 3121[1.00] | $s(C_{ph}H)(99)$ |
| 3276-3282 | 3292[1.00] | $s(NH)(100)$ |

Table 5.3. Assignment of ACN crystal phonon modes below 210 $cm^{-1}$ in terms of rigid body motions or intra-molecular modes of the isolated molecule. Intramolecular modes, in turn, assigned in Table 5.2. Calculations use the parameters of Table 5.1. Column I: frequency ($cm^{-1}$) of **k** = 0 crystal modes < 210 $cm^{-1}$. Column II: assignment to rigid molecular librational or translational motion, or nearest intramolecular mode (defined as mode with closest eigenvector **e** - numbers in square brackets give the dot product $\mathbf{e}_{isolated} \cdot \mathbf{e}_{crystal}$). Column III: symmetry character of crystal mode.

| I | II | III | I*(cont.)* | II*(cont.)* | III*(cont.)* |
|---|---|---|---|---|---|
| 23 | translational | B1g | 121 | librational | Au |
| 25 | translational | B3u | 121 | $\tau(CN)\,\gamma(phenyl)$[0.47] | B2g |
| 26 | translational | Au | 122 | librational | B3g |
| 30 | librational | Ag | 122 | librational | B3u |
| 39 | translational | Ag | 123 | $\tau(CN)\,\gamma(phenyl)$[0.74] | B2u |
| 41 | translational | B3g | 126 | $\tau(phenyl)$[0.76] | B3g |
| 42 | translational | B1u | 129 | $\tau(CN)\,\gamma(phenyl)$[0.65] | Ag |
| 43 | librational | B2g | 130 | $\tau(CN)\,\gamma(phenyl)$[0.51] | B1u |
| 45 | librational | B2u | 132 | librational | B2u |
| 49 | librational | Au | 135 | translational | B3u |
| 53 | librational | B3g | 135 | librational | B3g |
| 54 | librational | B2g | 136 | $\tau(CN)\,\gamma(phenyl)$[0.53] | B1g |
| 55 | librational | B1u | 138 | $\tau(methyl)$[0.60] | B1u |
| 63 | librational | B3u | 144 | $\tau(methyl)$[0.81] | Au |
| 66 | translational | B2g | 144 | $\tau(methyl)$[0.82] | B2u |
| 66 | librational | B2u | 145 | $\tau(methyl)$[0.71] | Ag |
| 68 | translational | Ag | 145 | translational | B1g |
| 70 | librational | Ag | 145 | librational | B1u |
| 71 | librational | B1g | 146 | $\tau(CN)\,\gamma(phenyl)$[0.87] | Au |
| 73 | librational | Au | 146 | $\tau(methyl)$[0.85] | B3u |
| 79 | librational | B2g | 148 | $\tau(methyl)$[0.92] | B2g |
| 79 | translational | B2u | 150 | $\tau(methyl)$[0.77] | B3g |
| 79 | $\tau(phenyl)$[0.82] | B3u | 151 | librational | B1u |
| 79 | librational | B3g | 157 | librational | Ag |
| 82 | translational | B1g | 158 | $\tau(methyl)$[0.60] | B1g |
| 83 | librational | B1u | 165 | $\tau(CN)\,\gamma(phenyl)$[0.53] | B2u |
| 85 | translational | Au | 168 | $\tau(CN)\,\gamma(phenyl)$[0.59] | B3u |
| 87 | translational | Ag | 170 | $\tau(CN)\,\gamma(phenyl)$[0.63] | B2g |
| 93 | translational | B2g | 172 | librational | B3g |
| 94 | $\tau(phenyl)$[0.71] | B1u | | | |
| 94 | librational | B1g | | | |
| 97 | $\tau(phenyl)$[0.66] | B1g | | | |
| 100 | $\tau(phenyl)$[0.51] | Au | | | |
| 101 | librational | B2u | | | |
| 102 | $\tau(CN)\,\gamma(phenyl)$[0.63] | B3g | | | |
| 104 | librational | Ag | | | |
| 107 | librational | Au | | | |
| 111 | translational | B2g | | | |
| 112 | librational | B3u | | | |

optical spectroscopic values. The assignments were mostly in agreement with published assignment schemes.

### 5.3.2.1. NH, CH, and phenyl CC stretch bands.

The calculated NH stretch band was centred on 3278 $cm^{-1}$. IR experiments have assigned NH stretch to a band at 3260 $cm^{-1}$ [Careri *et al.*, 1984; Tariq *et al.*, 1984]. Five calculated phenyl $C_{ph}H$ stretch bands lie between 3061 and 3078 $cm^{-1}$. IR experiments have identified four more widely split phenyl $C_{ph}H$ stretch bands between 3030 and 3090 $cm^{-1}$ [Careri *et al.*, 1984; Tariq *et al.*, 1984]. The calculated methyl $C_{me}H$ stretch bands appeared at 2917, 2973 and 2978 $cm^{-1}$ compared with 2920, 2940 and 2980 $cm^{-1}$ in IR spectra [Careri *et al.*, 1984; Tariq *et al.*, 1984]. Because the resolution of the TFXA spectrometer is too poor to make useful refinements of these modes these values were accepted. They lay within 2% of the reported IR fundamentals. Trial calculations with various CH and NH stretch parameters demonstrated that these modes are virtually independent of other modes in the crystal and adjustment of their frequencies is relatively straightforward. Slight inaccuracy in their frequencies similarly does not affect other dynamics of the crystal.

In the isolated benzene molecule there are two degenerate CC stretching modes, at 1600 $cm^{-1}$ [Goodman *et al.*, 1991]. In crystalline ACN the corresponding phenyl CC stretch bands are split by two effects; symmetry lowering by the acetamide substituent and the crystal field. In ACN, IR experiments have indicated phenyl CC stretching bands at 1603, and 1619 $cm^{-1}$ split by symmetry lowering, and each band further split (~ 6 $cm^{-1}$) by the crystal field [Careri *et al.*, 1984; Tariq *et al.*, 1984].

The symmetry lowering effect was fit in the calculations by introducing slightly different force constants for the CC bonds *meta*, *para*, and *ortho* to the substitution site. This resulted in a splitting of the degenerate benzene modes at 1600 $cm^{-1}$ to produce bands at 1600 and 1615 $cm^{-1}$. Each of these bands also illustrated the effect of crystal field splitting of the eight components. For example, in the band near 1615 $cm^{-1}$, there were six separate components between 1614 and 1615 $cm^{-1}$, a seventh at 1615.5 and an eighth at 1618$cm^{-1}$. Both forms of splitting for these phenyl ring modes (crystal field and peptide group symmetry lowering) therefore gave reasonable agreement with IR experiment.

### 5.3.2.2. Amide bands.

The calculated carbonyl stretch band (Amide I) was centred at 1665 $cm^{-1}$ in the crystal, split by crystal field effects to give components between 1661 and 1667 $cm^{-1}$. IR and Raman experiments at 50 K have identified the components of the Amide I band lying between 1659 and 1670 $cm^{-1}$, as well as an anomalous temperature dependent band at 1650 $cm^{-1}$ attributed to a soliton excitation of CO stretching, as discussed in the Introduction [Careri *et al.*, 1984]. The calculation therefore gave reasonable agreement with the crystal field splitting measured at low temperature for the conventional Amide I band (1659-1670 $cm^{-1}$), but offers no explanation of the anomalous band at 1650 $cm^{-1}$.

An IR and Raman active band at ~ 1550 $cm^{-1}$ has been assigned to C-N stretching mixed with in-plane bending of the amide hydrogen (Amide II) [Careri *et al.*, 1984; Tariq *et al.*, 1984]. However in the present calculations this band was predominantly CC stretching of the phenyl ring.

The major calculated contribution of Amide II was to a band centred at 1512 $cm^{-1}$, also mixed with CC phenyl ring stretching, and to a lesser extent to the band at 1600 $cm^{-1}$. A recent vibrational force field for N-methyl acetamide, derived from INS experiments, also places the amide II band near 1500 $cm^{-1}$ [Fillaux *et al.*, 1993].

NH in-plane bending was calculated to contribute also to four modes at 1165, 1181, 1184, and 1245 $cm^{-1}$ in the isolated ACN molecule, shifted upward to bands centred at 1175, 1185, 1209, and 1255 $cm^{-1}$ in the hydrogen bonded crystal. The bands at 1175, 1185, 1209 $cm^{-1}$ were predominantly mixed with CCH in-plane bending. IR spectroscopic measurements have identified CCH in-plane bending bands at 1160 and 1180 $cm^{-1}$ [Careri *et al.*, 1984; Tariq *et al.*, 1984]. The calculated band at 1255 $cm^{-1}$ was predominantly NH and CO in-plane bending mixed with CN, $C_{ph}N$ and $C_{me}C$ stretching. The form of this last band therefore closely resembles that typical of Amide III, usually assigned to excitations near 1260 $cm^{-1}$ in peptides and in NMA [Krimm and Bandekar, 1986; Fillaux *et al.*, 1993] though in ACN it has been assigned to a mode at 1320 $cm^{-1}$ [Careri *et al.*, 1984; Tariq *et al.*, 1984]. My IR experiments for ACN reveal a mode at 1267 $cm^{-1}$ with a complex split band at 1312-1330 $cm^{-1}$ in ACN (Fig. 5.1). The present calculations assign the 1267 $cm^{-1}$ band to Amide III, and the 1320 $cm^{-1}$ band to CCH in-plane bend and CC stretch. My IR experiments also identified a further weak band near 1209 $cm^{-1}$ (Fig. 5.1), though this was not previously reported by others. In the present Chapter this band was assumed to represent a fundamental, and not an overtone excitation. The calculations assigned this band predominantly to $C_{ph}N$ stretching mixed with NH in-plane bend and CCH in-plane bend. The subsequent Chapter will discuss this band further but briefly, comparison with INS

data for ACN-D5 and ACN-D8 suggests that the observed IR band is in fact an overtone of an excitation at 608 $cm^{-1}$, and that the assignment given in the present Chapter is in error. This, then, is one of the two bands referred to above which are in poor agreement with optical data. In fact on the basis of the isotopomer data it is possible that a band of similar form contributes to the complex split peak at 1320 $cm^{-1}$ (see Chapter VI), and the refinements described in Chapter VI provide an improved model of this band.

The calculated out-of-plane NH bending was also higher in the crystal (three complex split bands centred at 750, 778, and 785 $cm^{-1}$), than in the isolated molecule (678 $cm^{-1}$). The split bands arose from mixing of NH and $C_{ph}H$ out-of-plane bending, and with skeletal deformation of the peptide group. The broad IR band in this region has at least two components, near 755 and 770 $cm^{-1}$, which have also been assigned to $C_{ph}H$ and NH out-of-plane bending [Careri *et al.*, 1984; Tariq *et al.*, 1984; Barthes *et al.*, 1992; Barthes *et al.*, 1993].

### 5.3.2.3. CC phenyl torsions.

In isolated benzene, because of the molecular symmetry, two CC phenyl torsions are degenerate in optical spectra, occurring near 400 $cm^{-1}$, with a third non-degenerate CC phenyl torsional mode near 700 $cm^{-1}$ [Goodman *et al.*, 1991]. Substitution with the heavy acetamide group to form ACN splits the degeneracy, and CC phenyl torsional bands have been assigned to optical excitations at 415 and 510 $cm^{-1}$ in ACN indicating a splitting of 95 $cm^{-1}$ of the equivalent degenerate modes in benzene, with the third CC torsional band at 690 $cm^{-1}$ [Tariq *et al.*, 1984]. Trial calculations with a single force constant for all phenyl CC torsions

produced bands centred on 454, 490, and 693 $cm^{-1}$, *i.e.* there was a splitting of only 36 $cm^{-1}$ of the two lowest frequency bands. The form of the band at 454 $cm^{-1}$ represented simultaneous torsion of the two CC bonds meta to the N substitution site (chair deformation), whilst the higher frequency degenerate mode at 490 $cm^{-1}$ represented simultaneous torsion of the two CC bonds, ortho and para to the N substitution site. It can be expected therefore that these two modes should experience different contributions from off-diagonal interaction terms for torsion of first- and second-nearest neighbour CC bonds, if these were included in the matrix of second derivatives. Isolated molecular force field models of benzene, for example, either use significant off-diagonal terms in the dynamical matrix representing these interactions, or assign different force constants to symmetry coordinate representations of the modes [Wilson *et al.*, 1980; Goodman *et al.*, 1991]. Since the molecular mechanics potential function does not include explicit off-diagonal terms in the present model, the splitting of 85 $cm^{-1}$ for the degenerate pair could only be achieved by the introduction of a different torsional force constants for the ortho and para CC bonds (4.4 kcals/mol) compared to the meta CC bonds (2.0 kcals/mol). (For comparison, the trial parametrisations used a single force constant of 3.9 kcals/mol for all CC torsions). This solution to the problem is similar to that used in work on molecular force fields, in which force constants are often assigned directly to symmetry coordinates, rather than to internal coordinates [Wilson *et al.*, 1980]. Observing the difference in the form of the two split torsional modes (true for trial parametrisations with a single force constant also), the effect of off-diagonal interaction terms has been implicitly included by artificially assigning different force constants for CC torsional terms

appearing in each of the two modes. With this approach good agreement with observed frequencies was achieved with bands centred at 425 and 507 $cm^{-1}$, split by 82 $cm^{-1}$, and a third band centred at 682 $cm^{-1}$.

### 5.3.3. Inelastic neutron spectral intensities for fully hydrogenous ACN.

#### 5.3.3.1. Low frequency features (<400 $cm^{-1}$).

The experimental INS spectrum at 25 K is presented in Fig. 5.4 (up to 2000 $cm^{-1}$) and Fig. 5.5 (up to 400 $cm^{-1}$), together with the spectrum calculated from the harmonic model in the three phonon approximation.

Because of the large hydrogen displacement in the mode, the methyl torsional peak is by far the strongest feature of the experimental INS spectra. The peak is narrow and well resolved at 145 $cm^{-1}$ in the experimental spectrum. In Section 5.3.1.3 it was noted that a non-zero intrinsic methyl torsional force constant was necessary to reproduce the crystal geometry. The intrinsic methyl torsional term was also necessary to improve the calculated fit to the INS spectra. Test parameterisations with no intrinsic torsional term in the model produced a methyl torsional peak which was very broad, and lay at ~100 $cm^{-1}$. The experimental INS methyl peak was reproduced with the final parameterisation which included the intrinsic torsional barrier and a modified van der Waals radius for the methyl hydrogens of 1.2 Å, close to the value of 1.18 Å required in a recent molecular mechanics parametrization of the *ab initio* potential energy surface for methyl torsion in NMA [Baudry and Smith, 1994]. With these refinements, the methyl torsion lay at 115 $cm^{-1}$ in the isolated molecule and was raised by the crystal field to 145 $cm^{-1}$ in the crystal.

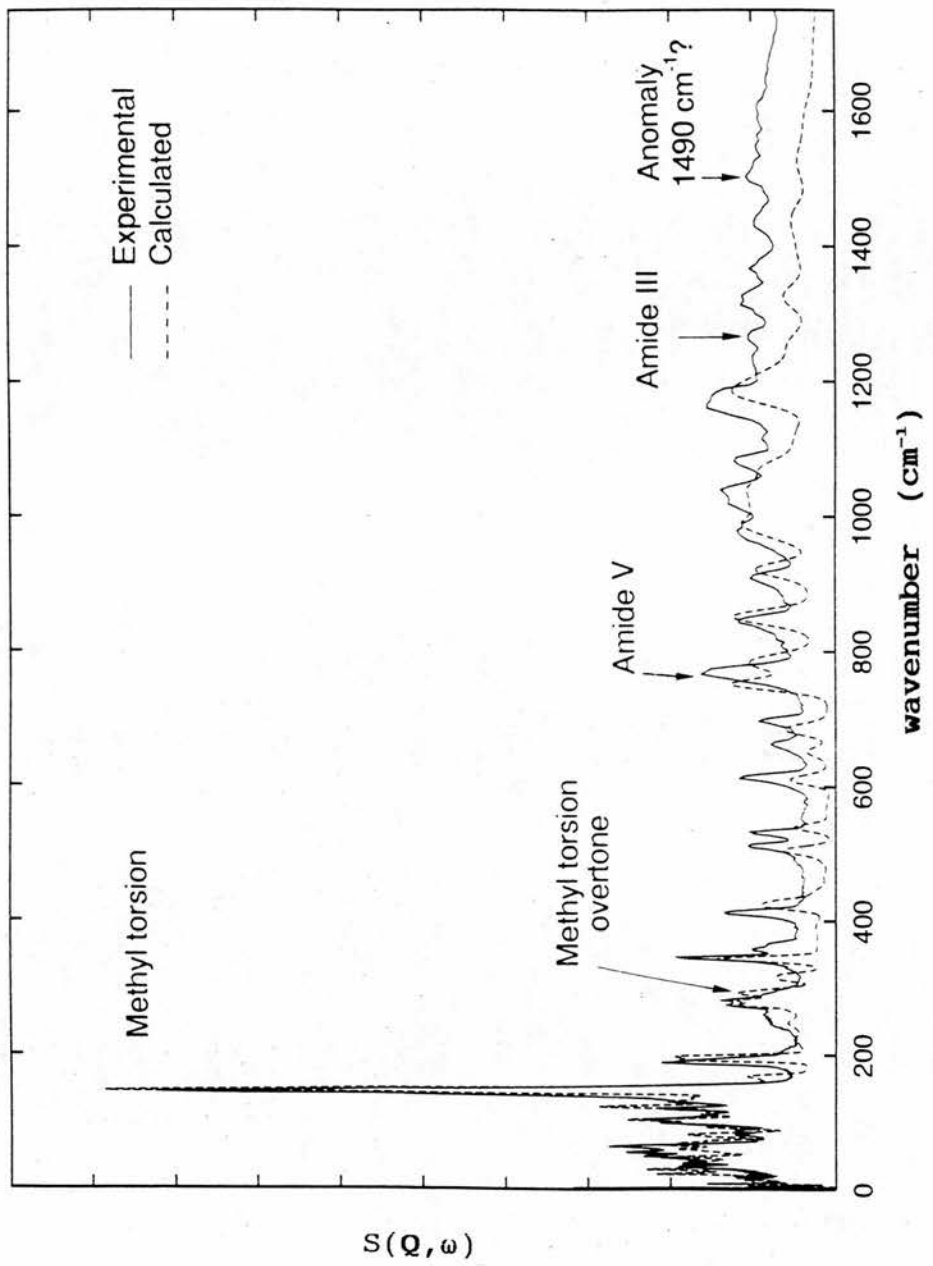


Figure 5.4. 25 K dynamic structure factor, $S(Q,\omega)$ for ACN from the INS experiment and calculated using the three phonon approximation to Eq. (5.2.18). The calculated spectrum is multiplied by a single scale factor to bring the integrated intensity of the methyl torsional peak into agreement with experiment.

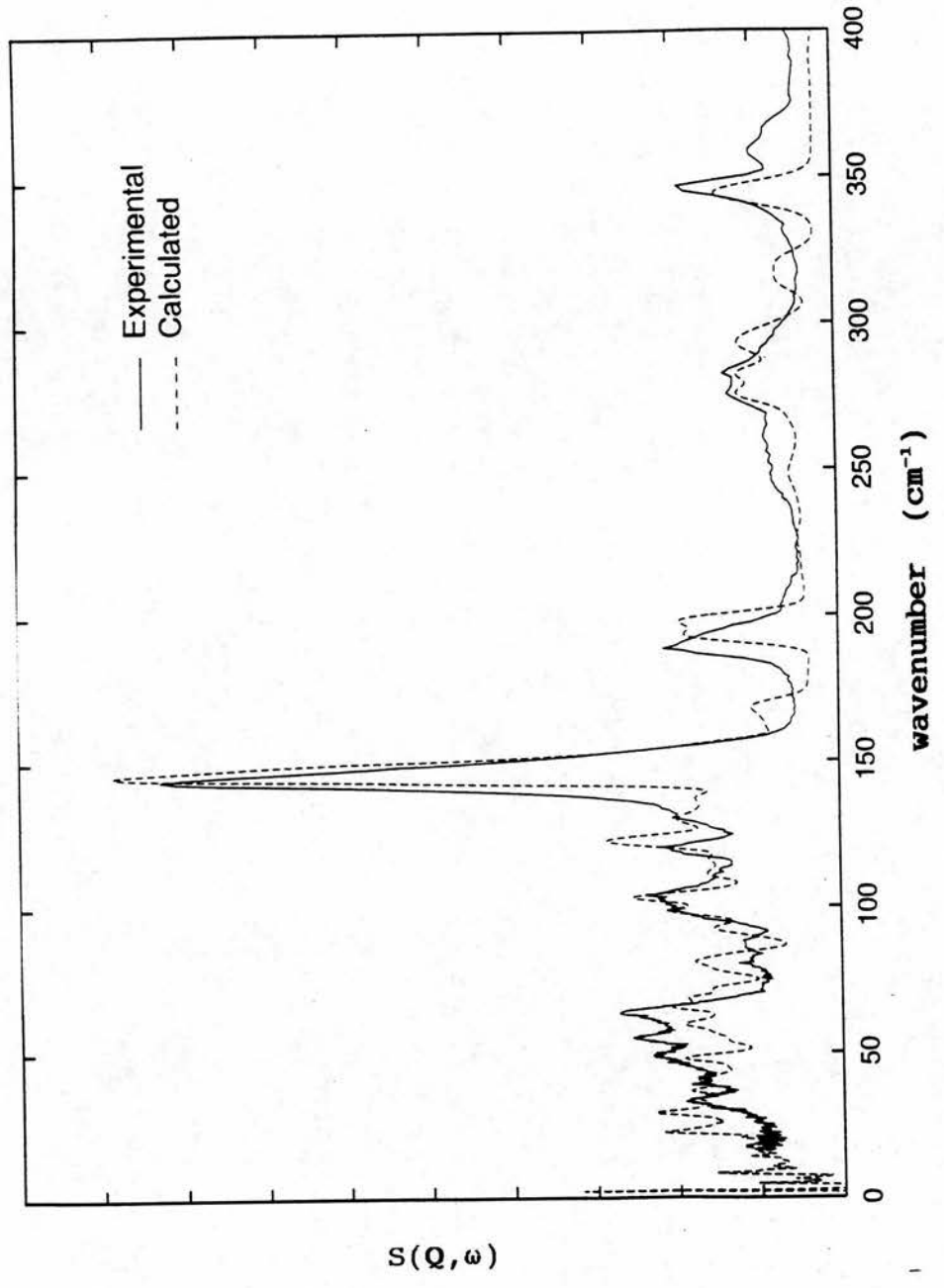


Figure 5.5. As for Fig. 5.4 on an expanded scale.

The total adiabatic methyl rotational barrier, including non-bonded effects, calculated by energy minimization with constrained methyl dihedral angles, was 0.7 kcal/mol in the isolated molecule and 1.0 kcal/mol in the crystal. The latter value is in very close accord with the barrier derived from quasi-elastic neutron scattering experiments [Barthes *et al.*, 1991]. The presence of an intrinsic barrier in the hydrogen bonded state is in agreement with recent molecular mechanics and *ab initio* calculations on water: N-methylacetamide complexes [Guo and Karplus, 1992; Baudry and Smith, 1994].

Despite these refinements of the methyl parameters, a component of methyl torsion remained at too low a frequency, ~130 $cm^{-1}$, and contributed to the overestimate of the peak intensity at 125 $cm^{-1}$. This point will be discussed further in Chapter VI. The remaining components of the peak at 125 $cm^{-1}$ involved phenyl out-of-plane bending coupled with CN torsion (Table 5.3). In fact these degrees of freedom were involved in a series of components, widely split by the crystal field, and raised from the isolated molecule frequency of 85 $cm^{-1}$ to between 102 and 170 $cm^{-1}$ (Table 5.2). For example the weak calculated band centred at 165 $cm^{-1}$ also involved combinations of these two degrees of freedom. It is possible that the experimental intensity observed as a shoulder on the low frequency side of the methyl torsional peak corresponds to this band. Similarly the phenyl torsional degree of freedom contributed a mode at 27 $cm^{-1}$ in the isolated molecule, but was raised by the non-bonded interactions of the crystal field to a series of 8 split peaks, between 80 and 125 $cm^{-1}$. It is notable that in the crystal there was no clear cut seperation between the low

frequency intra-molecular modes and the higher frequency lattice modes. For the isolated molecule, the soft intra-

molecular degrees of freedom lay low in the calculated spectrum. In fact the lowest frequency intra-molecular modes mix extensively with librational lattice modes, causing wide calculated splitting of the low frequency intra-molecular modes in the crystal. Such effects cannot be modelled by isolated molecular force fields. A molecular mechanics PEF can simulataneously model the intra- and inter-molecular features of the dynamics.

The average intensity of the lattice modes (<100 $cm^{-1}$) was ~20% of the methyl torsional peak at 145 $cm^{-1}$. The calculated spectrum <25 $cm^{-1}$ consisted of discrete peaks, whereas the experimental spectrum shows a gradually rising continuum. This may have been due partly to the discrete nature of the phonon calculations. The lowest lying phonon branches displayed significant dispersion (discussed in Section 5.3.5 below). The phonon calculations sampled a finite number of points on these dispersion curves, and so concentrated scattered intensity artificially at discrete frquencies. At frequencies > 25 $cm^{-1}$ the calculated and experimental spectra contained the same number of peaks at approximately correct frequencies. The average intensity of the lattice mode region was under-estimated in the calculations and the detailed relative peak intensities were not well reproduced. It is possible that some of the calculated underestimate arose from the contribution of heavy atom incoherent scattering, and possibly also from a contribution of coherent scattering, to the experimental spectrum. As noted, 89% of the total cross section for ACN is due to incoherent scattering from hydrogens and the amplitude weighting makes the proportion of incoherent scattered intensity higher for modes where hydrogen motion is independent of the heavy molecular skeleton. At low energy transfers in the collective lattice mode region however, this last mechanism has limited impact because

the modes involve rigid body motions of the ACN molecule. Thus incoherent scattering from the heavy atoms will contribute significantly more to the observed spectrum at low frequencies than at high frequencies. However, examination of the ACN-D5 data (see Chapter VI below) supported the idea that a contribution from coherent scattering or from incoherent scattering from heavy atoms was a source of only a portion of the calculated under-estimate in the low frequency region. Chapter VI describes improvements to the refined parameterisation which account for much of the remaining under-estimate of intensity for ACN.

The calculated total intensity of the split band centred at 195 $cm^{-1}$ was in good agreement with that of the band observed at 190 $cm^{-1}$. The calculated band was assigned to CN torsion and phenyl torsion mixed with skeletal deformation. CN torsion also contributed to a further band near 275 $cm^{-1}$, again coupled with phenyl torsion and out-of-plane bending (Table 5.2). A recent INS study of N-methyl acetamide also concluded that CN torsion contributes to modes near 120 and 180 $cm^{-1}$ [Fillaux *et al.*, 1993], and earlier work attributed the band at 275 $cm^{-1}$ to CN torsion [Krimm and Bandekar, 1986]. The calculated peak centred at 100 $cm^{-1}$ was in agreement with experiment and was assigned to phenyl torsion extensively mixed with librational lattice modes.

The band calculated at 316 $cm^{-1}$, which represented in-plane bending of the phenyl ring, was the second band (after that at 1209 $cm^{-1}$ discussed above) for which the calculated frequency was more than 3% away from the experimental value. Appropriate intensity which may correspond to this band appears in the experimental spectrum at 360 $cm^{-1}$, and also appears in IR spectra [Tariq *et al.*, 1984]. This band should therefore have lain above

the methyl in-plane bending band at 345 $cm^{-1}$, which itself was in good agreement with experiment. Chapter VI discusses refinements to the parameterisation which improve the modelling of this band.

### 5.3.3.2. Multiphonon scattering.

In Fig. 5.6 are presented spectra calculated in the one-phonon, two-phonon, and three-phonon approximations to Eq. 5.2.18. In the region <150 $cm^{-1}$ the calculated intensities were accurately represented in the one-phonon approximation. At higher frequencies multi-phonon scattering made an appreciable contribution to the total intensity. In the region between 150 and 300 $cm^{-1}$ two-phonon combinations of lattice and low frequency intra-molecular modes with the intense methyl torsional peak at 145 $cm^{-1}$ appeared. These produced background intensity in reasonable agreement with experiment. The calculated first overtone of the methyl torsion appeared at 290 $cm^{-1}$. This is not present experimentally. However, the calculated intensity at 260 $cm^{-1}$ was less than in the experiment (Fig. 5.5). This suggested that the methyl torsional potential might be significantly anharmonic, with the first overtone appearing in the experimental spectrum not as a sharp peak at the exact overtone frequency of 290 $cm^{-1}$, but lower and broader between 260 $cm^{-1}$ and 290 $cm^{-1}$. Anharmonicity in the methyl torsional potential is discussed further in Section 5.3.6 below.

Three-phonon terms produced further intensity between 350 and 500 $cm^{-1}$, again improving the fit to the experimental intensity. Thus the second and third order terms of the phonon expansion, in combination with the dominant methyl torsion, contributed to background intensity at increasing frequencies between 200 and 500 $cm^{-1}$. A broad contribution

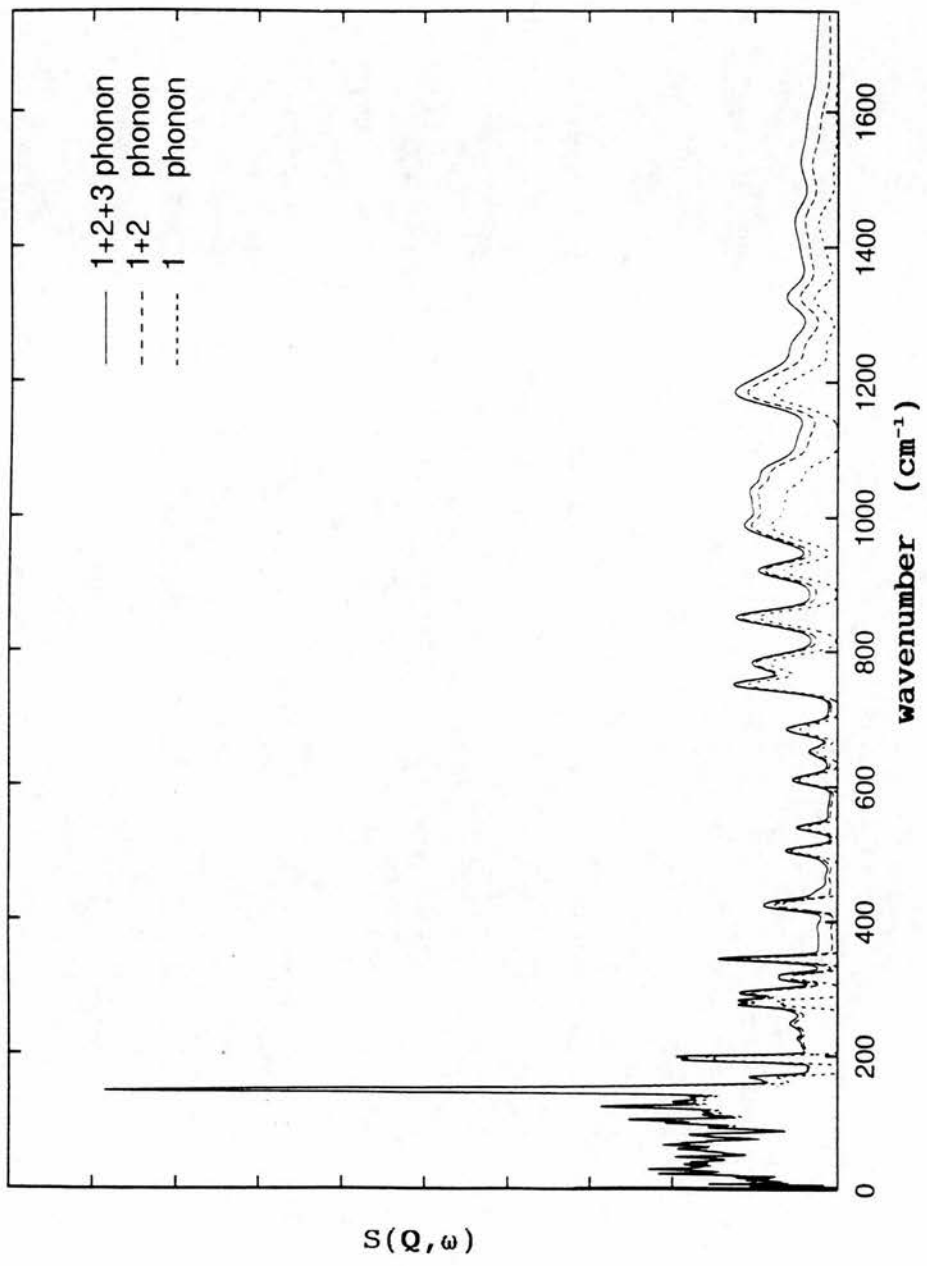


Figure 5.6. $S(Q,\omega)$ using the one-, two-, and three-phonon approximations to Eq. (5.2.18). The contribution of two- and three-phonon terms is evident.

from two- and three-phonon scattering was present in the region above 800 $cm^{-1}$, with a general improvement in the fit to the data. This is a consequence of the relation between $Q^2$ and $\omega$ for TFXA (Chapter III), which leads to an increasing weight for two-phonon scattering, proportional to $q^4$, and three-phonon scattering, proportional to $q^6$ at high energy transfer (Eq. 5.2.18). It is probable that extension of the calculations to fourth- and higher-order terms of the phonon expansion, at a prohibitive cost in computational time, would improve the agreement with experimental background above 400 $cm^{-1}$. The experimental and calculated intensities for the one phonon fundamentals agreed well over a wide range in energy transfer, from 20 to 4000 $cm^{-1}$ in Figs. 5.4, 5.5 and 5.7.

**5.3.3.3. Amide bands.**

For the amide hydrogen out-of-plane motion in the isolated molecule, two sets of torsional parameters were important. These were the torsions defined around the NC and $NC_{ph}$ bonds, combinations of which can describe pure out-of-plane motion of the amide hydrogen. A reasonable fit to the total intensity of the INS peak at 750-785 $cm^{-1}$ was obtained with the four degenerate torsional force constants for the NC bond at 2.41 kcal/mol each, and four degenerate $NC_{ph}$ torsional force constants of 0.69 kcal/mol each. In the isolated molecule the NH out-of-plane mode (Amide V) occured at 678 $cm^{-1}$. The crystal field raised the calculated frequency of the out-of-plane mode by about 80 $cm^{-1}$, to produce two complex split bands centred at 750,

778 $cm^{-1}$ in combination with phenyl hydrogen out-of-plane bending modes. Another band in this region, centred at 785 $cm^{-1}$, represented a complex in-plane skeletal deformation mode of the peptide group, and also involved NH out-of-

plane motion. These bands produced two peaks in the calculated INS spectrum between 750 and 790 $cm^{-1}$ where one broad peak is observed in the experimental spectrum, centred at 770 $cm^{-1}$. At least two bands are observed in the IR spectrum between 750 and 775 $cm^{-1}$ [Careri *et al.*, 1984; Barthes *et al.*, 1992; Barthes *et al.*, 1993]. Experimental IR components at 755, 762, and 772 $cm^{-1}$ have been assigned to phenyl $C_{ph}H$ and NH out-of-plane bending bands by isotopic substitution techniques. The resolution of the TFXA neutron spectrometer is insufficient to resolve the three peaks, and one broad peak appears in the INS spectrum. The splitting of the calculated INS peak thus resulted from inaccuracies of <3% in the calculated frequencies when compared with the IR experiments.

As noted in Section 5.3.2.2 NH in-plane bending was calculated to contribute to four bands centred at 1175, 1185, 1209, and 1255 $cm^{-1}$ in the hydrogen bonded crystal. The bands at 1175, 1185 $cm^{-1}$ were predominantly mixed with CCH in-plane bending and contributed to the intense INS peak centred at 1180 $cm^{-1}$ in Fig. 5.4. This peak appeared approximately 20 $cm^{-1}$ above its experimental position, because the corresponding experimental modes are at 1160 and 1180 $cm^{-1}$ in the IR, but are not seperately resolved in the INS spectrum. The calculated band centred at 1180 $cm^{-1}$ therefore obscured the calculated band at 1209 $cm^{-1}$, which is not resolved experimentally in the INS spectrum. The intensity of the Amide III band at 1255 $cm^{-1}$ was well reproduced, though it lay ~10 $cm^{-1}$ too low and was therefore not clearly resolved from the neighbouring peaks in the calculated spectrum. The INS peak at 1320 $cm^{-1}$ was underestimated, and this may have been due to the erroneous assignment of the 1209 $cm^{-1}$ peak as discussed above. Refinements discussed in Chapter VI provide an

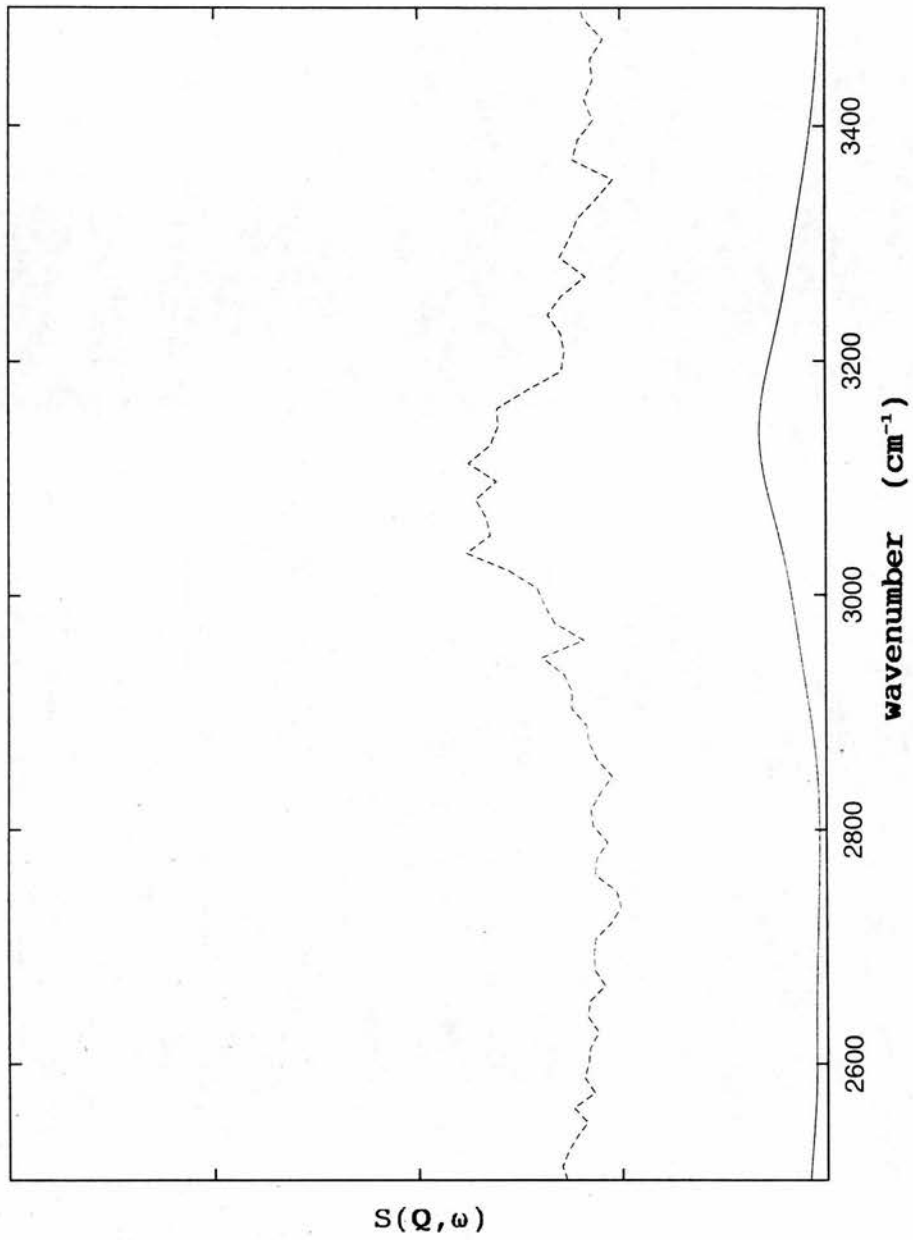


Figure 5.7. As for Fig. 5.4 at high energy transfer. The scale for the $S(Q,\omega)$ axis has been expanded five fold compared with Figures 5.4, 5.5 and 5.6.

improved fit to this band.

The intensity of the Amide II peak at 1512 $cm^{-1}$ in the calculation, was an under-estimate of the experimental INS band at 1500 $cm^{-1}$, although throughout this region there was an under-estimate in the background intensity as discussed in Section 5.3.2.2 above, due to neglect of higher order terms in the phonon expansion. There is recent IR and Raman evidence of an anomalous band near 1490 $cm^{-1}$ in ACN which grows markedly in intensity at low temperature and is absent in the N-deuterated compound [Barthes *et al.*, 1993; Sauvajol *et al.*, 1991]. This band was also observed in the IR experiments I performed to characterise the ACN sample used in the present INS experiments. The extra intensity appearing in the experimental INS spectrum at 1500 $cm^{-1}$ when compared with the calculation, suggested that this anomalous mode involves significant hydrogen atom motion. If the present assignment of Amide II to the 1510 $cm^{-1}$ peak is correct, the anomalous 1490 $cm^{-1}$ band may involve NH in-plane bend, as has been suggested recently for a similar anomalous band in N-methyl-acetamide [Araki *et al.*, 1991].

The energy resolution of the INS spectrometer worsens significantly at high energy transfers, to a full width half maximum of ~30 $cm^{-1}$ at 1600 $cm^{-1}$ and ~100 $cm^{-1}$ at 3000 $cm^{-1}$. Nevertheless, some tentative conclusions concerning high-frequency vibrations can be drawn. The lack of significant structure above the multi-phonon background in the experimental and calculated INS spectra in the region of Amide I at 1665 $cm^{-1}$ supported its calculated assignment predominantly to CO stretch which gives little INS intensity (Table 5.2). Similarly, the absence of significant intensity in the region of the anomalous mode at 1650 $cm^{-1}$, which is present in crystalline ACN below 100 K, supported its assignment to a mode involving little

hydrogen atom motion [Careri *et al.*, 1984]. INS experiments on NMA and polyglycine have been interpreted as demonstrating an unusually low-frequency NH stretch mode near 1575 $cm^{-1}$ [Kearley *et al.*, 1994]. The present ACN INS experimental spectra do not show any excess intensity attributable to such an anomalous NH stretch mode in this region. In the present model the NH stretch occured at 3275 $cm^{-1}$ close to the frequency of 3260 $cm^{-1}$ identified by IR experiments [Careri *et al.*, 1984; Tariq *et al.*, 1984]. It contributed to a broad INS peak centred on 3050 $cm^{-1}$ (Fig. 5.7) which was predominantly due to $C_{me}H$ and $C_{ph}H$ stretching modes. The calculated intensity of the broad band was comparable to the experimental intensity.

The work described so far reports the results of the final parameterisation in calculating experimental structural and spectroscopic quantities which were used as criteria to refine the parmeters of the calculations. In what follows in this Chapter no further adjustments of the parameters were made. The further comparisons with experiment which are described hereafter can therefore be considered as independent tests of the refined PEF.

### 5.3.4. Atomic Debye-Waller factors and mean square displacements.

The exponent $W_\alpha(\mathbf{Q})$ in the atomic Debye-Waller factor $\exp\{-2W_\alpha(\mathbf{Q})\}$, Eq. 5.2.19, is related to the anisotropic atomic mean square displacement as follows:

$$2W_\alpha(\mathbf{Q}) = \langle \{\mathbf{Q}.\mathbf{u}_\alpha\}^2 \rangle = Q^2 \langle u_{q\alpha}^2 \rangle \qquad (5.3.1)$$

where the brackets <...> indicate a thermal average over

the unperturbed states of the sample, and $\mathbf{u}_\alpha$ is the dynamical displacement of atom $\alpha$ from its equilibrium position. $u_{q\alpha}^2$ is the mean square displacement of atom $\alpha$ in the direction of $\mathbf{Q}$. The isotropic $W_\alpha^{iso}(\mathbf{Q})$ is the mean of the anisotropic form:

$$2W_\alpha^{iso}(\mathbf{Q}) = Q^2 \sum_x < \{u_{x\alpha}\}^2 >/3 = Q^2 <u_\alpha^2> \qquad (5.3.2)$$

Here x labels the components of the atomic displacement vector $\mathbf{u}_\alpha$. $<u_\alpha^2>$ is the isotropic mean square displacement of atom $\alpha$.

For the isotropic or anisotropic atomic Debye-Waller factors derived from x-ray or neutron diffraction experiments, in contrast, the exponent includes a dynamic contribution to the mean square displacement as given by Eqs. 5.3.1 and 5.3.2, *and* a static contribution due to crystalline disorder.

For comparison with neutron diffraction data, the dynamic components of the anisotropic mean square displacements for the hydrogen atoms were calculated according to Eq. 5.3.1 for $\mathbf{Q}$ in each of the principal crystallographic directions, from the anisotropic Debye-Waller exponents, expressed as a sum over the phonon normal modes (Eq. 5.2.19) at a temperature of 15 K. The absolute values of $<u_{x\alpha}^2>$, the anisotropy, and the variation in relative magnitudes for the various hydrogens were in excellent agreement, (Table 5.4), with the values derived from a neutron diffraction experiment on ACN performed at 15 K [Johnson, Eckert, and Barthes, personal communication]. Further support for the accuracy of the calculated anisotropic $<u_{x\alpha}^2>$ came from the INS intensity calculations, for which the Debye-Waller exponents were recalculated at a temperature of 25 K, the experimental temperature. The

Table 5.4. Calculated anisotropic mean square displacements for hydrogens compared with neutron diffraction results (Johnson *et al.*, personal communication). Calculations use the parameters of Table 5.1. Column I: Hydrogen atoms of ACN. Phenyl hydrogens are named according to their position relative to the N substitution site - which is labelled *. a, b, c refer to crystallographic directions. Column II: anisotropic mean-square displacements (Å²), from neutron diffraction data at 15 K [Johnson *et al.*, personal communication]. Column III: anisotropic mean square displacements (Å²), from harmonic analysis.

| I | | II | III | I | | II | III |
|---|---|---|---|---|---|---|---|
| methyl H | a | 0.0359 | 0.0352 | phenyl $H_{ortho}$ | a | 0.0126 | 0.0118 |
| | b | 0.0366 | 0.0438 | | b | 0.0273 | 0.0278 |
| | c | 0.0253 | 0.0258 | | c | 0.0279 | 0.0258 |
| | *isotropic* | .0326 | 0.0349 | | *isotropic* | 0.0226 | 0.0218 |
| methyl H | a | 0.0150 | 0.0160 | phenyl $H_{ortho}$ | a | 0.0215 | 0.0220 |
| | b | 0.0482 | 0.0510 | | b | 0.0189 | 0.0194 |
| | c | 0.0328 | 0.0336 | | c | 0.0265 | 0.0246 |
| | *isotropic* | .0320 | 0.0335 | | *isotropic* | 0.0223 | 0.0220 |
| methyl H | a | 0.0301 | 0.0286 | phenyl $H_{meta}$ | a | 0.0154 | 0.0162 |
| | b | 0.0162 | 0.0172 | | b | 0.0218 | 0.0210 |
| | c | 0.0483 | 0.0606 | | c | 0.0296 | 0.0256 |
| | *isotropic* | 0.0315 | 0.0354 | | *isotropic* | 0.0222 | 0.0209 |
| amide H | a | 0.0178 | 0.0192 | phenyl $H_{meta}$ | a | 0.0159 | 0.0160 |
| | b | 0.0110 | 0.0120 | | b | 0.0189 | 0.0194 |
| | c | 0.0258 | 0.0300 | | c | 0.0286 | 0.0250 |
| | *isotropic* | 0.0182 | 0.0204 | | *isotropic* | 0.0211 | 0.0201 |
| | | | | phenyl $H_{para}$ | a | 0.0203 | 0.0200 |
| | | | | | b | 0.0170 | 0.0164 |
| | | | | | c | 0.0264 | 0.0254 |
| | | | | | *isotropic* | 0.0212 | 0.0206 |

relation between $Q^2$ and $\alpha$ in TFXA spectra (Chapter III) leads to a rapid variation of the factor $\exp\{-2W_\alpha(\mathbf{Q})\}$ at high energy transfer. As a result relative peak intensities in the high frequency region are highly sensitive to $\langle u_{x\alpha}^2 \rangle$. As noted, experimental and calculated intensities for one phonon fundamentals agreed over a wide energy transfer range, 20-4000 $cm^{-1}$ (Figs. 5.4, 5.5, 5.7).

The dynamic components of the isotropic mean square displacements for the heavy atoms were calculated at 113 K from Eqs. 5.2.19, 5.3.1 and 5.3.2. These were compared, (Table 5.5), with the corresponding values obtained from the 113 K x-ray crystallographic analysis [Wasserman *et al.*, 1985]. The relative magnitudes for the various atoms were in agreement with the 113 K experimental values. The absolute values obtained were in good agreement for the heavy atoms of the acetamide group, but were underestimated by ~20% for the phenyl carbons. A test was made to check that the calculated values for mean square displacements were not underestimated by neglect of the lowest frequency acoustic phonons. Low frequency harmonic oscillators have larger displacements than high frequency oscillators of the same mass. Therefore it was possible that the discrete nature of the phonon calculations, which neglected the lowest frequency acoustic phonons, could underestimate the mean square displacements. A calculation made at a higher density of discrete points in **k**-space for a region near the origin was made, because the lowest frequency acoustic modes occur only at low values of **k** (Section 5.3.5 below). The higher density of points in a box round the origin of reciprocal space was equivalent to a crystal of 64000 unit cells, but the density of points throughout the remainder of the unit cell remained equivalent to 512 unit cells. A full calculation at the high density of **k**-points was not computationally possible in less than 4 months! The contribution to the mean square

Table 5.5. Calculated isotropic mean square displacements for heavy atoms compared with x-ray diffraction results. Calculations use the parameters of Table 5.1. Column **I**: Heavy atoms of ACN. Phenyl carbons are named according to their position relative to the N substitution site - which is labelled *. Column **II**: isotropic mean square displacements (Å²), from harmonic analysis. Column **III**: isotropic mean-square displacements (Å²), from x-ray diffraction data at 113 K [Wasserman *et al.*, 1985].

| I | II | III | I | II | III |
|---|---|---|---|---|---|
| $C_{me}$ | 0.026 | 0.026 | $C_{ph}$ *ortho* | 0.018 | 0.021 |
| C | 0.019 | 0.020 | $C_{ph}$ *ortho* | 0.018 | 0.022 |
| O | 0.026 | 0.026 | $C_{ph}$ *meta* | 0.019 | 0.025 |
| N | 0.018 | 0.020 | $C_{ph}$ *meta* | 0.020 | 0.025 |
| $C_{ph}$ * | 0.016 | 0.019 | $C_{ph}$ *para* | 0.020 | 0.025 |

displacements from the lowest frequency phonons was calculated at this higher density and found to change the total mean square displacements by less than 1%. Thus the neglect of the lowest frequency modes had little impact on the calculated mean square displacements, and for consistency the original values were retained throughout. There are two reasons for the limited impact of low frequency acoustic phonons on the mean square displacements. First, the effective mass of the low frequency oscillators tends to that of the whole acetanilide molecule, because these acoustic phonons represent rigid body motions of the molecules. Second the weight that these lowest frequency phonons have in the summation over the whole Brillouin zone is a small fraction of the total weight.

The good agreement between calculated and experimental low temperature anisotropic mean square displacments for all hydrogens at 15 K and isotropic mean square displacements for acetamide heavy atoms at 113 K indicated that the contribution to mean square displacements from static disorder at low temperatures is small. Since static disorder may be assumed to be independent of temperature in the first approximation, the underestimate of the mean square displacements for the phenyl carbon atoms at the higher temperature of 113 K can be interpreted as evidence of anharmonicity in the potential energy surface for phenyl ring motion.

### 5.3.5. Phonon Dispersion Curves.

The refined PEF was used to calculate phonon dispersion curves in the harmonic approximation for fully deuterated acetanilide. In Fig 5.8a, b and c, the calculated phonon dispersion curves are compared with published coherent INS measurements for fully deuterated acetanilide [Barthes *et al.*, 1988]. The symmetry character of each acoustic branch

is displayed. The symmetry of optic branches is given in Table 5.2. Appropriate anti-crossing behaviour for curves with the same symmetry character is apparent in all the dispersion curves. For example the two branches with $A_g$ symmetry character arising at 30 and 38 $cm^{-1}$ at k = 0 always display anti-crossing behaviour visible in Figs. 5.8a, b and c. In Fig. 5.8a the longitudinal branch, with symmetry B3u, shows anti-crossing behaviour with the second optic branch originating at 25 $cm^{-1}$ at **k** = 0, which also has B3u symmetry. These features testify to the utility of the method used for tracing the dispersion curves between the finite set of calculated points, as described in Section 5.2.3.2. Points on the dispersion curves obtained by Barthes *et al.* by coherent INS experiments at 260 K are also shown in Fig. 5.8a and 5.8b [Barthes *et al.*, 1988]. In the $b^*$ direction, parallel to the hydrogen bond, the calculated longitudinal branch superposes with the experimental data (Fig. 5.8b). However the coherent INS experiments suggest that the frequencies of the longitudinal branch rise by ~ 10% on lowering the temperature from 260 K to 10 K. As the harmonic approximation is more likely to be valid at 10 K than at 260 K, the calculated dispersion curves should represent a model of low-temperature lattice dynamics. Therefore the frequencies of the longitudinal branch may be slightly underestimated in the model. The two experimental points at largest values of **k** were assigned in the present work to the calculated optic branch on which they lie, which is of appropriate Ag symmetry. The coherent INS data on the transverse branch in the b* direction were experimentally compatible with symmetry B3u [Barthes *et al.*, 1988]. This is the symmetry of the higher frequency of the two transverse branches in the present calculations. The coherent INS experiments suggest that the temperature dependent shifts in the transverse branch are more marked

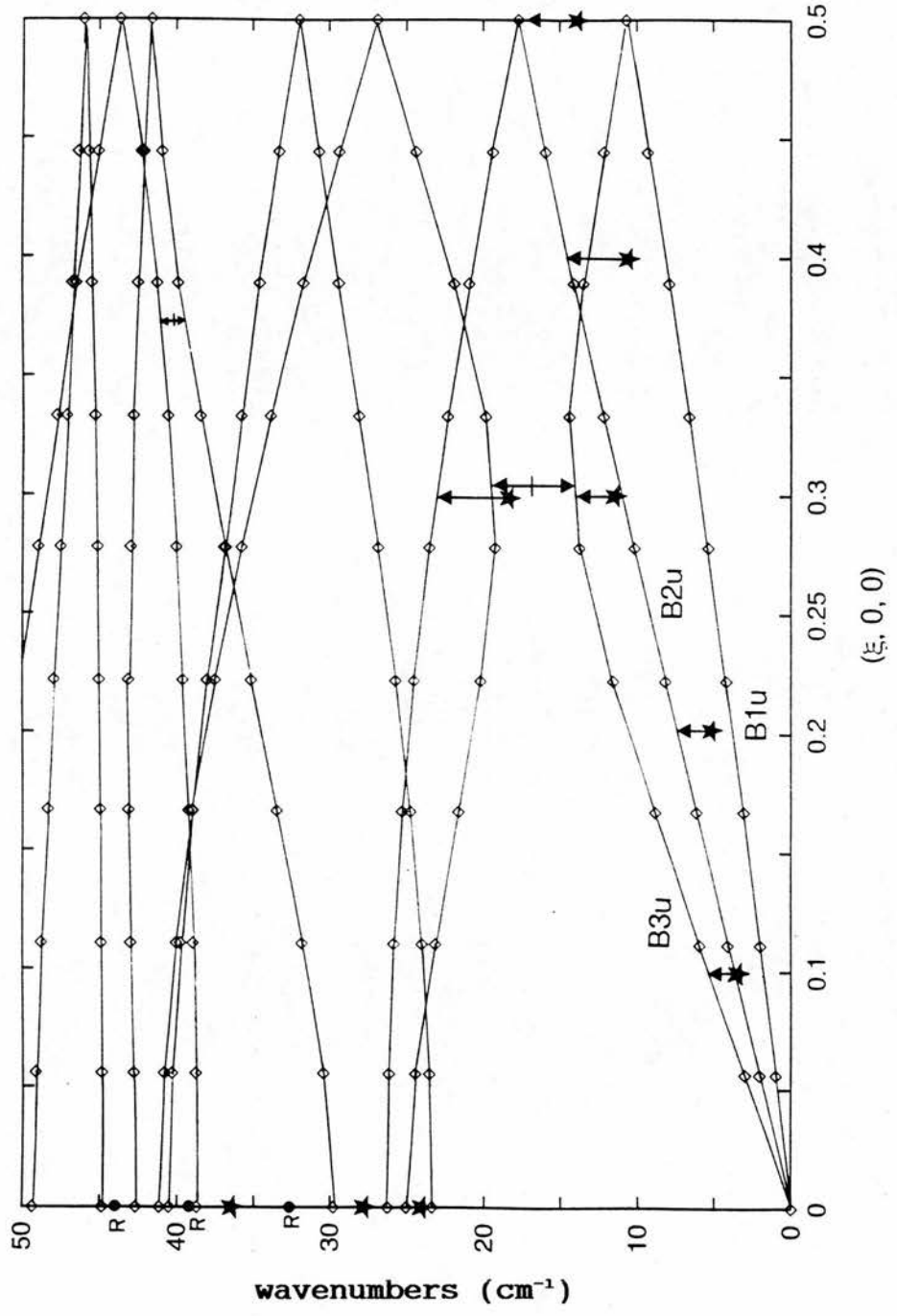


Figure 5.8a. Phonon dispersion relations for frequencies < 50 $cm^{-1}$ in *a** direction. Symmetry character of acoustic branches are shown (see Table 2 for optic branch symmetries). Double headed arrows indicate anti-crossing effects. Stars show experimental measurements from coherent INS experiments [Barthes *et al.*, 1988].

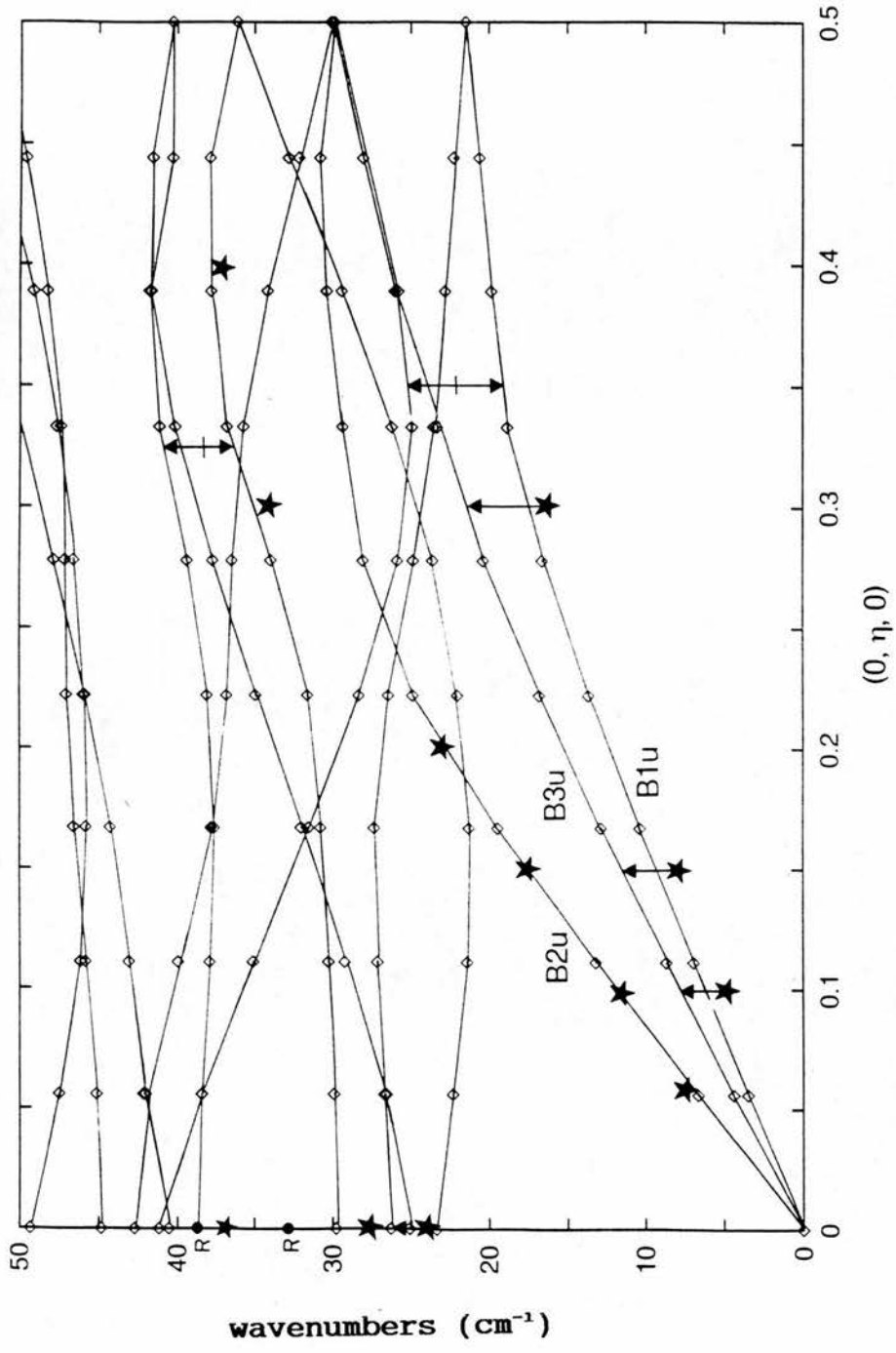


Figure 5.8b. Phonon dispersion relations < 50cm$^{-1}$ in *b** direction. Symmetry character of acoustic branches are shown (see Table 2 for optic branch symmetries). Double headed arrows indicate anti-crossing effects. Stars show experimental measurements from coherent INS experiments [Barthes *et al.*, 1988].

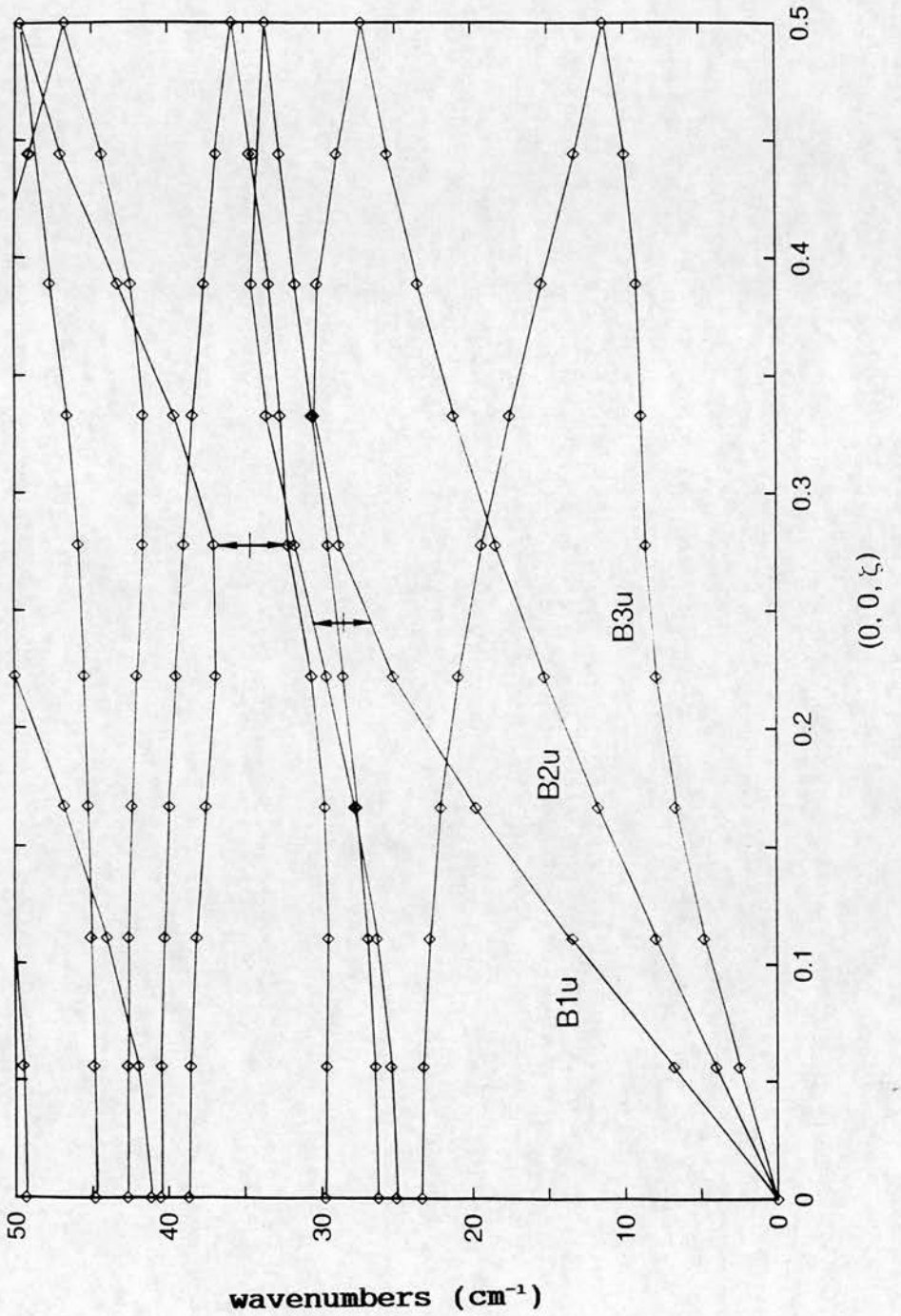


Figure 5.8c. Phonon dispersion relations <50 $cm^{-1}$ in $c^*$ direction. Symmetry character of acoustic branches are shown (see Table 5.2 for optic branch symmetries). Double headed arrows indicate anti-crossing effects.

than in the longitudinal direction, the frequencies being ~16% higher at 10 K than at 260 K. With this correction applied the transverse branch frequencies in the present harmonic calculations were within 15% of the 10 K frequencies. Similar considerations lead to the conclusion that in the $a^*$ direction the experimental data points should also be within ~15% of the corresponding 10 K values. No coherent INS data are available for the $c^*$ direction. An improved comparison between experiment and theory would benefit from a more complete set of experimental low-temperature phonon dispersion curves at higher experimental resolution.

### 5.3.6. Anharmonic dynamics from MD simulations.

To study the anharmonic dynamics of the crystal, the refined PEF was used to perform MD simulations.

#### 5.3.6.1. Calculation of S(Q,ω) from MD simulations.

The dynamic structure factor S(**Q**,ω) calculated from the MD at 80K for 6 values of **Q** is shown in Fig 5.9. A resolution function dependent on **Q** was included to reflect the resolution function of TFXA. The general features of the experimental spectra were apparent, especially at low **Q**, and low temperature. However, the difficulty of achieving an appropriate semi-classical correction throughout a wide energy transfer range was also apparent. The Gaussian approximation and the semi-classical correction are strictly valid only in the linear response regime ($h\omega < K_BT$) [Kneller, *et al.*, 1992]. Because the experimental data extend over a wide energy range, it was not possible to find a single correction scheme valid throughout. This lead to difficulties in comparison of relative peak intensities at widely separated energy transfers. Although the relative intensity of neighbouring peaks was reasonably well reproduced, the

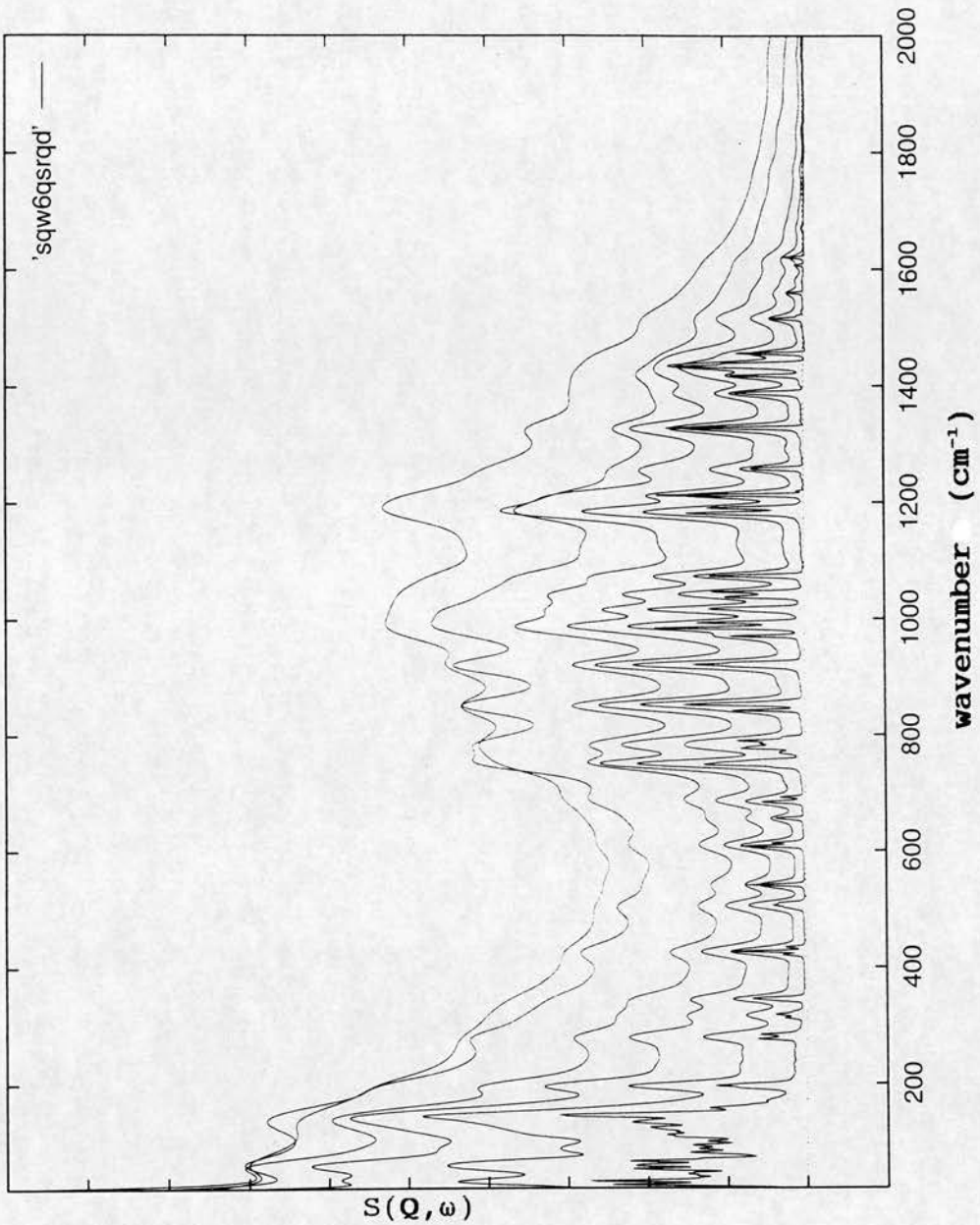


Figure 5.9. S(**Q**,ω) from 80 K molecular dynamics simulation at 6 values of **Q**, 3, 5.2, 7.4, 9.6, 11.8, and 14 Å$^{-1}$. A resolution function dependent on **Q** was introduced to mimic the energy dependent resolution function for TFXA. The true TFXA spectra can be imagined as tracing a curve through S(**Q**,ω) space intersecting the constant **Q** spectra shown. The problems with the semi-classical correction are apparent relative peak intensities at widely separated energy transfers agree poorly with harmonic calculations [Fig. 5.4-5.6].

comparison of widely separated peaks revealed consistent overestimate of the intensities of the higher frequency features. The major analysis of the MD results was therefore by calculation of the hydrogen weighted density of states from the velocity auto-correlation function (Eq. 5.2.28). In this way the contribution of individual atoms to the spectrum could be separately determined. This allowed examination of the anisotropy of different modes, and identifications of anharmonic shifts of the fundamental frequencies.

**5.3.6.2. Comparison of G(ω) from MD and from Harmonic Analyses.**

In Fig. 5.10 G(ω) calculated from the MD simulations is compared with that calculated from the harmonic analysis at 80 K. The frequencies of vibrations in the 80 K simulation are seen to lie very close to those obtained from the harmonic analysis. Intensities for the bands were mostly in close accord, an exception being the region < 150 $cm^{-1}$ and in particular the methyl torsional band at 145 $cm^{-1}$, which was broader but less intense in the MD at 80 K than in the harmonic analysis. These differences may have been related to the anharmonicity of the methyl torsional potential, which was revealed more clearly in higher temperature MD simulations (see below). The imposition of periodic boundary conditions in the MD simulations can also affect the density of states for the low-frequency lattice modes. A further effect, which may also have been responsible for the small intensity differences observed at higher frequencies is the possibility of incomplete equilibration of kinetic energy in the 80 K MD simulations.

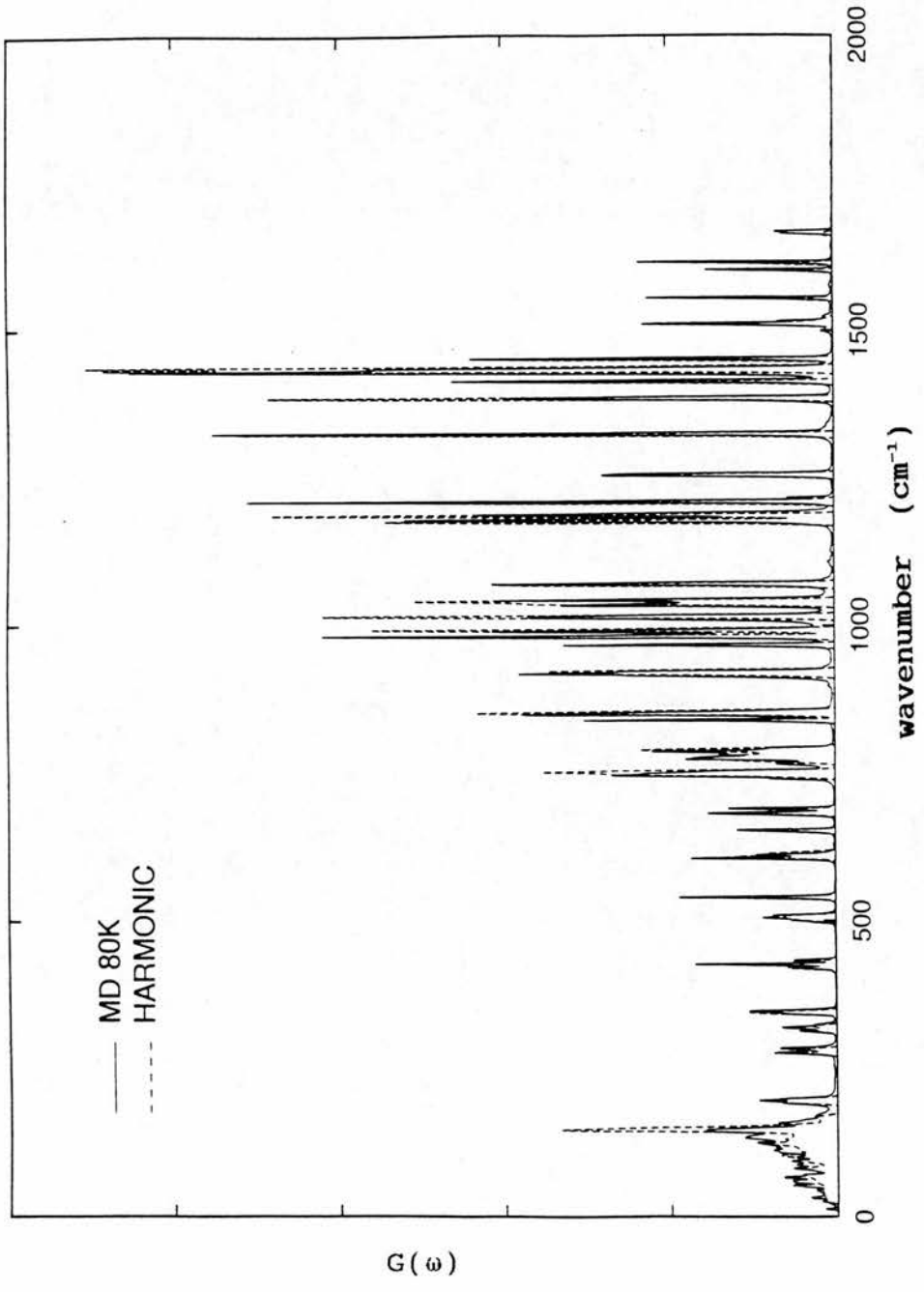


Figure 5.10. G(ω) for all hydrogens calculated from the harmonic analysis and from MD simulation at 80 K.

### 5.3.6.3. G(ω) for Amide Hydrogen.

Figure 5.11 displays the anisotropy of the density of states for the amide hydrogen alone, with Amide II and III motions seen to occur in the a-b plane, whilst the out-of-plane amide modes are seen between 750 and 800 $cm^{-1}$ in the c direction. Significant temperature dependence was observed in the simulations for these NH out-of-plane modes. Thus Fig 5.12 displays G(ω) for the amide hydrogen alone, calculated from the harmonic approximation and from the MD simulations at 80, 140 and 300K. As noted in Section 5.3.2 this region contained three seperate bands, all involving NH out-of-plane motion, as is apparent in Fig. 5.11. The peak maxima at 750 and 785 $cm^{-1}$ showed a 14 $cm^{-1}$ downward shift at 300 K and the bands were changed in form. At the higher temperature the bands became broadened, and the highest frequency band near 785 $cm^{-1}$ was shifted downward more than that centred on 778 $cm^{-1}$, so that it eventually merged with it at 300 K. These observations offered a qualitative explanation for the temperature dependence of NH out-of-plane bands in the IR spectrum [Barthes *et al.*, 1992; Barthes *et al.*, 1993], which show a downward shift of the corresponding bands in ACN, and disappearance of the seperately resolved band of highest frequency at high temperature, leaving only two resolved components at 300 K.

### 5.3.6.4. G(ω) for Methyl Hydrogens.

In Fig. 5.13 are presented G(ω) for the methyl hydrogens calculated from the harmonic approximation and from MD simulations at 80, 140 and 300K. The methyl torsional mode was at 145 $cm^{-1}$ in the harmonic approximation, and at 80 K, though it was broadened and less intense at 80 K. This was in agreement with Raman spectroscopic results at 80 K [Sauvajol *et al.*, 1989]. The methyl group torsional mode maximum was broadened further and shifted downward at

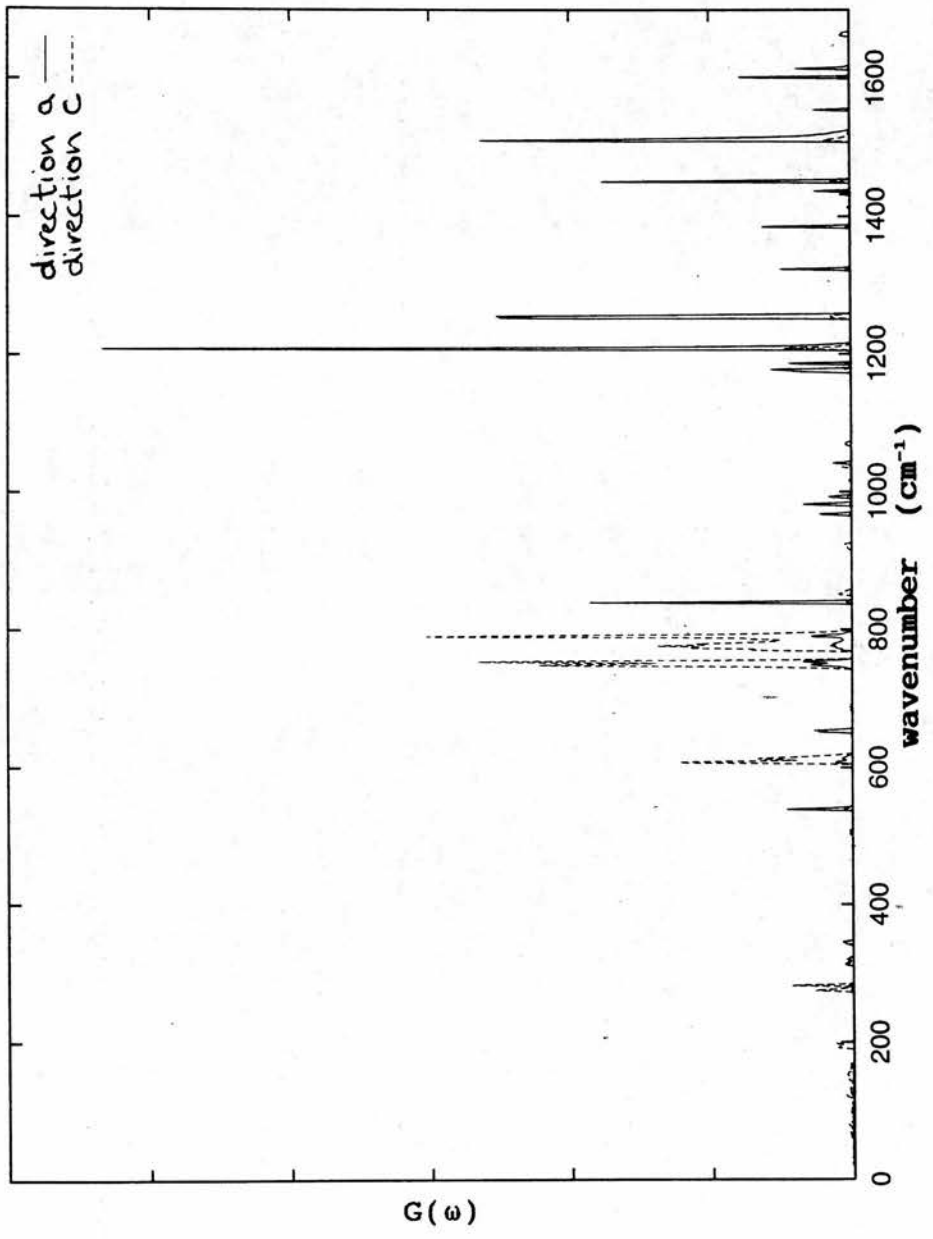


Figure 5.11. Anisotropy of amide H density of states, in a and c crystallographic directions.

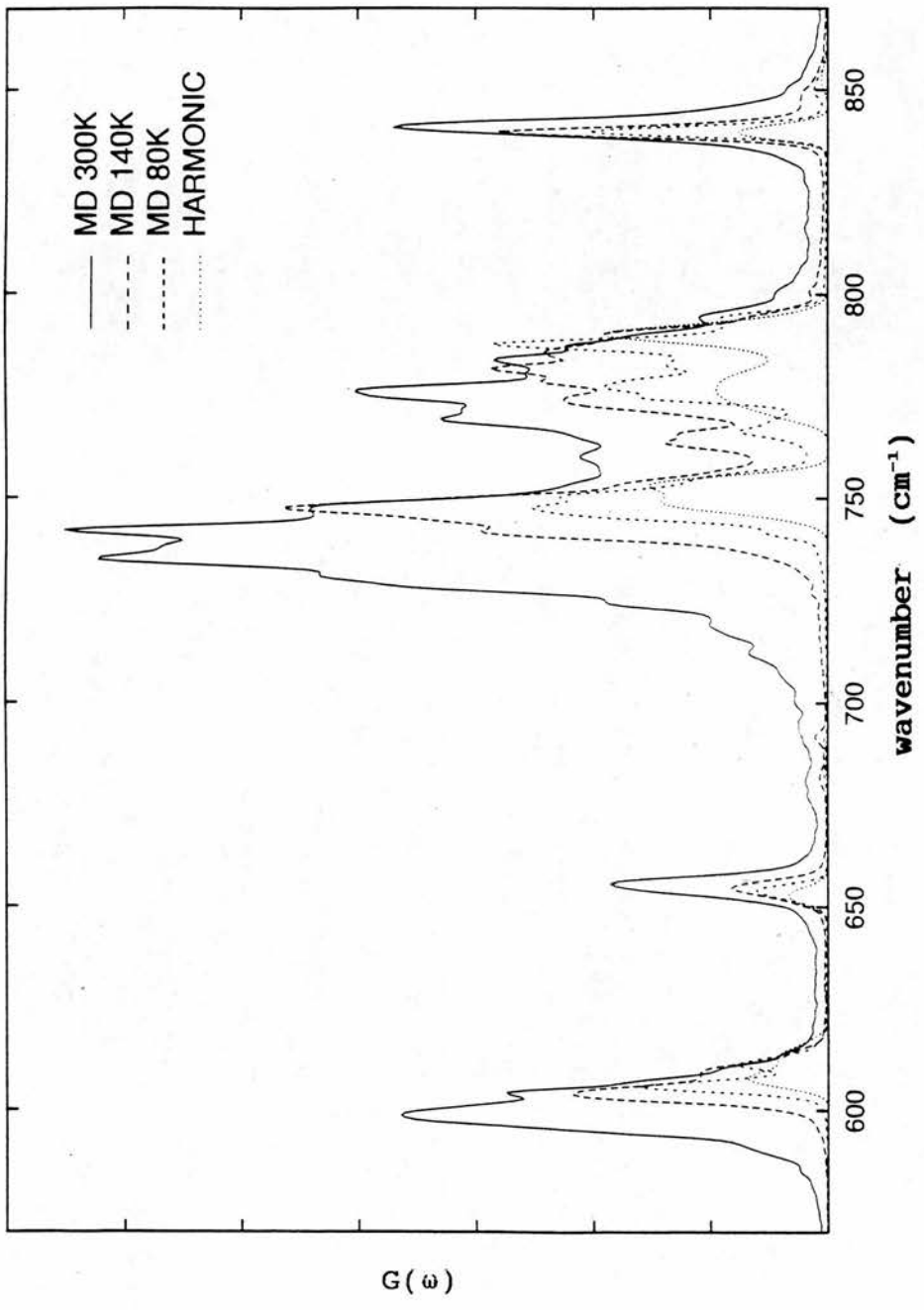


Figure 5.12. G(ω) for amide hydrogen calculated from harmonic approximation, with MD calculation at 80, 140 and 300K. Anharmonic shifts are evident.

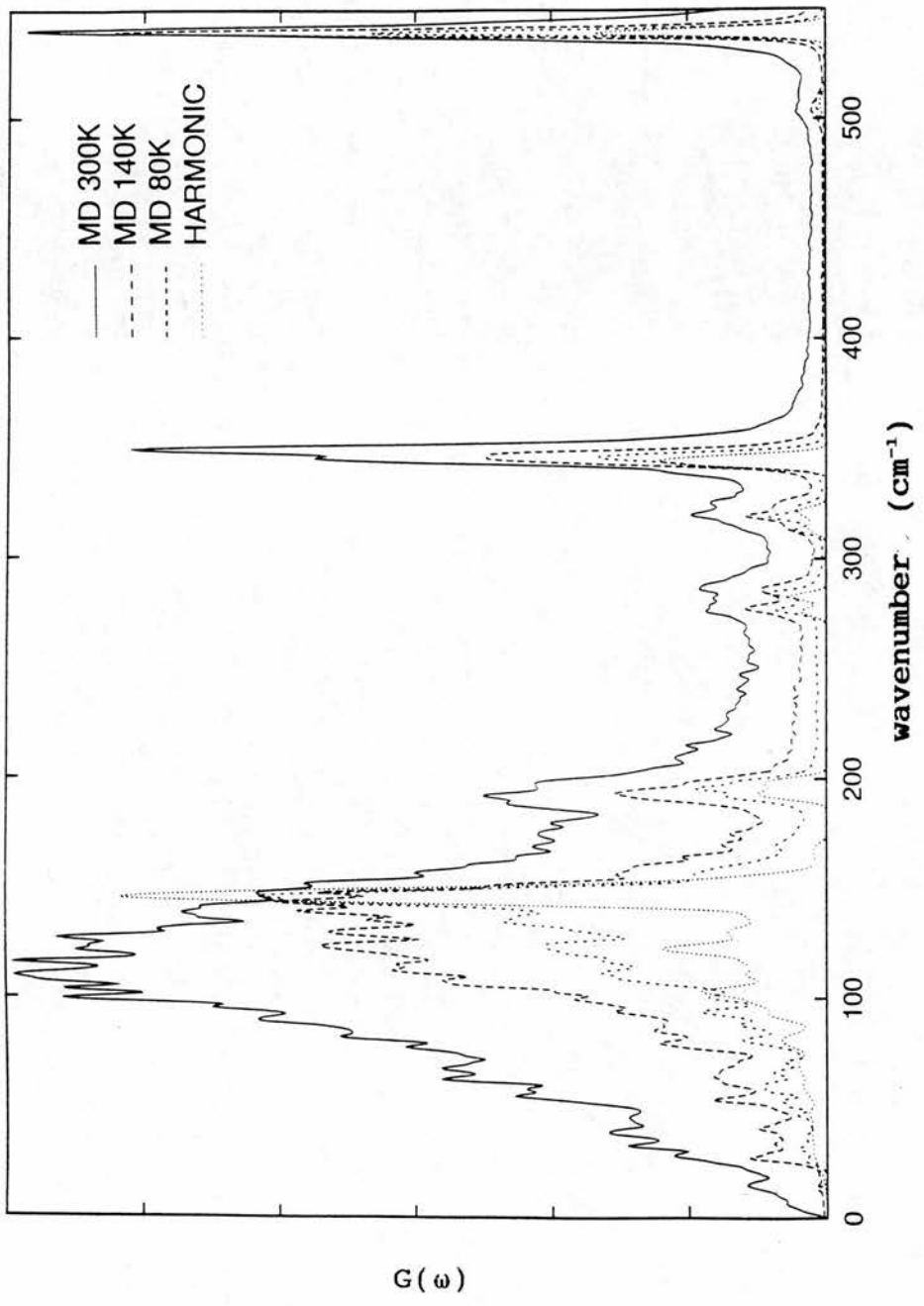


Figure 5.13. G(ω) for methyl hydrogens calculated from harmonic approximation, with MD calculation at 80, 140 and 300K. Anharmonic shifts are evident.

higher temperatures above 80 K to reach 115 $cm^{-1}$ at 300 K. This temperature dependence was in good agreement with that of Raman and INS experiments [Sauvajol *et al.*, 1989; Barthes *et al.*, 1992; Johnston *et al.*, 1991] which indicate the onset above 100 K of a downward shift and broadening, from 142 $cm^{-1}$ at 100 K, to 125 $cm^{-1}$ at 300 K. The downward shifts in the MD simulations were associated with the onset of torsional transitions of the methyl group, which were not seen in the MD simulations below 80K, but occur at 140 K and above. The time series for a methyl torsional angle, derived from the MD simulations at 140 K, is shown in Fig. 5.14. The time series suggested that the dynamics of the methyl group can be considered as a combination of torsional oscillations with rapid jumps between equivalent rotational positions.

The methyl torsional frequency shift may be of significance for the mechanism of generation of the anomalous amide I band at 1650 $cm^{-1}$. Deuteration of the methyl group abolishes the amide I anomaly indicating the involvement of methyl torsion in this anomaly [Sauvajol *et al.*, 1989]. One theory invokes temperature tuning of a Fermi resonance involving an optic mode above 100 $cm^{-1}$ [Johnston and Swanson, 1985], and the methyl torsional mode would be a candidate for this.

**5.3.6.5. Total density-of-states.**

A calculation of the mass weighted density of states, in which all atoms, including heavy atoms, received equal weight, is shown in Fig. 5.15. This method allows the examination of temperature dependence for modes involving little H atom motion. Despite the temperature tuning of the methyl torsion in the model, no anomaly in the temperature dependence of the amide I peak was apparent. Furthermore no additional band relevant to the anomalous mode is apparent. No dispersion of the amide I band which

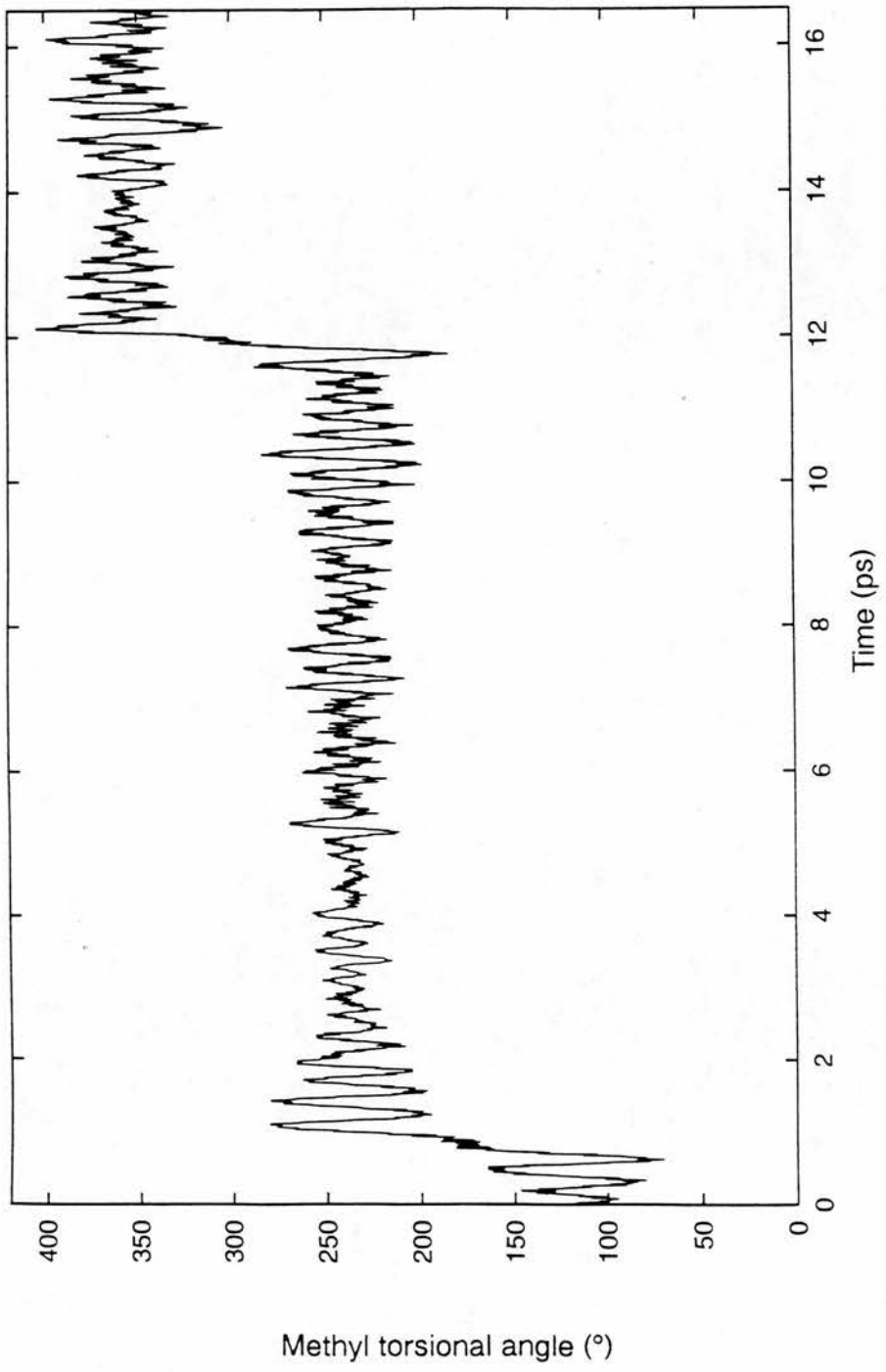


Figure 5.14. Time series of methyl torsional angle from MD simulation at 140K.

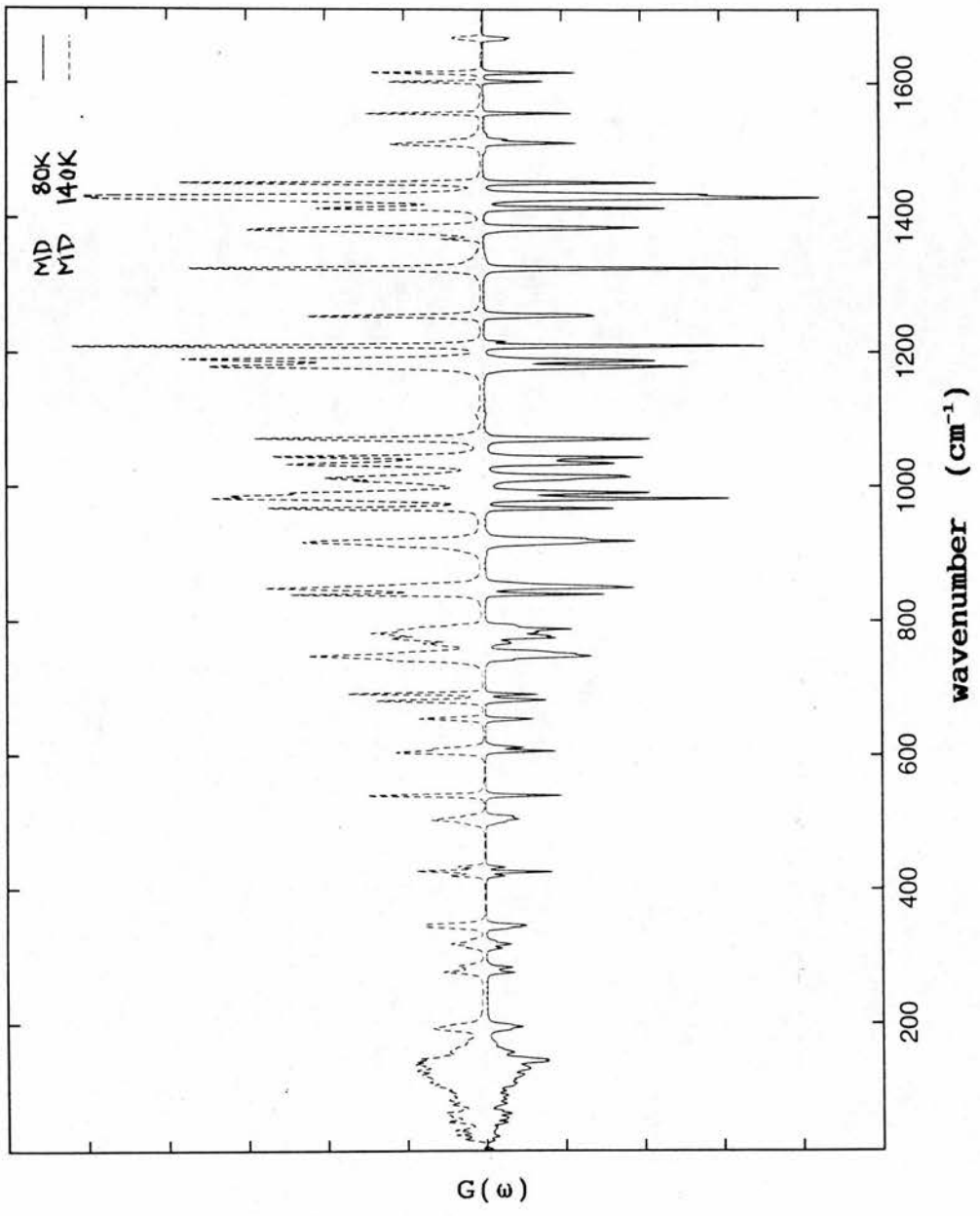


Figure 5.15. G(ω) calculated with equal weighting for all atoms of the ACN structure, from the MD simulations at 80 K (lower) and 140 K (upper).

might account for the additional feature in the optical spectra [Careri *et al.*, 1984], nor any unusual change of the C=O bond length with decreasing temperature [Wasserman *et al.*, 1985] was observed. The calculations have thus been unable to explain the anomalous Amide I peak at 1650 $cm^{-1}$ within the limitations of the present potential function, which does not include any explicit mode coupling term, and in the context of MD simulations utilizing periodic boundary conditions where, by construction, all excitations are periodic in space.

## 5.4. CONCLUSIONS.

The combined neutron/simulation approach provides a direct test of the accuracy of present simulation techniques in representing short-range femto- and picosend-timescale condensed phase dynamical effects. The CHARMM PEF has been extensively applied to the description of low frequency and anharmonic collective motions of proteins and model molecules [Karplus and Petsko, 1990]. Early work on the comparison of INS data with MD simulations using the CHARMM PEF have established a good agreement with experiment for low frequency features of the dynamics of proteins [Smith *et al.*, 1990a; Smith *et al.*, 1990b; Smith, 1991], and polymers [Dianoux, *et al.*, 1993; Dianoux *et al.*, 1994], as well as molecular crystals [Kneller, *et al.*, 1992]. These low frequency features reflect particularly the non-bonded interactions and soft intra-molecular degrees of freedom. Low frequency and relaxational dynamics are of particular relevance to the biological function of proteins [Karplus and Petsko, 1990; Frauenfelder *et al.*, 1991]. As noted above, however, coupling of high and low frequency intra-molecular motions may be an important mechanism leading to anharmonic behaviour, energy localization, and efficient energy transport. The work in this Chapter examined the

performance of CHARMM in reproducing high frequency features and anharmonicity in the dynamics of hydrogen bonded peptide groups, in the well characterized model system provided by crystalline ACN. The results of phonon calculations for the ACN crystal, performed with the CRYSTAL facility of the CHARMM program, were successfully used to calculate INS intensities in the three-phonon harmonic approximation, and demonstrated the utility of refining the parameters of the CHARMM PEF to produce a reasonable fit to experimental INS data over a wide frequency range, whilst modelling accurately the equilibrium geometry of the acetanilide crystal. Problems with the fit, and clues for further improvements, were revealed. Though the quality of the fit to the fundamental frequencies was not as good as the best attainable with molecular force field models for isolated molecules [Goodman *et al.*, 1991], the simultaneous calculation of INS intensities presents a more stringent test than calculation of frequencies alone. Similarly, though the fit to INS intensities was less good than the best attained with isolated molecular force fields [Fillaux *et al.*, 1993], it was achieved without the flexibility provided by explicit off-diagonal interaction terms in the dynamical matrix, with a similar ratio of refinable parameters to intra-molecular degrees of freedom, with no artificial dynamical separation of the degrees of freedom [Fillaux *et al.*, 1993], and whilst simultaneously modelling the equilibrium geometry of the crystal. Furthermore, one aim of the work was to use the data available from modern neutron scattering spectrometers to improve the parameters of the widely used CHARMM empirical PEF for a model of the peptide group, in the hope that these will be transferable to proteins. The accuracy of the fit to the INS data must be weighed against the utility of the resulting parametrization. Indeed the

refined PEF was used to study several features unattainable with molecular vibrational force fields for isolated molecules are evident. The external lattice mode region was calculated directly, allowing the calculation of phonon wings on high frequency features of the INS spectra. Crystal field effects were present in the calculated spectra, as evidenced by the fine splitting of fundamental bands. A value for the anisotropic atomic mean square displacements, Debye-Waller and temperature factors, including the contribution of lattice modes was calculated directly and compared with experiment. Most importantly, it was possible to apply the results of the parameter refinement to study anharmonic dynamics by MD simulations. MD results reproduced the qualitative temperature dependence of the NH out-of-plane bending mode of the peptide group, and the low frequency lattice modes of the crystal, as well as the methyl torsion in ACN. None of these effects can be studied directly using isolated molecule harmonic vibrational force fields. The final parameters of the refined model are not radically different from those in routine use with CHARMM currently, except in two important cases. These indicate how the CHARMM PEF might be improved in future, and illustrate the trade off between computational utility and accuracy of spectral simulation. The first case is the intra-molecular torsional term for the C-terminal methyl group. In agreement with several recent studies, the present calculations demonstrated a significantly enhanced barrier to methyl torsion when the peptide group is hydrogen bonded. The new parameters gave close agreement of calculated and experimental methyl torsional frequency and INS intensity. The calculated adiabatic barrier to methyl torsion in the crystal agreed exactly with the published value derived from quasi-elastic neutron scattering experiment [Barthes *et al.*, 1991]. This methyl torsion in

ACN is analogous to the Ramachandran Ψ torsion of the peptide backbone in proteins. Like other authors recently [Guo and Karplus, 1992; Baudry and Smith, 1994], it is possible to conclude that the Ψ torsional force constant should be increased on hydrogen bonding of peptide units in protein. However, it has been proposed that through-bond polarization produces this effect [Guo and Karplus, 1992]. If this is correct then the strength of the torsional force constant may depend on the instantaneous length of the neighbouring hydrogen bond, providing an important dynamical coupling mechanism for low frequency modes involving H-bond stretching and backbone torsion in proteins. This cannot be modelled by a static adjustment to the torsional force constant. For the acetanilide crystal, such an induced polarization effect, missing currently from the CHARMM PEF, might also provide a mechanism coupling amide I CO stretch with methyl torsion. Other investigators have included induced polarization effects on the peptide group in simplified MD studies of acetanilide, and observed localization of vibrational energy, and evolution of an anomalous amide I band with a temperature dependence close to that expected from soliton theory [Tenenbaum *et al.*, 1987]. The present model notably fails to explain this anomalous band, despite successfully reproducing other anharmonic features of the ACN crystal. In conclusion, it may be necessary to include induced polarization effects in models of high frequency dynamics of proteins, despite the computational cost, particularly when studying mode coupling and energy transport phenomena.

A second significant change to the CHARMM PEF was required to reproduce the splitting of phenyl ring torsional modes. It was necessary to introduce an *ad hoc* distinction between torsional force constants of phenyl CC bonds which, on grounds of local symmetry, might be

expected to be closely similar (though NOT identical). This unsatisfactory solution was intended to mimic the effect of harmonic terms coupling different internal coordinates, which appear as off-diagonal terms in the dynamical matrix of molecular vibrational force fields, but which cannot be explicitly included in CHARMM currently. Similarly, explicit interaction terms would allow improvement of the fit to frequencies for methyl deformation bands, and Amide II and III bands. The inclusion of induced polarization effects in CHARMM would provide a further implicit coupling of internal coordinates, without introducing explicit coupling terms. Explicit terms would be computationally expensive with an undesirable proliferation of refinable parameters in the model, from order N to order $N^2$, where N is the number of atoms.

The next Chapter descibes the collection of INS data for deuterated isotopomers of acetanilide and further refinements of the PEF.

Finally, to provide sufficiently long chains of primary ACN molecules to observe dynamic localization, whilst exploiting the computational advantage of periodic boundary conditions, it will also be necessary to perform simulations with larger primary box dimensions.

# CHAPTER VI - IMPROVED PARAMETERISATION TO FIT INS DATA FOR THREE ISOTOPOMERS OF ACETANILIDE.

## 6.1. INTRODUCTION.

As noted at the end of the last Chapter, I have collected INS data using the TFXA spectrometer for two further isotopomers of acetanilide, acetanilide-D5 (ACN-D5) and acetanilide-D8 (ACN-D8). This short Chapter will describe the INS experiments, and calculations performed for the isotopomers using the refined PEF of Chapter V. Though the fit to the new isotopic data using the parameterisation of Chapter V was reasonable, several significant problems were apparent. Further refinements of the CHARMM PEF were therefore made, on the basis of all the new data, using the PEF of Chapter V as a starting point. These further refinements, also described in the present Chapter, were undertaken to achieve a single final parameterisation which provided a reasonable fit of calculated spectra to experimental spectra for all three isotopomers at once. This represents a stringent test of the model. This Chapter should be read after Chapter V. I will try to avoid repetition of points which were already dealt with there. Thus the INS spectra were calculated in the harmonic approximation only, and the relevant theory has been discussed in Chapter V. There the dynamic structure factor was discussed in Section 5.2.1. The method of energy calculations and minimisations in the crystal were discussed in Section 5.2.3.1. The theory of harmonic lattice dynamics was discussed in Section 5.2.3.2, and the method of calculation of INS spectra from harmonic analyses was discussed in Section 5.2.4.

The only additional point of theory regards the method of treating the isotopic replacement. A single final refined parameter set was sought which can describe the dynamics of all three isotopomers, and the dynamical effect of the

isotopic substitution was represented simply through the difference in mass between hydrogen and deuterium. Thus the deuterium mass was used for the exchanged hydrogen atoms, instead of the hydrogen mass. Furthermore the crystal structure of ACN-D5 and ACN-D8 were assumed to be the same as that of ACN, for which crystal structures are published [Wasserman *et al.*, 1985; Brown and Corbridge, 1954]. These features of the model all rely on the validity of the Born-Oppenheimer approximation, as discussed for ACN-D9 in Section 5.2.3.2. [Merzbacher, 1970]. The use of this approximation is widely accepted in the analysis of spectroscopic data for isotopomers [Wilson *et al.*, 1980; Krimm and Bandekar, 1986].

Finally, lack of available computational time prevented the performance of MD simulations using the new parameterisation. The temperature dependence of the spectra under the new parameterisation has therefore not yet been explored. I hope such calculations will be performed in future by others in Dr. J. Smith's laboratory.

## 6.2. METHODS.

### 6.2.1. Neutron scattering experiments.

The two forms of deuterated acetanilide, ACN-D5 and ACN-D8, were purchased from CDN Isotopes, Vaudrieul, Quebec, Canada, as polycrystalline powders, better than 99.5% pure, and used without further purification. IR spectra were collected for the polycrystalline powder of ACN-D5 in potassium bromide discs on a Fourier Transform Infrared Nicolet 7000 Series Spectrometer in the Chemistry Department, Edinburgh University with the help of Dr. C. Pulham (Fig. 6.1). These spectra confirmed the crystalline form of the ACN-D5 sample, and were in agreement with those published for crystalline ACN-D5, including demonstration of the amide I anomaly [Careri *et*

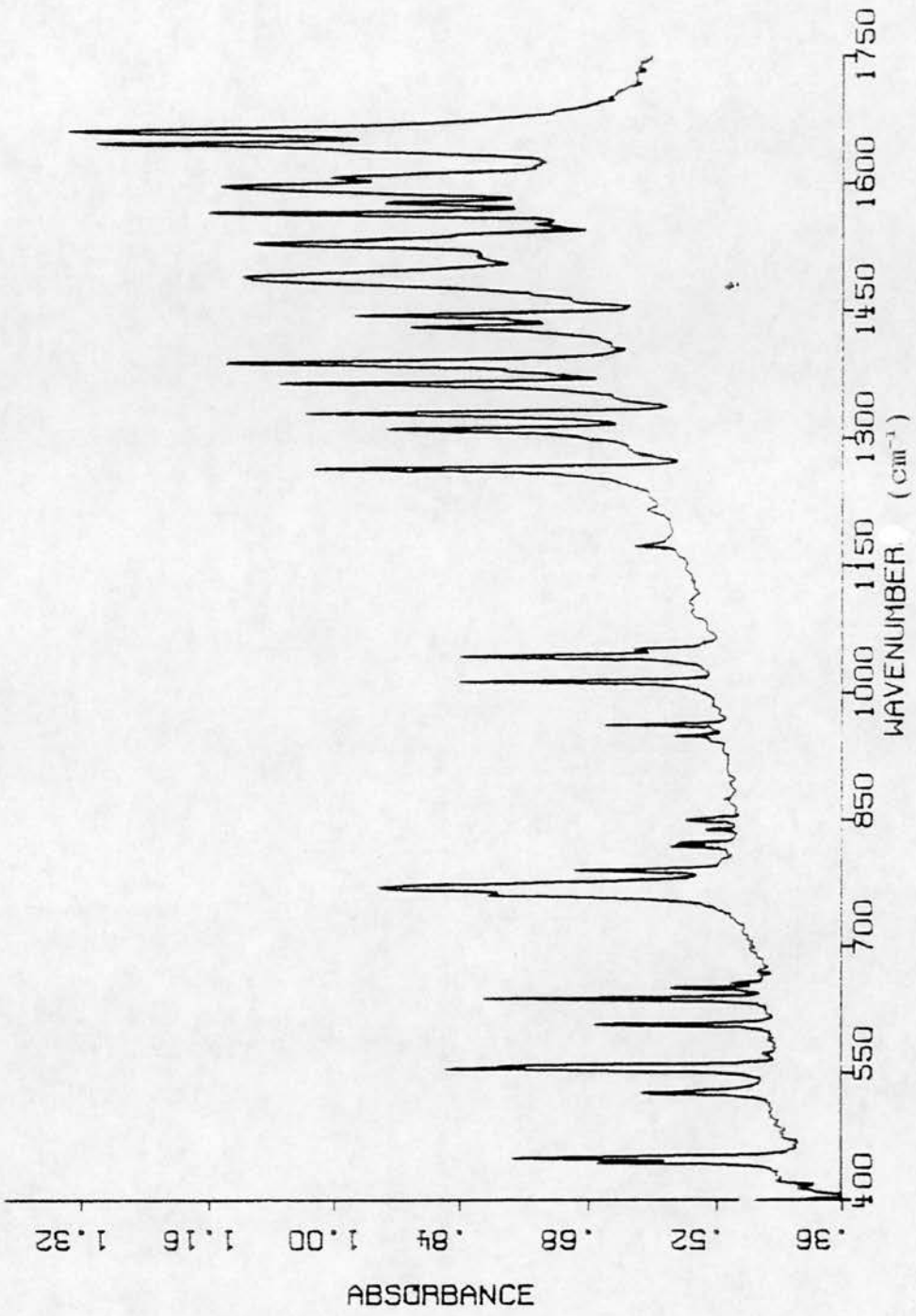


Figure 6.1. IR spectrum at 77 K for ACN-D5 in KBr discs, collected with the help of Dr. C. Pulham, using a Nicolet 7000 series Fourier transform infrared spectrometer, Chemistry Department Edinburgh. Energy resolution 4 $cm^{-1}$.

*al.*, 1984; Tariq *et al.*, 1984]. Dr. H.D. Middendorf collected the INS data for fully hydrogenous ACN, as noted in Chapter V, but he and I collected the data for the deuterated forms using the same experimental protocol. The samples were contained in aluminium cells. The depth of the sample along the axis of the incident neutron beam was 1 mm. A complete description of the experimental arrangement for TFXA has been given in Chapters III and V. The raw data from each detector were normalized to the incident neutron flux. In the backscattering geometry on TFXA, with the sample thickness used, multiple scattering, scattering from the sample can, and absorption are negligible and were neglected [Goyal *et al.*, 1986].

INS data was collected for ACN-D5 at 25 K (Fig. 6.2). For ACN-D8 the INS data were collected at 6 K (Fig. 6.3). The lower temperature for the ACN-D8 experiment was used because an appropriate cryostat had been mounted on the TFXA beamline for the experiment scheduled immediatly preceding ours. The lower temperature is expected to improve the validity of the harmonic approximation, though the general agreement achieved in Chapter V, in particular for the atomic mean square displacments (Table 5.4 and 5.5) suggests that the harmonic approximation is already good at 25 K. ACN, ACN-D5, and ACN-D8 spectra are compared in (Figs. 6.4 and 6.5).

### 6.2.2. Energy minimisations in the crystal.

The same protocol for energy calculations and energy minimisations as was described in Chapter V, Section 5.2.3.1, was applied again at each stage of the refinement to consistently obtain the minimised structure after each change to the parameterisation. The final parameterisation yielded a slightly different equilibrium crystal structure from that obtained in Chapter V. The differences are discussed below in the Section 6.3.3.

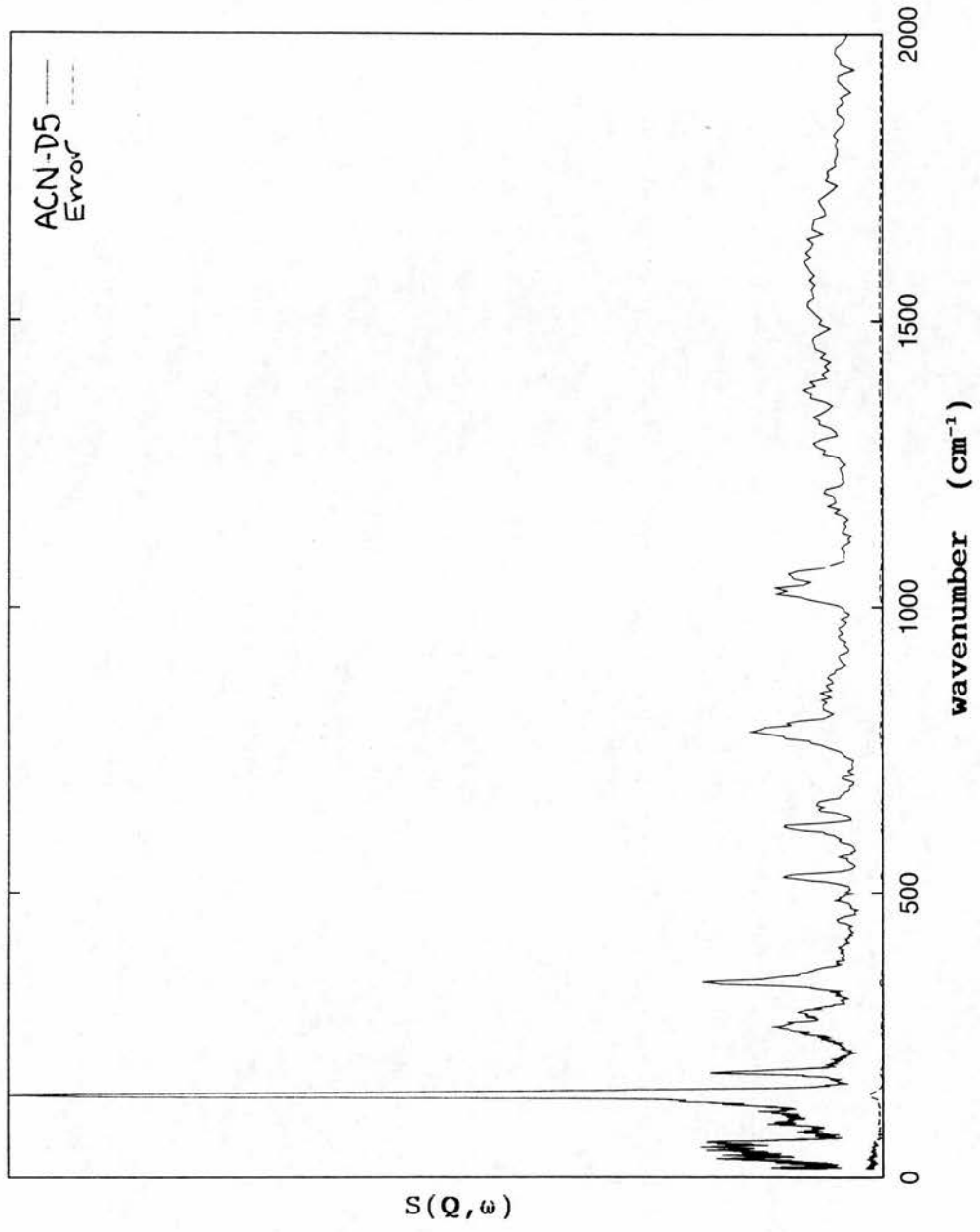


Figure 6.2. Experimental INS spectrum for ACN-D5 at 25 K, collected on the TFXA spectrometer, RAL. The statistical counting error, proportional to $(1/N)^{0.5}$ where N is the number of detected counts, is displayed on the figure.

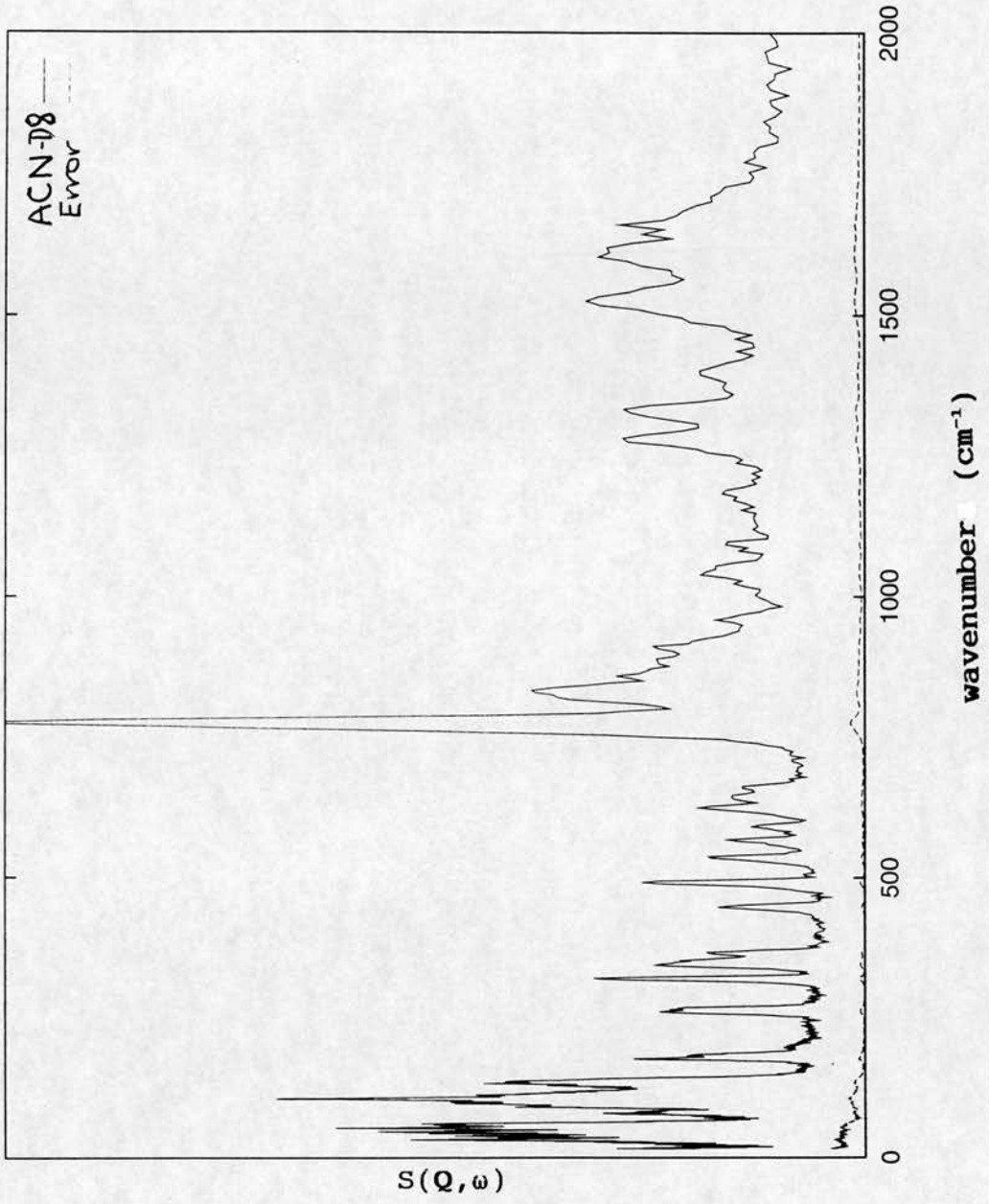


Figure 6.3. Experimental INS spectrum for ACN-D8 at 5 K, collected on the TFXA spectrometer, RAL. The statistical counting error, proportional to $(1/N)^{0.5}$ where N is the number of detected counts, is displayed on the figure.

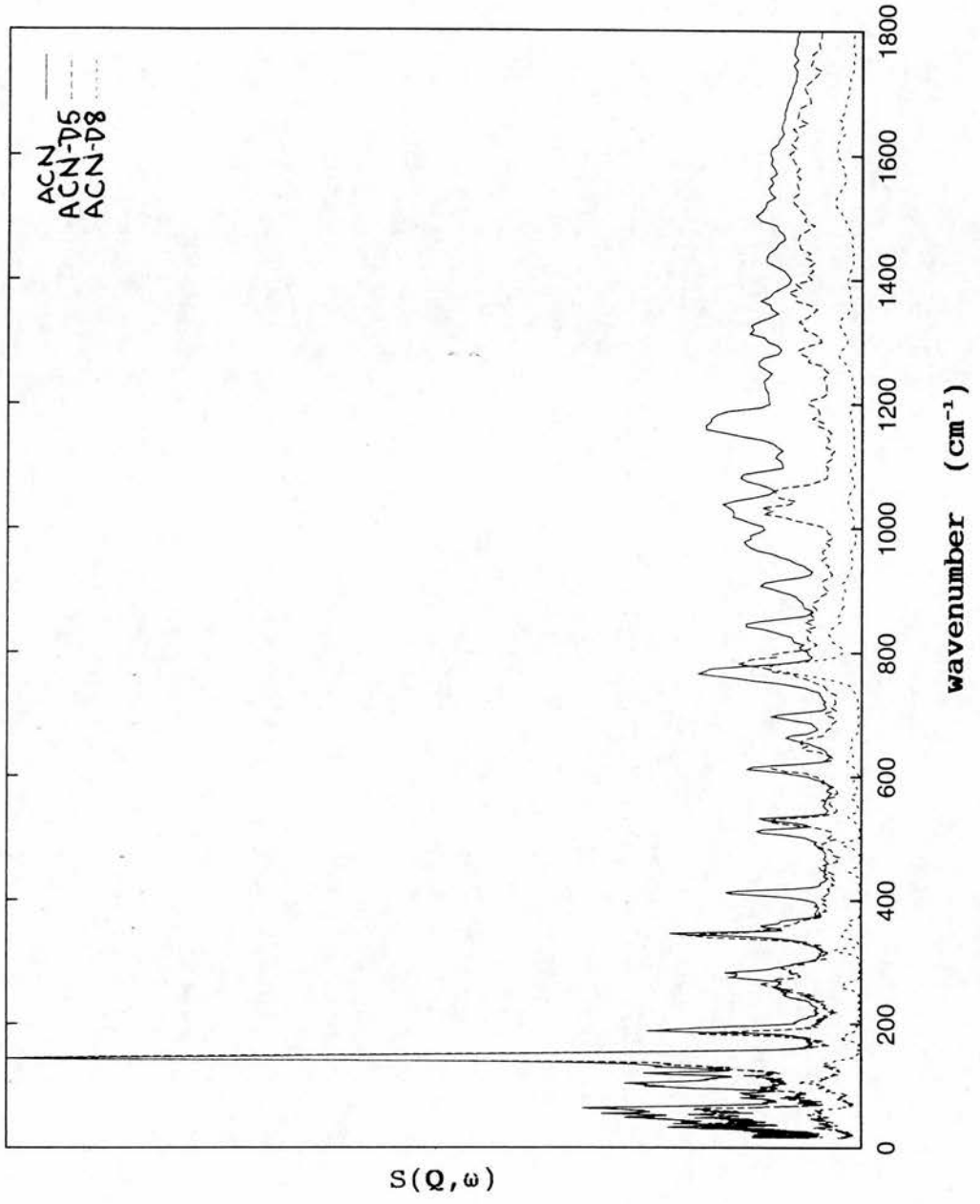


Figure 6.4. Experimental INS spectrum for ACN at 25 K, ACN-D5 at 25 K, ACN-D8 at 5 K, collected on the TFXA spectrometer, RAL.

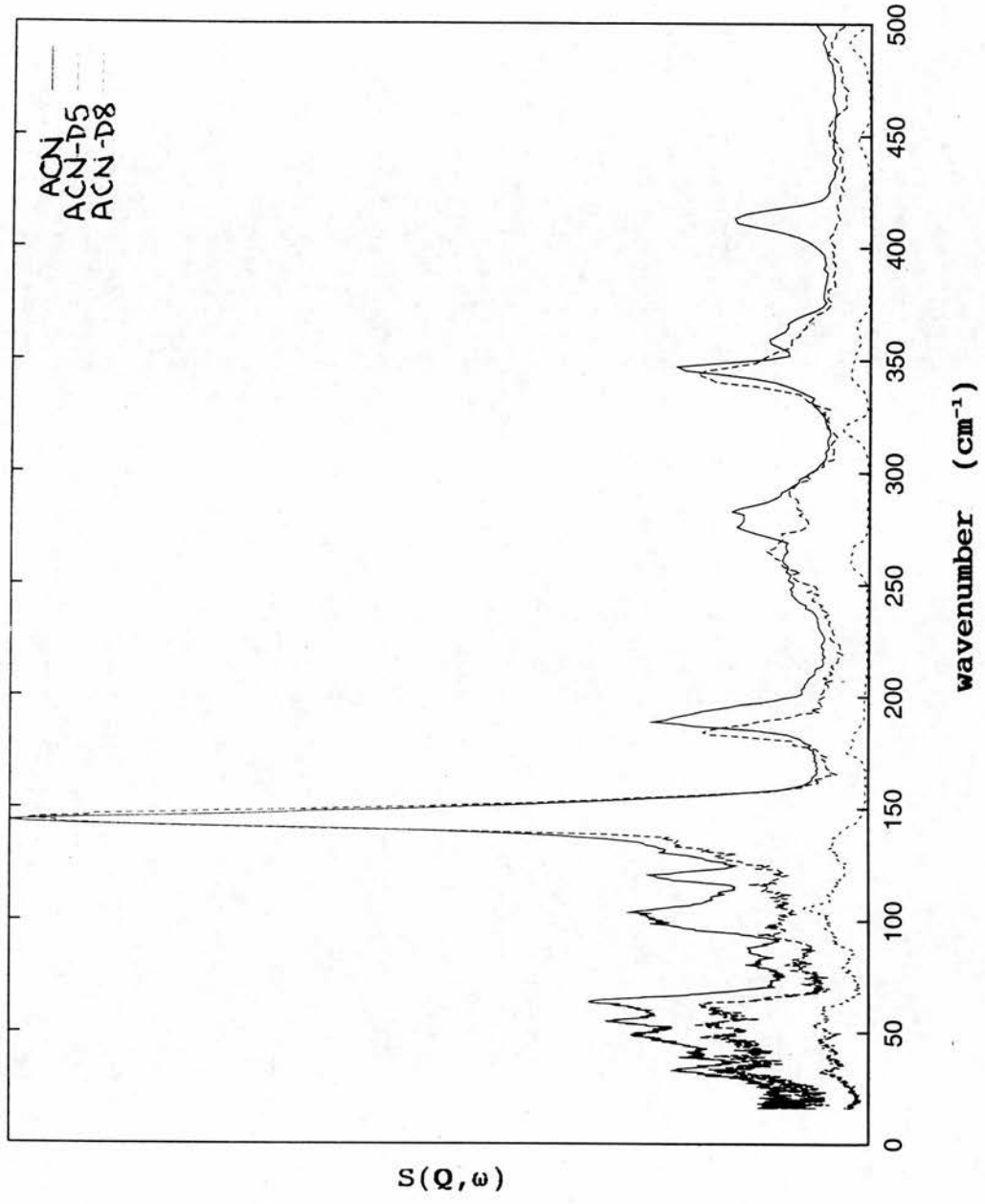


Figure 6.5. Comparison of experimental INS spectra for ACN at 25 K, ACN-D5 at 25 K and ACN-D8 at 5 K, collected on the TFXA spectrometer, RAL.

### 6.2.3. Harmonic analyses and calculation of INS intensities for ACN-D5 and ACN-D8.

As noted in Chapter V, for ACN 9 of 19 atoms are hydrogen and the total hydrogen incoherent scattering cross section is 89% of the total cross section. For ACN-D5, 4 of 19 atoms are hydrogen and the total hydrogen incoherent scattering cross section is 76% of the total cross section. To save computer time, phonon calculations were performed for ACN-D5 and ACN at a density of k-points in the Brillouin zone equivalent to a crystal of 64 unit cells, according to the methods described in Section 5.2.3.2. Incoherent INS intensities in the three phonon approximation were calculated from the harmonic analyses for ACN-D5 and ACN as described in Section 5.2.4. For ACN-D8 harmonic calculations were restricted to the Brillouin zone centre, $\mathbf{k} = 0$. INS spectra were calculated at 6 K in the one-phonon incoherent approximation from the resulting set of optical phonons, with the limited aim of identifying the main bands for amide hydrogen motion, in particular NH stretching and NH in-plane and out-of-plane bending. The anisotropic Debye-Waller factor for the amide hydrogen was derived from the calculation for the fully hydrogenous acetanilide. These approximations were made for the following reasons. The incoherent scattering cross section for the amide hydrogen is only 40% of the total scattering cross section of ACN-D8. Care is therefore needed in the interpretation of experimental results for ACN-D8 in terms of incoherent scattering. One cannot hope for a good fit to the experimental data in the lattice mode region, or for any spectral regions which are not dominated by amide hydrogen motion, without including the contribution of all atoms. This is prohibitively expensive of computer time. Multiphonon calculations, which require an estimate of the lattice mode region, are therefore not useful. The main amide bands show little dispersion.

Therefore calculations at the Brillouin zone centre should yield calculated frequencies and an estimate of relative intensities for these bands in approximate agreement with a more complete calculation throughout the Brillouin zone. The calculations of mean square displacements for ACN and ACN-D5 by the methods described above demonstrated that the anisotropic mean square displacements of the amide hydrogen were essentially independent of deuteration of other hydrogens of the structure, and were also essentially independent of temperature below 15 K, because the values were dominated by quantum ground state vibrations. Therefore, to save computer time, the anisotropic mean square displacments for the amide hydrogen derived from a more complete calculation throughout the Brillouin zone at 7 K for ACN, as described above, were used in the calculation of INS intensities for ACN-D8.

Calculations for ACN-D5 and ACN-D8 were first conducted using the refined parameter set of Chapter V, Table 5.1, with the equilibrium crystal structure of that Chapter, to test that parameterisation for the isotopomers. As discussed in the Section 6.3 below, a number of problems were apparent for that parameterisation. Therefore further manual refinements were made to improve these features of the parameterisation, using the parameters of Chapter V as a starting point. These refinements continued through repeated cycles of harmonic analyses, calculation of INS intensities for all three isotopomers as described above, comparison with experiment, and readjustment, until a new final refined parameter set was obtained which yielded more satisfactory agreement with experiment.

## 6.3. RESULTS.

### 6.3.1. Experimental and calculated INS spectra for ACN-D5 and ACN-D8 using the parameterisation of Chapter V.

The calculated spectra, without adjustments to the final refined parameter set of Chapter V (Table 5.1), are compared with the experimental spectrum in Fig. 6.6 and 6.7 for ACN-D5. The experimental ACN-D8 spectrum is compared with those for ACN-D5 and ACN in Fig. 6.4 and the calculated spectrum for ACN-D8 displayed in Fig. 6.8. At frequencies above 135 $cm^{-1}$ the overall agreement of the calculated ACN-D5 INS spectrum with the experimental spectrum was comparable to that for ACN. All the peaks calculated to involve only phenyl hydrogen motion produced zero intensity in agreement with experiment. Others which involved phenyl hydrogen motion along with amide or methyl hydrogen motion showed shifts and intensities in reasonable agreement with the experimental intensities. Thus agreement with the intensity of the NH out-of-plane bending bands between 750 and 800 $cm^{-1}$ was reasonable for ACN-D5, although one band lay too low at 735 $cm^{-1}$. For ACN-D8 the intensity between 750 and 800 $cm^{-1}$ was slightly underestimated, as a consequence of several bands not involving NH motion in this region (Table 6.9). These bands can be expected to produce a significant fraction of the experimental intensity for ACN-D8 by virtue of the proportionately larger contribution of incoherent scattering by heavy atoms (see Section 6.2.3 above). The intensity of phenyl ring CC torsions, which involve significant phenyl H atom motion, disappeared from both the experimental and the calculated ACN-D5 spectra, supporting the assignment to bands at 425, 505 and 685 $cm^{-1}$ for ACN, corresponding to experimental bands at 415, 515 and 690 $cm^{-1}$. Similarly the phenyl CCH in-plane and out-of-plane bending modes at 690, 840, 850, 910, 1160, 1180 and 1310 $cm^{-1}$ disappeared from the experimental and the

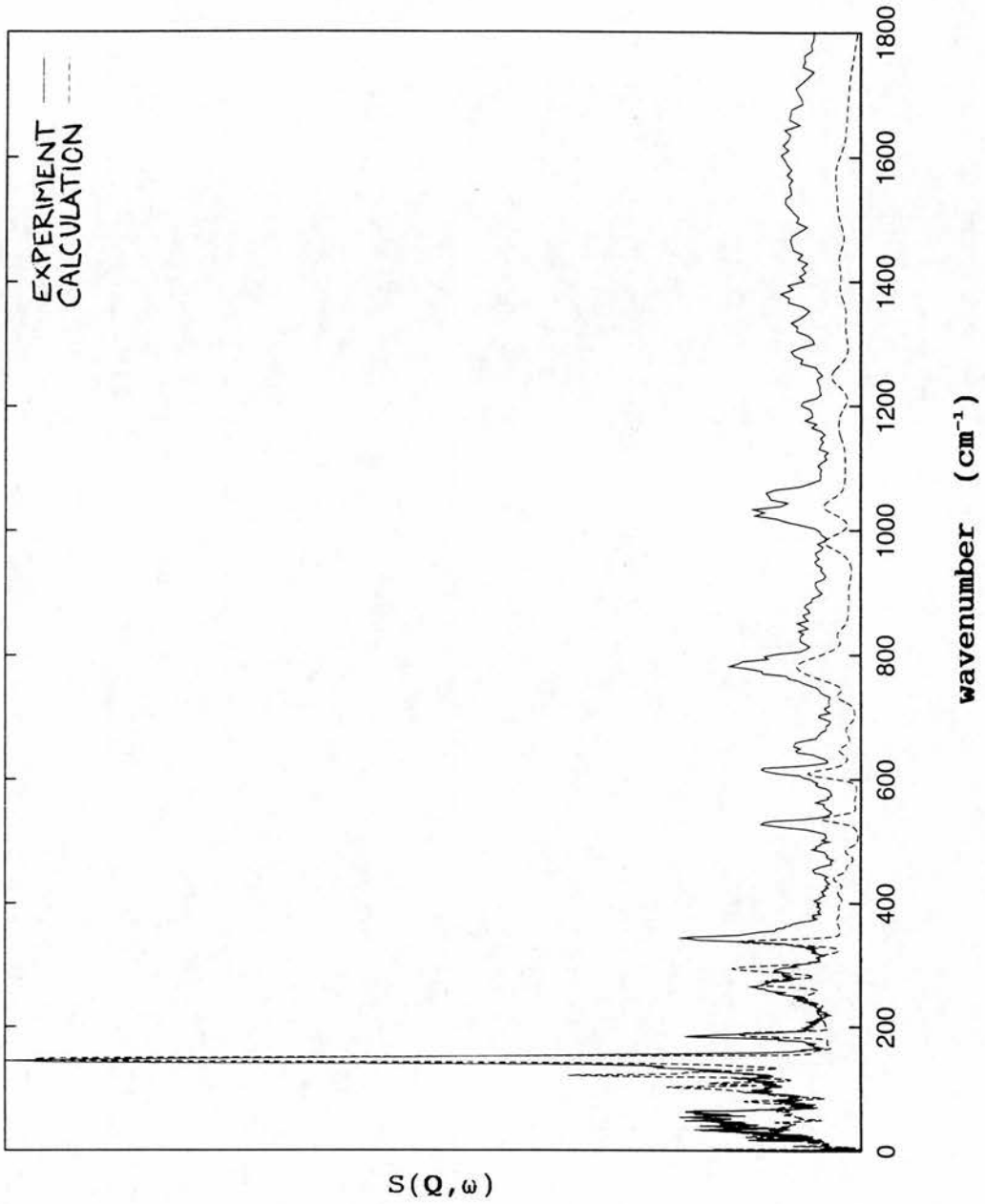


Figure 6.6. INS spectrum calculated using the parameters of Table 5.1, Chapter V, in the three phonon approximation compared with experimental INS spectrum for ACN-D5.

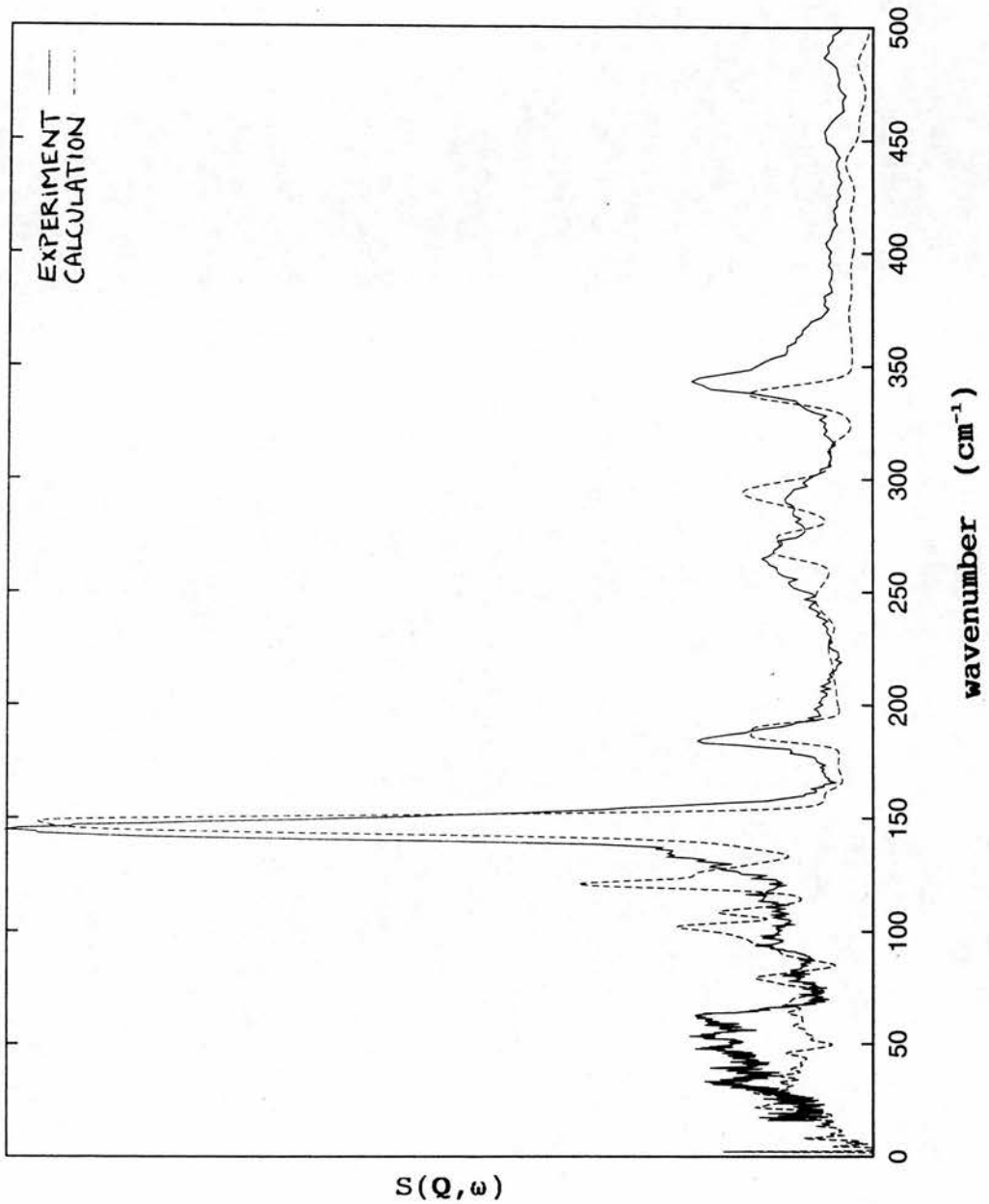


Figure 6.7. As for Fig. 6.6 on an expanded energy scale.

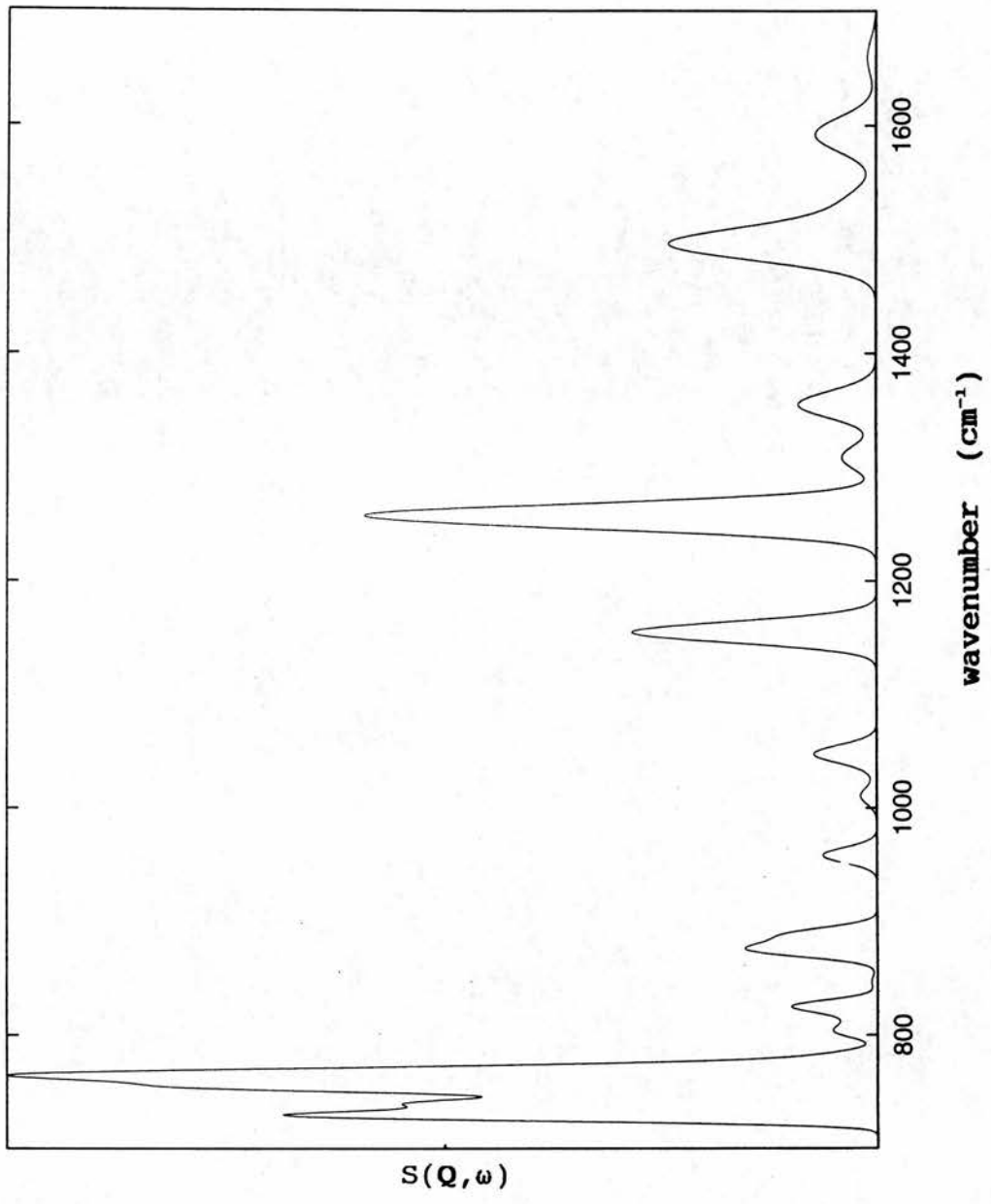


Figure 6.8. INS spectrum for ACN-D8 calculated using the parameters of Table 5.1, Chapter V, in the one-phonon approximation at the Brillouin zone centre.

calculated ACN-D5 spectra, supporting the Chapter V assignments for ACN (Table 5.2). However the ACN-D5 and ACN-D8 INS spectra are less complex than for ACN so that several significant problems with the parameterisation of Chapter V became apparent, which were obscured in the ACN INS spectra by the multiplicity of features. This was particularly true for the ACN-D8 spectrum. Taken together, the data for all three isotopomers suggested further refinements of the PEF were required. The problems with the parameterisation of Chapter V will be discussed next.

**6.3.1.1. The NH and $CNC_{ph}$ in-plane bending modes.**

A significant problem concerned the NH in-plane bending bands. The IR experiments for ACN-D5 revealed that the split peak at 1312-1330 $cm^{-1}$ in ACN becomes more clearly split in ACN-D5 to give components at 1330 and 1310 $cm^{-1}$ (Fig. 6.1 and 5.1). This suggested that at least one band near 1320 $cm^{-1}$ must involve phenyl degrees of freedom, so that it is shifted by the isotopic substitution in ACN-D5, whereas at least one other band must involve methyl or amide degrees of freedom so that its components at 1310 and 1330 $cm^{-1}$ are responsible for the features in the ACN-D5 IR spectra at these frequencies (Fig. 6.1). The IR and INS data for ACN-D5 also show the Amide III peak at 1270 $cm^{-1}$ (Fig. 6.1 and 6.2). In fact the experimental ACN-D8 INS spectrum also shows peaks of equal intensity at 1270 and 1310 $cm^{-1}$ (Fig. 6.3), which must therefore both represent modes involving NH motion, in agreement with the conclusions from the data for ACN-D5. Furthermore the ACN-D5 and ACN-D8 experimental INS spectrum have no strong intensity near 1210 $cm^{-1}$. On the other hand the calculations using the parameters of Chapter V, wrongly produced strong INS intensity at 1210 and 1245 $cm^{-1}$ for ACN-D5 and ACN-D8 (Figs. 6.6 and 6.8). This problem was obscured in the ACN calculation by the strong INS feature

at 1180 $cm^{-1}$ (Fig. 6.4). The calculated intensity of the peak at 1320 $cm^{-1}$ was markedly underestimated for ACN-D5 and ACN-D8 using the parameterisation of Chapter V (Figs. 6.3, 6.4, 6.6 - 6.8).

Together, therefore, the INS and IR spectra of ACN and ACN-D5, and the INS data for ACN-D8, suggested that the assignment in Chapter V of NH in-plane bending to a mode at 1210 $cm^{-1}$ was wrong, and that a reparameterisation was required which would yield a band involving amide hydrogen motion near 1320 $cm^{-1}$ for all three isotopomers. Under this assumption the IR peaks in ACN-D5 at 1310 and 1330 $cm^{-1}$ are two IR active components of this single band. A second band involving phenyl degrees of freedom should be present at 1320 $cm^{-1}$ in ACN, which is shifted downfield by deuteration in ACN-D5 and ACN-D8. The amide III band should appear near 1270 $cm^{-1}$ for all three isotopomers.

Further evidence of the need for reparameterisation of the NH in-plane bending modes came from the experimental INS data for ACN-D5 and ACN-D8 between 1500 and 1700 $cm^{-1}$ (Figs. 6.2, 6.3, 6.4, 6.6 and 6.8). This data clearly shows that the NH in-plane bending does not produce intensity at 1550 $cm^{-1}$ in ACN-D8, but instead contributes intensity to two peaks near 1500 and 1600 $cm^{-1}$. Deuteration of the other hydrogens, phenyl or methyl, is not expected to produce dramatic shifts in these features. It can therefore be assumed that NH in-plane motion should also contribute intensity at 1500 and 1600 $cm^{-1}$ in ACN-D5 and in ACN spectra. The calculations of INS intensity for all three isotopomers using the parameterisation of Chapter V correctly identified a contribution of NH in-plane motion to the bands at 1500 $cm^{-1}$ and 1600 $cm^{-1}$, with very little at 1550 $cm^{-1}$, but failed to assign a large enough contribution to the peak at 1600 $cm^{-1}$ (Table 5.2).

The problem with the the $CNC_{ph}$ in-plane bending band at 316 $cm^{-1}$ in the calculated ACN spectra, which was discussed

in Chapter V, Section 5.3.3.1 (Fig. 5.5), was also apparent in the calculated ACN-D5 spectra using the parameterisation of Chapter V (Fig. 6.6). As for ACN, the ACN-D5 experimental INS data had less intensity at the position of the exact overtone frequency for the methyl torsional peak than expected from the calculations, confirming the anharmonic nature of this mode as discussed in Section 5.3.3.2. As expected the methyl torsional intensity was abolished in ACN-D8 INS spectra by deuteration of the methyl hydrogens, confirming the assignment of the band (Fig. 6.4).

**6.3.1.2. Methyl rocking and deformation bands.**

The ACN-D5 data demonstrate that the calculated frequency of the methyl rocking mode at 980 $cm^{-1}$ was too low and should appear nearer 1010 $cm^{-1}$. In fact a similar shift in the calculated ACN spectrum would improve the agreement with the triplet peak in the experimental spectrum of ACN also - the calculated intensity in Chapter V was overestimated at 980 $cm^{-1}$ and underestimated at 1010 $cm^{-1}$ (Fig. 5.4). Similarly the methyl deformation bands calculated near 1430 $cm^{-1}$ should lie slightly higher near 1450 $cm^{-1}$, though the calculated intensities were in good agreement with experiment (Fig. 6.6). On the other hand the methyl deformation band observed near 1370 $cm^{-1}$ in the experimental INS spectra and in the IR spectra for both ACN and ACN-D5, lay too high at 1385 $cm^{-1}$ in the calculated spectra (Figs. 5.1, 5.4, 6.1 + 6.6). As expected the methyl rocking and deformation peaks were abolished in ACN-D8 INS spectra by deuteration of the methyl hydrogens, confirming the assignment of the bands (Figs. 6.2 - 6.4).

**6.3.1.3. 100 to 140 $cm^{-1}$ region for ACN-D5.**

The gross overestimate of the scattered intensity in the region between 100 and 140 $cm^{-1}$ in the ACN-D5 spectrum was

the most significant problem with the parameterisation of Chapter V (Fig. 6.6). As noted in Chapter V, early attempts to model the spectrum of ACN demonstrated problems with splitting of the methyl torsional peak, and the coupling of methyl torsion to lattice modes, so that components of methyl torsion contributed to intensity between 100 and 130 $cm^{-1}$. The final refined parameterisation of Chapter V included adjustments to the van der Waals parameters and the methyl torsional potential which improved this situation considerably, though as noted in Section 5.3.3.1, an overestimate of the peak at 130 $cm^{-1}$ persisted even for ACN (Fig. 5.5). The calculation for ACN-D5 using the parameterisation of Chapter V confirmed that considerable coupling of methyl torsion to modes between 100 and 130 $cm^{-1}$ persisted, but also that the phenyl out-of-plane motion in this region coupled extensively with CN torsion, so that significant methyl motion occurred in these mode also. Together these effects were responsible for the overestimate of calculated intensity between 100 and 130 $cm^{-1}$ in ACN-D5 spectrum (Fig. 6.7).

**6.3.1.4. Lattice mode region below 100 $cm^{-1}$.**

At low frequency in the lattice mode region the experimental ACN-D5 INS intensity was markedly underestimated by the calculations, to a greater extent even than the underestimate in the ACN calculations discussed in Chapter V, Section 5.3.3.1. For lattice modes little effect of deuteration on the dynamics can be expected, because lattice modes represent rigid body motions of the whole acetanilide molecule [Chapter V, Table 5.2], and are therefore relatively insensitive to the minor mass change produced by deuteration of the phenyl group hydrogens. For these reasons the calculated and experimental INS intensity for the lattice mode region

was of a similar form for ACN and for ACN-D5, but scaled down for ACN-D5 by the reduction in scattering cross section produced by deuteration. For the calculations the scale factor was 4/9, reflecting the deuteration of five of 9 hydrogens in ACN-D5. The experimental intensity for ACN-D5 is reduced by a factor of only 5/9. This difference is due to the contribution of heavy atom and deuterium incoherent scattering to the experimental intensity at low frequency in ACN-D5 (Fig. 6.7). The contribution of heavy atoms and deuterium is particularly apparent at low frequencies in ACN-D5 for the following reasons. As noted above, the incoherent scattering from hydrogen is only 76% of the total scattering for ACN-D5, whereas it is 89% for ACN. For localised group vibrations at higher frequencies the weighting of the scattered intensity by the amplitude of motion makes the contribution from light hydrogens more dominant. At low frequency in the lattice mode region however, the modes involve essentially rigid body motion of whole acetanilide molecules, and so a more significant contribution from heavy atoms can be expected. However the fact that there was a global underestimate of the lattice mode region for both ACN and ACN-D5 calculations cannot be explained by this effect. This suggested therefore that an error in the parameterisation of Chapter V was partly responsible for the problem.

In summary, four important targets for improving the parameterisation of Chapter V were identified by consideration of all the isotopomer data:

**(i)** the NH in-plane bending bands between 1270 and 1600 $cm^{-1}$ and $CNC_{ph}$ in-plane bending band at 316 $cm^{-1}$.

**(ii)** the methyl rocking and deformation bands.

**(iii)** the intensity between 100 and 140 $cm^{-1}$ in ACN-D5.

**(iv)** the intensity of the lattice mode region in ACN and ACN-D5. Efforts to improve these features will now be discussed in turn.

Table 6.1. Further refinments to the parameters of Chapter V, Table 5.1, based on the INS data for all three isotopomers of acetanilide. Units are $k_b$ kcal/mol/Å$^2$, $b_o$ Å, k kcal/mol/radian$^2$, $Y_o$ degrees, $k_u$ kcal/mol/Å$^2$, $u_o$ Å, k kcal/mol, $\delta$ degrees, $k_\omega$ kcal/mol/radian$^2$, $\omega_o$ degrees, $\epsilon$ kcal/mol, $r_{min}/2$ Å, $\epsilon_{1:4}$ kcal/mol, $r_{min}/2$ Å. The atomic partial charges, in units of the electron charge, for the phenyl group atoms, labelled relative to the carbon * at the N-substitution site are: a - carbons: * 0.0788, *ortho* -0.16845, *meta* -0.10275, *para* -0.1562. a - hydrogens: *ortho* 0.15075, *meta* 0.1339, *para* 0.1341.

| BONDS | $k_b$ | $b_0$ | | |
|---|---|---|---|---|
| $C_{ph}C_{ph}(ortho)$ | 372.0 | 1.375 | | |
| $C_{ph}C_{ph}(para)$ | 380.0 | 1.375 | | |
| $C_{ph}C_{ph}(meta)$ | 372.0 | 1.375 | | |
| $C_{me}C$ | 235.0 | 1.505 | | |
| $C_{me}H$ | 322.0 | 1.085 | | |
| $C_{ph}H$ | 344.0 | 1.080 | | |
| $CN$ | 310.0 | 1.360 | | |
| $C_{ph}N$ | 330.0 | 1.445 | | |
| $NH$ | 417.0 | 0.997 | | |
| $CO$ | 620.0 | 1.237 | | |
| ANGLES | $k_\vartheta$ | $\theta_0$ | $k_u$ | $u_0$ |
| $C_{ph}C_{ph}C_{ph}$ | 35.0 | 120.0 | 35.0 | 2.4162 |
| $C_{ph}NC$ | 55.0 | 120.0 | 55.0 | 2.425 |
| $HNC$ | 32.0 | 123.0 | 10.0 | 2.02 |
| $HNC_{ph}$ | 32.0 | 117.0 | 24.0 | 2.15 |
| $HC_{me}C$ | 30.0 | 109.5 | 30.0 | 2.163 |
| $HC_{me}H$ | 34.5 | 108.4 | 5.5 | 1.802 |
| $HC_{ph}C_{ph}(ortho)$ | 25.5 | 120.0 | 22.0 | 2.1525 |
| $HC_{ph}C_{ph}(meta)$ | 25.5 | 120.0 | 25.0 | 2.1525 |
| $HC_{ph}C_{ph}(para)$ | 25.5 | 120.0 | 22.0 | 2.1525 |
| $NC_{ph}C_{ph}$ | 52.0 | 120.0 | 10.0 | 2.5 |
| $NCC_{me}$ | 70.0 | 116.5 | | |
| $OCC_{me}$ | 70.0 | 123.0 | | |
| $OCN$ | 70.0 | 121.5 | | |

Table 6.1 (continued)

| DIHEDRALS | $k_\phi$ | $n$ | $\delta$ | | |
|---|---|---|---|---|---|
| $C_{ph}C_{ph}C_{ph}C_{ph}(ortho/para)$ | 4.10 | 2 | 180.0 | | |
| $C_{ph}C_{ph}C_{ph}C_{ph}(meta)$ | 2.45 | 2 | 180.0 | | |
| $C_{me}CNH, C_{me}CNC_{ph}$ | 2.40 | 2 | 180.0 | | |
| $OCNH, OCNC_{ph}$ | 2.40 | 2 | 180.0 | | |
| $HNC_{ph}C_{ph}$, $CNC_{ph}C_{ph}$ | 0.6 | 2 | 180.0 | | |
| $HC_{ph}C_{ph}C_{ph}$ | 3.95 | 2 | 180.0 | | |
| $HC_{ph}C_{ph}H$ | 2.35 | 2 | 180.0 | | |
| $NC_{ph}C_{ph}C_{ph}$ | 3.00 | 2 | 180.0 | | |
| $NC_{ph}C_{ph}H$ | 2.35 | 2 | 180.0 | | |
| $NCC_{me}H$ | 0.1 | 3 | 0.0 | | |
| $OCC_{me}H$ | 0.1 | 3 | 0.0 | | |
| IMPROPER | $k_\omega$ | $\omega_0$ | | | |
| $CC_{me}NO$ | 85.0 | 0.0 | | | |
| VAN DER WAALS AND PARTIAL CHARGES | $\epsilon$ | $r_{min}/2$ | $\epsilon_{1:4}$ | $r_{min\ 1:4}/2$ | partial charge |
| $C$ | -0.110 | 2.0000 | | | 0.50 |
| $C_{ph}$ | -0.070 | 1.9924 | | | [a] |
| $C_{me}$ | -0.080 | 2.0600 | -0.01 | 1.9000 | -0.247 |
| $H$ | -0.046 | 0.2245 | | | 0.28 |
| $H_{me}$ | -0.022 | 1.1800 | | | 0.1078 |
| $H_{ph}$ | -0.030 | 1.3582 | -0.030 | 1.3582 | [b] |
| $N$ | -0.200 | 1.8500 | -0.200 | 1.5500 | -0.49 |
| $O$ | -0.120 | 1.7000 | -0.120 | 1.4000 | -0.45 |

Table 6.2. The assignment of the crystal phonon bands for ACN above 160 $cm^{-1}$ in terms of intra-molecular modes of the isolated molecule. Intra-molecular modes, in turn, assigned in terms of the potential energy distribution amongst internal coordinates used in construction of CHARMM potential energy function for the ACN molecule. Each phonon band carries eight modes, one each of the eight symmetry classes. Calculations use the parameters of Table 6.1.

| I | II | III |
|---|---|---|
| *[a] | 48[—] | $\tau(phenyl)(82)$ |
| *[a] | 83[—] | $\tau(CN)(67)\ \gamma(phenyl)(21)$ |
| *[a] | 127[—] | $\tau(methyl)(97)$ |
| 190-208 | 166[0.96] | $\gamma(phenyl)(42)\ \tau(CN)(20)\ \tau(phenyl)(8)$ |
| 270-282 | 270[0.98] | $\gamma(phenyl)(36)\ \tau(CN)(20)\ \tau(C_{ph}C_{ph})(12)$ |
| 341-345 | 334[0.98] | $\delta(CC_{me})(36)\ s(NC_{ph})(12)\ s(CN)(11)$ |
| 353-363 | 350[0.97] | $\delta(NC_{ph}C_{ph})(39)\ \delta(CC_{me})(18)\ \delta(CO)(15)$ |
| 419-428 | 412[0.99] | $\tau(C_{ph}C_{ph})(55)\ \gamma(C_{ph}H)(35)$ |
| 495-504 | 487[0.99] | $\tau(C_{ph}C_{ph})(53)\ \gamma(C_{ph}H)(30)$ |
| 532-538 | 526[0.99] | $\delta(CO)(53)\ s(CC_{me})(11)\ s(NC_{ph})(5)\ \delta(CC_{me})(8)$ |
| 601-613 | 571[0.86] | $\gamma(CO)(72)\ \gamma(NH)(23)$ |
| 659-661 | 647[0.91] | $\tau(C_{ph}C_{ph})(33)\ \gamma(NH)(12)\ \delta(C_{ph}C_{ph}C_{ph})(7)$ $s(CC_{me})(6)\ \delta(CO)(5)$ |
| [b] | 664 | $\gamma(NH)(56)\ \gamma(CO)(21)$ |
| 677-681 | 674[0.96] | $\tau(C_{ph}C_{ph})(53)\ \gamma(C_{ph}H)(25)$ |
| 689-692 | 686[0.97] | $\delta(C_{ph}C_{ph}C_{ph})(22)\ \gamma(C_{ph}H)(21)\ \tau(C_{ph}C_{ph})(21)\ s(CC_{me})(9)$ |
| 738-749 | 738[0.65][b] | $\gamma(C_{ph}H)(78)$ |
| 764-788 | 738[0.54][b] | $\gamma(C_{ph}H)(78)$ |
| 802-813 | 803[0.90] | $s(CN)(18)\ \delta(CNC_{ph})(14)\ s(CO)(13)\ \delta(C_{ph}C_{ph}C_{ph})(8)\ s(C_{ph}C_{ph})(7)$ $\delta(NCC_{me})(5)$ |
| 826-833 | 819[0.93] | $\delta(C_{ph}C_{ph}C_{ph})(23)\ s(CN)(19)\ s(CC_{me})(15)$ $s(CO)(10)\ s(C_{ph}C_{ph})(10)\ s(NC_{ph})(8)$ |
| 844-853 | 833[0.98] | $\gamma(C_{ph}H)(99)$ |
| 915-923 | 909[0.99] | $\gamma(C_{ph}H)(99)$ |
| 957-959 | 954[0.99] | $s(C_{ph}C_{ph})(38)\ \delta(C_{ph}C_{ph}C_{ph})(28)\ \delta(C_{ph}C_{ph}H)(10)$ |
| 979-981 | 978[0.75] | $methyl\ rock(44)\ \gamma(C_{ph}H)(39)$ |
| 986-989 | 975[0.55] | $\gamma(C_{ph}H)(94)$ |
| 1006-1009 | 991[0.91] | $\gamma(C_{ph}H)(99)$ |
| 1034-1036 | 1024[0.71] | $methyl\ rock(76)\ \gamma(CO)(15)$ |

Table 6.2 (continued)
Column I: frequency range (wavenumbers) of **k** = 0 phonon bands with frequency > 160 $cm^{-1}$ ( Note a - for lower frequency bands see Table 6.9). Column II: frequency of corresponding isolated molecular mode (defined as mode with closest eigenvector **e** - numbers in square brackets give the dot product $\mathbf{e}_{isolated} \cdot \mathbf{e}_{crystal}$). Note b - the bands at 752-765 $cm^{-1}$, 762-774, 775-788 $cm^{-1}$ in the crystal were mixed extensively with γNH - the dot products with the isolated molecular γNH mode at 634 $cm^{-1}$ were [0.45], [0.37], [0.3] respectively. Column III: assignments for isolated molecule modes (numbers in round brackets give percentage contribution to the potential energy of the mode, terms contributing > 5% are listed). s = bond stretch, δ = in-plane bend, γ = out-of-plane bend, τ = torsion.

| I*(cont.)* | II*(cont.)* | III*(cont.)* |
|---|---|---|
| 1036-1040 | 1027[0.71] | $s(C_{ph}C_{ph})(73)$ $\delta(C_{ph}C_{ph}H)(19)$ |
| 1061-1065 | 1057[1.00] | $s(C_{ph}C_{ph})(50)$ $\delta(C_{ph}C_{ph}H)(41)$ |
| 1163-1166 | 1157[0.95] | $\delta(C_{ph}C_{ph}H)(77)$ $s(C_{ph}C_{ph})(21)$ |
| 1175-1176 | 1168[0.95] | $\delta(C_{ph}C_{ph}H)(85)$ $s(C_{ph}C_{ph})(14)$ $\delta(NH)(9)$ |
| 1267-1272 | 1260[0.95] | $\delta(C_{ph}C_{ph}H)(35)$ $\delta(NH)(18)$ $s(C_{ph}C_{ph})(17)$ $s(C_{ph}N)(21)$ |
| 1288-1294 | 1281[0.95] | $s(CC_{me})(23)$ $\delta(CO)(16)$ $\delta(NH)(13)$ $s(CN)(14)$ $\delta(C_{ph}C_{ph}H)(9)$ $s(NC_{ph})(8)$ |
| 1335-1336 | 1324[0.99] | $\delta(C_{ph}C_{ph}H)(82)$ |
| 1377-1381 | 1372[0.99] | $methyl\ deformation(90)$ |
| 1413-1414 | 1410[0.99] | $\delta(C_{ph}C_{ph}H)(46)$ $s(C_{ph}C_{ph})(35)$ |
| 1433-1434 | 1430[0.91] | $methyl\ deformation(98)$ |
| 1437 | 1438[0.91] | $methyl\ deformation(95)$ |
| 1465-1468 | 1459[0.99] | $\delta(C_{ph}C_{ph}H)(43)$ $s(C_{ph}C_{ph})(39)$ $\delta(NH)(8)$ |
| 1517-1528 | 1506[0.97] | $s(C_{ph}C_{ph})(35)$ $\delta(NH)(26)$ $s(CN)(13)$ $s(NC_{ph})(5)$ $\delta(C_{ph}C_{ph}H)(10)$ |
| 1552 | 1552[0.99] | $s(C_{ph}C_{ph})(84)$ $\delta(C_{ph}C_{ph}H)(14)$ |
| 1582-1584 | 1571[0.93] | $s(C_{ph}C_{ph})(68)$ $\delta(NH)(16)$ |
| 1606-1619 | 1599[0.94] | $s(C_{ph}C_{ph})(64)$ $\delta(C_{ph}C_{ph}H)(14)$ $\delta(NH)(9)$ |
| 1667-1673 | 1665[0.99] | $s(CO)(70)$ $s(CC_{me})(5)$ $s(CN)(6)$ $\delta(CC_{me})(8)$ |
| 2917 | 2915[1.00] | $s(C_{me}H)(99)$ |
| 2973 | 2971[1.00] | $s(C_{me}H)(99)$ |
| 2976 | 2974[1.00] | $s(C_{me}H)(99)$ |
| 3074-3075 | 3070[1.00] | $s(C_{ph}H)(99)$ |
| 3076-3079 | 3070[1.00] | $s(C_{ph}H)(99)$ |
| 3066-3068 | 3073[1.00] | $s(C_{ph}H)(99)$ |
| 3087 | 3084[1.00] | $s(C_{ph}H)(99)$ |
| 3089-3090 | 3088[1.00] | $s(C_{ph}H)(99)$ |
| 3288-3294 | 3304[1.00] | $s(NH)(100)$ |

### 6.3.2. Adjustments to the parameters of Chapter V.

In this section the adjustments leading to the final refined parameter set used in this Chapter are briefly described. These illustrate the time consuming empirical nature of the method. The final parameter set resulting from the adjustments is displayed in Table 6.1. For comparison with the assignments of Chapter V, calculated frequencies and assignments at $\mathbf{k} = 0$ are listed in Tables 6.2 and 6.3 for ACN. Calculated isotropic and anisotropic mean square displacements are compared with experiment in Tables 6.4 and 6.5. Calculated frequencies and assignments at $\mathbf{k} = 0$ are listed in Tables 6.6 and 6.7 for ACN-D5, and in Tables 6.8 and 6.9 for ACN-D8. In Tables 6.2, 6.6, and 6.8 the crystal modes $< 210$ $cm^{-1}$ are listed together with details of the crystal field splitting effects which were very marked for the low lying intra-molecular degrees of freedom. For those modes most accurately described by rigid-body motions of the molecules in the crystal lattice, the librational or translational character of the modes is specified. The symmetry character of the lowest lying bands is also presented in Tables 6.2, 6.6, and 6.8. Above 200 $cm^{-1}$ there was relatively little splitting of the eight components of each band, and so for clarity only the frequency range of the bands are listed in Tables 6.3, 6.7, and 6.9. For each crystal band, the equivalent mode in the isolated molecule was defined as that mode for which the average value of the dot product, formed with the eigenvectors of the modes in the crystal band, was largest. The frequency shift for each mode on passing from the isolated molecule to the crystal gives a measure of the influence of the crystal field. The value of the dot product, as defined above, gives a measure of the change in the form of each molecular mode on passing to the crystal, and is also displayed in Tables 6.3, 6.7, and 6.9. The INS spectra, calculated using the parameters of

Table 6.3. Assignment of ACN crystal phonon modes below 210 $cm^{-1}$ in terms of rigid body motions or intra-molecular modes of the isolated molecule. Intramolecular modes, in turn, assigned in Table 6.2. Calculations use the parameters of Table 6.1. Column **I**: frequency ($cm^{-1}$) of $\mathbf{k} = 0$ crystal modes < 210 $cm^{-1}$. Column **II**: assignment to rigid molecular librational or translational motion, or nearest intramolecular mode (defined as mode with closest eigenvector **e** - numbers in square brackets give the dot product $\mathbf{e}_{isolated} \cdot \mathbf{e}_{crystal}$). Column **III**: symmetry character of crystal mode.

| I | II | III | I*(cont.)* | II*(cont.)* | III*(cont.)* |
|---|---|---|---|---|---|
| 23 | translational | B1g | 109 | librational | B3g |
| 24 | translational | Au | 109 | librational | Au |
| 25 | translational | B3u | 111 | $\tau(phenyl)$[0.75] | B2u |
| 28 | librational | Ag | 112 | librational | B2g |
| 37 | librational | Ag | 113 | $\gamma(phenyl)$[0.60] | B3u |
| 37 | librational | B3g | 114 | $\tau(phenyl)$[0.71] | Ag |
| 39 | librational | B2g | 116 | $\tau(phenyl)$[0.52] | B1g |
| 40 | librational | B2u | 117 | $\gamma(phenyl)$[0.64] | B2u |
| 41 | translational | B1u | 120 | $\tau(phenyl)$[0.59] | B3g |
| 47 | translational | B3g | 121 | $\gamma(phenyl)$[0.84] | B1u |
| 47 | translational | Au | 125 | $\gamma(phenyl)$[0.94] | Au |
| 48 | translational | B2g | 126 | librational | B1u |
| 51 | librational | B1u | 130 | $\gamma(phenyl)$[0.77] | B1g |
| 54 | translational | B2u | 131 | $\gamma(phenyl)$[0.75] | Ag |
| 54 | translational | B2g | 131 | translational | B3g |
| 56 | translational | Ag | 133 | translational | B3u |
| 57 | librational | B3u | 136 | translational | B1u |
| 59 | librational | B1g | 137 | librational | B1g |
| 62 | librational | Au | 142 | $\gamma(phenyl)$[0.72] | B3u |
| 67 | librational | Ag | 142 | $\gamma(phenyl)$[0.55] | B2u |
| 70 | librational | B2u | 146 | $\tau(methyl)$[0.95] | Au |
| 75 | $\tau(phenyl)$[0.71] | B3u | 147 | $\tau(methyl)$[0.86] | B2u |
| 75 | translational | Au | 148 | $\gamma(phenyl)$[0.64] | B2g |
| 75 | librational | B2g | 149 | $\tau(methyl)$[0.87] | B1u |
| 76 | translational | B3g | 149 | $\tau(methyl)$[0.76] | B3g |
| 77 | librational | B1u | 150 | $\tau(methyl)$[0.88] | B3u |
| 79 | translational | B1g | 151 | $\tau(methyl)$[0.89] | B2g |
| 86 | librational | B1g | 152 | $\tau(methyl)$[0.92] | Ag |
| 89 | translational | Ag | 153 | $\tau(methyl)$[0.49] | B3g |
| 89 | $\tau(phenyl)$[0.79] | B1u | 153 | $\tau(methyl)$[0.87] | B1g |
| 90 | librational | B1g | | | |
| 92 | librational | Au | | | |
| 94 | translational | B2g | | | |
| 99 | $\gamma(phenyl)$[0.48] | B3g | | | |
| 101 | $\gamma(phenyl)$[0.59] | Ag | | | |
| 102 | $\tau(phenyl)$[0.67] | B2g | | | |
| 103 | translational | Au | | | |
| 104 | librational | B3u | | | |
| 104 | librational | B2u | | | |

Table 6.4. Calculated anisotropic mean square displacements for hydrogens compared with neutron diffraction results (Johnson *et al.*, personal communication). Calculations use the parameters of Table 6.1. Column **I**: Hydrogen atoms of ACN. Phenyl hydrogens are named according to their position relative to the N substitution site - which is labelled *. a, b, c refer to crystallographic directions. Column **II**: anisotropic mean-square displacements (Å²), from neutron diffraction data at 15 K [Johnson *et al.*, personal communication]. Column **III**: anisotropic mean square displacements (Å²), from harmonic analysis.

| I | | II | III | I | | II | III |
|---|---|---|---|---|---|---|---|
| methyl H | a | 0.0359 | 0.0342 | phenyl $H_{para}$ | a | 0.0126 | 0.0120 |
| | b | 0.0366 | 0.0419 | | b | 0.0273 | 0.0291 |
| | c | 0.0253 | 0.0284 | | c | 0.0279 | 0.0270 |
| | *isotropic* | .0326 | 0.0348 | | *isotropic* | 0.0226 | 0.0227 |
| methyl H | a | 0.0150 | 0.0161 | phenyl $H_{meta}$ | a | 0.0215 | 0.0224 |
| | b | 0.0482 | 0.0537 | | b | 0.0189 | 0.0209 |
| | c | 0.0328 | 0.0336 | | c | 0.0265 | 0.0261 |
| | *isotropic* | .0320 | 0.0345 | | *isotropic* | 0.0223 | 0.0232 |
| methyl H | a | 0.0301 | 0.0283 | phenyl $H_{meta}$ | a | 0.0154 | 0.0164 |
| | b | 0.0162 | 0.0183 | | b | 0.0218 | 0.0225 |
| | c | 0.0483 | 0.0600 | | c | 0.0296 | 0.0274 |
| | *isotropic* | 0.0315 | 0.0355 | | *isotropic* | 0.0222 | 0.0221 |
| amide H | a | 0.0178 | 0.0179 | phenyl $H_{ortho}$ | a | 0.0159 | 0.0160 |
| | b | 0.0110 | 0.0120 | | b | 0.0189 | 0.0205 |
| | c | 0.0258 | 0.0308 | | c | 0.0286 | 0.0261 |
| | *isotropic* | 0.0182 | 0.0202 | | *isotropic* | 0.0211 | 0.0209 |
| | | | | phenyl $H_{ortho}$ | a | 0.0203 | 0.0204 |
| | | | | | b | 0.0170 | 0.0171 |
| | | | | | c | 0.0264 | 0.0260 |
| | | | | | *isotropic* | 0.0212 | 0.0212 |

Table 6.5. Calculated isotropic mean square displacements for heavy atoms compared with x-ray diffraction results (Wasserman *et al.*, 1985). Calculations use the parameters of Table 6.1. Column I: Heavy atoms of ACN. Phenyl carbons are named according to their position relative to the N substitution site - which is labelled *. Column II: isotropic mean square displacements (Å²), from harmonic analysis. Column III: isotropic mean-square displacements (Å²), from x-ray diffraction data at 113 K [Wasserman *et al.*, 1985].

| I | II | III | I | II | III |
|---|---|---|---|---|---|
| $C_{me}$ | 0.028 | 0.026 | $C_{ph}$ *ortho* | 0.019 | 0.021 |
| C | 0.019 | 0.020 | $C_{ph}$ *ortho* | 0.019 | 0.022 |
| O | 0.026 | 0.026 | $C_{ph}$ *meta* | 0.021 | 0.025 |
| N | 0.019 | 0.020 | $C_{ph}$ *meta* | 0.022 | 0.025 |
| $C_{ph}$ * | 0.016 | 0.019 | $C_{ph}$ *para* | 0.022 | 0.025 |

Table 6.6. The assignment of the crystal phonon bands above 160 $cm^{-1}$ in terms of intra-molecular modes of the isolated molecule. Intra-molecular modes, in turn, assigned in terms of the potential energy distribution amongst internal coordinates used in construction of CHARMM potential energy function for the ACN molecule. Each phonon band carries eight modes, one each of the eight symmetry classes. Calculations use the parameters of Table 6.1.

| I | II | III |
|---|---|---|
| $*^a$ | 47[—] | $\tau(phenyl)(81)$ |
| $*^a$ | 81[—] | $\tau(CN)(66)\ \gamma(phenyl)(22)$ |
| $*^a$ | 127[—] | $\tau(methyl)(99)$ |
| 183-199 | 159[0.96] | $\gamma(phenyl)(40)\ \tau(CN)(20)\ \tau(phenyl)(8)$ |
| 260-273 | 261[0.98] | $\gamma(phenyl)(33)\ \tau(CN)(21)\ \tau(C_{ph}C_{ph})(13)$ |
| 335-339 | 328[0.96] | $\delta(CC_{me})(24)\ \delta(NC_{ph}C_{ph})(14)\ s(NC_{ph})(9)\ s(CN)(11)$ |
| 342-355 | 340[0.95] | $\delta(NC_{ph}C_{ph})(32)\ \delta(CC_{me})(24)\ \delta(CO)(15)$ |
| 379-388 | 371[0.99] | $\tau(C_{ph}C_{ph})(48)\ \gamma(C_{ph}H)(47)$ |
| 447-456 | 441[0.99] | $\tau(C_{ph}C_{ph})(32)\ \gamma(C_{ph}H)(54)$ |
| 529-535 | 523[0.99] | $\delta(CO)(56)\ s(CC_{me})(10)\ \delta(CC_{me})(7)$ |
| 550-558 | 543[0.98] | $\gamma(C_{ph}H)(87)\ \tau(C_{ph}C_{ph})(10)$ |
| 602-612 | 570[0.83] | $\gamma(CO)(72)\ \gamma(NH)(22)$ |
| 619-624 | 608[0.94] | $\gamma(C_{ph}H)(62)\ \tau(C_{ph}C_{ph})(28)$ |
| 650-653 | 646[0.80] | $\gamma(C_{ph}H)(81)$ |
| 653-659 | 648[0.80] | $\gamma(C_{ph}H)(78)$ |
| $^b$ | 663 | $\gamma(NH)(48)\ \gamma(C_{ph}H)(19)\ \gamma(CO)(19)$ |
| 673-675 | 669[0.84] | $\gamma(NH)(31)\ \delta(C_{ph}C_{ph}C_{ph})(18)\ s(CC_{me})(10)\ \gamma(CO)(10)$ |
| 732-734 | 734[0.80]$^b$ | $\gamma(C_{ph}H)(69)$ |
| 758-762 | 758[0.95] | $\delta(C_{ph}C_{ph}H)(30)\ \gamma(C_{ph}H)(29)\ s(C_{ph}C_{ph})(18)$ |
| 762-774 | 767[0.77]$^b$ | $\gamma(C_{ph}H)(94)$ |
| 775-778 | 767[0.60]$^b$ | $\gamma(C_{ph}H)(94)$ |
| 794-797 | 788[0.89] | $\gamma(C_{ph}H)(63)\ \tau(C_{ph}C_{ph})(26)$ |
| 799-804 | 797[0.90] | $\delta(C_{ph}C_{ph}H)(33)\ \gamma(C_{ph}H)(20)$ $s(C_{ph}C_{ph})(12)\ s(CN)(9)\ s(CO)(5)$ |
| 810-819 | 810[0.97] | $\delta(C_{ph}C_{ph}H)(37)\ s(CN)(11)\ s(CO)(7)\ s(C_{ph}C_{ph})(7)$ |
| 825-829 | 818[0.92] | $\delta(C_{ph}C_{ph}H)(29)\ \delta(C_{ph}C_{ph}C_{ph})(26)$ $s(CN)(12)\ s(CC_{me})(9)\ s(CO)(7)\ s(C_{ph}C_{ph})(7)$ |
| 835-841 | 831[0.93] | $\delta(C_{ph}C_{ph}H)(88)$ |
| 857-859 | 848[1.00] | $\delta(C_{ph}C_{ph}H)(82)\ s(C_{ph}C_{ph})(10)$ |
| 956-958 | 952[1.00] | $s(C_{ph}C_{ph})(61)\ \delta(C_{ph}C_{ph}C_{ph})(19)\ \delta(C_{ph}C_{ph}H)(10)$ |
| 980-981 | 978[0.99] | $methyl\ rock(79)\ s(CO)(7)$ |
| 1022-1023 | 1016[0.97] | $\delta(C_{ph}C_{ph}H)(85)$ |
| 1034-1040 | 1024[0.97] | $methyl\ rock(73)\ \gamma(CO)(14)$ |

Table 6.6 (continued)
Column I: frequency range (wavenumbers) of **k** = 0 phonon bands with frequency > 160 $cm^{-1}$ ( Note a - for lower frequency bands see Table 6.9). Column II: frequency of corresponding isolated molecular mode (defined as mode with closest eigenvector **e** - numbers in square brackets give the dot product $\mathbf{e}_{isolated}.\mathbf{e}_{crystal}$). Note b - the bands at 752-765 $cm^{-1}$, 762-774, 775-788 $cm^{-1}$ in the crystal were mixed extensively with γNH - the dot products with the isolated molecular γNH mode at 634 $cm^{-1}$ were [0.45], [0.37], [0.3] respectively. Column III: assignments for isolated molecule modes (numbers in round brackets give percentage contribution to the potential energy of the mode, terms contributing > 5% are listed). s = bond stretch, $\delta$ = in-plane bend, $\gamma$ = out-of-plane bend, $\tau$ = torsion.

| I*(cont.)* | II*(cont.)* | III*(cont.)* |
|---|---|---|
| 1183-1186 | 1181[1.00] | $s(C_{ph}C_{ph})(43)$ $\delta(C_{ph}C_{ph}H)(23)$ $s(NC_{ph})(23)$ |
| 1279-1283 | 1270[0.99] | $s(C_{ph}C_{ph})(24)$ $\delta(NH)(22)$ $s(CC_{me})(14)$ $s(CN)(10)$ |
| 1318-1321 | 1315[0.99] | $s(C_{ph}C_{ph})(41)$ $\delta(C_{ph}C_{ph}H)(14)$ $\delta(CO)(9)$ $s(CC_{me})(8)$ $s(CN)(8)$ $\delta(NH)(5)$ |
| 1378-1381 | 1372[0.98] | *methyl deformation*(91) |
| 1390-1391 | 1386[0.97] | $s(C_{ph}C_{ph})(56)$ $\delta(C_{ph}C_{ph}H)(16)$ $s(NC_{ph})(15)$ |
| 1433-1434 | 1430[0.90] | *methyl deformation*(98) |
| 1436-1437 | 1437[0.90] | *methyl deformation*(97) |
| 1500-1508 | 1489[0.97] | $s(C_{ph}C_{ph})(41)$ $\delta(NH)(25)$ $s(CN)(13)$ |
| 1537-1539 | 1533[0.97] | $s(C_{ph}C_{ph})(81)$ $\delta(C_{ph}C_{ph}H)(6)$ |
| 1568 | 1562[0.96] | $s(C_{ph}C_{ph})(80)$ $\delta(NH)(5)$ |
| 1596-1612 | 1585[0.94] | $s(C_{ph}C_{ph})(41)$ $\delta(NH)(20)$ $s(C_{ph}N)(18)$ $s(CN)(7)$ |
| 1666-1672 | 1665[0.99] | $s(CO)(70)$ $s(CC_{me})(5)$ $s(CN)(5)$ $\delta(CC_{me})(7)$ |
| 2266-2267 | 2262[1.00] | $s(C_{ph}H)(99)$ |
| 2267-2269 | 2264[1.00] | $s(C_{ph}H)(99)$ |
| 2272-2273 | 2267[1.00] | $s(C_{ph}H)(99)$ |
| 2277-2278 | 2273[1.00] | $s(C_{ph}H)(99)$ |
| 2284-2285 | 2281[1.00] | $s(C_{ph}H)(99)$ |
| 2917 | 2915[1.00] | $s(C_{me}H)(99)$ |
| 2973-2974 | 2971[1.00] | $s(C_{me}H)(99)$ |
| 2976 | 2974[1.00] | $s(C_{me}H)(99)$ |
| 3288-3294 | 3304[1.00] | $s(NH)(100)$ |

Table 6.7. Assignment of ACN-D5 crystal phonon modes below 210 $cm^{-1}$ in terms of rigid body motions or intra-molecular modes of the isolated molecule. Intramolecular modes, in turn, assigned in Table 6.6. Calculations use the parameters of Table 6.1. Column **I**: frequency ($cm^{-1}$) of **k** = 0 crystal modes < 210 $cm^{-1}$. Column **II**: assignment to rigid molecular librational or translational motion, or nearest intramolecular mode (defined as mode with closest eigenvector **e** - numbers in square brackets give the dot product $\mathbf{e}_{isolated} \cdot \mathbf{e}_{crystal}$). Column **III**: symmetry character of crystal mode.

| I | II | III | I*(cont.)* | II*(cont.)* | III*(cont.)* |
|---|---|---|---|---|---|
| 23 | translational | B1g | 102 | $\gamma(phenyl)$[0.69] | B3g |
| 24 | translational | Au | 107 | $\tau(phenyl)$[0.66] | Au |
| 25 | translational | B3u | 108 | $\tau(phenyl)$[0.76] | B2u |
| 27 | librational | Ag | 108 | $\tau(phenyl)$[0.77] | Ag |
| 36 | librational | B3g | 108 | translational | B2g |
| 36 | librational | Ag | 112 | $\gamma(phenyl)$[0.59] | B3u |
| 38 | librational | B2g | 115 | translational | B1g |
| 39 | librational | B2u | 115 | $\gamma(phenyl)$[0.71] | B2u |
| 40 | translational | B1u | 117 | librational | B1u |
| 45 | librational | Au | 119 | $\tau(phenyl)$[0.58] | B3g |
| 45 | translational | B3g | 119 | $\gamma(phenyl)$[0.87] | B1u |
| 46 | librational | B2g | 122 | $\gamma(phenyl)$[0.95] | Au |
| 50 | librational | B1u | 125 | $\gamma(phenyl)$[0.81] | Ag |
| 53 | translational | B2u | 127 | $\gamma(phenyl)$[0.72] | B1g |
| 53 | translational | B2g | 129 | translational | B3g |
| 53 | librational | B3u | 131 | translational | B3u |
| 55 | translational | Ag | 135 | translational | B1u |
| 56 | librational | B1g | 136 | $\gamma(phenyl)$[0.56] | B2u |
| 60 | translational | Au | 136 | translational | B1g |
| 64 | librational | Ag | 137 | $\gamma(phenyl)$[0.70] | B3u |
| 69 | librational | B2u | 141 | $\gamma(phenyl)$[0.67] | B2g |
| 72 | $\tau(phenyl)$[0.69] | B3u | 145 | $\gamma(phenyl)$[0.59] | B3g |
| 73 | librational | B1u | 146 | $\tau(methyl)$[0.95] | B2u |
| 74 | librational | B2g | 146 | $\tau(methyl)$[0.95] | Au |
| 74 | translational | Au | 149 | $\tau(methyl)$[0.88] | B1u |
| 76 | librational | B3g | 149 | $\tau(methyl)$[0.93] | B3u |
| 78 | translational | B1g | 149 | $\tau(methyl)$[0.89] | B3g |
| 81 | $\tau(phenyl)$[0.60] | B1g | 150 | $\tau(methyl)$[0.93] | B2g |
| 87 | librational | Au | 151 | $\tau(methyl)$[0.94] | Ag |
| 87 | librational | B1g | 152 | $\tau(methyl)$[0.88] | B1g |
| 87 | $\tau(phenyl)$[0.82] | B1u | | | |
| 89 | translational | Ag | | | |
| 92 | librational | B2g | | | |
| 97 | librational | B3g | | | |
| 99 | librational | B2u | | | |
| 100 | librational | Ag | | | |
| 100 | librational | B3u | | | |
| 100 | librational | Au | | | |
| 101 | $\tau(phenyl)$[0.70] | B2g | | | |

Table 6.8. The assignment of the crystal phonon bands above 160 $cm^{-1}$ in terms of intra-molecular modes of the isolated molecule. Intra-molecular modes, in turn, assigned in terms of the potential energy distribution amongst internal coordinates used in construction of CHARMM potential energy function for the ACN molecule. Each phonon band carries eight modes, one each of the eight symmetry classes. Calculations use the parameters of Table 6.1.

| I | II | III |
|---|---|---|
| *[a] | 45[—] | $\tau(phenyl)(81)$ |
| *[a] | 75[—] | $\tau(CN)(66)\ \gamma(phenyl)(20)$ |
| *[a] | 93[—] | $\tau(methyl)(93)$ |
| 176-195 | 154[0.96] | $\gamma(phenyl)(42)\ \tau(CN)(18)\ \tau(phenyl)(8)$ |
| 256-269 | 255[0.98] | $\gamma(phenyl)(34)\ \delta(CC_{me})(9)\ \tau(CN)(19)\ \tau(C_{ph}C_{ph})(12)$ |
| 321-324 | 315[0.98] | $\delta(CC_{me})(41)\ \delta(C_{ph}C_{ph}C_{ph})(5)\ s(NC_{ph})(11)\ s(CN)(5)$ |
| 337-350 | 333[0.97] | $\delta(NC_{ph}C_{ph})(42)\ \delta(CO)(14)\ \delta(CC_{me})(8)\ s(C_{ph}C_{ph})(5)$ |
| 379-388 | 372[0.99] | $\tau(C_{ph}C_{ph})(48)\ \gamma(C_{ph}H)(42)\ \gamma(phenyl)(8)$ |
| 447-456 | 441[0.99] | $\tau(C_{ph}C_{ph})(32)\ \gamma(C_{ph}H)(53)$ |
| 497-503 | 491[0.99] | $\delta(CO)(53)\ s(CC_{me})(13)\ s(C_{ph}N)(5)$ |
| 544-550 | 536[0.88] | $\gamma(CO)(67)\ \delta(CC_{me}H)(11)\ \gamma(C_{ph}H)(8)$ |
| 554-564 | 544[0.85] | $\gamma(C_{ph}H)(78)\ \gamma(NH)(9)$ |
| 618-622 | 608[0.93] | $\gamma(C_{ph}H)(53)\ \tau(C_{ph}C_{ph})(26)\ \gamma(NH)(12)$ |
| [b] | 634 | $\gamma(NH)(64)\ \gamma(C_{ph}H)(22)$ |
| 642-644 | 640[0.97] | $\gamma(C_{ph}H)(31)\ \delta(C_{ph}C_{ph}C_{ph})(18)$ $s(CC_{me})(10)\ s(C_{ph}C_{ph})(7)\ \delta(C_{ph}C_{ph}H)(5)$ |
| 653-659 | 648[0.94] | $\gamma(C_{ph}H)(94)$ |
| 666-667 | 660[0.99] | $\delta(C_{ph}C_{ph}C_{ph})(45)\ \gamma(C_{ph}H)(11)$ $\delta(C_{ph}C_{ph}H)(16)\ s(CC_{me})(7)\ s(C_{ph}C_{ph})(7)$ |
| 728-731 | 728[0.75] | $\gamma(C_{ph}H)(66)\ \tau(C_{ph}C_{ph})(14)$ |
| 748-750 | 750[0.81] | $\gamma(C_{ph}H)(40)\ \delta(C_{ph}C_{ph}H)(12)\ s(C_{ph}C_{ph})(9)$ |
| 752-765 | 750[0.35][b] | $\gamma(C_{ph}H)(40)\ \delta(C_{ph}C_{ph}H)(12)\ s(C_{ph}C_{ph})(9)$ |
| 768-770 | 763[0.90] | $\gamma(C_{ph}H)(33)\ \delta(CC_{me}H)(22)$ $\delta(C_{ph}C_{ph}H)(13)\ s(C_{ph}C_{ph})(8)\ s(CN)(10)$ |
| 775-777 | 767[0.95][b] | $\gamma(C_{ph}H)(86)$ |
| 794-797 | 789[0.94] | $\gamma(C_{ph}H)(68)\ \tau(C_{ph}C_{ph})(28)$ |
| 799-804 | 798[0.90] | $\delta(C_{ph}C_{ph}H)(46)\ \gamma(C_{ph}H)(8)$ $s(C_{ph}C_{ph})(15)\ s(CO)(6)$ |
| 813-826 | 811[0.80] | $\delta(C_{ph}C_{ph}H)(32)\ s(CN)(12)\ s(CO)(13)\ s(C_{ph}C_{ph})(6)$ |
| 821-824 | 816[0.85] | $\delta(C_{ph}C_{ph}H)(29)\ \delta(C_{ph}C_{ph}C_{ph})(25)$ $s(CO)(5)\ s(C_{ph}C_{ph})(8)\ s(C_{ph}N)(5)$ |
| 835-841 | 831[0.95] | $\delta(C_{ph}C_{ph}H)(85)$ |
| 857-859 | 848[0.99] | $\delta(C_{ph}C_{ph}H)(83)\ s(C_{ph}C_{ph})(10)$ |
| 870-887 | 865[0.97] | $methyl\ rock(44)\ \gamma(CO)(30)\ \tau(CN)(20)$ |
| 957-959 | 953[1.00] | $s(C_{ph}C_{ph})(58)\ \delta(C_{ph}C_{ph}C_{ph})(19)\ \delta(C_{ph}C_{ph}H)(10)$ |
| 1022-1023 | 1017[0.99] | $\delta(C_{ph}C_{ph}H)(89)$ |
| 1031-1032 | 1028[0.95] | $methyl\ deformation(96)$ |

Table 6.8 (continued)
Column **I**: frequency range (wavenumbers) of **k** = 0 phonon bands with frequency > 160 $cm^{-1}$ ( Note a - for lower frequency bands see Table 6.9). Column **II**: frequency of corresponding isolated molecular mode (defined as mode with closest eigenvector **e** - numbers in square brackets give the dot product $\mathbf{e}_{isolated} \cdot \mathbf{e}_{crystal}$). Note b - γ $C_{ph}H$ band (752 - 765 $cm^{-1}$) in crystal was mixed with γNH - the dot product with the isolated molecular γNH mode at 634 $cm^{-1}$ was [0.12]. Column **III**: assignments for isolated molecule modes (numbers in round brackets give percentage contribution to the potential energy of the mode, terms contributing > 5% are listed). s = bond stretch, δ = in-plane bend, γ = out-of-plane bend, τ = torsion.

| I *(cont.)* | II *(cont.)* | III *(cont.)* |
|---|---|---|
| 1036 | 1033[0.89] | *methyl deformation*(94) |
| 1051-1053 | 1053[0.92] | *methyl deformation*(86) |
| 1183-1186 | 1181[1.00] | $s(C_{ph}C_{ph})(42)$ $\delta(C_{ph}C_{ph}H)(24)$ $s(NC_{ph})(22)$ |
| 1281-1285 | 1272[0.98] | $s(C_{ph}C_{ph})(25)$ $\delta(NH)(21)$ $s(CC_{me})(18)$ $s(CN)(9)$ $\delta(CO)(8)$ |
| 1320-1322 | 1316[0.98] | $s(C_{ph}C_{ph})(39)$ $\delta(C_{ph}C_{ph}H)(14)$ $\delta(CO)(9)$ $s(CC_{me})(12)$ $s(CN)(9)$ $\delta(NH)(5)$ |
| 1390-1391 | 1386[0.99] | $s(C_{ph}C_{ph})(54)$ $\delta(C_{ph}C_{ph}H)(19)$ $s(NC_{ph})(15)$ $\delta(NH)(6)$ |
| 1499-1508 | 1489[0.97] | $s(C_{ph}C_{ph})(40)$ $\delta(NH)(25)$ $s(CN)(13)$ |
| 1537-1539 | 1533[0.97] | $s(C_{ph}C_{ph})(80)$ $\delta(C_{ph}C_{ph}H)(6)$ |
| 1568 | 1562[0.96] | $s(C_{ph}C_{ph})(78)$ $\delta(NH)(5)$ |
| 1596-1611 | 1585[0.94] | $s(C_{ph}C_{ph})(42)$ $\delta(NH)(20)$ $s(C_{ph}N)(18)$ $s(CN)(7)$ |
| 1666-1668 | 1665[0.99] | $s(CO)(70)$ $s(CC_{me})(6)$ $s(CN)(5)$ $\delta(CC_{me})(7)$ |
| 2096 | 2095[1.00] | $s(C_{me}H)(99)$ |
| 2205-2206 | 2203[1.00] | $s(C_{me}H)(99)$ |
| 2209-2210 | 2209[1.00] | $s(C_{me}H)(99)$ |
| 2266-2267 | 2262[1.00] | $s(C_{ph}H)(99)$ |
| 2267-2269 | 2264[1.00] | $s(C_{ph}H)(99)$ |
| 2272-2273 | 2266[1.00] | $s(C_{ph}H)(99)$ |
| 2277-2278 | 2272[1.00] | $s(C_{ph}H)(99)$ |
| 2284-2285 | 2280[1.00] | $s(C_{ph}H)(99)$ |
| 3288-3294 | 3304[1.00] | $s(NH)(100)$ |

Table 6.9. Assignment of ACN-D8 crystal phonon modes below 210 $cm^{-1}$ in terms of rigid body motions or intra-molecular modes of the isolated molecule. Intramolecular modes, in turn, assigned in Table 6.8. Calculations use the parameters of Table 6.1. Column I: frequency ($cm^{-1}$) of **k** = 0 crystal modes < 210 $cm^{-1}$. Column II: assignment to rigid molecular librational or translational motion, or nearest intramolecular mode (defined as mode with closest eigenvector **e** - numbers in square brackets give the dot product $\mathbf{e}_{isolated} \cdot \mathbf{e}_{crystal}$). Column III: symmetry character of crystal mode.

| I | II | III | I*(cont.)* | II*(cont.)* | III*(cont.)* |
|---|---|---|---|---|---|
| 22 | translational | B1g | 95 | $\tau(methyl)$[0.71] | B1g |
| 23 | translational | Au | 96 | $\tau(methyl)$[0.59] | B3g |
| 24 | translational | B3u | 99 | $\tau(phenyl)$[0.56] | B2u |
| 27 | librational | Ag | 100 | librational | B3g |
| 35 | translational | Ag | 102 | librational | Au |
| 36 | librational | B3g | 106 | $\gamma(phenyl)$[0.62] | B3u |
| 37 | librational | B2g | 106 | librational | Ag |
| 38 | librational | B2u | 106 | translational | B2g |
| 39 | translational | B1u | 107 | $\tau(methyl)$[0.82] | B1u |
| 45 | librational | Au | 110 | librational | B3u |
| 45 | translational | B3g | 110 | $\gamma(phenyl)$[0.81] | B1u |
| 46 | translational | B2g | 111 | $\tau(methyl)$[0.69] | B3u |
| 49 | librational | B1u | 113 | $\gamma(phenyl)$[0.74] | B1g |
| 52 | translational | B2u | 116 | $\gamma(phenyl)$[0.67] | Ag |
| 53 | translational | B2g | 116 | $\tau(methyl)$[0.65] | B2u |
| 53 | librational | B3u | 116 | $\tau(methyl)$[0.60] | Au |
| 54 | translational | Ag | 116 | $\gamma(phenyl)$[0.73] | Au |
| 55 | librational | B1g | 118 | librational | B1u |
| 59 | librational | Au | 120 | $\tau(methyl)$[0.77] | B2g |
| 63 | librational | Ag | 124 | translational | B3g |
| 66 | translational | B2u | 129 | $\tau(methyl)$[0.57] | Ag |
| 69 | translational | Au | 130 | translational | B3u |
| 70 | $\tau(phenyl)$[0.71] | B3u | 131 | translational | B1g |
| 71 | librational | B2g | 131 | $\tau(methyl)$[0.60] | B3g |
| 73 | librational | B1u | 133 | $\tau(phenyl)$[0.22] | B1u |
| 73 | librational | B3g | 136 | $\gamma(phenyl)$[0.53] | B3u |
| 75 | librational | B1g | 136 | librational | B2u |
| 79 | librational | B1g | 139 | $\tau(methyl)$[0.59] | B1g |
| 81 | $\tau(phenyl)$[0.77] | B1u | 140 | $\gamma(phenyl)$[0.65] | B2g |
| 84 | $\tau(phenyl)$[0.61] | Ag | 144 | $\gamma(phenyl)$[0.57] | B3g |
| 84 | $\tau(phenyl)$[0.54] | B1g | | | |
| 85 | $\tau(phenyl)$[0.65] | B2g | | | |
| 86 | librational | Au | | | |
| 87 | translational | Ag | | | |
| 90 | $\gamma(phenyl)$[0.46] | B3g | | | |
| 91 | librational | B3u | | | |
| 92 | translational | B2g | | | |
| 94 | translational | Au | | | |
| 95 | librational | B2u | | | |

Table 6.1 consistently for all three isotopomers, are compared with experiment in the next Sections, and are displayed in Fig. 6.9 to 6.15.

**6.3.2.1. The NH and $CNC_{ph}$ in-plane bending modes.**

As noted in the conclusions of Chapter V, the CHARMM PEF lacks explicit off-diagonal terms of the dynamical matrix, which allow the direct representation of interactions between displacements of internal degrees of freedom. During repeated attempts at reparameterisation, no set of bonded parameters could be found which would reproduce the 1320 $cm^{-1}$ band involving NH in-plane bending, without producing large shifts in the amide II bands at 1500 and 1600 $cm^{-1}$. This suggested that interactions between the main components of these bands, namely NH in plane bend, CN stretch, and $C_{ph}N$ stretch are responsible for the particular distribution of bands observed experimentally. The only terms in the CHARMM force field which can be used to implicitly represent interactions of this sort are non-bonded terms (Chapter III and Chapter V). Van der Waals and electrostatic terms for the participating atoms have a non-specific effect on all bands in which the same atoms play a role, and are especially important in determining low frequency lattice bands. On the other hand, Urey Bradley 1:3 terms, which represent the interaction between atoms separated by only 2 bonds (hence '1:3' terms), can be manipulated to yield a more specific effect. These terms are harmonic in the deviation away from an equilibrium distance between atoms 1 and 3 of a three atom group (Chapter III). With this in mind, efforts to improve the NH and $CNC_{ph}$ in-plane bending bands were concentrated on introducing appropriate Urey Bradley terms for the CNH, $CNC_{ph}$ and $C_{ph}NH$ groups. In fact a chemical rational for the introduction of these Urey Bradley terms exists. The phenyl ring is an aromatic system, and the peptide group

CN bond is known to share some double bond character with the CO group. It may be that the conjugated character of the two constituents of acetanilide, phenyl ring and peptide group, accounts for a strong interaction between motions involving CN and $NC_{ph}$ and NH. This is the type of interaction represented by Urey Bradley terms. It will be interesting to see whether *ab initio* quantum chemical calculations, when they are possible for acetanilide, will indicate interactions of this type. Meantime the introduction of the Urey Bradley terms remains essentially pragmatic and empirical, based on the improvements in the calculated spectra which they allowed.

In fact, this approach allowed the band at 1210 $cm^{-1}$ in all three isotopomers to be shifted to near 1295 $cm^{-1}$, or within 2% of the target frequency of 1320 $cm^{-1}$, without destroying the representation of the Amide II and III bands. Indeed the distribution of intensity between 1200 and 1600 $cm^{-1}$ for all three isotopomers was also improved (Figs. 6.11, 6.13 and 6.15). Furthermore the $CNC_{ph}$ Urey Bradley term also shifted the band at 310 $cm^{-1}$ to 360 $cm^{-1}$ for ACN, with a greatly improved representation of this band for ACN and ACN-D5 (Figs. 6.12 + 6.14).

**6.3.2.2. Methyl rocking and deformation bands.**

Extensive efforts failed to shift the frequency of the band at 980 $cm^{-1}$ without simultaneously worsening the fit to the other methyl bands. Adjustments of all the relevant terms including Urey Bradley terms, were tried without success. In particular trial re-parameterisations demonstrated that an increase in the frequency of the band at 980 $cm^{-1}$ could not be achieved without a simultaneous increase in the frequency of the methyl deformation bands at 1385 $cm^{-1}$. Furthermore an increase in the frequency of the methyl deformation bands near 1430 $cm^{-1}$ also produced an undesirable increase in the frequency of the band near

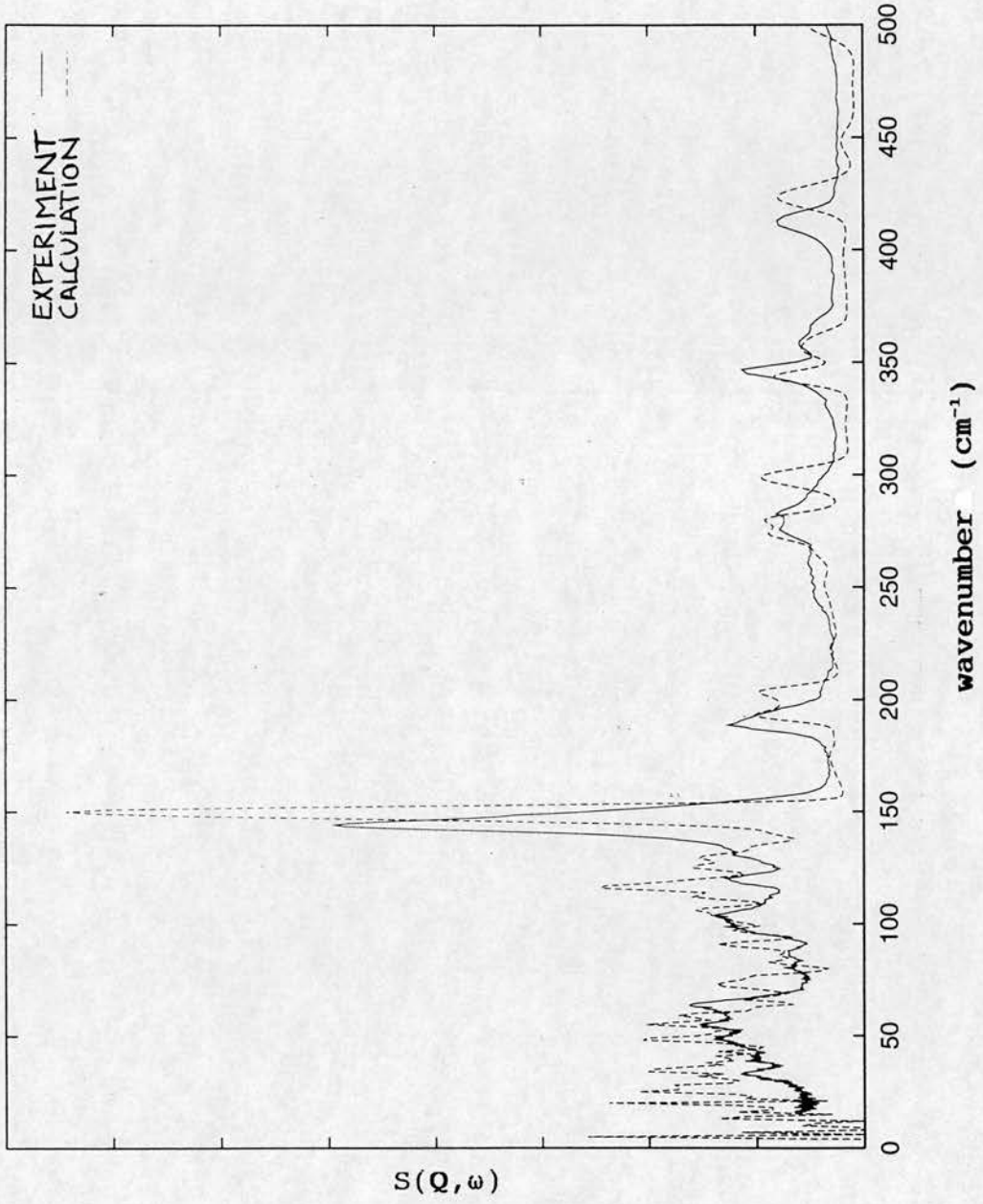


Figure 6.9. INS spectrum calculated using the parameters of Table 6.1 in the three phonon approximation compared with experimental INS spectrum for ACN. The effect of the reduced crystal field splitting of the methyl peak produces a tall narrow peak, though the integrated intensity agrees with experiment (Fig. 6.12).

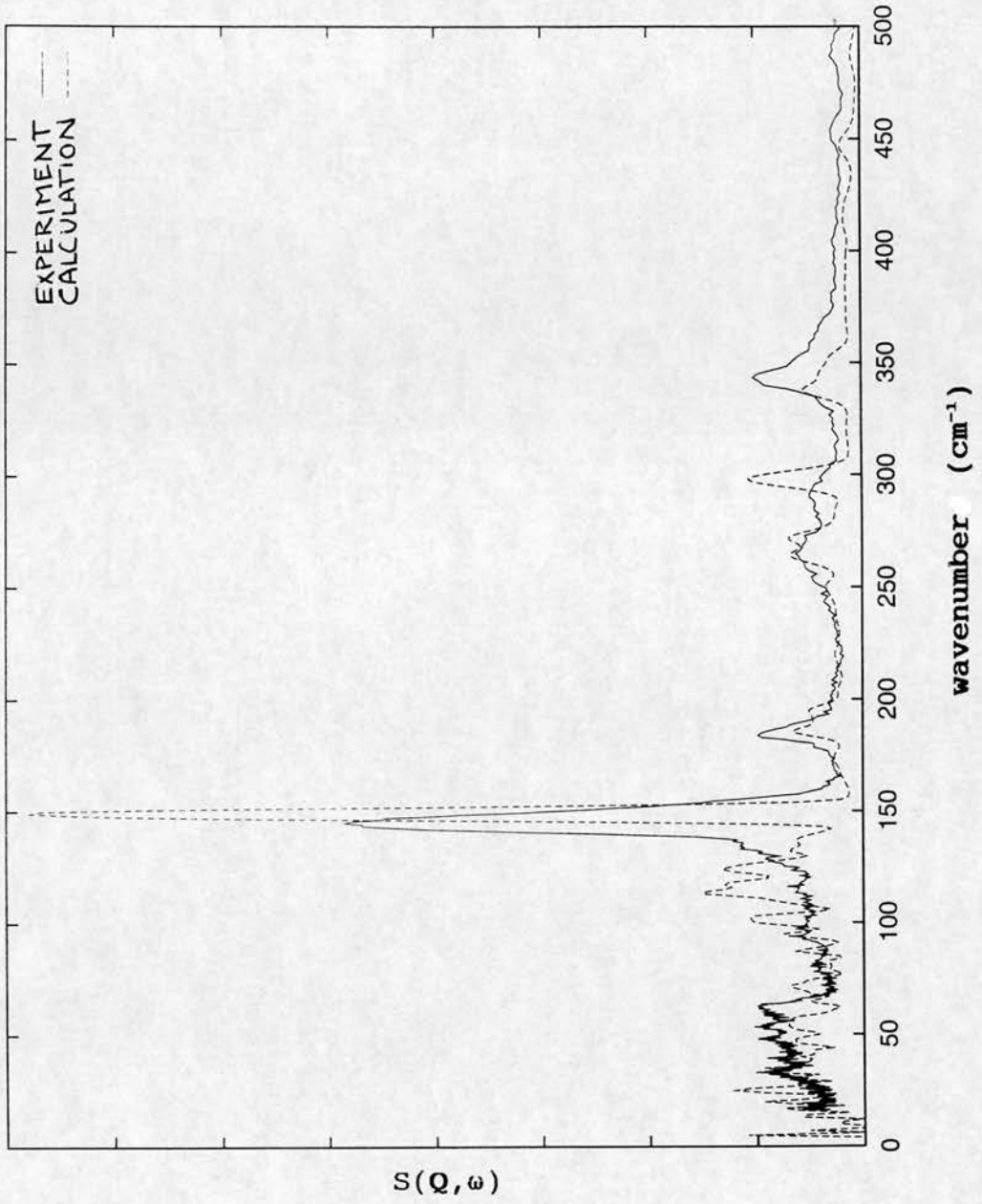


Figure 6.10. INS spectrum calculated using the parameters of Table 6.1 in the three phonon approximation compared with experimental INS spectrum for ACN-D5. The effect of the reduced crystal field splitting of the methyl peak produces a tall narrow peak, though the integrated intensity agrees with experiment (Fig. 6.14).

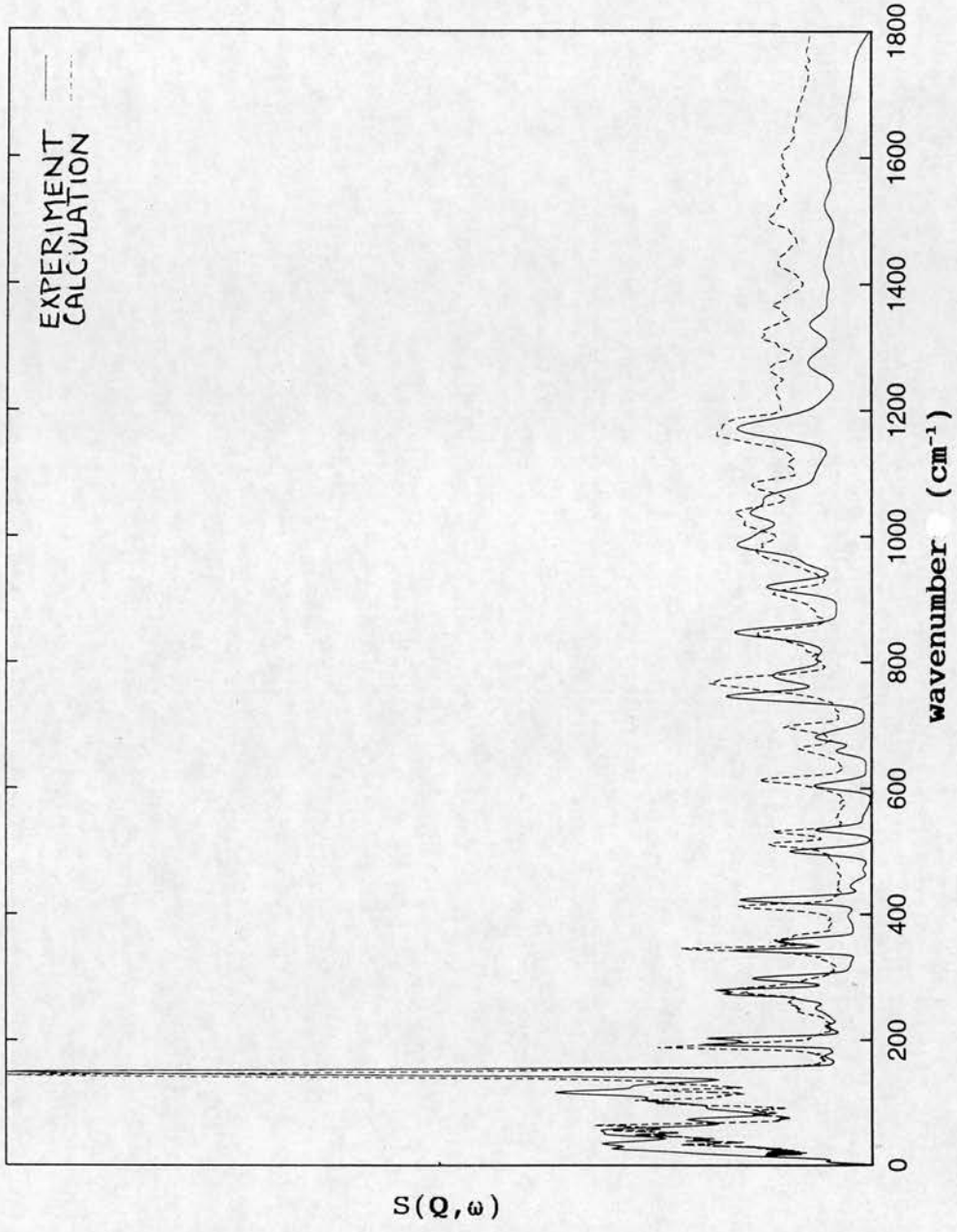


Figure 6.11. INS spectrum calculated using the parameters of Table 6.1 in the three phonon approximation compared with experimental INS spectrum for ACN. The width of the normalised Gaussian resolution function has been artificially broadened below 160 $cm^{-1}$, to demonstrate the agreement of the integrated intensity for the calculated and experimental methyl torsional peak.

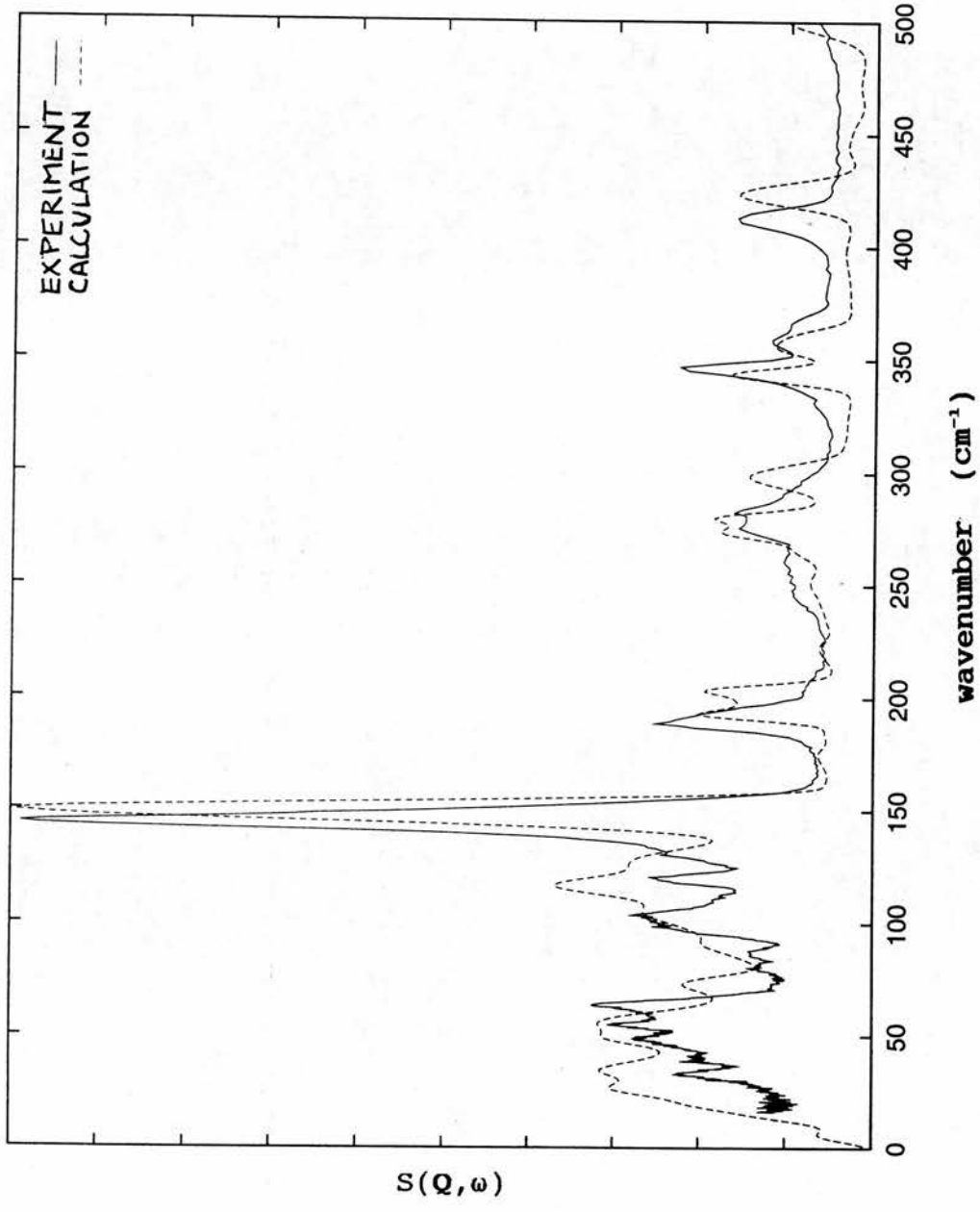


Figure 6.12. As for Fig. 6.11 on an expanded energy scale.

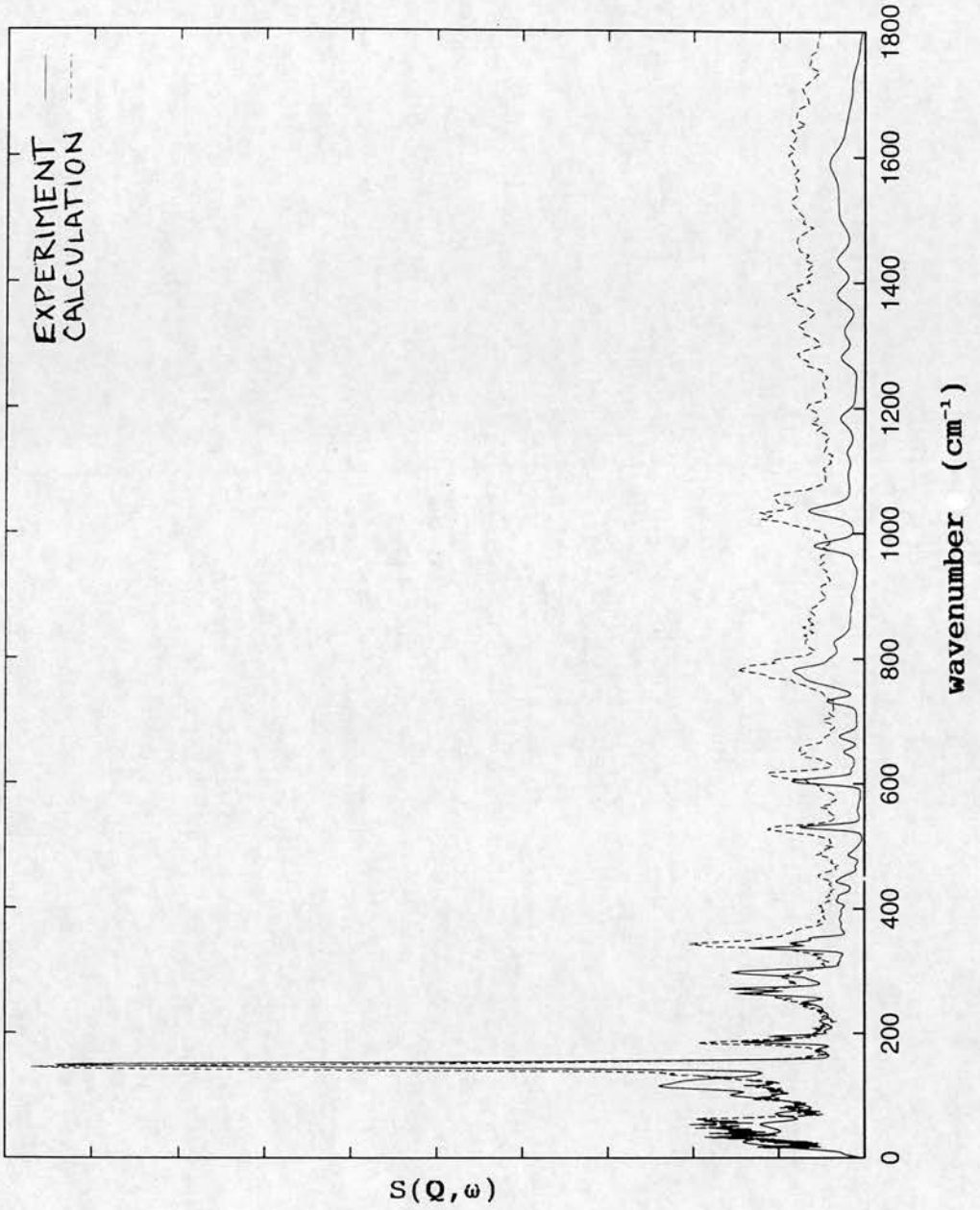


Figure 6.13. INS spectrum for ACN-D5 calculated using the parameters of Table 6.1 in the three phonon approximation compared with experimental INS spectrum for ACN-D5. The width of the normalised Gaussian resolution function has been artificially broadened below 160 $cm^{-1}$, to demonstrate the agreement of the integrated intensity for the calculated and experimental methyl torsional peak.

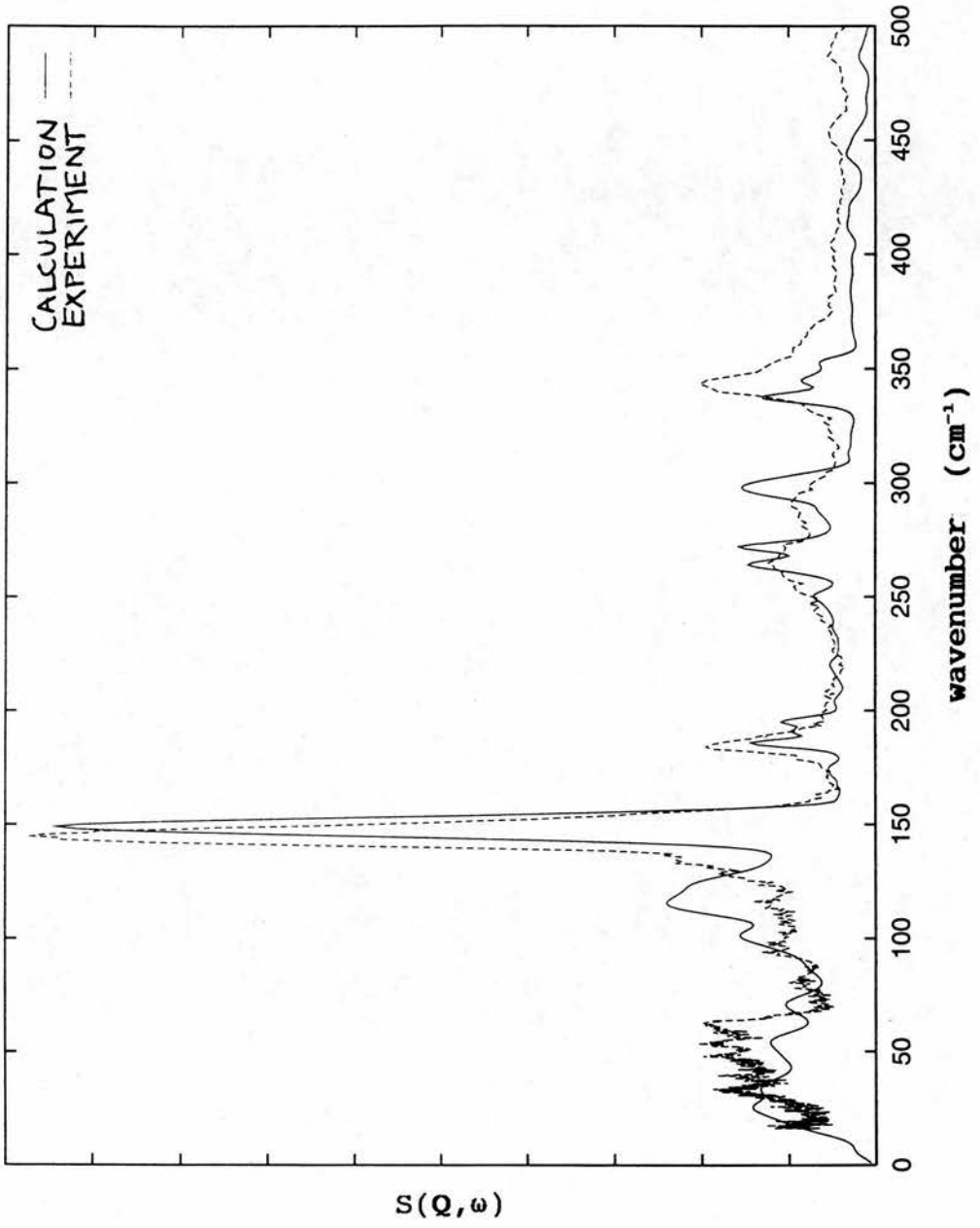


Figure 6.14. As for Fig. 6.13 on an expanded energy scale.

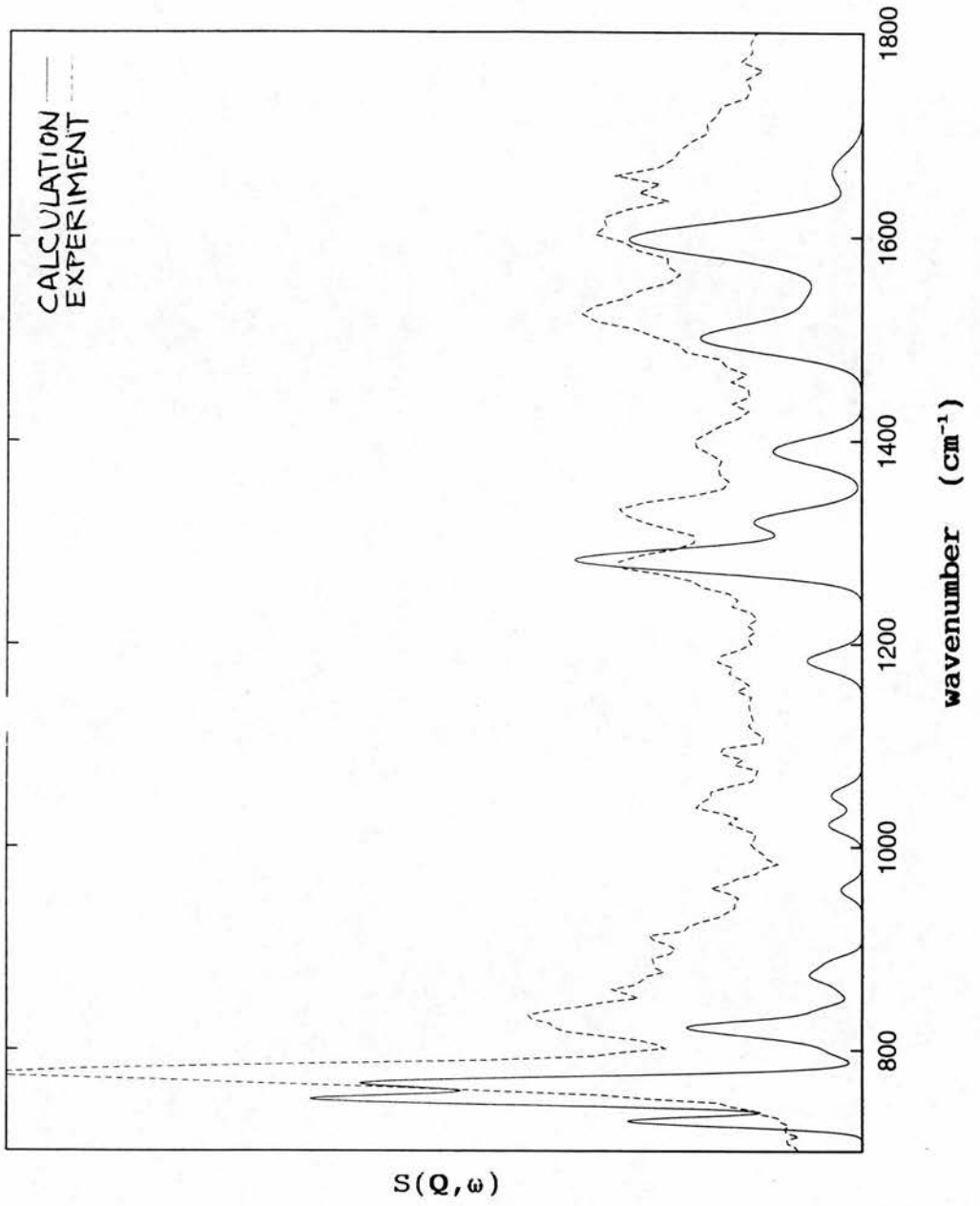


Figure 6.15. INS spectrum for ACN-D8 calculated using the parameters of Table 6.1 in the one-phonon approximation at the Brillouin zone centre, compared with experimental INS spectrum for ACN-D8.

1385 $cm^{-1}$. An increase in the difference between the methyl deformation bands at 1385 and 1430 $cm^{-1}$ could perhaps be achieved by introduction of further explicit interaction terms for the influence of displacement of one methyl degree of freedom on the other methyl degrees of freedom. The computational difficulties associated with such interaction constants were discussed in the conclusions to Chapter V. Perhaps more specific interaction terms of this type would also allow the independent adjustment of the frequency of the band at 980 $cm^{-1}$ to 1010 $cm^{-1}$. The parameterisation of Chapter V for the methyl group angle bending terms was retained. Accepting this parameterisation, the total intensity of the two calculated bands at 980 and 1040 $cm^{-1}$ was in reasonable agreement with the total observed intensity at 1010 and 1040 $cm^{-1}$, and the error in calculated frequencies for all the methyl rocking and deformation bands was less than 3% (Fig. 6.11 + 6.13).

**6.3.2.3. 100 to 140 $cm^{-1}$ region for ACN-D5.**

As noted above, using the parameterisation of Chapter V, Table 5.1, a contribution of methyl torsion produced part of the overestimate of the intensity in this region for ACN-D5 and ACN. Following the direction of the adjustments made in Chapter V, the present reparameterisation involved further increase of the methyl torsional force constant, so that an intrinsic 3-fold torsional force constant of 0.1 kcal/mol was introduced for each of the six torsional terms defined around the $C_{co}C_{Me}$ axis, with a minimum where a CH bond eclipses the NH bond. The methyl hydrogen van der Waals radius was reduced to 1.18 Å as indicated by *ab initio* quantum chemical calculations for hydrogen bonded N-methyl acetamide [Baudry and Smith, 1993]. This reduced the overestimate of the intensity between 100 and 140 $cm^{-1}$ for ACN-D5, at the expense of shifting the methyl

torsional peak approximately 5 $cm^{-1}$ too high, and with a reduction in the crystal field splitting of the components of the peak by approximately 3 $cm^{-1}$. Marked excess intensity persisted however as a consequence of the coupling of CN torsion with phenyl out-of-plane bending [Tables 6.3 + 6.7], which lay centred at 120 $cm^{-1}$, whilst appropriate intensity between 130 and 140 $cm^{-1}$ was underestimated. However attempts to raise the frequency of this phenyl out-of-plane bending band further was not possible without degrading the fit to higher frequency features. Figs. 6.9 for ACN and 6.10 for ACN-D5 show the calculated spectra multiplied by a single scale factor to bring the integrated intensity of the methyl torsional peak into agreement with experiment. The effect of the reduced crystal field splitting is to give the appearance of a sharp and tall peak in the calculated spectrum. Because the resolution of TFXA at this energy transfer is approximately 3 $cm^{-1}$ only, a reduction in the calculated crystal field splitting of the components of the peak by a few wave numbers is not compensated by the resolution function, and leads to the excessive concentration of intensity in a narrow band. The agreement with the integrated intensity was good however, as is illustrated in Figs. 6.12 for ACN and 6.14 for ACN-D5, where the half-width of the normalised Gaussian resolution function used in the calculations is increased artificially by 3 $cm^{-1}$ for the methyl torsional peak and its overtones.

**6.3.2.4. Lattice mode region below 100 $cm^{-1}$.**

As noted above the intensity in this region was underestimated for both ACN and ACN-D5 by calculations based on the parameters of Chapter V. This problem was improved by a reduction in the force constant for phenyl torsion, so that relative torsional motion of the phenyl and peptide moieties coupled with lattice modes lower in

the calculated spectrum, below 80 $cm^{-1}$. The improvements in the total calculated intensity of the lattice mode region are evident in Figs. 6.12 and 6.14. It is clear that the reparametersiation does yield a marginally improved fit of the spectrum below 200 $cm^{-1}$, though the coupling of CN torsion to phenyl out-of-plane bending remains a problem causing a significant overestimate of calculated intensity at 130 $cm^{-1}$ in ACN-D5.

### 6.3.3. Energy-minimised crystal structure with the new parameterisation.

The energy minimised crystal structure yielded by the final parameterisation was compared with the x-ray crystal structure [Wasserman *et al.*, 1985], as in Chapter V, Section 5.3.1. The RMS difference for the heavy atom positions (those well defined in the X-ray experiment) for an individual ACN molecule was 0.05 Å. The total RMS deviation for all molecules in the unit cell i.e. including differences in relative position and orientation of the eight ACN molecules in the unit cell, was 0.16 Å for the energy minimization. Hence the agreement with the x-ray structure was comparable to that obtained in Chapter V, Section 5.3.1. Minor differences arose for the phenyl and methyl rotational angles, because these were the terms most significantly altered during the reparameterisation.

#### 6.3.3.1. Phenyl Ring.

In the 113 K crystal x-ray structure the phenyl ring makes an angle of 15.5° relative to the peptide plane. This angle was 19.5° in the energy-minimized model, *i.e* within 4° of the x-ray value. An aromatic T structure was evident in the model, in agreement with the x-ray structure. The adiabatic potential energy as a function of the phenyl ring rotation was calculated by constraining the N-$C_{ph}$ dihedral angle of one ACN molecule in the unit

cell, whilst energy-minimizing all other conformational degrees of freedom for the crystal. The resulting potential energy barrier was 20.5 kcal/mol.

**6.3.3.2. Methyl Group.**

In the x-ray crystal structure a methyl group CH bond makes an angle of 5° with the plane of the peptide group. In the final refined parameter set an intrinsic 3-fold torsional force constant of 0.1 kcal/mol was introduced for each of the six torsional terms defined around the $C_{co}C_{Me}$ axis, with a minimum where a CH bond eclipses the NH bond. This lead to an energy minimized structure in which a methyl CH bond makes an angle of 0° with the plane of the peptide group, *i.e.* within 5° of the x-ray value. The total adiabatic methyl rotational barrier, including non-bonded effects, calculated by energy minimization with constrained methyl dihedral angles, was 1.28 kcal/mol in the crystal.

**6.3.4. Atomic Debye-Waller factors and mean square displacements.**

As in Chapter V, Section 5.3.4, for comparison with neutron diffraction data, the dynamic components of the anisotropic mean square displacements for the hydrogen atoms were calculated with the parameterisation of Table 6.1 according to Eq. 5.3.1 for **Q** in each of the principal crystallographic directions, from the anisotropic Debye-Waller exponents, expressed as a sum over the phonon normal modes (Eq. 5.2.19) at a temperature of 15 K. The absolute values of $\langle u_{x\alpha}^2 \rangle$, the anisotropy, and the variation in relative magnitudes for the various hydrogens were in excellent agreement, (Table 6.4), with the values derived from a neutron diffraction experiment on ACN performed at 15 K [Johnson, Eckert, and Barthes, personal communication].

The dynamic components of the isotropic mean square displacements for the heavy atoms were calculated at 113 K from Eq. 5.2.19, 5.3.1 and 5.3.2. These were compared, (Table 6.5), with the corresponding values obtained from the 113 K x-ray crystallographic analysis [Wasserman *et al.*, 1985]. The relative magnitudes for the various atoms were in agreement with the 113 K experimental values. The absolute values obtained were in good agreement for the heavy atoms of the acetamide group, but were underestimated by ~15% for the phenyl carbons. Overall, in fact the agreement with experimental mean square displacment values was slightly better for the present parameterisation than for that of Chapter V (compare Tables 6.4 and 6.5 with Tables 5.4 and 5.5).

## 6.4. CONCLUSIONS.

Relying on INS data for three isotopomers of acetanilide further improvements to the parameterisation of Chapter V were made, producing better agreement of calculated with experimental INS spectra. The improved parameterisation clearly demonstrates that NH in-plane bending motion contributes intensity at 1270, 1320, 1500 and 1600 $cm^{-1}$. The conclusions of Chapter V, regarding the presence of excess INS intensity near 1490 $cm^{-1}$ for ACN and ACN-D5 corresponding to an anomalous IR band, the splitting of amide II intensity between features at 1500 and 1600 $cm^{-1}$, and the lack of evidence of an anomalously low lying NH stretch frequency near 1575 $cm^{-1}$ in acetanilide, were confirmed. An error in the assignment of NH in-plane bending motion to a peak at 1210 $cm^{-1}$ was eliminated. Improvements in the distribution of methyl rocking and deformation bands could not be made within the current form of the CHARMM PEF, but the calculated peaks for all three isotopomers remained within 3 % of experimental values. The lattice mode region and the region between 100

and 130 $cm^{-1}$ was better represented by reducing the force constant for phenyl torsion, and increasing the force constant for methyl torsion, at the expense of shifting the methyl torsional band 5 $cm^{-1}$ too high, and reducing the crystal field splitting of the methyl torsional band. The overall agreement with the experimental crystal structure was retained and the comparison of calculated mean square displacments with experimental values for both heavy and light atoms was improved. Future molecular dynamics calculations will be required, using the parameters of the present Chapter. These will determine whether the new parameterisation also reproduces the experimental temperature dependence of acetanilide dynamics, as found in Chapter V.

## CHAPTER VII - OUTLOOK FOR FUTURE WORK.

Detailed discussions for each of the experimental Chapters have been given there (Chapters IV-VI). Some more general concluding remarks will be made in this Chapter, and some personal views of the future discussed.

### 7.1. FUTURE DIRECTIONS FOR THEORETICAL IMPROVEMENTS.

Broadly speaking Chapter IV has shown that important information regarding fundamental properties of polypeptides and natural proteins, including density-of-state information for the protein and its associated water, can be extracted successfully from inelastic neutron scattering data by the use of analytical approximations. On the other hand, there exist detailed numerical models for proteins in general, which provide a unified framework in which to investigate structural, dynamical and functional properties, by means of an empirically parameterised PEF. The numerical calculations of Chapter IV serve to show that, for the CHARMM PEF as an example, significant improvements of the empirical parameters are still necessary to achieve quantitative agreement with INS experiments.

#### 7.1.1. Problems.

The size of the computational problem for polypeptides is currently a significant obstruction to the direct improvement of parameters, even for homopolymers like PPII and simple heteropolymers like $(PPG)_{10}$. Chapter V and VI, however, demonstrate the successful application of INS data to the refinement of parameters for the molecular crystal of acetanilide, a peptide model compound. Refinements based on the harmonic approximation allow reasonably accurate modelling of the low temperature INS intensity data for three different isotopomers of acetanilide, and reproduce temperature dependent spectral

properties. This represents a fairly stringent test of the dynamical model. The acetanilide crystal is not orders of magnitude more simple than the homopolypeptides, which might form the starting point for more direct efforts at refinement for proteins. An advance would be provided by a program for dynamics calculations for infinite helical homopolymers or simple heteropolymers, using the harmonic approximation or periodic boundary conditions, and such a program would reduce the number of refinable parameters to those for a single amino acid residue for homopolymers, or a few for heteropolymers. Such a computational problem might actually be significantly smaller than that of Chapters V and VI.

The major disadvantages of the approach are thus practical. The refinements described in Chapter V used repeated cycles of very time-consuming manual adjustment of parameters, and lengthy calculations at 125 points throughout the Brillouin zone, and in the three-phonon approximation. Further work on improving the efficiency of this cycle might be undertaken. For example, the calculations of Chapter V showed that for spectral properties up to 250 $cm^{-1}$, one-phonon calculations are almost as good as three-phonon calculations, and a good deal quicker. For higher frequency features, however, three-phonon calculations may not be enough! The issue of the number of points in the Brillouin zone required to give a good finite approximation to the full INS spectrum might also be explored. As described in Chapter VI, 27 points in the Brillouin zone gave as good a representation of the low frequency features of the spectra, between 40 and 250 $cm^{-1}$, as did the fuller calculations of Chapter V. Calculations at the Brillouin zone centre alone were sufficient for the high frequency features.

### 7.1.2. Some solutions.

Thus two different regimes of approximation might yield maximum efficiency for refinement efforts. In the low frequency region, points throughout the Brillouin zone are required to adequately sample the dispersive low frequency bands, but the one phonon approximation is sufficient. In the higher frequency region, multiphonon calculations are necessary, but calculations of the fundamantals can be restricted to the Brillouin zone centre. One could envisage a program of refinement in which the low frequency features were refined first, by calculations throughout the Brillouin zone in the one phonon approximation. Then high frequency features could be refined, using the low frequency region to calculate multi-phonon terms. This amounts to a dynamical separation of the problem and is only appropriate if the terms which influence the low frequency region are liable to be of minor significance only to the high frequency region, and *vice versa*. Fortunately the nature of the CHARMM PEF lends itself to such a two stage approach. My experience with the refinement in Chapter V and VI indicates that the low frequency features are dominated by non-bonded van der Waals and electrostatic terms and by dihedral angle torsional parameters, whereas high frequency features are relatively insensitive to non-bonded terms, and depend more on bond angle, bond stretch and Urey-Bradley terms. An exception concerns out-of-plane bending motions, which are sensitive both to electrostatic and to dihedral terms, but may lie in the intermediate region of the spectrum, between 300 and 1000 $cm^{-1}$. A preliminary identification of high frequency spectral features determined by out-of-plane bending motions would be required therefore, so that this data could be included during the refinement of the low frequency elements. Coherent neutron scattering measurements of dispersion curves for fully deuterated

single crystals would then offer by far the most stringent test of the low frequency features of a dynamical model. A recent analysis of coherent INS data for fully deuterated L-alanine in terms of the CHARMM PEF parameterised to fit *ab initio* quantum calculations illustrates this point [Micu *et al.*, in press].

### 7.1.3. A measure of spectral agreement.

Ideally the refinement process should be automated, in the same way as the refinement of x-ray diffraction structures has been automated. A central tool for such an automation would be a means of numerically expressing the disagreement between a calculated spectrum and an experimental one. Such a measure would provide a target against which to refine the calculations, and might best be defined by discretising the problem. The calculated and simulated spectra would be subdivided into a set of contiguous spectral regions, the integrated intensity measured in each region compared. The global disagreement in integrated intensity would be expressed in terms of a root mean square deviation between corresponding members of these discrete sets of numbers. Weighting of the regions would allow account to be taken of the statistical quality of different spectral regions. The fineness of the subdivision would correspond with the resolution of the refinement, and the maximum efficiency would be provided by a subdivision corresponding with the experimental resolution of the experimental spectrum. The technique would avoid computationally expensive efforts to convolute a resolution function with the calculated spectrum.

Thus one could imagine defining an N=1 dimensional space, in which N degrees of freedom correspond with N refinable parameters, and the N+1th degree of freedom corresponds with the measure of spectral disagreement. Then the computational problem could be expressed in terms of

minimisation of the disagreement as a function of the parameters, analogous to the minimisation of the crystallographic R factor as a function of atomic coordinates in x-ray structure refinement. For example, the connection between the parameters of the dynamical model and the spectrum proceeds through a numerical calculation in the harmonic approximation, and the four dimensional Fourier transformation of the result, whereas the connection between the coordinates of a model structure and the x-ray pattern proceeds directly through a three dimensional Fourier transformation. But the four dimensional Fourier transformation of an harmonic model is not so difficult, by virtue of the orthogonality of harmonic eigenfunctions and their unique characterisation by a wavevector and an energy. Computationally expensive steps arise for convoluting a calculated spectrum with a resolution function, or in generating multi-phonon corrections. Its worth remembering, however, that the labour involved in the modern refinement of enormous protein x-ray structures pales into insignificance when compared with the efforts invested in solving the earliest single domain protein crystal structures, before the application of modern computational techniques to the task. But the early efforts paved the way for the later ones, and the fruits of all this labour have been very great. Would the same benefit come from a similar effort for dynamical data?

### 7.1.4. Is it worth it?

It might be argued that the empirical nature of the parameters obtained from such a process makes the effort relatively fruitless. After all, refinement of x-ray structures gives parameters with very tangible physical meaning, namely the coordinates and mean square displacments of atoms in a crystal. Are the parameters

obtained by a refinement of a dynamical model independently meaningful, or do they serve merely to uselessly reproduce the experimental data against which they are refined? In the first place, of course, a list of these energy parameters cannot be displayed in the same way that stunning visual representations of x-ray structures can be, with real benefit in improved structural insight. The display of dynamical properties may not be very practical, or useful - though in fact movie pictures of dynamical trajectories from simulations can be produced on appropriate graphic display work stations. On the other hand calculations using the parameters might be very useful indeed if they reduced some of the labour involved in finding new protein ligands or even clinically useful drugs.

One central question in this regard is - can the empirical parameters obtained for one system be transferred usefully to another? The way parameters are defined in CHARMM certainly implies they might be - bond stretch parameters are defined between atom 'types' for example, and are not specific to the structure from which they are derived. But does this convention correspond with reality? Is an atom of 'type' A in a given structure really comparable to an atom of 'type' A in another structure? Perhaps the only way to answer this question is to try. The early results are encouraging after all - and certainly seem to add something practical to the isolated knowledge of a protein structure. Could knowledge of the structure of influenza sialidase, or HIV protease, have allowed the design of inhibitors *de novo*, without the empirical calculation of binding energies, using an empirically parameterised PEF?

Geometric criteria for chemical fitting might be viewed as one end of a continuum of more and more detailed efforts to predict binding affinities in theory. Surely a

process of refinement of empirical parameters against a variety of data can only improve the value of the predictions made. But can the refinement process be sufficiently automated to make the effort worth while? Somewhere along the continuum there is a maximum efficiency for the cost/benefit analysis of applying more detailed theory to obtained more refined predictions. The recent successes with HIV protease and Influenza sialidase suggest that this point does not correspond merely with the knowledge of a proteins structure. It is my opinion that consistent efforts to improve the efficiency of refinement along the lines suggested above will move this point of maximum efficiency in the direction of detailed dynamical models. These are future directions for development of the theoretical techniques used in this thesis.

## 7.2. FUTURE DIRECTIONS FOR EXPERIMENTAL WORK.

The desirable properties of neutron scattering - simultaneous resolution of energy and momentum transfer, analytical relationship directly with atomic position correlation functions through Fourier transformation, absence of selection rules, contrast variation, make INS data particularly suited to a program of this sort, and I expect such data to hold a central place in future efforts to refine dynamical models. The following, then, are future directions for the experimental work described in this thesis.

### 7.2.1. Other systems of biological interest.

Other molecular crystals of biological relevance can also be studied in this way. TFXA spectra for two polycrystalline examples, L-Alanine and acetyl-alanyl-methylamide, which were collected during this thesis, are discussed briefly in Appendix B. The analysis of these

spectra in terms of a numerical model using the CHARMM program has been started by Jerome Baudry and Dr. J. Smith at Saclay, in collaboration with myself and Dr. H.D. Middendorf.

The neutron data used in this thesis was dominated by incoherent scattering from the hydrogens of the polycrystalline samples. The incoherence, the polycrystallinity, and the relation between Q and $\omega$ for the TFXA spectrometer (Chapter III), ensure that for a given energy transfer (and hence fixed |Q|), the observed spectra are averaged over all possible orientations of Q with respect to the molecular axes, and there is no delta function for the momentum transfer in the scattering expression (Chapter II). The Q dependence is therefore reduced to a scalar effect on observed intensities, through the Debye-Waller factor, and the eigenvector dependence of the observed intensities (Chapter II, IV-VI). Useful information which depends on the |Q| dependent properties, can still be obtained as demonstrated in Chapters IV-VI of this thesis. This is particularly true for atomic mean square displacements, based on the sensitivity of the Debye-Waller factor at high energy transfers, and for mode eigenvectors, based on the intensity of spectral peaks. As shown in Chapter IV, the TFXA spectrometer offers significant spectral detail for intermediate and high frequency features of a natural protein and its model polypeptides, together with high resolution spectra at low energy transfers. Similar data for globular proteins would be also be of interest, offering strict tests of dynamical models for natural proteins with important functional properties. In fact globular proteins have been much more extensivley investigated by computational techniques than has collagen. As a start in this direction Dr. J. Smith, Dr. H.D. Middendorf and I have secured a TFXA allocation next

year for investigation of the bovine pancreatic trypsin inhibitor, one of the most extensively studied globular proteins. Computational models of this protein have been under development by Dr. J. Smith's group for some time.

**7.2.2. Coherent neutron scattering.**

The full potential of neutron scattering for the evaluation of low frequency features of dynamical models will only be realised when coherent scattering properties are measured for fully deuterated single crystals, using triple axis spectrometers. The triple axis design allows momentum transfer **Q** to be varied independently of the energy transfer $\omega$. As noted in Chapter V, Dr. U. Wanderlingh of the physics department in Messina is currently attempting to grow large single crystals of various isotopomers of acetanilide, fully deuterated examples of which should be suitable for triple axis experiments. As noted in Chapter V, similar experiments have been previously performed [Barthes *et al.* 1988], but with only partial success, and a more complete data set would be valuable. Furthermore, as mentioned briefly in Chapter I, neutron Compton scattering can measure the momentum distribution of individual hydrogen species in large molecular single crystals. This can give important information on the form of the potential energy well for the hydrogen investigated. Single crystals of ACN-D8, with only the amide hydrogen unexchanged, would be suitable for experiments of this kind. The fullest exploitation of such data requires large single crystals, and these are currently unobtainable for proteins, but orientation dependent properties could be extracted for collagen, because the macroscopic orientation of tendon fibres corresponds closely with the orientation of the collagen long molecular axis. Dr. H.D. Middendorf, Dr. J. Bradshaw and I have an allocation later next year on the triple

axis spectrometer MARI at RAL to make preliminary investigations for collagen, non-covalently deuterated in $D_2O$.

Finally, I'd like to draw attention to Appendix A, which discusses an idea I have had for the model independent exploitation of coherent neutron scattering data from single crystals at low temperature, though experiments to test the idea may be some way in the future.

APPENDIX A. AN IDEA FOR THE MODEL INDEPENDENT EXPLOITATION OF COHERENT INELASTIC SCATTERING DATA FROM MOLECULAR CRYSTALS AT VERY LOW TEMPERATURES.

**A.1. Theory.**

Coherent inelastic neutron scattering (INS) depends on temporal and spatial properties of the target. There is a remarkable analytical relationship via Fourier transformation between scattering from a given initial and final target state and the structure and dynamics of those states. This is exemplified in the basic expression for the double differential cross section in the first Born approximation for scattering *from a given initial and final target state*:

$$d^2\sigma/d\Omega dE = k_f/k_i \; (m/2\pi\hbar^2)^2 \qquad (A.1.1)$$

$$\times \; \left| \; \langle\psi_{ki}|\langle\psi_{tf}|V|\psi_{ti}\rangle|\psi_{ki}\rangle \; \right|^2 \; \delta[E_{ti}-E_{tf}+E_{ki}-E_{kf}]$$

where the initial state labelled i, and the final state labelled f of the combined system, target and neutron, is represented by a product of unperturbed target eigenfunction, $|\psi_{ti/f}\rangle$ with energy $E_{ti/f}$, with unperturbed neutron eigenfunction, $|\psi_{ki/f}\rangle$ with wavevector $k_{i/f}$ and energy $E_{ki/f}$, and V is an operator on the state space of the target giving the perturbation due to the interaction, usually taken as the Fermi pseudo-potential.

Despite this analytical relationship, the direct, model independent exploitation of the unique spectral information of INS is currently not undertaken. The reason for this is that the full expression for scattering from a target in thermal equilibrium includes an *incoherent* summation over initial and final target states:

$$d^2\sigma/d\Omega dE = k_f/k_i \; (m/2\pi\hbar^2)^2 \; \Sigma_{tf,ti} \; p_{ti} \qquad (A.1.2)$$

$$\times \; \left| \; \langle\psi_{ki}|\langle\psi_{tf}|V|\psi_{ti}\rangle|\psi_{ki}\rangle \; \right|^2 \; \delta[E_{ti}-E_{tf}+E_{ki}-E_{kf}]$$

where $p_{ti}$ is the probability of finding the target in the initial state labelled i. This means that an inverse Fourier transformation yields the thermal average of the pair correlation function - the contribution of individual states of the target system cannot be seperately determined. The problem arises because the initial and final target states are not experimentally controlled. Therefore the quantitative interpretation of experimental INS spectra currently requires comparison with analytical, usually harmonic, model calculations, or with numerical calculations from an empirical model of the PEF of the target as described in Chapters IV - VI of this thesis.

Is it possible to circumvent these problem and obtain directly a picture of target dynamics for crystals, in the same way as diffraction techniques provide a direct, model independent, determination of equilibrium structures for crystals? I will now present an idea for the model independent extraction of dynamical information for molecular crystals at very low temperatures from coherent INS experiments. No experimental test of this idea has yet been attempted.

The idea is particularly suited to systems showing strong anharmonicity, or involving soft harmonic modes, in which large spatial displacments in the modes are typical, but it could be applied to an harmonic system also. Strongly anharmonic crystals cannot be studied by the conventional two stage means of first making the harmonic approximation and then including the anharmonicity as a perturbation, because the anharmonic terms are not small relative to the harmonic terms. Harmonic states with large spatial displacements are difficult to study by the harmonic

approximation and phonon expansion, because the phonon expansion may not converge for phonons with large displacements.

Some simple organic molecular crystals display anharmonic dynamics. Recently attention has focused on the possibility of a double well potential for the hydrogen bond in crystals of N-methyl acetamide, raising the prospect of a similar double well potential for hydrogen bonds in $\alpha$-helices of proteins [Kearley *et al.*, 1994]. The harmonic double well with low barrier provides an example of strong anharmonicity in which the anharmonicity leads to an extended coherent vibrational ground state crossing the barrier. Another example is the rotational dynamics of methyl groups in 4-methyl pyridine crystals, in which *collective* tunneling of methyl groups through the rotational potential barrier has been observed, though it was modelled as a sine Gordon breather state [Fillaux *et al.*, 1991; Carlile and Prager, 1993]. Nevertheless the existence of coupling of the methyl rotations in infinite chains of methyl groups implies the relevant ground state should be locally spatially extended over the 3 fold rotational barrier and coherent over many unit cells. At any rate this last is the circumstance most suited to my idea.

To illustrate the idea, I consider a fully deuterated single crystal target and limit the discussion to crystals with point groups which have irreducible representations of dimension 1 only, so that the energy eigenspaces of the target are not degenerate under point group operations. Assuming periodic boundary conditions, the eigenstates of the crystal also belong to irreducible representations of the finite translation subgroup of the crystal space group [Streitwolf, 1971]. Irreducible representations of the translation group are also of dimension one. Thus, neglecting accidental degeneracies, the eigenstates of the

crystal are uniquely characterised by an energy $\hbar\omega_i$ and wavevector $\boldsymbol{\kappa}_i$. Because of the periodicity of the crystal, the wavevector may equally well be labelled formally by $\boldsymbol{\kappa}_i$ or by $\boldsymbol{\tau} + \boldsymbol{\kappa}_i$ where $\boldsymbol{\tau}$ is a vector of the reciprocal lattice. Conventionally the wavevectors are chosen from the first Brillouin zone, but they may be chosen around any reciprocal lattice point.

A simplification will be applied first. Practicalities will be discussed thereafter. Returning to the basic expression for the double differential cross section in the first Born approximation:

$$d^2\sigma/d\Omega dE \qquad (A.1.3)$$

$$= k_f/k_i \; (m/2\pi\hbar^2)^2 \; \Sigma_{tf,ti} \; p_{ti}$$

$$\times \left| \int \exp(-i(\mathbf{k}_f.\mathbf{r}))\langle\psi_{tf}|V|\psi_{ti}\rangle\exp(i(\mathbf{k}_i.\mathbf{r}))d\mathbf{r} \right|^2$$

$$\times \; \delta[E_{ti}-E_{tf}+E_{ki}-E_{kf}]$$

$$= k_f/k_i \; (m/2\pi\hbar^2)^2 \; \Sigma_{tf,ti} \; p_{ti}$$

$$\times \left| \int \exp(i(\mathbf{Q}.\mathbf{r}))\langle\psi_{tf}|V|\psi_{ti}\rangle d\mathbf{r} \right|^2 \; \delta[E_{ti}-E_{tf}+E_{ki}-E_{kf}]$$

where the scattering vector $\mathbf{Q} = \mathbf{k}_i - \mathbf{k}_f$. This is equivalent to Eq. (A.1.2) with the initial and final plane wave states for the neutron written explicitly, to reveal the role of the spatial Fourier transform of $\langle\psi_{tf}|V|\psi_{ti}\rangle$, $\int \exp(i(\mathbf{Q}.\mathbf{r}))\langle\psi_{tf}|V|\psi_{ti}\rangle d\mathbf{r}$, in determining the scattering. This expression is independent of any particular model for the target state dynamics.

The simplification referred to above consists in assuming that *the initial target state could be controlled experimentally.* Then the initial target state would have a fixed energy and wavevector. Given a fixed initial

target state and by virtue of the conservation equations for energy and momentum transfer:

$$E_{ti}-E_{tf} = E_{kf}-E_{ki}$$

and:

$$\mathbf{Q} = \boldsymbol{\kappa}_f - \boldsymbol{\kappa}_i + \boldsymbol{\tau}$$

where $\boldsymbol{\tau}$ is any reciprocal lattice vector, the final target eigenstate can be selected (neglecting accidental degeneracy) by choosing the energy transfer $E_{kf}-E_{ki}$ and momentum transfer $\mathbf{k}_f - \mathbf{k}_i = -\mathbf{Q}$. (These can be varied independently on triple axis spectrometers). Notably a series of points $\mathbf{Q} = \boldsymbol{\kappa}_f - \boldsymbol{\kappa}_i + \boldsymbol{\tau}$, for all reciprocal lattice vector $\boldsymbol{\tau}$ all refer to the same final target eigenstate. The idea exploits this fact. Eq. A.1.3 then reads:

$$d^2\sigma/d\Omega dE \qquad \text{(A.1.4)}$$

$$= k_f/k_i \; (m/2\pi\hbar^2)^2$$

$$\times \left| \int \exp(-i(\mathbf{k}_f.\mathbf{r}))\langle\psi_{tf}|V|\psi_{ti}\rangle\exp(i(\mathbf{k}_i.\mathbf{r}))d\mathbf{r} \right|^2$$

$$= k_f/k_i \; (m/2\pi\hbar^2)^2 \left| \int \exp(i(\mathbf{Q}.\mathbf{r}))\langle\psi_{tf}|V|\psi_{ti}\rangle d\mathbf{r} \right|^2$$

with $|\psi_{tf}\rangle$ and $|\psi_{ti}\rangle$ fixed. Apart from the prefactor $k_f/k_i$, and using the Fermi pseudopotential expression for V, Eq. A.1.4 is the square of the spatial Fourier transform of the overlap integral between the target wavefunctions $|\psi_{tf}\rangle$ and $|\psi_{ti}\rangle$ in atomic position space, with the contribution of each atom weighted by its scattering length.

Restricting attention to coherent scattering:

$k_i/k_f \; d^2\sigma/d\Omega dE$ (A.1.5)

$$= \left| \int \exp(i(\mathbf{Q}.\mathbf{r}))\langle\psi_{tf}|\Sigma_\alpha \, b_\alpha \, \delta(\mathbf{r}-\mathbf{R}_\alpha)|\psi_{ti}\rangle d\mathbf{r} \right|^2$$

$$= \left| \langle\psi_{tf}|\Sigma_\alpha \, b_\alpha \, \exp(i(\mathbf{Q}.\mathbf{R}_\alpha)|\psi_{ti}\rangle \right|^2$$

$$= I(\mathbf{Q}) = |A(\mathbf{Q})|^2$$

where $\alpha$ labels the atoms of the target, $b_\alpha$ is the coherent scattering length, and $\mathbf{R}_\alpha$ is the position operator for atom $\alpha$. If, for example, $|\psi_{ti}\rangle = |0\rangle$, i.e. the ground state achieved at 0 K, then elastic scattering data provide the square of the Fourier transform of the overlap integral of the ground state with itself.

More generally, assuming that the initial target state has been selected, intensity data, $I(\mathbf{Q})$, corresponding to Eq. A.1.5 could be collected as a function of $\mathbf{Q}$ for any fixed energy transfer, and not just for elastic scattering. The square root of the intensity gives the absolute value of the complex amplitude $A(\mathbf{Q})$ of the Fourier component, $\exp\{i\mathbf{Q}.\mathbf{r}\}$, of a Fourier series representing the weighted overlap integral $\langle\psi_{tf}|\Sigma_\alpha \, b_\alpha \, \delta(\mathbf{r}-\mathbf{R}_\alpha)|\psi_{ti}\rangle$. For a crystal significant intensity would be expected at a discrete set of $\mathbf{Q}$ vectors, and the intensities of this discrete set could be measured. By choosing the energy and momentum transfers as described above, the overlap integral of the initial target state with a chosen final target state could be studied. Again it should be noted that this does not depend on any model for the crystal dynamics but only on the symmetry of the crystal. As long as the point group for the crystal has irreducible representations of dimension one only, selection of the energy and momentum transfers is sufficient to determine the final target state, given an intital target state, because the eigenspaces of the

target are naturally non-degenerate. In practice, for such a crystal symmetry, the accuracy of selection of the final target state rests on the energy and momentum resolution of the scattering experiment, and the coherence length and coherence lifetime of the crystal eigenstates.

Examining again Eq. A.1.5, and by analogy with x-ray or neutron diffraction, a phase problem can be defined, the solution of which would yield the phase of the complex numbers $A(\mathbf{Q})$, and thereby allow reconstruction of the overlap integral. Notably this weighted overlap integral $\langle\psi_{tf}|\Sigma_\alpha\ b_\alpha\ \delta(\mathbf{r}-\mathbf{R}_\alpha)|\psi_{ti}\rangle$ is not real valued but takes complex values. The time evolution of the overlap integral is given by $\exp\{i(E_{ti}-E_{tf})t/\hbar\}$ which is determined by the energy transfer $(E_{ki}-E_{kf})$ through the delta function of Eq. A.1.3, and the spatial variation of the phase of the overlap integral on passing from one unit cell to the next is determined by $\exp\{i\mathbf{r}.(\boldsymbol{\kappa}_f - \boldsymbol{\kappa}_i)\}$. If, as assumed, the initial and final states are eigenstates of energy for the target, the value of the overlap integral is stationary in time. If the final target state is assumed to differ from the initial state by a single quantum excitation of a mode of interest, the overlap integral will evolve in time.

To resolve the variation of the atomic wavefunction around the equilibrium position in an harmonic crystal, $|\mathbf{Q}|$ values of the order of $1/d$ where $d$ is the spatial extent of the ground state wavefunction are needed. This requires larger $|\mathbf{Q}|$ than are currently achieved even in the best resolved neutron diffraction experiments. But for anharmonic target dynamics in contrast, the ground state wavefunction may be considerable larger spatially, and resolvable at $|\mathbf{Q}|$ values currently obtained. In fact it is just the circumstance of a spatially extended ground state which makes the phonon expansion relatively useless.

A further refinement of this idea could be attempted, if the spatial resolution of the neutron scattering

experiment was sufficient to resolve details of the atomic wavefunction, and this might be particularly relevant to spatially extended wavefunctions typical of strongly anharmonic or soft harmonic modes. The experiment could be repeated with the same target initial state and a different final state by selection of a different energy transfer and a different set of momentum transfers. If several pairs of initial and final states were studied in this way, the time evolution of any arbitrary target state represented by any arbitrary superposition of those pairs of energy eigenstates, could be determined directly. Thus if $\langle\psi_{tm}|\Sigma_\alpha\ b_\alpha\ \delta(\mathbf{r}-\mathbf{R}_\alpha)|\psi_{tl}\rangle$ is known for all l,m, then:

$$\langle\psi_t|\Sigma_\alpha\ b_\alpha\ \delta(\mathbf{r}-\mathbf{R}_\alpha)|\psi_t\rangle \qquad \text{(A.1.6)}$$

$$= \sum_{l,m} C_l C_m \langle\psi_{tm}|\Sigma_\alpha\ b_\alpha\ \delta(\mathbf{r}-\mathbf{R}_\alpha)|\psi_{tl}\rangle$$

can be constructed for arbitrary $C_l$, $C_m$, where l,m run over the same set of eigenvectors, and are normalised complex coefficients of the expansion of the target state $|\psi_t\rangle$ in terms of the eigenvectors $|\psi_{tl}\rangle = |\ldots,n_{hi},\ldots,\ldots,n_{dj},\ldots\rangle$ :

$$|\psi_t\rangle = \sum_l C_l\ |\psi_{tl}\rangle \qquad \text{(A.1.7)}$$

In fact the square of Eq. A.1.6 can be viewed as the expectation value for the density of the scattering cross section as a function of r in the state $|\psi_t\rangle$. In Eq. A.1.6 however, because $|\psi_t\rangle$ is not an eigenstate of energy for the target Hamiltonian, the expectation value is not stationary, but will evolve as a function of time. This is because the several overlap integrals formed between initial and final state pairs $|\psi_{tl}\rangle$ and $|\psi_{tm}\rangle$, interfere, by virtue of their complex values. The time evolution of these complex values is different for each pair of

eigenstates in the superposition, in accordance with the difference in their energies. Therefore the expectation value of the scattering density as a function of r evolves in time. Such a moving picture of the scattering density could be constructed for any target states $|\psi_t\rangle$ with arbitrary coefficients $C_1$. The moving pictures could be interpreted in terms of the underlying atomic dynamics, by virtue of the simplicity and short range of the Fermi pseudo-potential, and exploiting knowledge of the crystal structure. Insight into the dynamics of the target would be obtained directly.

There are many questions about the practicalities of this idea, but given the potential information available from a successful program of this sort it seems worthwhile to try to address them. I will discuss some problems which have occurred to me.

**A.2. Practicalities.**

As noted above the spatial resolution with which the wavefunction could be viewed is determined by the maximum value of $|\mathbf{Q}|$ for which the energy and momentum transfer could be sufficiently resolved. Thereafter the most significant problem concerns the experimental selection of an initial target state, and the coherence lifetime and coherence length of the initial and final states, which set a fundamental limit on the energy and momentum resolution of the scattering experiment. A feature of the crystalline solid state is the existence of a continuum of energy eigenstates at low energies. Furthermore, point group symmetries of the crystal may produce natural degeneracies of the energy eigenfunctions. Accidental degeneracies may also exist. As noted above the discussion is restricted meantime to crystals with space groups allowing no natural degeneracies. At equilibrium, at high temperature, the energy eigenstates are populated in

accordance with the Boltzmann distribution, and at low temperature in accordance with the appropriate Bose-Einstein quantum distribution. In Eq. A.1.2 these statistical distributions are reflected in the summation over a large number of initial states $|\psi_{ti}\rangle$, weighted by the probability of their occupation, $p_{ti}$. At absolute zero the system reaches the vibrational ground state.

The most obvious means of restricting the statistical distribution of initial target states is to maintain a very low temperature. At 10 K, which is routinely attainable experimentally, only the excitations ($< 3$ cm$^{-1}$) are significantly populated above the ground state, whereas at 0.03 K, attainable on the IRIS spectrometer at the Rutherford Appleton Laboratory, only the excitations up to 0.1 cm$^{-1}$ are significantly populated above the ground state. These very low frequency excitations are generally very long wavelength acoustic modes involving translational rigid body motions of the molecules of the crystal. In practice at 0.03 K the range of wavevectors for the thermally activated acoustic modes may be significantly less than either the Q resolution of the experiment, or the wavelength of the excitations may be considerably greater than the coherence length of the anharmonic excitations studied. The thermal activation of the very low frequency acoustic modes might then be safely ignored and the *incoherent* sum arising in Eq. A.1.2 from the inclusion of several different thermally activated initial states, neglected. The thermal average over the low frequency harmonic acoustic modes will introduce an uncertainty into the atomic positions slightly larger than the dimension of the ground state harmonic vibrational wavefunctions for these modes. Similarly the excitations with lowest frequency and wavevector are those most likely to contribute to accidental degeneracies of the final target eigenstate. Accidental degenracies will therefore

be ignored.

Another restriction on the applicability of the idea should be noted. This is represented by a crystal with multiple minima seperated by energy barriers much larger than the ground state energy of the wells, so that the tunneling splitting energy is not resolvable by the neutron scattering method. In this case, at very low temperature, the target eigenstates will be multiply degenerate, with molecules trapped in a statistical distribution of slightly different conformations. Such degeneracy of the eigenstates, with spatial disorder on a scale similar to interatomic distances would prevent the more detailed applications of the idea.

The question of the coherence lifetime of vibrational states has been mentioned above in connection with the energy resolution attainable in experiments of this sort. In fact even at very low temperature the lifetime of vibrational eigenstates can range from the order of ps for stretching modes, to 100's of ns for torsional and librational modes. These latter may therefore be most suitable for study with neutron scattering. Interestingly, torsional potential energy surfaces are typically anharmonic, and allow large atomic displacements, and are therefore of particular interest for the techniques described above. Furthermore the technique is only relevant to systems with collective excitations with extended coherence lengths. Clearly local tunneling transitons are not amenable to study in this way. Together these considerations indicate that a good test case for the idea of might be provided by the collective rotational tunneling dynamics of methyl groups in fully deuterated 4-methyl pyridine. The simplest application of the idea would be the performance of a truly elastic scattering experiment at very low temperature with maximum $|Q|$ sufficiently large to resolve the extended ground state

wavefunction. The energy resolution is already available for the tunneling transitions, which are in the 2-4 $cm^{-1}$ range, well above the region (up to 0.1 $cm^{-1}$) populated thermally at 30 mK. The first extension of the idea to inelastic scattering could then attempt to resolve the overlap of the ground state with the first excited tunneling state. A similar programme of experiments could be envisaged to examine collective tunneling effects in molecular crystals with double well hydrogen bonds. Collective tunneling of hydrogens in chains of hydrogen bonded peptide groups could have significance for mechanisms of proton transport, or energy transport in biological systems.

## APPENDIX B. - INS DATA FOR CRYSTALS OF L-ALANINE AND OF ACETYL-ALANYL-METHYLAMIDE.

The neutron scattering experiments and analysis described in Chapters V and VI for acetanilide are a model of the exploitation of INS data to improve the parameterisation of molecular crystals of biological relevance, in the hope that accurate parameterisations for model molecules, representing fragments of proteins, can be transferred successfully to natural polypeptides. This appendix will record the INS data collected with the TFXA spectrometer at RAL during the final year of this thesis for two further such model systems, crystalline L-Alanine, and crystalline acetyl-alanyl-methylamide. The analysis of this data in terms of numerical calculations with the CHARMM program has been started by Dr. J. Smith and J. Baudry at Saclay [Smith, personal communication].

### B.1. INS data for l-alanine.

Recently the low frequency dispersion curves measured by coherent neutron scattering data for single crystals of fully deuterated L-Alanine at room temperature [Durand *et al.*, 1993] were successfully modelled by *ab initio* quantum chemical calculations, parameterisation in terms of the CHARMM molecular mechanics force field, and harmonic analyses using the CRYSTAL facility of the CHARMM program [Micu *et al.*, in press]. This approach is illustrative of the first stage of the two stage approach to the refinement of molecular mechanics potential functions described in Chapter VII - namely the refinement and testing of low frequency features of the PEF independently of the high frequency features. The second stage has been started by myself and Dr. Middendorf, in collaboration with Dr. J. Smith, Dr. A Micu, and J. Baudry, by the collection of INS data in the spectral range 20 - 400 $cm^{-1}$ on the TFXA spectrometer at RAL. Fully hydrogenous L-

Alanine was purchased from BDH Chemicals Ltd. Poole Dorset, U.K., in crystalline form, better than 99% pure and was used without further purification. L-Alanine crystals have the space group $P2_12_12_1$ with four zwitterionic molecules per unit cell [Durand *et al.*, 1993; Micu *et al.*, in press]. Approximately 2 grams of the polycrystalline powder was mounted in aluminium sachets 1.5 mm deep on the TFXA spectrometer and data collected at 25 K. Further details of the TFXA spectrometer are given in Chapter III. The spectrum is shown in Fig. B.1, along with the counting statistics. The data extends from low frequency features at 20 $cm^{-1}$ through the intermediate frequency region containing features attributable to hindered torsional motions of the alanine methyl group, near 270 $cm^{-1}$, and the $NH_3$ terminal group, near 480 $cm^{-1}$ and up to the X-H stretching features near 3000 $cm^{-1}$ [Wang and Storms, 1971a,b; Machida *et al.*, 1978; Forss, 1982]. This data will provide a further stringent test for the torsional parameters derived from the *ab initio* calculations, which effect both low frequency features and intermediate frequency out-of-plane bending and torsional features. The data will also provide a test of higher frequency features of the dynamical model.

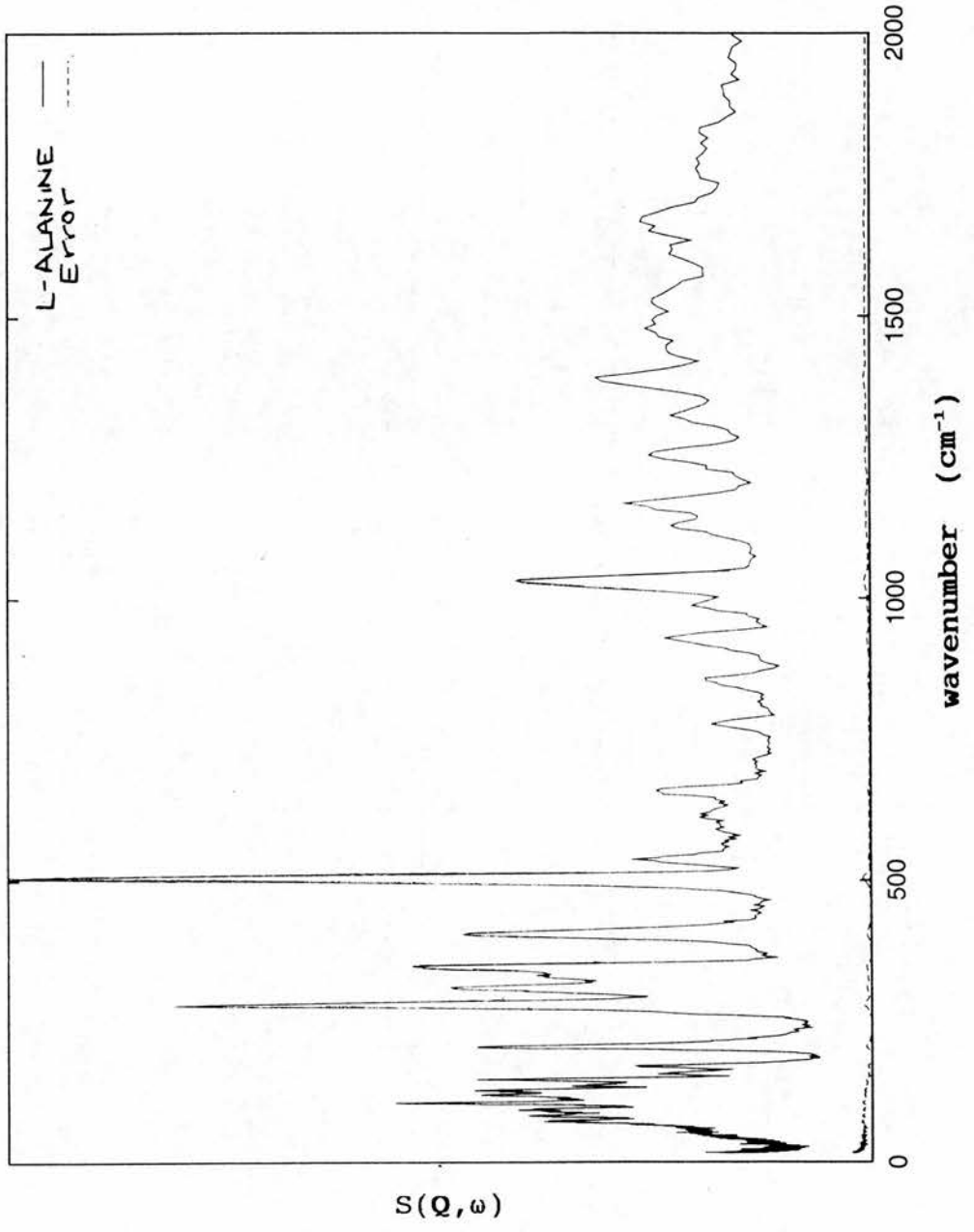


Figure B.1. Experimental INS spectrum for L-alanine at 25 K, collected on the TFXA spectrometer, RAL. The statistical counting error, proportional to $(1/N)^{0.5}$ where N is the number of detected counts, is displayed on the figure.

**B.2. INS data for acetyl-alanyl-methylamide.**

Acetyl-alanyl-methylamide is loosely called alanine dipeptide, because it contains two model peptide bonds, between the acetyl group and the amino group of the alanine residue, and between the carboxy group of the alanine residue, and the methylamide group. This is the feature that makes the material interesting as a model compound for the development of parameters for the peptide bond of proteins. Indeed this molecule can be viewed as a step in an ascending chain of complexity leading from n-methyl acetamide, the archetypal peptide bond model compound, towards polypeptides. Currently the molecule is too large for *ab initio* quantum calculations, and thus experimental tests of empirical parameterisations are essential.

Recently the quasi-elastic and low frequency inelastic neutron scattering spectrum of fully hydrogenous alanine dipeptide has been analysed in terms of the CHARMM molecular mechanics force field, using molecular dynamics calulations [Kneller *et al.*, 1992]. The neutron scattering data in that study was dominated by incoherent scattering. The inelastic data was collected at 150 and 300 K, using the IN6 spectrometer at the Institut Laue Langevin, Grenoble, and suffered in terms of resolution of the low frequency spectral features as a consequence of the high temperatures used, which render the dynamics significantly anharmonic. The data was restricted to the region below 300 $cm^{-1}$. Further INS experiments for crystalline alanine dipeptide in the spectral range 20-4000 $cm^{-1}$ using the TFXA spectrometer at low temperature have therefore been performed by myself and Dr. Middendorf in collaboration with Dr. J. Smith, Dr. A Micu, and Jerome Baudry.

Fully hydrogenous alanine dipeptide was purchased from BACHEM Feinchemikalien AG, Switzerland, better than 99% pure. Alanine dipeptide is known to adopt two crystals

forms, and the form of interest in the earlier neutron scattering study, was that formed on recrystallisation from methanol. The alanine dipeptide was therefore dissolved in boiling methanol, and allowed to cool slowly overnight. The resulting polycrystalline powder was thoroughly dried *in vacuo* overnight, and used without further purification. The resulting alanine dipeptide crystals have the space group is $P2_12_12_1$ with eight molecules per unit cell [Kneller *et al.*, 1992]. Approximately 2 grams of the polycrystalline powder was mounted in an aluminium sachet 1.5 mm deep on the TFXA spectrometer and INS data were collected at 4 K. Further details of the TFXA spectrometer are given in Chapter III. The spectrum is shown in Fig. B.2, along with the counting statistics, and shows a marked improvement in the resolution of low frequency features over the earlier IN6 data, and furthermore extends with good resolution throughout the intermediate and high frequency range.

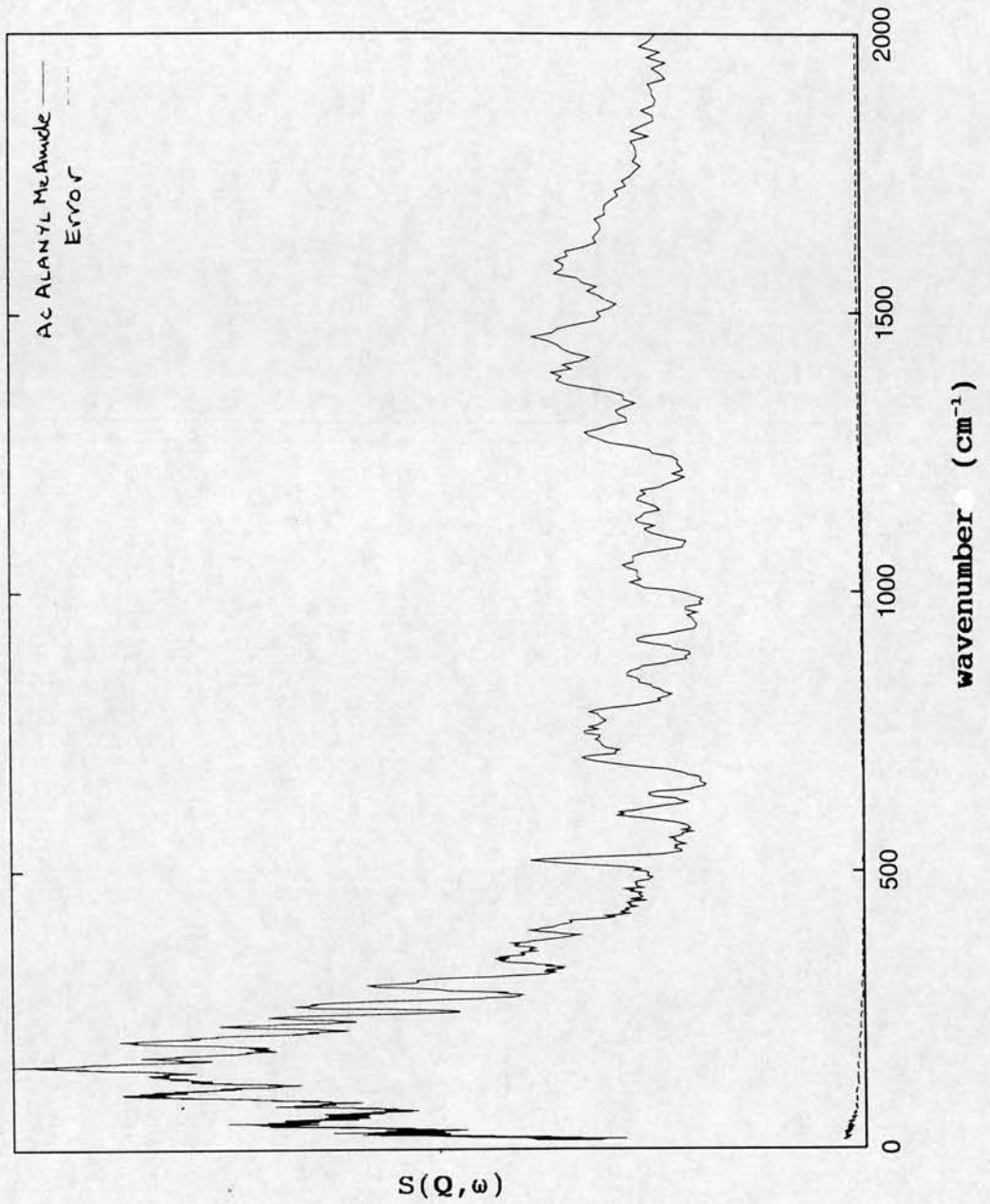


Figure B.2. Experimental INS spectrum for acetyl alanyl methylamide at 25 K, collected on the TFXA spectrometer, RAL. The statistical counting error, proportional to $(1/N)^{0.5}$ where N is the number of detected counts, is displayed on the figure.

PUBLICATIONS ARISING FROM THIS WORK.

Hayward, R.L., H.D. Middendorf, U. Wanderlingh, J.C. Smith. Dynamics of crystalline acetanilide: analysis using inelastic neutron scattering and computer simulation. *J. Chem. Phys.* In press.

Middendorf H.D., R.L. Hayward, S.F. Parker, J. Bradshaw, A. Miller. Vibrational neutron spectroscopy of collagen and model polypeptides. *Biophys. J.* In press.

**REFERENCES.**


Adzhubei, A.A., M.J.E. Sternberg. 1993. Left handed polyproline-II helices commonly occur in globular proteins. *J. Mol. Biol.* 229:472.

Alary, F., J. Durup, Y.H. Sanejouand. 1993. Molecular-dynamics study of the hydration structure of an antigen-antibody complex. *J.Phys.Chem.* 97:13864.

Alexander, D.M. and J.A. Krumhansl. 1986. Localised excitations in hydrogen-bonded molecular-crystals. *Phys. Rev.* B 33:7172.

Allen, M.P. and D.J. Tildesley. 1987. *Computer simulation of liquids.* Clarendon Press, Oxford.

Ansari, A., J. Berendzen, D. Braunstein, B.R. Cowen, H. Frauenfelder, M.K. Hong, I.E.T. Iben, J.B. Johnson, P. Ormos, T.B. Sauke, R. Scholl, A. Schulte, P.J. Steinbach, J. Vittitow, R.D. Young. 1987. Rebinding and relaxation in the myoglobin pocket. *Biophys. Chem.* 26:337.

Araki, G., K. Suzuki, H. Nakayam, K. Ishii. 1991. Polaron-like vibrational bands of molecular crystals with one-dimensional hydrogen-bond chains: N-methylacetamide. *Phys. Rev.* B 43:12662.

Arnott, S., and S.D. Dover. 1968. The structure of poly-L-proline II. *Acta Cryst.* B24:599.

Barthes, M., R. Almairac, J.L. Sauvajol, R. Currat, J. Moret and J.L. Ribet. 1988. Neutron scattering investigation of deuterated crystalline acetanilide. *Europhys. Lett.* 7:55.

Barthes, M., R. Almairac, J.L. Sauvajol, J. Moret, R. Currat and J. Dianoux. 1991. Incoherent neutron scattering in acetanilide and three deuterated derivatives. *Phys. Rev.* B 43:5223.

Barthes, M., J. Eckert, S.W. Johnston, J. Moret, B.I. Swanson and C.J. Unkefer. 1992. Anomalous vibrational modes in acetanilide as studied by inelastic neutron scattering. *J. Phys. I France.* 2:1929.

Barthes, M., H. Kellouai, G. Page, J. Moret, S.W. Johnson, and J. Eckert. 1993. H-localised mode in chains of hydrogen-bonded amide groups. *Physica D.* 68:45.

Baudry, J. and J.C. Smith. 1994. Molecular mechanics analysis of peptide group hydrogen bonding cooperativity and influence on Φ and Ψ rotational barriers. *J. Mol. Struct.* 308:103.

Bauminger, E.R., S.G. Cohen, I. Nowik, S. Ofer, J. Yariv. 1983. Dynamics of heme iron in crystals of metmyoglobin and deoxymyoglobin. *Proc. Natl. Acad. Sci. U.S.A.* 80:736.

Bella, J. M. Eaton, B. Brodsky, H.M. Berman. 1994. Crystal and molecular structure of a collagen like peptide at 1.9 Å resolution.
*Science.* 266:75.

Bellisent-Funel, M.-C., J. Texeira, S. H. Chen, B. Dorner, H. D. Middendorf, L. Crespi. 1989. Low frequency collective modes in dry and hydrated proteins. *Biophys. J.* 56:713.

Berendzen, J., D. Braunstein. 1990. Ligand-binding studies in myoglobin using temperature derivative spectroscopy. *Proc. Natl. Acad. Sci. U.S.A.* 87:1.

Berkovitchyellin, Z., W.S. Bennett, A. Yonath. 1992. Aspects in structural studies on ribosomes. *Crit. Rev. Biochem. Mol. Biol.* 27:403.

Berndt K.D., J. Beunink, W. Schroder, K. Wuthrich. 1992. Determination of high quality nuclear magnetic resonance solution structure of the bovine pancreatic trypsin inhibitor and comparison with three crystal structures. *J. Mol. Biol.* 227:757.

Berney, C.V., and S. Yip. 1980. Inelastic neutron scattering spectroscopy. *In* Methods of Experimental Physics. Vol. 16A. R.A. Fava, editor. Academic Press, New York. 205.

Berney, C.V., V. Renugopalakrishnan, and R.S. Bhatnagar. 1987. Collagen: an inelastic neutron scattering study of low-frequency vibrational modes. *Biophys. J.* 52:343.

Bhatnagar, R.S., N. Pattabiraman, K.R. Sorenson, R. Langridge, R.D. MacElroy, and V. Renugopalakrishnan. 1988. Inter-chain proline:proline contacts contribute to the stability of the triple helical conformation. *J. Biomol. Struct. Dyn.* 6:223.

Boon J.P. and S. Yip, *Molecular Hydrodynamics,* (MacGraw-Hill, New York, 1980).

Brigham, E.O. 1974. *The Fast Fourier Transform* (Prentice Hall, Englewood Cliffs).

Brodsky-Doyle, B., E.G. Bendit, and E.R. Blout. 1975. Infrared spectroscopy of collagen and collagen-like polypeptides. *Biopolymers.* 14:937.

Brooks, B., R. Bruccoleri, B. Olafson, D. States, S. Swaminathan and M. Karplus. 1983a. CHARMM: A program for macromolecular energy, minimisation and dynamic calculations. *J. Comp. Chem.* 4:187.

Brooks, B., M. Karplus. 1983b. Harmonic dynamics of proteins: normal modes and fluctuations in bovine pancreatic trypsin inhibitor. *Proc. Natl. Acad. Sci. U.S.A.* 80:6571.

Brooks, C.L. III., M. Karplus, B.M. Pettitt. 1988. Proteins: A theoretical perspective of dynamics structure and thermodynamics. *Advances in Chemical Physics* 71. John Wiley and Sons, New York.

Brown, C.J. and D.E.C. Corbridge. 1954. The crystal structure of acetanilide. *Acta Cryst.* 7:711.

Brünger, A.T., C.L. Brooks, M. Karplus. 1985. Active site dynamics of ribonuclease. *Proc. Natl. Acad. Sci. U.S.A.* 82:8458.

Brünger, A.T., J. Kuriyan, M. Karplus. 1987. Crystallographic R-factor refinement by molecular dynamics. *Science.* 235:458.

Caflisch, A., A. Miranker, M. Karplus. 1993. Multiple copy simultaneous search and construction of ligands in binding sites - applications to inhibitors of HIV-1 aspartic proteinase. *J. Med. Chem.* 36:2142.

Careri, G., U. Buontempo, F. Galluzzi, A.C. Scott, E. Gratton, and E. Shyamsunder. 1984. Spectroscopic evidence for Davydov-like solitons in acetanilide. *Phys. Rev.* B30:4689.

Carlile, C. and M. Prager. 1993. Rotational tunneling spectroscopy with neutrons. *Int. J. Mod. Phys.* B 7:3113

Case, D.A. 1994. Normal mode analysis of protein dynamics. *Curr. Opin. Struct. Biol.* 4:285.

Cheam, T.C., S. Krimm. 1985. Infrared intensities of amide modes in N-methyl acetamide and poly(glycine) I from *ab initio* calculations of dipole moment derivatives of N-methyl acetamide. *J. Chem. Phys.* 82:1631.

Cheng, X.D., B.P. Schoenborn. 1991.Neutron-diffraction study of carbonmonoxymyoglobin. *J.Mol.Biol.* 220:381.

Clayden, N.J., D. Williams, C.A. Omahoney. 1990. Phenylene ring dynamics in 1,4 diphenoxybenzene. *J. Chem Soc. Perkin Trans.* II:729.

Clementi, E., G. Corongiu, M. Aida, U. Niesar and G.R. Kneller. 1990. In *Modern Techniques in Computational Chemistry,* edited by E. Clementi (ESCOM, Leiden).

Cowan P.M., S. McGavin. 1955. Structure of poly-L-proline. *Nature.* 176:501.

Crick, F.H.C., and A. Rich. 1955. The structure of polyglycine II. *Nature (Lond.).* 176:780.

Cusack, S. and S. Lees. 1984. Variation of longitudinal acoustic velocity with water content in rat-tail tendon fibers. *Biopolymers.* 23:337.

Cusack, S., J. Smith, J.L. Finney, M. Karplus. 1988. Inelastic neutron scattering analysis of picosecond internal protein dynamics. Comparison of harmonic theory with experiment. *J.Mol.Biol.* 202:903.

Cusack, S., W. Doster. 1990. Temperature dependence of the low frequency dynamics of myoglobin. *Biophys. J.* 58:243.

Desjarlais, R.L., G.L. Seibl, I.D. Kuntz, P.S. Furth, J.C. Alvarez, P.R. Ortiz de Montellano, D.L. Decamp, L.M. Babe, C.S. Craik. 1990. Structure based design of non-peptide inhibitors specific for the Human Immunodeficiency Virus-I protease. *Proc. Natl. Acad. Sci. U.S.A.* 87:6644.

Dianoux, A.J., G.R. Kneller, J.L. Sauvajol and J.C. Smith. 1993. The polarised density of states of crystalline polyacetylene - molecular dynamics analysis and comparison with neutron scattering results. *J. Chem. Phys.* 99:5586.

Dianoux, A.J., G.R. Kneller, J.L. Sauvajol and J.C. Smith. 1994. Dynamics of sodium doped polyacetylene. *J. Chem. Phys.* 101:663.

Diem, M., R.S. Bhatnagar, M.E. Druyan, and V. Renugopalakrishnan. 1984. Solution phase Raman spectroscopic studies on synthetic collagen analogs: prolyl-prolyl-glycine and (prolyl-prolyl-glycine)$_{10}$. *Biopolymers.* 23:2955.

Dobson, C.M., M. Karplus. 1986. Internal motions in proteins: Nuclear magnetic resonance measurements and dynamic simulations. *Meth.Enzym.* 131:362.

Doherty, D.C., A.J. Hopfinger. 1994. Molecular modelling of polymers: Molecular dynamics simulation of the rotator phase of $C_{21}H_{44}$. *Phys. Rev. Lett.* 72:661.

Doster, W., A. Bachleitner, R. Dunau, M. Hiebl, E. Lüscher. 1986. Thermal properties of water in myoglobin crystals and solutions at subzero temperatures. *Biophys. J.* 50:213.

Doster, W., S. Cusack, W. Petry. 1989. Dynamical transition of
myoglobin revealed by inelastic neutron scattering. *Nature.* 337:754.

Doster, W., S. Cusack, W. Petry. 1990. Dynamical instability of liquid like motions in a globular protein observed by inelastic neutron scattering. *Phys.Rev.Lett.* 65:1080.

Duff K.C., P.J. Gilchrist, A.M. Saxena, J.P. Bradshaw. 1994. Neutron-diffraction reveals the site of Amantadine blockade in the influenza-A M2 ion-channel. *Virology.* 202:287.

Dunbrack, R.L., J. Josephmccarthy, A.D. Mackerell, M. Karplus. 1992. An empirical energy function for proline derived from *ab initio* calculations and experimental data. *FASEB J.* 6:A132.

Durand, D., M.J. Field, M. Quilichini, J.C. Smith. 1993. Lattice vibrations in crystalline L-Alanine. *Biopolymers.* 33:725.

Dwivedi, A.M., and S. Krimm. 1982. Vibrational analysis of peptides, polypeptides and proteins. XV. Crystalline polyglycine II. *Biopolymers.* 21:2377.

Eilbeck, J.C., P.S. Lomdahl and A.C. Scott. 1984. Soliton structure in crystalline acetanilide. *Phys. Rev.* B30:4703.

Eisen, M.B., D.C. Wiley, M. Karplus, R.E. Hubbard. 1994. Hook - a program for finding novel molecular architectures that satisfy the chemical and steric requirements of a macromolecule binding site. *Prot. Struct. Funct. Genet.* 19:199.

Elber, R. and M. Karplus. 1987. Multiple conformational states of proteins: a molecular dynamics simulation of myoglobin. *Science.* 235:318.

Fanconi, B., E.W. Small, and W.L. Peticolas. 1971. Phonon dispersion curves and normal coordinate analysis of poly-L-alanine. *Biopolymers.* 10:1277.

Fanconi, B., and L. Finegold. 1975. Vibrational states of the biopolymer polyglycine II: theory and experiment. *Science (Wash.DC).* 190:458.

Fann, W., L. Rothberg, M. Roberson, S. Benson, J. Madey, S. Etemad and R. Austin. 1990. Dynamical test of Davydov-type solitons in acetanilide using a picosecond free-electron laser. *Phys. Rev. Lett.* 64:607 .

Faure, Ph., A. Micu, D. Parahia, J. Doucet, J.C. Smith, P. Benoit. 1994. Correlated intramolecular motions in lysozyme and x-ray diffuse scattering. *Nature Struct. Biol.* 1:124.

Fillaux, F., C. Carlile, G. Kearley. 1991. Inelastic neutron scattering study of low temperature of the quantum sine-Gordon breather in 4-methyl pyridine with partially deuterated methyl groups. *Phys. Rev. B.* 44:12280

Fillaux, F., J.P. Fontaine, M.H. Baron, G. Kearley, and J. Tomkinson. 1993. Inelastic neutron-scattering study of the proton dynamics in N-methyl acetamide at 20K. *Chemical Physics.* 176:249.

Finermoore, J.S., A.A. Kossiakoff, J.H. Hurley, T. Earnest, R.M. Stroud. 1992. Solvent structure in crystals of trypsin determined by x-ray and neutron-diffraction. *Prot.Struct.Funct.Gen.* 12:203-222.

Förner, W.. 1993. Effects of temperature and interchain coupling on Davydov's solitons. *Physica* D 68:68.

Forss, S. 1982. A Raman spectroscopic temperature study of $NH_3$ torsional motion as related to hydrogen bonding in the L-alanine crystal. *J. Raman. Spec.* 12:266.

Fraser, R.D.B., T.P. MacRae. 1979. The crystalline structure of collagen fibrils in tendon. *J. Mol. Biol.* 127:129.

Fraser, R.D.B., T.P. MacRae, E. Suzuki. 1979. Chain conformation in the collagen molecule. *J. Mol. Biol.* 129:463.

Fraser, R.D.B., T.P. MacRae, A. Miller, and E. Suzuki. 1983. Molecular conformation and packing in collagen fibrils. *J. Mol. Biol.* 167:497.

Fraser, R.D.B., T.P. MacRae, and A. Miller. 1987. Molecular packing in type I collagen fibrils. *J. Mol. Biol.* 193:115.

Frauenfelder, H. G. A. Petsko, D. Tsernoglou. 1979. Temperature dependent x-ray diffraction as a probe of protein structural dynamics. *Nature.* 280:558.

Frauenfelder, H. 1989. New looks at protein motions. *Nature.* 338:623.

Frauenfelder, H., S.G. Sligar, P.G. Wolynes. 1991. The energy landscapes and motions of proteins. *Science.* 254:1598.

Frushour, B.G., and J.L. Koenig. 1975. Raman scattering of collagen, gelatin, and elastin. *Biopolymers.* 14:379.

Gallagher, W., F. Tao, C. Woodward. 1992. Comparison of hydrogen-exchange rates for bovine pancreatic trypsin-inhibitor in crystals and in solution. *Biochemistry.* 31:4673.

Gehlen, J.N., M. Marchi, D. Chandler. 1994. Dynamics affecting the primary charge transfer in photosynthesis. *Science.* 263:499.

Go, N. 1990. A theorem on amplitudes of thermal atomic fluctuations in large molecules assuming specific conformations calculated by normal mode analysis. *Biophys.Chem.* 35:105.

Goodman, L., A.G. Ozkabak, S.N. Thakur. 1991. A benchmark vibrational potential surface: ground-state benzene. *J. Phys. Chem.* 95:9044.

Goyal, P.S., J. Penfold, J. Tomkinson. 1986. In *RAL* 86-070, a report of Rutherford Appleton Laboratory, Chilton, Didcot, Oxfordshire.

Grigera, J.R., and H.J.C. Berendsen. 1979. The molecular details of collagen hydration. *Biopolymers*. 18:47.

Grimm, H., H. Stiller, C.F. Majkrzak, A. Rupprecht, and U. Dahlborg. 1987. Observation of acoustic umklapp phonons in water stabilised DNA. *Phys. Rev. Lett.* 59:1780.

Grover, J.R., E.A. Walters, E.T.Hui. 1987. Dissociation energies of the benzene dimer and cation dimer. *J. Phys. Chem.* 91:3233

Gupta, V.D., R.D. Singh, and A.M. Dwivedi. 1973. Vibrational spectra and dispersion curves of poly-L-proline II chains. *Biopolymers*. 12:1377.

Guo, H., M. Karplus. 1992. *Ab initio* studies of hydrogen bonding of N-methyl acetamide - structure, cooperativity and internal rotational barriers. *J. Phys. Chem.* 92:7273.

Harris F.J. 1978. Report. *Proc. IEEE* 66:51.

Hartmann, H., F. Parak, W. Steigmann, G.A. Petsko, D. Ringe Ponzi, H. Frauenfelder. 1982. Conformational substates in a protein: structure and dynamics at 80K. *Proc. Natl. Acad. Sci. U.S.A.* 79:4967.

Hayward, R.L., H.D. Middendorf, U. Wanderlingh, and J.C. Smith. 1994. Dynamics of crystalline acetanilide: analysis using neutron scattering and computer simulation. *J. Chem. Phys.* (in press).

Hendle, J., A.F. Cuckmann, W. Ashle, D. Schomburg, R.D. Schmid. 1993. Structure/activity relationship of adenine modified NAD derivatives with respect to porcine heart lactate dehydrogenase isozyme H-4 simulated with molecular mechanics. *Eur. J. Biochem.* 213:947.

Hochstrasser, R.M., D.K. Negus. 1984. Picosecond fluorescence decay of tryptophans in myoglobin. *Proc. Natl. Acad. Sci. U.S.A.* 81:4399.

Hoeve, C.A.J., and A.S. Tata. 1978. The structure of water absorbed in collagen. *J. Phys. Chem.* 82:1661.

Hong, M.K., D. Braunstein, B.R. Cowen, H. Frauenfelder, I.E.T. Iben, J.R. Mourant, P. Ormos, A. Schulte, P.J. Steinbach, A.H. Xie, R.D. Young. 1990. Conformational substates and motions in myoglobin - external influences on structure and dynamics. *Biophys. J.* 58:429.

Hopfinger, A.J. 1971. The lattice energetics of some polypeptide chains. *Biopolymers*. 10:1299.

Hulmes, D.J.S. and A. Miller. 1979. Quasi-hexagonal molecular packing in collagen fibrils. *Nature*. 282:878.

Hulmes, D.J.S., J.C. Jesior, A. Miller, C. Berthocolominas, C. Wolff. 1981. Electron microscopy shows periodic structure in collagen fibril cross-sections. *Proc. Natl. Acad. Sci. U.S.A.* 78:3567.

International Tables of X-ray Crystallography. 1983. D. Reidel Pub. Co. Dordrecht:Holland/Boston:U.S.A.

Isemura, T., H. Okabayashi, and S. Sakakibara. 1968. Steric structure of L- proline oligopeptides. I. Infrared absorption spectra of the oligopeptides and poly-L-proline. *Biopolymers*. 6:307.

Jobic, H., and H.J. Lauter. 1988. Calculation of the effect of the Debye-Waller factor on the intensity of molecular modes measured by neutron inelastic scattering. *J. Chem. Phys.* 88:5450.

Johnston, C.T. and B.I. Swanson. 1985. Temperature dependence of the vibrational spectra of acetanilide: Davydov solitons or Fermi coupling. *Chem. Phys. Lett.* 114:547.

Johnston, C.T., S.F. Agnew, J. Eckert, L. H. Jones, B.I. Swanson and C.J. Unkefer. 1991. Low-frequency single-crystal Raman, far-infrared and inelastic neutron scattering studies of acetanilide at low temperature. *J. Phys. Chem.* 95:5281.

Jones, E.Y. 1985. Structural and dynamic studies on biological macromolecules. *D. Phil. Thesis, University of Oxford.*

Karplus, M., G.A. Petsko. 1990. Molecular dynamics simulations in biology. *Nature*. 347:631.

Kearley, G.J., F. Fillaux, M.-H. Baron, S. Bennington, and J. Tomkinson. 1994. A new look at proton transfer dynamics along hydrogen bonds in amides and peptides. *Science (Wash.DC)*. 264:1285.

Kneller G.R. 1988. *Report no. 2215*. Kernforschungsanlage, Julich GmbH.

Kneller, G.R., W. Doster, M. Settles, S. Cusack, J.C. Smith. 1992. Methyl group dynamics in the crystalline alanine dipeptide: a combined computer simulation and inelastic neutron scattering analysis. *J.Chem.Phys.* 97:8864.

Kneller, G. and J.C. Smith. 1994. Liquid-like side-chain dynamics in myoglobin. 242:181.

Kneller G.R., *Comp. Phys. Comms.* (in press).

Kollman, P.A. 1994. Theory of macromolecule-ligand interactions.
*Curr. Opin. Struct. Biol.* 4:240.

Krimm, S., and J. Bandekar. 1986. Vibrational spectroscopy and conformation of peptides, polypeptides, and proteins. *Adv. Prot. Chem.* 38:181-364.

Krumhansl, J.A. in *Energy Transfer Dynamics,* edited by T.W. Barrett and H.A. Pohl (Springer-Verlag, Berlin 1987).

Kuczera, K., J. Kuriyan, M. Karplus. 1990. Temperature dependence of the structure and dynamics of myoglobin. A simulation approach.
*J. Mol. Biol.* 213:351.

Kuntz, I.D. 1994. Theory and simulation. *Curr. Opin. Struct. Biol.* 4:231.

Levitt, M., C. Sander, P.S. Stern. 1985. Protein normal mode dynamics: trypsin inhibitor, crambin, ribonuclease and lysozyme. *J.Mol.Biol.* 181:423.

Levy, R.M., R.P. Sheridan, J.W. Keepers, G.S. Dubey, S. Swaminathan, and M. Karplus. 1985. Molecular dynamics of myoglobin at 298 K. *Biophys. J.* 48:509.

Li, J-C., and D.K. Ross. 1992. Neutron scattering studies of ice dynamics. *In* Physics and Chemistry of Ice. Parts I and II. N. Maeno and T. Hondoph, editors. Hokaido University Press, Sapporo, Japan. 27.

Li, M.H., P. Fan, B. Brodsky, J. Baum. 1993. 2-dimensional NMR assignments and conformation of $(Pro\text{-}Hyp\text{-}Gly)_{10}$ and a designed collagen triple helical peptide. *Biochemistry.* 32:7377.

Lin, L-N., J.F. Brandts. 1979. Role of cis-trans isomerism of the peptide bond in protease specificity. Kinetic studies on small proline containing peptides and on polyproline. *Biochemistry.* 18:5037.

Loncharich, R. J. and B. R. Brooks. 1990. Temperature dependence of dynamics of hydrated myoglobin. Comparison of force field calculations with neutron scattering data. *J. Mol. Biol.* 215:439.

Lounnas, V., B.M. Pettitt. 1994. A connected cluster of hydration around myoglobin - correlation between molecular-dynamics simulations and experiment. *Prot.Struct.Funct.Gen.* 18:133.

Lovesey, S. 1984. *Theory of Thermal Neutron Scattering from Condensed Matter,* International Series of Monographs on Physics 72 (Oxford Science, Oxford).

Machida, K., A. Kagayama, Y. Saito, T. Uno. 1978. Polarised Raman spectra and intermolecular potential of L-alanine crystal. *Spectrochimica Acta.* 34A:909.

MacKerell, A.D., L. Nilson, R. Rigler, U. Heinemann, W. Saenger. 1989. Molecular dynamics simulations of ribonuclease T1: comparison of the free enzyme and the 2'GMP-enzyme complex. *Prot. Struct. Funct. Gen.* 6:20.

Martel, P. 1992. Biophysical aspects of neutron scattering of vibrational modes in proteins. *Prog. Biophys. Mol. Biol.* 57:129.

McCammon, J.A., S.C. Harvey. 1987. Dynamics of proteins and nucleic acids. *Cambridge University Press, Cambridge.*

Meng, E.C., B.K. Sholchet, I.D. Kuntz. 1992. Automated docking with grid based energy evaluation. *J. Comp. Chem.* 13:505.

Merzbacher, E. 1970. Quantum Mechanics. John Wiley and Sons, Inc. New York.

Micu, A., D. Durand, J.C. Smith. *J. Phys. Chem.* in press.

Middendorf, H.D. 1984. Biophysical applications of quasi-elastic and inelastic neutron scattering. *Ann. Rev. Biophys. Bioeng.* 13:425.

Middendorf, H.D., J.T. Randall. 1985. Neutron Spectroscopy and Protein Dynamics. *In* Structure and Motion: Membranes, Nucleic acids and Proteins. E. Clementi, G. Corogiu, M.H. Sarma, and R.H. Sarma, eds. Adenine Press, New York. 219.

Middendorf, H.D. Neutron studies of the dynamics of globular proteins. 1992. *Physica* B182:415.

Miller, A. 1984. Collagen: the organic matrix of bone. *Phil. Trans. R. Soc. Lond. B* 304:455.

Miranker, A., C.V. Robinson, S.E. Radford, R.T. Aplin, C.M. Dobson. 1993. Detection of transient protein folding populations by mass spectrometry. *Science.* 262:896.

Niehaus, G.U., J.R. Mourant, H. Frauenfelder. 1992. Spectroscopic evidence for conformational relaxation in myoglobin. *Proc. Natl. Acad. Sci. U.S.A.* 89:2902.

Nocek, J.M., E.D.A. Stemp, M.G. Finnegan, T.I. Koshy, M.K. Johnson, E. Margoliash, A.G. Mauk, M. Smith, B.M. Hoffman. 1991. Low-temperature, cooperative conformational transition within [Zn-cytochrome-c peroxidase, cytochrome-c] complexes - variation with cytochrome. *J. Amer. Chem. Soc.* 113:6822.

Noguti, T., N. Go. 1982. Collective variable description of small-amplitude conformational fluctuations in a globular protein. *Nature (Lond.).* 296:776.

Okuyama, K., K. Okuyama, S. Arnott, M. Takayanagi, and M. Kakudo. 1981. Crystal and molecular structure of a collagen-like polypeptide $(Pro\text{-}Pro\text{-}Gly)_{10}$. *J. Mol. Biol.* 152:427.

Ormos, P., A. Ansari, D. Braunstein, B.R. Cowen, H. Frauenfelder, M.K. Kong, I.E.T. Iben, T.B. Sauke, P.J. Steinbach, R.D. Young. 1990. Inhomogenous broadening in spectral bands of carbonmonoxymyoglobin. *Biophys. J.* 57:191.

Parak, F., E.W. Knapp, D. Kucheida. 1982. Protein dynamics: Mossbauer spectroscopy on deoxymyoglobin crystals. *J. Mol. Biol.* 161:177.

Parak, F., H. Hartmann, K.D. Aumann, H. Reuscher, G. Rennekamp, H. Bartunik, W. Steigemann. 1987. Low temperature x-ray investigation of structural distributions in myoglobin. *Eur. Biophys. J.* 15:237.

Parak, F., H. Hartmann, M. Schmidt, G. Corongiu, E. Clementi. 1992. The hydration shell of myoglobin. *Eur. Biophys. J.* 21:313-320.

Penfold, J., and J. Tomkinson. 1986. The ISIS time-focussed crystal analyser spectrometer, TFXA. Report RAL-86-019. Rutherford Appleton Laboratory, Chilton, U.K.

Perutz, M.F., F.S. Matthews. 1966. An x-ray study of azide methaemoglobin. *J. Mol. Biol.* 21:199.

Peto, S., P. Gillis, and V.P. Henri. 1990. Structure and dynamics of water in tendon from NMR relaxation measurements. *Biophys. J.* 57:71.

Petrich, J.W., J.C. Lambry, K. Kuczera, M. Karplus, C. Poyart, J.L. Martin. 1991. Ligand binding and protein relaxation in heme proteins: a room temperature analysis of NO geminate recombination. *Biochemistry.* 30:3975.

Postorino, P., F. Fillaux, J. Mayers, J. Tomkinson, R.S. Holt. 1991. The anisotropy of the proton momentum distribution in $KHCO_3$. *J. Chem. Phys.* 94:4411.

Ramachandran, G.N., and R. Chandrasekharan. 1968. Interchain hydrogen bonds via bound water molecules in the collagen triple helix. *Biopolymers.* 6:1649.

Rasmussen, B.F., A.M. Stock, D. Ringe, G.A. Petsko. 1992. Crystalline ribonuclease A loses function below the dynamical transtion at 220 K. *Nature.* 357:423.

Reiher, W.E., M. Karplus. 1993. Refinement of potentials for molecular mechanics simulations using *ab initio* calculations. *Abs. Papers. Am. Chem. Soc.* 206:3.

Renugopalakrishnan, V., G. Chandrakasan, S. Moore, T.B. Hutson, C.V. Berney, R.S. Bhatnagar. 1989. Bound water in collagen: Evidence from Fourier Transform Infrared anf Fourier Transform photoacoustic spectroscopic study. *Macromolecules.* 22:4121.

Ripoll, D.R., C.H. Faerman, P.H. Axelson, I. Suliman, S. Sussmann. 1993. An electrostatic mechanism for substrate guidance down the aromatic gorge of acetylcholinesterase. *Proc. Nat. Acad. Sci. U.S.A.* 90:5128.

Sakakibara, S., Y. Kishida, K. Okuyama, N. Tanaka, T. Ashida, M. Kakudo. 1972. Single crystals of $(ProProGly)_{10}$ a synthetic polypeptide model of collagen. *J. Mol. Biol.* 65:371.

Sansom, C.E., J. Wu, I.T. Weber. 1992. Molecular mechanics analysis of inhibitor binding to HIV-1 protease. *Protein Eng.* 5:659.

Samatey, F.A., G. Zaccai, D.M. Engelman, C. Etchebest, J.L. Popot. 1994. Rotational orientation of transmembrane alpha-helices in bacteriorhodopsin - a neutron-diffraction study. *J.Mol.Biol.* 236:1093.

Sasisekharan, V. 1959. The structure of Polyproline II. *Acta Cryst.* B 897.

Sasisekharan, V. 1960. The structure of Polyproline II. *J. Polymer. Sci.* 47:373.

Sauvajol, J.L., R. Almairac, J. Moret, M. Barthes and J.L. Ribet. 1989. Temperature dependence of the Raman spectum of fully deuterated acetanilide. *J. Raman Spec.* 20:517.

Sauvajol, J.L., G. de Nunzio, R. Almairac, J. Moret, M. Barthes. 1991. Anomalous excitation in hydrogen bonded molecular crystals - a Raman scattering study of specifically deuterated acetanilide. *Solid State Comm.* 77:199.

Sawyer, T.K., D.J. Staples, L. Liu, A.G. Tomaselli, J.O. Hui, K. OConnell, H. Schostarez, J.B. Hester, J. Moon, W.J. Howe. 1992. HIV Protease inhibitor structure activity selectivity and active site molecular modelling of high affinity Leu[CH(OH)$CH_2$]Val modified viral and nonviral substrate analogs. *Int. J. Pep. Prot. Res.* 40:274.

Schlichting, I., J. Berendzen, G.N. Phillips, R.M. Sweet. 1994. Crystal structure of photolysed carbonmonoxy-myoglobin. *Nature.* 371:808.

Scott A.C., E. Gratton, E. Shysamunder and G. Careri. 1985. IR overtone spectrum of the vibrational soliton in crystalline acetanilide. *Phys. Rev.* B 32:5551.

Scott, A.C., I.J. Bigio and C.T. Johnston. 1989. Polarons in acetanilide. *Phys. Rev.* B 39:12883.

Scott A.C. 1992. Davydov's soliton. *Phys. Rep.* 217:1.

Skourtis, S.S., A.J.R. da Silva, W. Bialek, J.N. Onuchic. 1992. A new look at the primary charge seperation in bacterial photosynthesis. *J. Phys. Chem.* 96:8034.

Smith, M., A.G. Walton, and J.L. Koenig. 1969. Raman spectra of poly-L-proline in aqueous solution. *Biopolymers.* 8:173.

Smith, J. C. 1985. Protein dynamics studied by inelastic neutron scattering. *Ph.D. Thesis. Birkbek College, London University.*

Smith, J. C., S. Cusack, B. Tidor, M. Karplus. 1990(a). Inelastic neutron scattering analysis of low frequency motions in proteins: harmonic and damped harmonic models of bovine pancreatic trypsin inhibitor. *J.Chem.Phys.* 93:2974.

Smith, J., K. Kuczera, M. Karplus. 1990(b). Dynamics of myoglobin: comparison of simulation results with neutron scattering spectra. *Proc. Natl. Acad. Sci. U.S.A.* 87:1601.

Smith, J.C. 1991. Protein dynamics: comparison of simulations with inelastic neutron scattering experiments. *Q. Rev. Biophys.* 24:227.

Smith L.J., M.J. Sutcliffe, C. Redfield, C.M. Dobson. 1993. Structure of hen lysozyme in solution. *J. Mol. Biol.* 229:930.

Steinbach, P.J., A. Ansari, J. Berendzen, D. Braunstein, K. Chu, B.R. Cowen, D. Ehrenstein, H. Frauenfelder, J.B. Johnson, D.C. Lamb, S. Luck, J.R. Mourant, G.U. Niehaus, P. Ormos, R. Philipp, A. Xie, R.D. Young. 1991. Ligand binding to heme proteins: connection between dynamics and function. *Biochemistry.* 30:3988.

Streitwolf, H.W. 1971. Group theory in solid state physics. *University Physics Series.* Ed. B. Donovan. Macdonald and Co., London.

Squires, G.L. 1978. *Introduction to the Theory of Thermal Neutron Scattering* Cambridge University Press, Cambridge.

Tageuchi, H., and I. Harada. 1990. Ultraviolet resonance Raman spectroscopy of X-proline bonds – a new marker of hydrogen bonding at the imide C=O site. *J. Raman. Spec.* 21:509.

Tan, R.C., T.N. Truong, J.A. McCammon, J.L. Sussman. 1993. Acetylcholinesterase - Electrostatic steering increases the rate of ligand binding. *Biochemistry.* 32:401.

Tariq S., N. Ali and P.K. Verma. 1984. Vibrational assignments of acetanilide, p-bromoacetanilide and p-aminoacetanilide. *Indian J. Pure Appl. Phys.* 22:268.

Tenenbaum, A., A. Campa and A. Giansanti. 1987. On the unconventional amide I band in acetanilide. *Phys. Lett.* A 121:126.

Tilton, R.F., J.C. Dewan, G.A. Petsko. 1992. Effects of temperature on protein structure and dynamics: x-ray crystallographic studies of the protein ribonuclease A at nine different temperature from 98 to 320 K. *Biochemistry.* 31:2469.

Traub, W., U. Shmueli. 1963. Structure of poly-L-proline I. *Nature.* 198:1165.

Twyman, J.M., C.M. Dobson. 1988. Aromatic ring dynamics in crystalline penicillins from variable temperature C13 cross polarisation magic angle spinning nuclear magnetic resonance. *J. Chem Soc. Chem. Comm.* 12:786.

Twyman, J.M., C.M. Dobson. 1990. Aromatic ring dynamics in crystalline solids by exchange spectroscopy. *Mag. Res. Chem.* 28:163.

van Hove, L. 1954. Correlation in space and time and Born approximation scattering in systems of interacting particles. *Phys. Rev.* 95:249.

Velikson, B., T. Garel, J.C. Niel, H. Orland, J.C. Smith. 1992. Conformational distribution of heptalanine: analysis by a new Monte Carlo chain growth method. *J.Comp. Chem.* 13:1216.

Vonitzstein, M., W.Y. Wu, G.B. Kok, M.S. Pegg, J.C. Dyason, B. Jin, I.V. Phan, M.L. Smythe, H.F. White, S.W. Oliver, P.M. Colman, J.N. Varghese, D.M. Ryan, J.M. Woods, R.C. Bethell, V.J. Hotham, J.M. Camer, C.R. Penn. 1993. Rational design of potent sialidase-based inhibitors of influenza virus replication. *Nature.* 363:418.

Vos, M.H., F. Rappaport, J-C. Lambert, J. Breton, J-L. Martin. 1993. Visualisation of coherent nuclear motion in a membrane protein by femtosecond spectroscopy. *Nature.* 363:320.

Wagner, G., K. Wutrich. 1986. Observation of internal mobility of proteins by nuclear magnetic resonance in solution. *Meth. Enzym.* 131 L:307.

Wallin S.A., E.D.A. Stemp, A.M. Everest, J.M. Nocek, T.L. Netzel, B.M. Hoffman. 1991. Multiphasic intracomplex electron-transfer from cytochrome-c to Zn cytochrome-c peroxidase - conformational control of reactivity. *J. Amer. Chem. Soc.* 113:1842.

Wang, C.H., R.D. Storms. 1971a. Temperature dependent Raman study and molecular motion in L-alanine single crystal. *J. Chem. Phys.* 55:3291.

Wang, C.H., R.D. Storms. 1971b. Raman study of hydrogen bonding and long-wavelength lattice modes in an L-alanine single crystal. *J. Chem. Phys.* 55:5110.

Wang, Q., R.W. Schonlein, L.A. Peteanu, R.A. Mathies, C.V. Shank. 1994. Vibrationally coherent photochemistry in the femtosecond primary event of vision. *Science.* 266:422.

Warner, M., S.W. Lovesey, and J. Smith. 1983. The theory of neutron scattering from mixed harmonic solids. *Z. Phys. B - Condensed Matter.* 51:109.

Wasserman, H.J., R.R. Ryan and S.P. Layne. 1985. Structure of acetanilide at 113 K. *Acta Cryst.* C 41:783.

Wess, T.J., A. Miller, and J.P. Bradshaw. 1990. Cross-linkage sites in type I collagen studied by neutron diffraction. *J. Mol. Biol.* 213:1.

White, J.W. 1976. Inelastic neutron scattering from synthetic and biological polymers. *In* Neutron scattering for the analysis of biological structures. *Brookhaven Symp. Biol. 27.* B.P. Schoenborn, editor. Upton, N.Y., Brookhaven Natl. Lab. VI3.

Wilson, E.B., J.C. Decius, P.C. Cross. 1980. *Molecular Vibrations.* (Dover Publications, New York).

Windsor, C.G. 1981. Pulsed Neutron Scattering. Taylor & Francis, London.

Wlodawer, A., L. Sjolin. 1983. Structure of ribonuclease A: results of joint neutron and x-ray refinement at 2.0 angstrom resolution. *Biochemistry.* 22:2720.

Yonath, A., and W. Traub. 1969. Polymers of tripeptides as collagen models IV. Structure analysis of poly(L-prolyl-glycyl-L-proline). *J. Mol. Biol.* 43:461.

Zemach A.C. and R.J. Glauber. 1956. The dynamics of neutron scattering by molecules. *Phys. Rev.* 101:118.

Zhang X.J., B.W. Matthews. 1994. Conservation of solvent-binding sites in 10 crystal forms of T4-lysozyme. *Prot. Sci.* 3:1031.